Subwavelength Grating Based Microcavity and Its Applications in Many-body Polariton Systems

by

Zhaorong Wang

A dissertation submitted in partial fulfillment
of the requirements for the degree of
Doctor of Philosophy
(Electrical Engineering)
in The University of Michigan
2017

Doctoral Committee:

Associate Professor Hui Deng, Co-Chair
Professor Duncan G. Steel, Co-Chair
Professor Theodore B. Norris
Assistant Professor Kai Sun

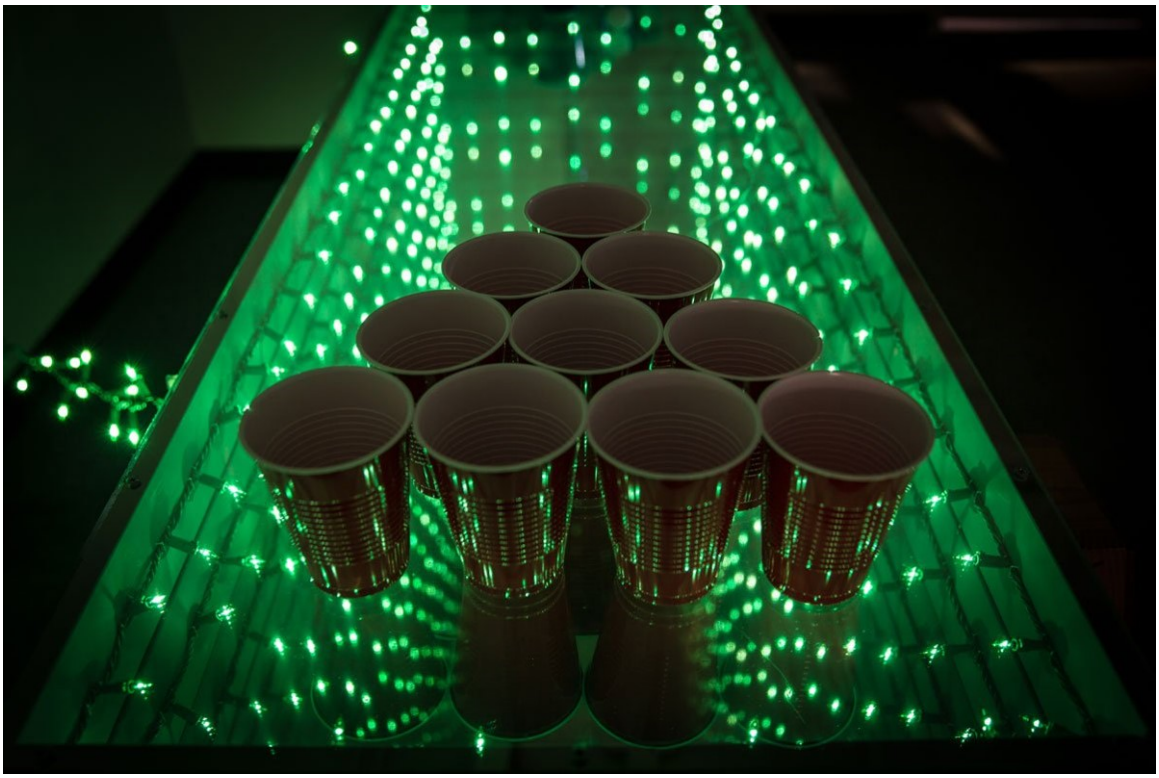

This is an optical cavity, used for a party...

(photo credit: http://makezine.com/projects/easy-mega-infinity-mirror/)

To my parents for all their caring and love and putting me through the best education possible.

To all my teachers and mentors from elementary school to present. I wouldn't have gone this far without their guidance, encouragement and support.

ACKNOWLEDGEMENTS

First I must thank my research advisor Professor Hui Deng for her guidance and support over the past 6 years. Professionally she sets a very good example for me. I admire her intellectual sharpness and high professional standard. I'm grateful for the solid training she gave me, in research, in writing and presenting. At the same time, she remains kind and approachable. Her door is always open to me and all her students. She is patient in listening to me in my first few years no matter how trivial the issues I brought up. Her genuine inquisitiveness and attention to detail make our discussions very effective and enjoyable. She also showed me a respectable attitude against bias in thinking and treating people. She is always nonjudgmental to her students, so I can share anything with her, good news or bad news. Throughout the years, I appreciate that she never coerces; she only suggests, and encourages students' own interest and motive. She never instructs; she stimulates students' own thinking. She seems never push on students but listen to our problems and suggest solutions and workarounds, even at the worst situations, and even though she was a stressed pre-tenure assistant professor until recent. She also shields us from the stressful grant proposals and provides us with ample fundings. I am thankful that she fully supported me most of the years so I can focus my time on research. I also never felt financially constrained in purchasing any equipments or software for my research.

Additionally I appreciate she maintained a good management system. Particularly I found writing a progress report and presenting it in weekly individual meetings very

useful. Writing the weekly reports (powerpoint) has become indispensable for me to clear my thoughts and keep a valuable record for future recall. I will probably keep this good habit in my future jobs, even if there were no such requirement. The weekly meeting and small group meetings is also the precious time for me to receive timely feedback. I appreciate she invests the time to be with us regularly. She also stays clear of micro-management. She gives us ample freedom and believe us all have good intentions and have the capability to organize research and life effectively.

It is my luck that I can learn and do research under Hui's guidance, in the best years of my life.

Next I would like to thank other members on my doctoral committee– Prof. Duncan Steel, Prof. Ted Norris and Prof. Kai Sun. It was Prof. Steel, appointed professor in both EE and physics department, who initially agreed to be my co-advisor, which allowed me to join Hui's group in physics department. I'm grateful for his kindness in facilitating my transition from a EE group to a physics group, so that I can pursue my physics interests from the bottom of my heart. He gave me many good advices when I first entered the lab and started doing serious experiments.

Prof. Norris is another professor who influenced me a lot over the years. His course, Classical Optics, is the most useful course I've taken in grad school, which forms the basis of many parts of this thesis. His insightful understanding of almost every optics topics helped me to build a crystal-clear knowledge framework. Coincidentally, he is one of the founding researchers in the field of microcavity polaritons. His early papers in the 90s helped me clear many confusions in the field. I often seek advices from him on new research topics in the field, such as carrier dynamics and nonlinear regime of polaritons. he can always pick a good book from his bookshelf, either a well-written book chapter he contributed in some summer school or other people's contributions. I love to ask him questions, either on fundamental topics or new research directions. His breadth in knowledge and capability to see the

connections between different topics really inspired me a lot over the years.

Prof. Sun is another professor who helped me on many occasions during my PhD years. His advanced condensed matter physics course exhibits for the first time the beauty of theoretical condensed matter physics to me. I was introduced of many the newest theoretical understandings and trends in solid-state physics. He is also my enlightener of many-body physics, which forms the basis of part of this thesis. He is always kind. I enjoyed every discussion with him. He can explain things with easy-to-understand languages, while keeping the mathematical rigor. I'm lucky to come across such a good theorist in my mostly experimentalist PhD life.

I appreciate all of their direct and indirect help during the past 6 years. And I thank them for sparing time of serving the committee of my dissertation.

Next I would like to thank all Deng Group members, Bo Zhang, Paul Bierdz, Lei Zhang, Tyler Hill, Seonghoon Kim, Glenn Leung and many newly joined students and post-docs. Among them, Lei was my first referral to this group. I learned the group's business through him when I first decided to join the group. He was also my first peer-mentor. He taught me a lot in the lab and left me a legacy of an RCWA code which I initially used to simulate the hybrid cavity presented in this thesis. He is highly competent in every business and research topic in our lab, and he is always willing to help. I can recall many scenes of he explaining complex concepts to me on the white board whenever I asked. I resonate very much with one of his philosophies: if one cannot explain a thing to others, he does not truly understand it. He is so passionate about research, able to see the value of our on-going projects and loves to share his new research ideas. These all influenced me tremendously from my starting stage of research to present. I felt lucky enough to have a role model like him.

Bo is the senior student in the group I spent most of the time with. He is in charge of the fabrication of the sample presented in this thesis. This thesis is not possible without his success in the sample fabrication. We shared the distress when the sample

failed repeatedly in the early days, and the excitement of a first working sample in the summer of 2012. I shadowed him in the lab to learn how to characterize our sample. He is knowledgeable in the polariton field, introduced me many concepts and experimental works from other groups. He also gave me many mental support. He encouraged me when I was stuck in research and celebrated with me when I achieved something important. He is the senior student I always trust and turn for advices at each turning point of my PhD life, especially later in my job seeking. I cannot expressed more gratitude to him as a mentor and a friend.

I simply cannot thank all group members in details here, but this thesis cannot be done without the collaborative work we did together, the encouragement we gave each other and inspirations I received through discussions with each of them. We are a great team!

Next I would like to thank all collaborators during my thesis projects. They are University of Wuerzburg group led by Sven Höfling. I'm very grateful to them for providing the high-quality sample wafers, without which this thesis is not possible. A theorist participated in my nonlinear regime project is Prof. Rolf Binder in University of Arizona. He is an expert in investigating semiconductor optics with quantum many-body theories. I learned a lot from him in each Skype meeting and through his writings. Without his good work, I wouldn't be able to find a working theory for the new findings I had in our cavity system. I thank him for the large amount of time he put in this project and persisting in seeking better theories which made the project more and more interesting. I hope Jiaqi or other new students in our group could carry on this good project.

Lastly I would like to thank all my friends who supported me throughout this long PhD journey. To mention a few, Zhidong Du in Purdue university is my best college friend. His early research experience in experimental AMO physics induced my interests in optical physics, which caused me to choose my current group. His

encouragement and comfort when I was in low mental state kept me going. We can call for hours to discuss physics problems, his projects and my projects. We share tips and resources on many things of our common interests. Eric Yue Ma from Stanford University is my best high school friend. We know each other through participating in Physics Olympiad in China. We share very similar interests, similar intuition about physics. Although we are not in the exactly same field, discussions with him enlightened me every time. He is another role model of me in conducting scientific research. Long Chen is my best friend here in Ann Arbor. He is in a very similar research field with me and shared many common interests. I like figuring out things together with him. I'm also very grateful for his caring in one medical emergency when I lost walking capability for days. I would also like to thank my girlfriend Kefan, for her continuous understanding and appreciation of my work, even though I had to ask her to spend one Christmas with me in the lab for an important experiment I have to finish. We traveled together to many beautiful places in Michigan and across the U.S.. Her company definitely made my PhD life more colorful and memorable. I also want to thank Chen Feng, Xiang Sun, Tianxiang Qi, Si Hui, Shengtao Wang, Jiahua Gu, Wenjian Xu for all their help and company in my PhD journey. We spent great time together. I thank Jia Xu, Jingyi Fang, Ming Zhong, Anbo Chen, Jingjing Li, Feng Zhao, Ming Yao and again Bo Zhang and Lei Zhang for their help in my job seeking. I thank Liz Dreyer and Cheng Zhang for their good leadship in optical society at UM (OSUM). I also thank all OSUM officers. OSUM makes me feel the belongingness to the field of optics. I thank my many roommates during my PhD years, especially Di Fu, who lived with me for the longest time. I thank them for giving me a good living environment and positive life attitude. We had much fun together. I also want to thank Kang's, a Korean restaurant I visited often to enjoy tasty food. For all other friends who helped me during my PhD, I'm sorry I cannot mention you all here. I sincerely express my gratitude to all of you!

TABLE OF CONTENTS

LIST OF FIGURES

Figure

LIST OF APPENDICES

Appendix

ABSTRACT

Subwavelength Grating Based Microcavity and Its Applications in Many-body Polariton Systems

by

Zhaorong Wang

Chair: Hui Deng

Semiconductor microcavity polaritons have attracted intense research in the past 20 years because of its deep connections with macroscopic quantum phenomena such as Bose-Einstein condensation (BEC), superfluidity and superconductivity. Experimental polariton systems have evolved as powerful research tools for many-body physics, and have shown promise for novel devices such as ultra-low threshold laser and polaritonic integrated circuit. A central issue to all experimental polariton systems is how to effectively confine and manipulate polaritons. Existing systems all have their limitations such as small modulation depth, destructive to the active medium, and difficult to fabricate or reproduce. In this thesis, we develop a sub-wavelength grating (SWG) based microcavity to generate and control polaritons, which overcomes the limitations of existing systems and has unique properties leading to new physics that was inaccessible before.

We demonstrated discrete polariton modes in a fully confined zero dimensional SWG cavity and lasing in the ground state via a thorough set of optical measurements. This shows that the new SWG-cavity can not only support polariton modes but also

maintains low loss and allows the formation of coherent polariton condensate. This is the prerequisite of using our system to study macroscopic quantum phenomena and novel many-body physics.

Further, polariton nonlinearity was studied from a unique perspective, revealing phenomena contrary to commonly held understanding. Thanks to the polarization anisotropy of the SWG mirror, exciton reservoir of our system can be directly probed through the emission of the weakly-coupled excitons that co-exist with the strongly-coupled polaritons. We show that polariton nonlinearity originate mainly not from exciton energy renormalization, but saturation. The saturation pair density was matched to theoretical values. Reflectance measurements unambiguously show that, at high pump density, excitons already undergo Mott-transition while polariton and polariton lasing is maintained. This is in contrary to previous belief of polariton lasing is realized at far below Mott-density of excitons. Our results point to the light mediated electron-hole binding in a BCS-like state of polaritons.

Finally, we demonstrated polariton mode engineering through the design of SWG. Specifically, a SWG is optimized to reduce the mode volume of the cavity, which enhances the coupling strength between excitons and vacuum photons by up to 67% compared to conventional GaAs polariton systems. The larger coupling strength can help increase the operating temperature of polariton systems. Further, SWG cavities with engineered dispersion are demonstrated by designing the angular phase response of SWG mirror. Polariton dispersion is therefore strongly modified, which may enable different polariton dynamics and even exotic quantum orders. As an experimental effort of mode engineering, we demonstrate coupled 0D SWG cavities and quasi-1D polariton lattice. Theoretical modeling using harmonic potential traps and gaussian potential barriers matches well with experiments. The potential depth ranges from 4 meV to 20 meV. These engineered SWG polariton systems provide an unique venue for research on lattice physics and quantum optical circuits.

CHAPTER I

Introduction

The past few decades have seen exciting breakthroughs in the field of solid-state optics. A prominent example is the development of an assortment of semiconductor heterostructures, which are the basis of many Nobel-prize winning work – coupled charge device (CCD), semiconductor laser and blue light-emitting diode (LED). Their usage in lighting, imaging and optical communication have deeply changed people's lives and accelerated technological revolutions in many aspects. These breakthroughs and inventions cannot happen without the fundamental understandings from quantum mechanics, atomic physics and solid-state physics accumulated in the first half of 20th century. In turn, novel solid-state optical systems provide unique laboratories for the study of their mother fields and further deepen people's understanding.

Microcavity polariton system is such an excellent example of providing both fundamental research value and device application prospect. Microcavity polaritons (short as polaritons below) are hybrid quasi-particles formed by a superposition of an exciton and a cavity photon. Since its debut in the 90s [12], polariton systems have reproduced many spontaneous coherence phenomena such as Bose-Einstein condensation (BEC) [13, 14, 15], superfluidity [16] and quantized vortices [17] which are previously exclusively realized in atomic systems prepared with extreme conditions [18, 19]. Due to polaritons' half-matter half-light nature, they inherit good properties

from both. The small effective mass from their photon part made BEC possible at elevated temperature. And the strong Coulomb interactions from the exciton part made their many-body phases interesting and designable. They have been proposed to form the building blocks of quantum simulators [20, 21, 22]. Their strong nonlinearity and fast response time has been demonstrated to form the key components in integrated photonic circuits[23, 24, 25, 26]. Last but not least, the polaritons feature finite lifetime compared in contrast to their atomic counterparts. The system needs to be constantly pumped to maintain the particle density. This open and dissipative nature of the polariton systems expands people's understanding of non-equilibrium spontaneous coherence physics [27, 28].

A good experimental system cannot live without good means of control and engineering. Polariton systems have their unique advantages– they can be controlled via either the exciton part or the photon part. One can apply electric field, magnetic field, mechanical stress or simply vary pumping to control the exciton part. Thanks to the advances of nano-fabrication technologies, the photon part of polariton systems can also be engineered with unprecedented freedom. This thesis adopts the later approach– engineering the photon part through the design of a novel cavity architecture.

The theme of this thesis is the exploration of one engineering route – making subwavelength grating (SWG) based microcavity for designable and scalable polariton systems. The major achievements are:

- In-house design and fabrication of the SWG-based microcavity
- Demonstration of polariton lasing with desired properties
- Simultaneous observation of polariton lasing and Mott-transitioned excitons thanks to SWG's polarization asymmetry
- Mode engineering for robust polaritons, dispersion-engineered polaritons and

coupled polaritons useful for quantum simulators and polaritonic devices

In this introductory chapter, I will give an overview of the basic pictures in the microcavity polariton research field. Specifically, (i) What basic physics the polariton systems are based off; (ii) What new physics the polariton systems enables; (iii) Previous efforts devoted to explore these new physics. Finally I will introduce the organization of this thesis.

1.1 Semiconductor is the New Vacuum

Vacuum for Quasi-particles

A basic understanding of solid-state physics is, electrons are moving in the periodic potential created by the ions in the lattice. The eigen-energies of the electrons form so-called energy bands in the momentum space or k-space. The energy bands may or may not overlap. The non-overlapping energy bands form an energy gap called bandgap. The bandgap of semiconductor (usually 0.5eV – 4eV or 2.5 μm – 300 nm) is particularly interesting because it corresponds to the visible photon energy and some near infrared and violet. The two energy bands forming the energy gap are called valence band (lower) and conduction band (higher). A direct bandgap from semiconductors such as GaAs and CdTe is illustrated in Figure 1.1. Semiconductors are insulators, with valence band filled up with electrons at zero-temperature while the conduction band is empty. This is the ground state of the semiconductor. Thermal excitation or photo-excitation can move electrons from the valence band into the conduction band (Fig. 1.2 left).

Here comes one of the most important pictures in solid-state physics– the electrons at the bottom of the conduction band move "freely" with an effective mass determined by the curvature of the energy-momentum dispersion. Similarly the electrons at the top of the valence band also move freely with effective mass determined by the

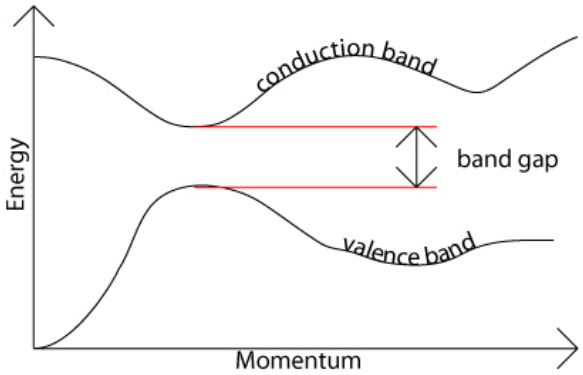

Figure 1.1: Illustration of Direct Bandgap. (Image credit: https:// www.doitpoms.ac.uk /tlplib/semiconductors/direct.php)

curvature there. This means, the semiconductor is no different than a free-space or vacuum for the electrons. It is just the masses of the electrons are modified by the new vacuum (eg. $m_e^* \sim 0.06m_e$ for GaAs). Since we are considering small amount of excitations from the ground-state, it is helpful to consider the motion of the electron vacancies in the valence band instead of the large quantities of electrons. The electron vacancy is named "hole", a quasi-particle with positive charge, positive effective mass (eg. $m_h^* \sim 0.5m_e$ for GaAs), well defined energy and momentum. We thus can construct a hole band to replace the valence band (Fig. 1.2 right). The quasi-particle picture largely simplifies the description of electronic and optical properties of semiconductors.

In the quasi-particle picture, an exciton can be understood as the bound state of one free electron (negatively charged) and one free hole (positively charged) in the host semiconductor vacuum. It is analogous to the hydrogen atom which is the bound state of an electron and a proton. The exciton's motion can thus be decomposed into the center of mass motion with the total mass $m_{exc} = m_e^* + m_h^*$ and the relative motion with reduced mass $\mu_{exc} = m_e^* m_h^*/(m_e^* + m_h^*)$. By now, we have created artificial atoms in semiconductors! These artificial atoms can further bound into for instance bi-excitons and positively or negatively charged trions, which are responsible for many optical features in semiconductors. A large part of semiconductor optics is

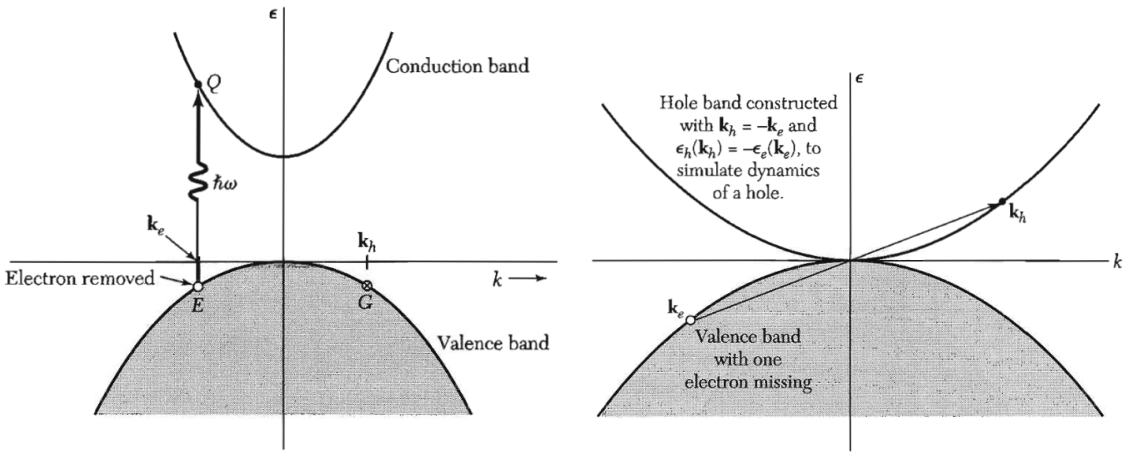

Figure 1.2: Illustration of photo excitation of semiconductor (left) and construction of hole band (right). (Image taken from Kittel [1])

built around exciton physics. Virtually every optoelectronic device utilizes excitons in their operations. Even at room temperature, where the excitons in most III-V semiconductor devices are not stable due to the thermal ionization, the excitonic effect still plays important roles in light detection, generation and lasing.

Then what's the good of using the artificial atoms instead of the real ones? The answer is they can be easily manipulated and property-tailored to one's needs, creating distinct matter states. First, the properties of the quasi-particles can be constructed by selecting different host semiconductors. Instead of choosing single element from the periodic table, one can also choose from a myriad of compound semiconductors, such as GaAs, AlAs and CdTe, even alloys or doped version of them. They have vastly different bandgaps and band structures including degenerate or non-degenerate spin states. The resulting excitons therefore have diverse energies and binding energies (Fig. 1.3), oscillator strengths and spin polarizations. Second, the excitons can be easily confined and controlled. Semiconductors with different energy bands can be fabricated into heterostructures. The best known example is the quantum well (QW) [29], a sandwich structure formed by a smaller bandgap thin layer in the middle, as illustrated in Figure 1.4. The motion of electrons and holes are confined in the thin

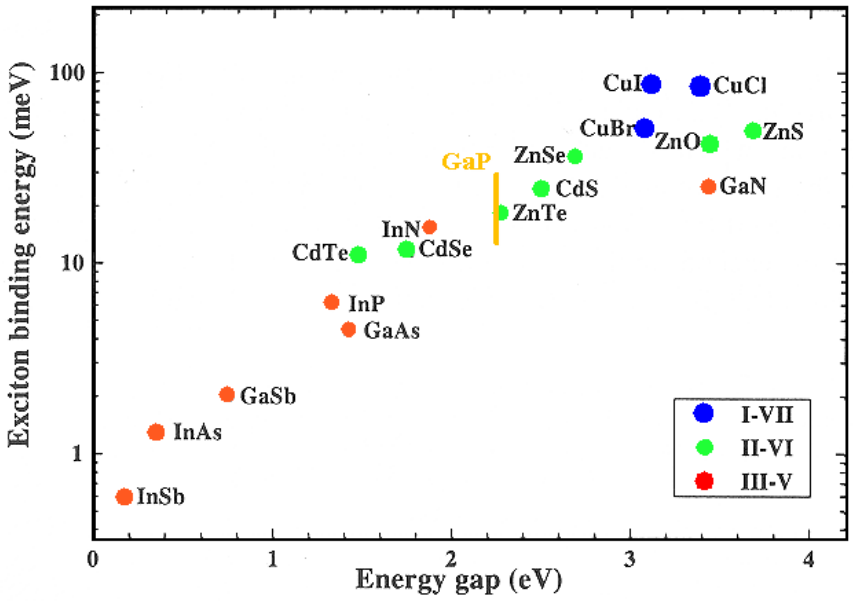

Figure 1.3: The binding energy and bandgap of common direct bandgap semiconductors (bulk). (Image credit: https://www.tf.uni-kiel.de/matwis/amat/)

well region because of the potential barriers at the two sides. Discrete energy bands (particle in box) are formed, covering the in-plane momentum space. This confinement increases the probability of electron-hole bounding, making the exciton effect in QW particularly eminent. Because of the "squeezing" effect on excitons (bulk GaAs Bohr radius ∼30nm) by the QW (thickness ∼10nm), the oscillator strength and binding energy is significantly improved in QWs (Table 1.1). Lastly, crystal growth and nano-fabrication technologies can make the final sculpture of the semiconductor systems. For example, molecular beam epitaxy (MBE) can grow multiple QWs a few atomic layers apart from each other, producing coupled QWs and QW superlattice useful for infrared laser applications. The grown layered structures can be further "cut" into 1D wire or 0D dot, forming the lower dimensional quantum wires and quantum dots, which are another two vast research fields. This thesis will focus on GaAs QWs because they can be made nearly defect-free with most mature fabrication technology.

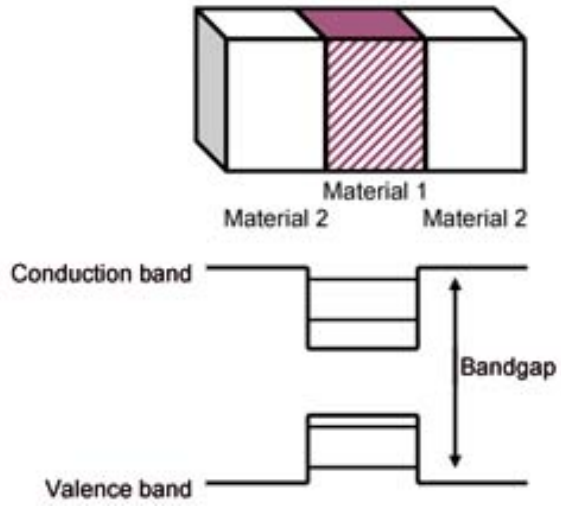

Figure 1.4: Band diagram of a typical quantum well. (Image credit: http://www.ir-nova.se/qwip/)

Table 1.1: Summary of excitonic properties for common semiconductor families (reproduced from [30])

	III-Arsenides	II-tellurides	III-Nitrides	ZnO
Binding energy (meV)				
Bulk	4.9	11	25–27	60
QW	7-9	~ 22	~ 50	~ 90
Bohr radius (nm)				
Bulk	11.2	12.2	2.8	2.3
QW	~ 10	NA	~ 1.7	~ 2
QW oscillator strength (cm^{-2})	4.8×10^{12}	2.3×10^{13}	4.8×10^{13}	NA

Vacuum for Photons

Semiconductors as dielectric materials can also host photons. Photons are the quanta of electromagnetic (EM) modes, which are obtained by solving Maxwell's equations under certain boundary conditions. Specificaly, in a source-free space with lossless dielectric materials (Fig. 1.5), the electromagnetic modes are determined by an eigenvalue equation [2]:

$$\nabla \times \left(\frac{1}{\epsilon(\mathbf{r})} \nabla \times \mathbf{H}(\mathbf{r}) \right) = \left(\frac{\omega}{c} \right)^2 \mathbf{H}(\mathbf{r}). \tag{1.1}$$

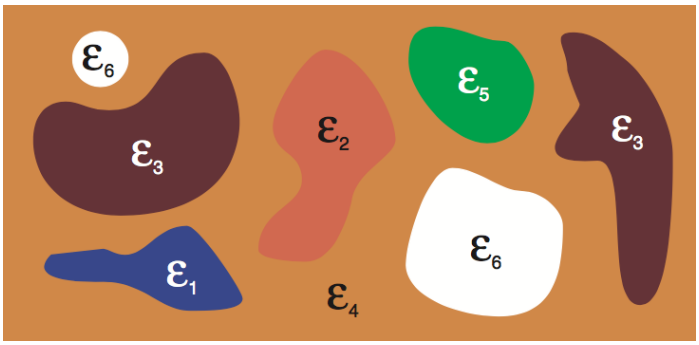

Figure 1.5: A composite of macroscopic regions of homogeneous dielectric media. Taken from ref[2]. There are no charges or currents. In general, $\epsilon(\mathbf{r})$ in equation (1.1) can have any prescribed spatial dependence, but our attention will focus on materials with patches of homogeneous dielectric, such as the one illustrated here.

$\mathbf{H}(\mathbf{r})$ is the magnetic field. $\epsilon(\mathbf{r})$ is the permittivity as a function of space coordinates. The operators before $\mathbf{H}$ on the left hand side can be considered as a big operator. It is a Hermitian operator. With the magnetic field $\mathbf{H}(\mathbf{r})$, the electric field can be obtained by

$$\mathbf{E}(\mathbf{r}) = \frac{i}{\omega\epsilon_0\epsilon(\mathbf{r})}\nabla \times \mathbf{H}(\mathbf{r}). \tag{1.2}$$

Suppose one solves the eigenvalue problem (1.1) and obtain a complete set of EM modes $\{E_j, H_j\}$, j is the mode index, the next step is quantization. For the simplest free-space, the modes are plane waves $E_j\mathbf{e}_j e^{i\mathbf{k}_j\cdot\mathbf{r}}$. one can write the quantized electric field operator as [31]

$$\hat{\mathbf{E}}(\mathbf{r}) = i\sum_j E_j(\hat{a}_j\mathbf{e}_j e^{i\mathbf{k_j}\cdot\mathbf{r}} - \hat{a}_j^\dagger\mathbf{e}_j e^{-i\mathbf{k_j}\cdot\mathbf{r}}), \tag{1.3}$$

where $\mathbf{e}_j$ is the polarization unit vector of the mode j, E_j is a (real) normalization constant, $\hat{a}_j$ ($\hat{a}_j^\dagger$) is the destruction (creation) operator for a mode having propagation vector k_j and polarization $\mathbf{e}_j$.

As can be seen, the quantization is merely multiplying a destruction (creation) operator to each EM mode. The core task is still solving the classical equation (1.1)

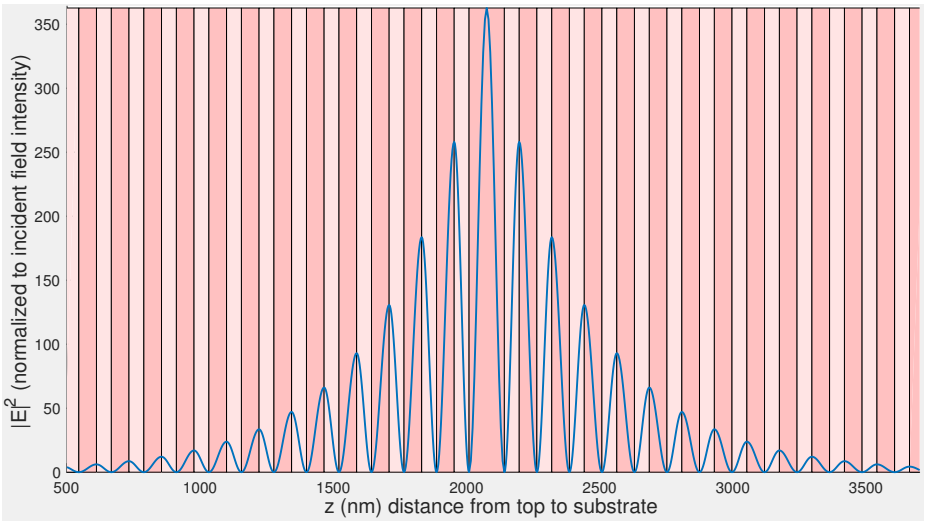

Figure 1.6: What a cavity photon looks like. Or the field distribution at cavity resonance. Darker pink is AlAs (refractive index = 3.02 at 800nm), lighter pink region is $Al_{0.15}Ga_{0.85}As$ (refractive index = 3.58 at 800nm). DBR layers all have $\lambda/4$ optical path length (OPL). The center cavity layer has $\lambda/2$ OPL. $\lambda = 800nm$ is the design wavelength.

for the composite dielectric media (Fig. 1.5). In other words, what photons the composite dielectric media can support is totally determined by the dielectric constant distribution $\epsilon(\mathbf{r})$. One thus can design the arrangement of the homogeneous dielectric media, in our context the semiconductors, in particular ways to harvest the photons of one's interest.

Semiconductor microcavities serve exactly this purpose. The most commonly used semiconductor microcavity is the Fabry-Perot cavity constructed by two distributed Bragg reflectors (DBRs). DBR consists of periodic high and low refractive index dielectric layers that mimic the lattice structure in a crystal. It thus gains a photonic "bandgap" so that light with frequency in the bandgap cannot pass, or is totally reflected. DBRs can be used as ultra-high reflectance mirrors in a Fabry-Perot cavity. An optimized GaAs/AlAs based DBR cavity is shown in Fig. 1.6. The blue line shows the E-field distribution of the fundamental mode of the cavity (with zero in-plane wavenumber). The thickness of each layer determines the resonance frequency (at certain in-plane wavenumber) and the field distribution of the cavity. Therefore

the energy-momentum dispersion and mode profile of the photons created in this cavity can be engineered by using different combinations of semiconductor stacks. This is just a simple example of 2D translational-invariant DBR cavity. By breaking more symmetries, there are endless possibilities to create photons in 2D, 1D and 0D with diverse properties. I will come to this in the last chapter– photon engineering using subwavelength gratings.

1.2 Microcavity Polaritons

When multiple elementary excitations are supported by the semiconductor vacuum, they could couple and form new elementary modes. Microcavity Polaritons are such modes resulting from the strong coupling between QW excitons and cavity photons. For example, one can integrate a QW at the largest anti-node of the photon field (Fig. 1.7). The exciton supported by the QW is therefore coupled to the photon field via dipole interaction. Polaritons can be well described by coupled oscillators. The Hamiltonian can be generically written as (in rotating-wave approximation)

$$\hat{H} = \hbar\omega_c \hat{a}^\dagger \hat{a} + \hbar\omega_x \hat{b}^\dagger \hat{b} + \hbar\Omega(\hat{b}^\dagger \hat{a} + \hat{a}^\dagger \hat{b}), \tag{1.4}$$

where $\hbar\omega_c$ is the photon energy with ω_c being the cavity resonance frequency, $\hbar\omega_x$ is the QW exciton energy. $\hbar\Omega$ is the coupling strength, called the Rabi energy (frequency). $\hbar\Omega = \mathbf{d} \cdot \mathbf{E}_0$, where $\mathbf{d}$ is the dipole moment of an exciton, $\mathbf{E}_0$ is the vacuum fluctuation photon field. Because of this the Rabi energy is also called vacuum Rabi splitting.

The above Hamiltonian can be diagonalized (renormalized) by the transformations

$$\hat{P} = X\hat{b} + C\hat{a}, \quad \hat{Q} = -C\hat{b} + X\hat{a}. \tag{1.5}$$

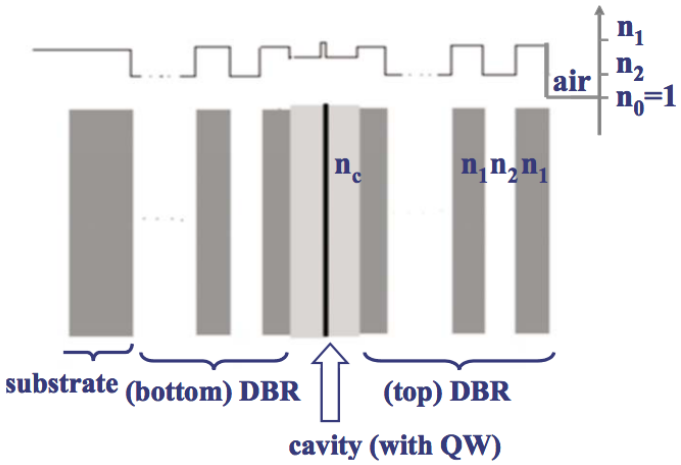

Figure 1.7: Sketch of a semiconductor $\lambda/2$ microcavity with QW. Taken from Ref [3]

Then the Hamiltonian becomes

$$\hat{H} = E_{LP}\hat{P}^{\dagger}\hat{P} + E_{UP}\hat{Q}^{\dagger}\hat{Q}. \tag{1.6}$$

Here $(\hat{P}^{\dagger}, \hat{P})$ and $(\hat{Q}^{\dagger}, \hat{Q})$ are the creation and annihilation operators of the new eigenmodes of the system or quasi-particles, called lower polaritons (LP) and upper polaritons (UP). The coefficients X and C are referred to as the Hopfield coefficients [32]. They satisfy

$$|X|^2 + |C|^2 = 1. \tag{1.7}$$

They represent the fractions of excitons and photons respectively in the new quasi-particles polaritons.

The most important parameter of the quasi-particles– effective mass can be obtained by the harmonic mean of the exciton mass and photon mass weighted by the Hopfield coefficients

$$\frac{1}{m_{LP}} = \frac{|X|^2}{m_{exc}} + \frac{|C|^2}{m_{cav}}, \quad \frac{1}{m_{UP}} = \frac{|C|^2}{m_{exc}} + \frac{|X|^2}{m_{cav}}, \tag{1.8}$$

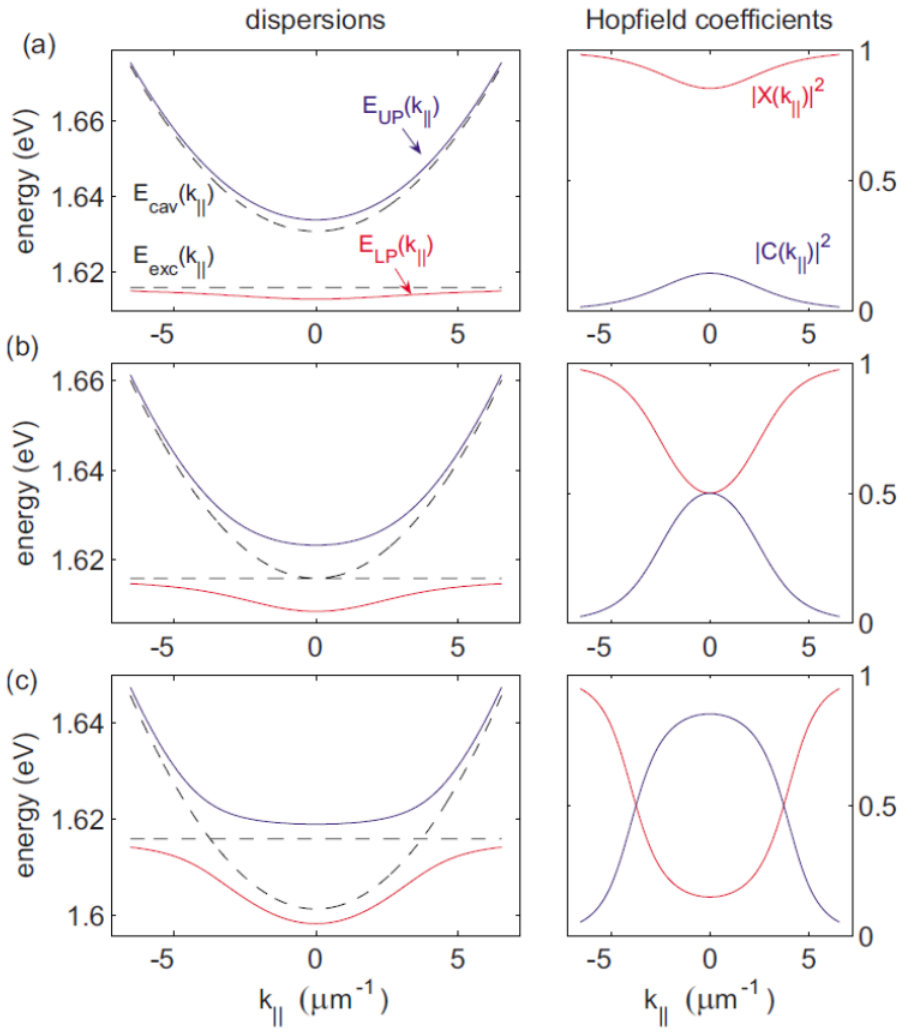

Figure 1.8: Polariton dispersion with different detunings. Taken from Ref [3]

Because the photon effective mass is usually much smaller than the exciton's ($10^{-5}m_e$ vs $10^{-1}m_e$), the polaritons' effective mass is dominant by the photon's mass, thus much smaller than any atomic counterpart. This feature makes Bose-Einstein condensation at elevated temperature possible.

Implicit in above equations, all operators and coefficients are functions of the good quantum number of the system. For the 2D semiconductor microcavity and 2D QW concerned, the in-plane wavenumber is the good quantum number. The energies of the polaritons as a function of the in-plane wavenumber (energy dispersion) can be

found to be

$$E_{LP,UP}(k_{||}) = \frac{1}{2}[\hbar\omega_x + \hbar\omega_c \pm \sqrt{4\hbar^2\Omega^2 + \hbar^2(\omega_c - \omega_x)^2}]. \tag{1.9}$$

Examples of the polariton energy dispersion with different detuning are shown in Fig. 1.8. The exciton dispersion is basically flat in the k-space range we are considering. The photon dispersion is for conventional DBR cavities, with effective mass $\sim 10^{-5} m_e$. We will see in the last chapter, the photon dispersion can be engineered by using subwavelength grating.

1.3 Many-body Phases of Polaritons

The most studied and well-understood many-body phase of the polaritons is the BEC phase. Polariton is the superposition of an exciton and a photon. Photon is a boson. Exciton is a composite particle made of two fermions. It also obey boson statistics as long as their density is low enough such that they do not overlap, that is

$$n_{exc} < 1/a_B^2 \tag{1.10}$$

where a_B is the Bohr radius of the exciton. Therefore polaritons at this low density condition also obey boson statistics. Condensation is possible if lower polaritons in the ground state accumulate over certain critical density within their lifetime.

The condensation usually happens in the following processes. First, external pump, usually a laser (Fig. 1.9 red arrow), generates hot electron hole pairs (above bandgap). As the aim is to show spontaneous coherence of the polaritons, they are introduced in a way such that the original coherence of the laser is lost. These electron and hole pairs can thermalize among themselves, to form equilibrium electron-hole plasma (EHP). Depending on the system, the EHP may relax down to the lower

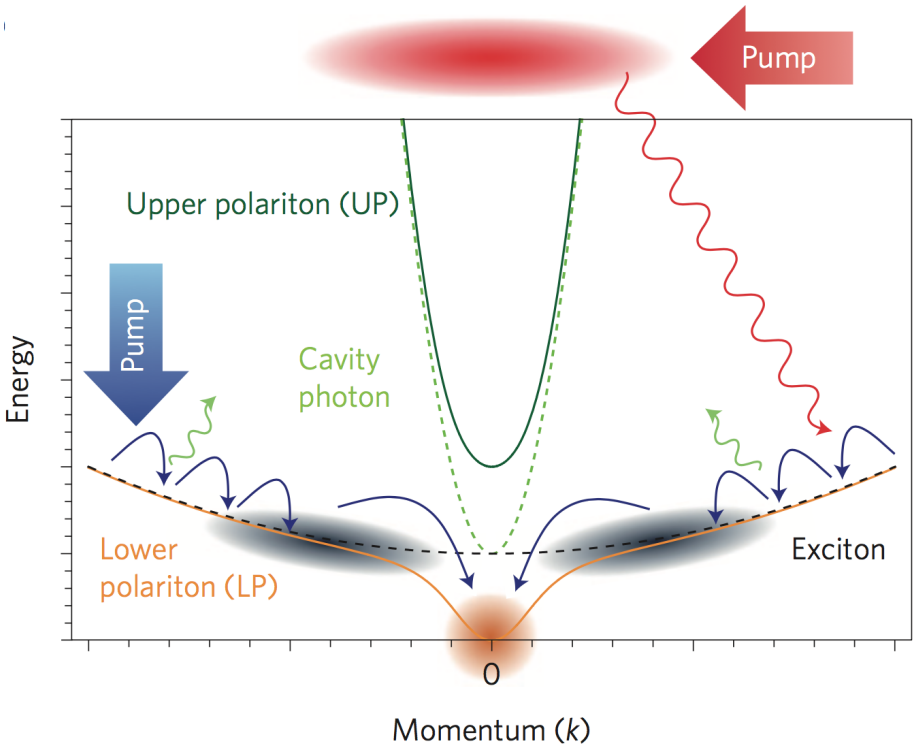

Figure 1.9: Illustration of polariton condensation. Taken from Ref [4]

polariton branch by optical phonon scattering. But they are still more energetic than the LP ground state. Acoustic phonons can bring the high-energy (high-k) polaritons to a so-called bottleneck region (black shade), where the LP dispersion becomes steeper owing to the Rabi splitting. The phonon scattering becomes inefficient at this region. A second scattering mechanism, polariton-polariton(P-P) scattering, bring one polaritons to the ground state, one to higher state which is again cooled by the phonons. The P-P scattering relies on the strong coulomb interaction of their exciton parts. Also, the inflection shape of the LP dispersion makes the simultaneous energy and momentum conservation possible.

Note one of the controversial issues relating to excitonpolariton BECs is whether it should be called a BEC at all. BEC has a long check list of properties that distinguish it from other states (see Ref [4]). The most difficult criteria to meet for polariton system are the thermal equilibrium and Bose distribution above threshold, owing to

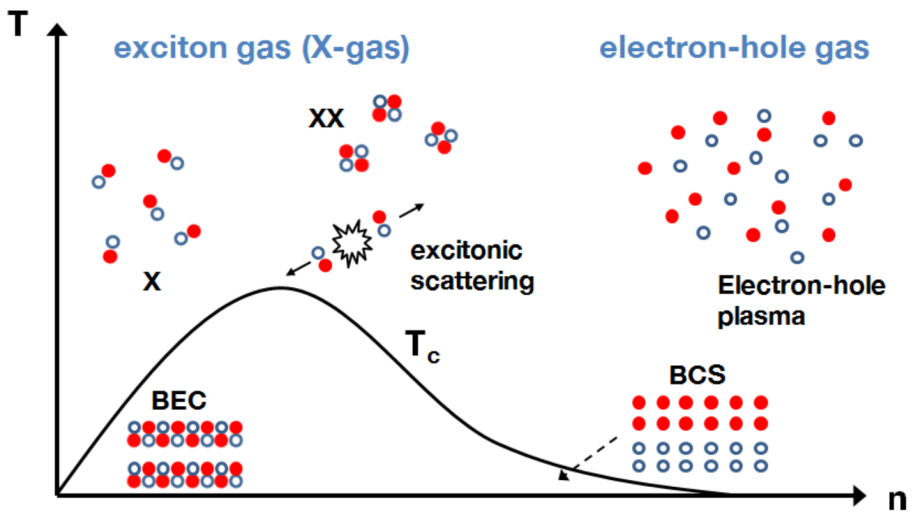

Figure 1.10: Phase diagram of electron-hole system (without cavity). Taken from Ref [5]

polariton's finite lifetime. Without these two criteria met, polariton BEC should only be called polariton laser. Even though, polariton laser is substantially different from photon laser like vertical cavity surface-emitting laser (VCSEL). In this thesis, we only demonstrate polariton laser, do not attempt to demonstrate BEC, although we use BEC in describing the many-body phases.

What if the low density condition Eq. 1.10 breaks down? For an excitons system without a cavity, excitons will go through the Mott transition, forming electron hole plasma at temperature above T_c. If BEC is initially prepared (below T_c), the system will go through a continuous BEC-BCS crossover. The physical picture of this crossover is that at low densities the electrons and holes within the exciton are relatively strongly bound by their mutual Coulomb attraction, and condense at sufficiently low temperatures owing to their bosonic nature. At higher densities, their mutual attraction becomes screened by the large population of electrons and holes, forming loosely correlated Cooper pairs, described by a BCS wavefunction. This physical picture is summarized in Fig. 1.10.

The cavity makes the situation complex in two ways. One is at high densities the

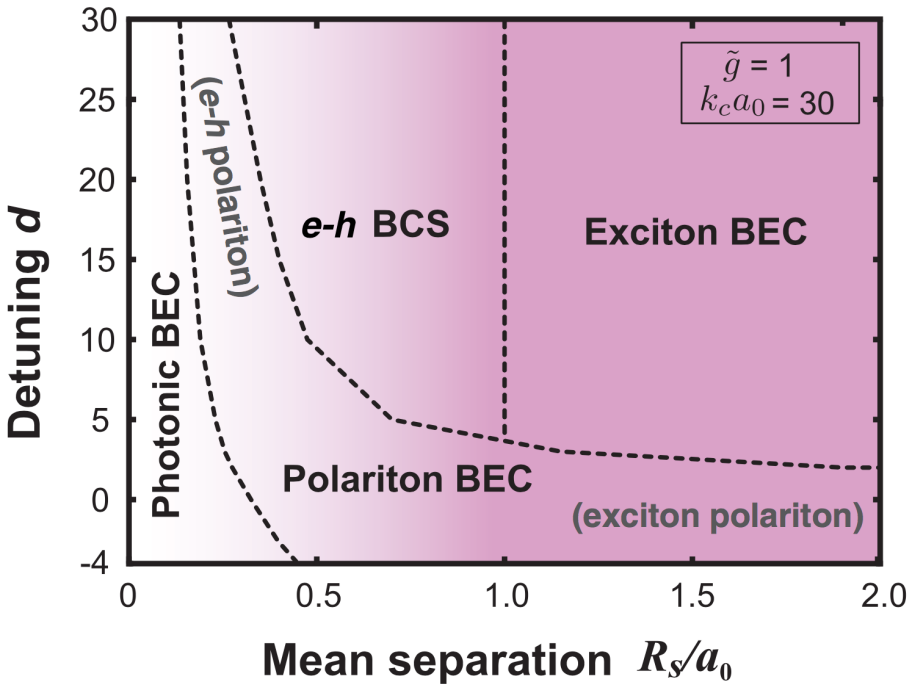

Figure 1.11: Phase diagram of electron-hole-photon system at zero temperature. Taken from Ref [6]. The detuning is defined as $d = (E_{cav} - E_{exc})/\varepsilon_0$, where ε_0 is the three-dimensional (3D) exciton Rydberg energy. X-axis is the mean separation between two excitons in the unit of Bohr radius. The region where Coulomb attraction dominates the photon-mediated interaction in the formation of e-h pairs is shaded (pink).

photons completely dominate the dynamics [33, 34, 6], because the electrons and holes have a maximum allowable population due to the Pauli exclusion principle, whereas photons do not. The polaritons can be described in a photon BEC state [35]. Another effect is, the photon will induce an effective attraction between electrons and holes, which compensates for the increasing screening effect. The result is enhanced electron-hole binding and smaller Bohr radius, which increases the Mott transition density, preventing excitons from dissociating. One possible phase diagram regarding photon-coupled exciton system is shown in Fig. 1.11. This area has been actively researched over recent years [36, 37, 38]. In this thesis, I will present the high-density results from our SWG-based system and show its unique advantages over other systems in Chapter 5.

1.4 Engineered Polariton Systems

Just like the optical lattice technique revolutionized the cold atoms BEC research, specially engineered polariton systems created endless possibilities for both fundamental studies and device applications. The first and most important engineering direction is the confinement and dimensionality control of polariton systems. Many applications such as matter-wave circuits/polariton circuits[23, 39, 40], novel phases transition[33] [41], and lattice quantum simulators[21] all requires lower dimensional (0D or 1D) confinement, control and coupling.

Engineering via Excitons

One viable path to control the polariton system is through the exciton part. Mechanical stress created potential[42, 15], external electrical or magnetic fields[43, 44, 45], or even optical stark effects[46] have been used to tune the energy and effectively confine the polaritons in predefined potential wells. However, the potential landscape created in these experimental constructions is far from effective as for the dimensionality control. Also, they rely on bulky external setups that are hard to be incorporated into stand-alone devices.

Another direct and simple way to manipulate the exciton part of a polariton system is to utilize the repulsive interaction between excitons. By using different pumping densities [47] and different pumping geometries[48, 49], locally trapped polaritons can be realized. However, these devices are still heavily relying on the external experimental equipment. And the exciton density and the controlling potentials are not decoupled, complicating the control.

Engineering via Photons

Thanks to the advances of nano-fabrication, microcavities can be precisely modified for better control. In particular, one popular way is by using different surface

patterning using metal patches[50, 51, 52, 53]. The metal patches change the boundary condition locally, resulting in slightly different cavity resonances under the surface metals. The periodic patterns create periodic potentials for the polaritons. Instead of having the continuous dispersions in momentum space for traditional 2D polariton systems, energy gaps appear at certain critical points in k-space. Effective polariton lattices are successfully constructed (2D honeycomb lattices) and condensation at certain symmetry points are well explained and predicted. However, this technique is still limited in its modulation strength. Making truly lower dimensional system, such as 0D and 1D, still remains challenging.

Another effective way is to embed a low-dimension "mesa" inside the sample before completion of the epitaxial growing [54, 55]. In this way, the polariton system is conveniently confined within the mesa area. The signature discrete energy levels have been observed in these systems, which indicates effective lateral confinements. However, due to the intrinsic defects for the MBE re-growth, polariton lasing or condensation has not been observed until very recent [56].

In order to have the low dimensional systems and keep the polariton lasing / condensation, pillar etching used to be the most successful technique to modify the polariton systems[57, 58, 59, 60, 61]. 0D, 1D or even lattice systems with polariton lasing/condensation have been achieved. Since the sample mirrors are still using DBR, it is normally several microns thick. Making these straight and tall pillars always requires long-time and accurately delivered plasma etching. The plasma bombardment is effective to sculpt the pillars yet it is damaging to the active media − quantum well layers as well. As a result, the exciton layer is not well protected and the free exciton states on the surface of the pillars are non-negligible. Besides, the energy detuning (energy difference between cavity photon and quantum well exciton) is highly location dependent. Single pillar or in-situ photon energy tuning is almost impossible due to the intrinsic limitations for all DBR based samples.

Comparing all the challenges and limitations in existing techniques mentioned above, the SWG-based microcavity presented in this thesis has its clear advantages. It fundamentally modifies the photon modes, with large modulation depth. The fabrication is relatively simple, while keeping the QW intact. The grating can even be electro-mechanically tuned [62] to allow real-time and in-situ tuning of the polaritons. I will discuss in detail in later chapters.

1.5 Thesis Organization

Because the major achievement of this thesis is the demonstration of a new microcavity polariton system. I will spend 3 chapters on it. Chapter 2 covers the basics and design details of the conventional DBR-based microcavity polariton system. A thorough understanding of the old system will guide us in designing new systems, and besides, our new system shares part of the components with the old one. Chapter 3 introduces the design of our new system– subwavelength grating based microcavity, including the motivation and major properties of the system, design rules and simulation tools we use, and finally an example of the design. In Chapter 4, I move from the design stage to the fabrication and characterization stage of our new system. I will briefly introduce the fabrication technique we use, which is the major work of a colleague Dr. Bo Zhang. Then I will describe the experimental methods we use to characterize the fabricated sample and show some experiment results revealing the unique properties of polaritons in our system. Finally, I will demonstrate polariton lasing in our new system.

The second part of this thesis is about exploring new physics through our new system. Chapter 5 describes the nonlinear regime of our system, where exciton density is increased to near Mott-transition density. Contrary to the common belief that the exciton Coulomb interaction is the main source of nonlinearity in GaAs based polariton system. Our results show a (oscillator strength) saturation dominated energy

shifts. Surprising results from the reflection measurement also reveal the deviation from the normal Bosonic description of polaritons. I will present a Fermionic approach to model the energy shifts, lineshape change, loss/gain associated with this nonlinear regime. I will discuss the implications on the actively researched polariton BCS-BEC crossover and photon-mediated electron-hole coupling.

Last part is a collection of engineering efforts for better polariton modes, to meet the needs of various applications. Chapter 6 discusses the best Rabi splitting one can achieve using planar cavities. The insights gained there will guide the design of microcavities for room-temperature polaritons and novel 2D material integrations. Chapter 7 discusses a fundamental aspect of the microcavity photons– their energy dispersion. I will show the energy dispersion of the cavity photons can be modified by orders of magnitudes by designing SWGs with different phase responses. It could enable not only distinct polariton dynamics but also Purcell enhancement in the weak-coupling regime. Chapter 8 describes the creation of lower-dimensional polariton systems and the inter-coupling between them. Two and three coupled 0D polariton quantum boxes are created and matched well with particle-in-box simulation. 1D coupled arrays of polariton boxes are also created, exhibiting the expected Brillouin-zone folding dispersion. These coupled systems could be the building blocks of quantum simulators and polaritonic integrated circuits.

Finally I will conclude and discuss the future works following this thesis.

CHAPTER II

Conventional DBR-based Microcavity Systems

The importance of distributed Bragg reflectors (DBRs) in opto-electronics cannot be overstated. They are ubiquitous as high-reflectance dielectric mirror in every optics-lab. They are also used as cavity mirrors in VCSEL lasers and fiber lasers, as well as band-stop filters in waveguides. Its popularity partly owing to its simplicity both in theory and fabrication. Although it can be described by fancy photonic crystal theory (periodic photonic structure), qualitative understanding it wouldn't require more than physics 101. In this chapter, I will first introduce the pictorial description of the DBR cavity. In most scenarios, this is the starting point and guiding rule. Then I follow up with the rigorous mathematical description. Specifically, a powerful formulation called "transfer matrix" is formally derived, which is the basis of many of the calculations in this thesis. Finally, the QW is introduced as a dispersive medium into the same framework to produce polaritons.

2.1 Pictorial Description of DBR Cavities

I first describe the working principle of a DBR. A DBR consists of alternating high and low refractive index layers, all made into $\lambda/4$ optical path length (OPL) thick. The thicknesses are set so to maximize the constructive interference among the reflections at each layer boundary. To see that, one can draw the multiple reflec-

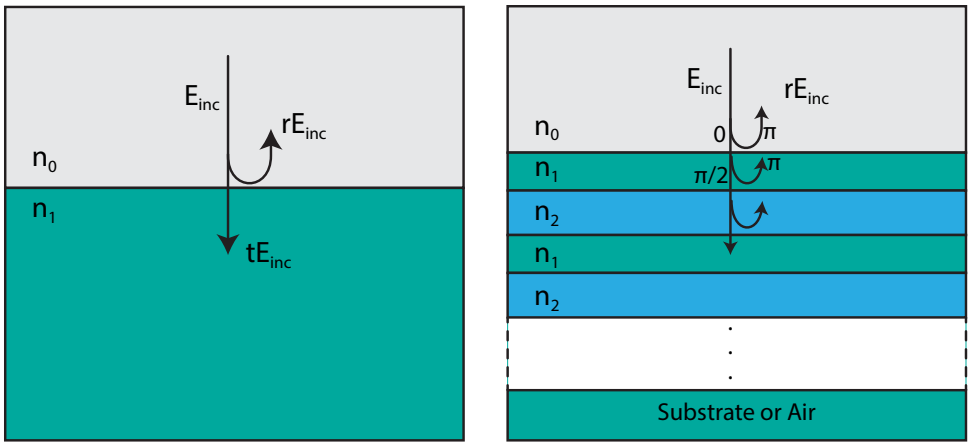

Figure 2.1: Illustration of Fresnel reflection (left) and DBR reflection (right).

tion/transmission diagram as shown in Fig. 2.1 right. For simplicity, we only consider normal incidence.

First consider the reflection/transmission at the interface of two dielectric materialsFig. 2.1 left. The reflection/transmission coefficients (Fresnel coefficient) are given by

$$r = \frac{n_1 - n_2}{n_1 + n_2}, \quad t = \frac{2n_1}{n_1 + n_2} \tag{2.1}$$

I highlight two points from this simple equation: (i) the reflection amplitude is determined by the refractive index contrast between the two dielectric (ii) the reflection phase is π when the incident medium has lower refractive index ($n_1 < n_2$), 0 when the opposite is true. However the transmission coefficient is always positive, i.e., no phase shift.

To maximize the reflection of a DBR, regardless of how much light is reflected from each layer (determined by the index contrast), the ideal condition is to stack all the waves in-phase. That is, when all the wave branches travel to the some position, they should have the same phase or differ by integer number of 2π. We can examine the DBR shown in Fig. 2.1 right. Suppose $n_0 < n_1$ and $n_2 < n_1$, the incident wave (set its phase as zero just above the DBR) gains a π phase in its reflected branch, but gains nothing in its transmitted branch. But the transmitted branch will gain $\pi/2$

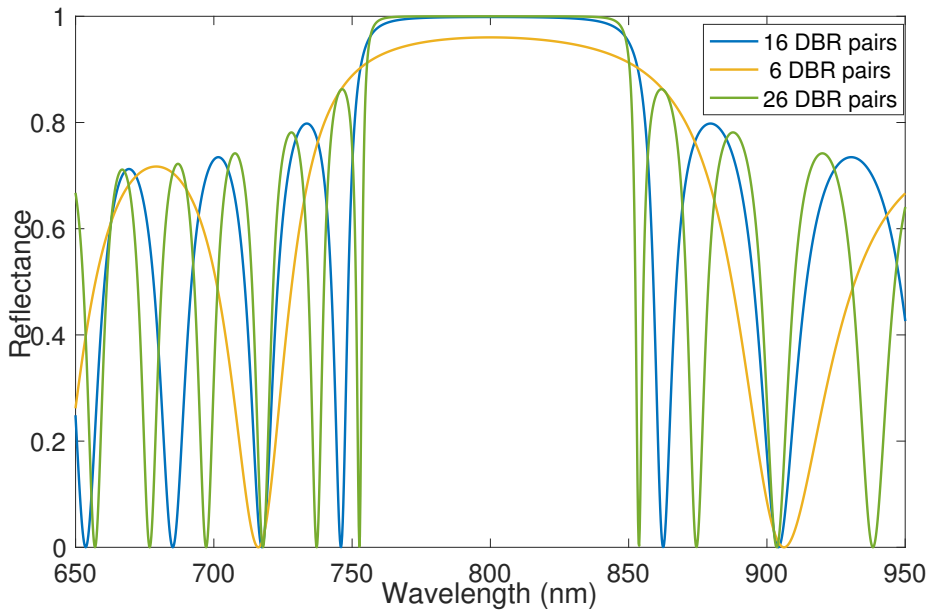

Figure 2.2: Reflectance of DBR with different pair numbers. $n_1 = 3.58$, $n_2 = 3.02$ and $n_c = 3.02$. DBR layers all have $\lambda/4$ optical path length (OPL).

traveling phase at the next interface, because each layer is set to be $\lambda/4$ OPL. Because $n_2 < n_1$, the reflected wave gains no phase delay at this interface, but accumulates another $\pi/2$ when it travels to the top interface. Finally it reaches just above DBR with totally π phase, same as the first reflected branch. Therefore they constructively interfere. One can keep drawing the graph and see all the wave branches reach the top interface with the same phase.

We can be more quantitative, since the problem can be solved analytically. A strategy could be, first solve the reflection/transmission coefficients for a dielectric slab. It basically reduces to the sum of a geometric series. Then solve for the multi-layer DBR recursively since it is periodic in nature. The details can be found in standard textbook such as Born&Wolf. The maximum reflection coefficient (at the design wavelength λ as in the $\lambda/4$) of a N-pair DBR is given by

$$r_{2N} = \frac{1 - \frac{n_3}{n_0}(\frac{n_1}{n_2})^{2N}}{1 + \frac{n_3}{n_0}(\frac{n_1}{n_2})^{2N}} \tag{2.2}$$

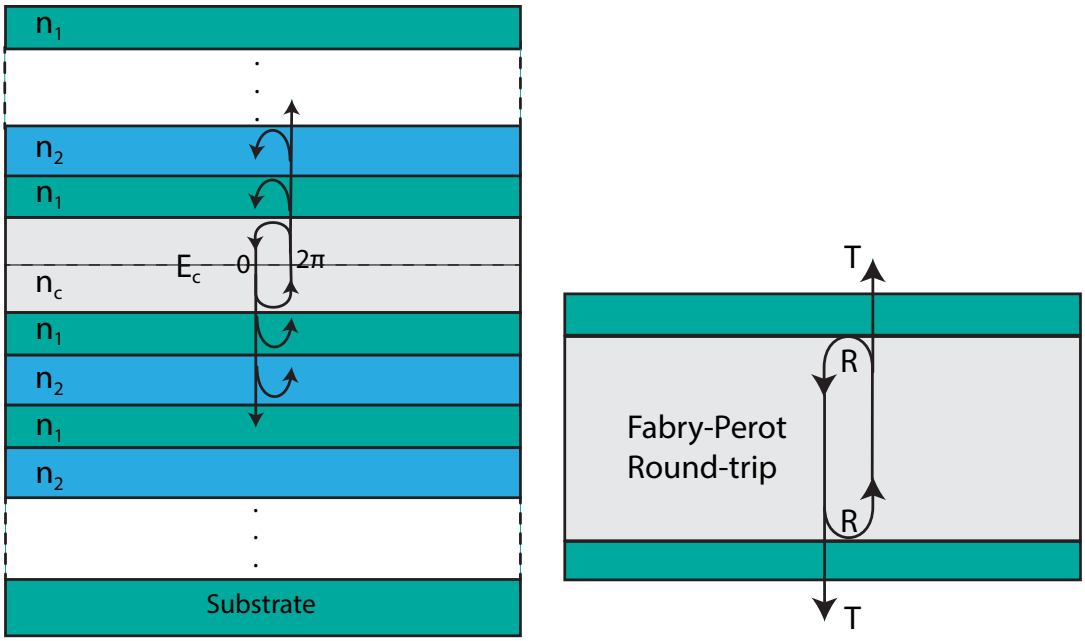

Figure 2.3: Illustration of graphical understanding of DBR cavity.

where n_3 is the refractive index of the substrate (Fig. 2.1 right).

In this way, even though the reflection at each interface is not very strong because of the limited index contrast (n_1/n_2), it can be magnified by the $2N$ in the exponent. The total reflection of DBR can be as large as 99.9% or higher depending on the number of DBR pairs. Examples of DBR reflection spectra are shown in Fig. 2.2.

The same conclusion will also apply to the case when $n_0 > n_1$ and $n_2 > n_1$, but not for other combinations. This leads to a very important DBR design rule: always keep high/low alternating index placement including the entry and exit media. Sometimes one needs to add a cushion layer to the existing pairs, making the DBR pairs actually (2N+1) instead of 2N. Any violation of this rule will decrease the reflectance from its ideal value, as well as disturb the reflection phase from 0 or π.

We can use the same graphical method to understand the DBR cavity. As illustrated in Fig. 2.3, the aim is to maximize the E-field amplitude E_c at the center of the cavity layer. Because the structure is symmetric about the central plane of the cavity, we can start from the central plane and consider the downward propagating

wave only. We have two possible configurations: (i) $n_c < n_1$ and $n_1 > n_2$ (ii) $n_c > n_1$ and $n_1 < n_2$. I will go through the first scenario. In the first configuration, the lower index cavity layer is set to be $\lambda/2$ thick. Starting from the center plane (phase=0), the wave accumulates a $\pi/2$ phase and then gain a π reflection phase at the cavity/DBR interface. When it travels to the central plane again, it gains a phase of 2π which perfectly constructive-interferes with the incident wave. Further, the wave travels up and reflected by the top DBR structure and return with a 4π phase, resetting itself. This process will keep going many times since the reflectance of the DBR is very high. The end result is two series of counter-propagating waves constructively interfere. This is consistent with the Fabry-Perot cavity, where the two cavity mirrors are metal mirror exhibiting about π reflection phase. However, for the configuration (ii), one needs λ OPL cavity in order to accumulate the same 2π phase at the central plane.

If we simplify the DBRs as simple mirrors, as illustrated in Fig. 2.3 right, the DBR cavity is simply a Fabry-Perot cavity. All the knowledge we obtain there will apply here. For example, the transmission is a Lorentzian. The resonance frequency over linewidth ratio, called finesse (or quality factor; they are the same in $\lambda/2$ cavity), can be written as

$$\mathcal{F} = Q_{\lambda/2} = -\pi/\ln(R) \approx \pi/(1-R) \tag{2.3}$$

The last approximation is when R is close to 1.

We can also determine the positions of field nodes and anti-nodes by the same graphical method. For example, consider a plane at a small distance away from the central plane. The reflected wave cannot accumulate 2π at the same location. So they no longer perfectly constructive-interfere, resulting in a lower field amplitude. At the cavity/DBR interface, there is only the π reflection phase resulting in a complete cancellation in field amplitude. This is the node of the system. One can also work out for the nodes and anti-nodes in the DBR region. They all locate at the interfaces

of the DBR layers, as shown in the beginning Fig. 1.6.

2.2 Mathematical Description of DBR Cavities

Above is just a very simple pictorial understanding of the DBR cavity, nothing more than qualitative. It cannot answer the following important questions:

- resonance of the cavity under oblique incidence (important to obtain photon dispersion)
- resonance of the cavity with non-optimal layer thicknesses (considering fabrication control is not perfect)
- the stop-band width of the DBR mirror and the reflection phase at any wavelength within the stop-band (important for constructing Fabry-Perot cavity)

Fortunately there is a very simple yet powerful computational method called "transfer matrix" method that can solve all the above questions. Actually it is general for electromagnetic (EM) wave propagation across any stratified homogeneous medium (multilayer stack). Every layer in the stack can only support two counter-propagating plane waves. The complex amplitudes of the two waves can completely describe the EM field in a specific layer, which is usually written to be a 2-component field vector. When the EM field is transfered from one layer to the next layer, the field vector in the next layer can be related to the old field vector by a 2-by-2 matrix, which will be derived in the following sections. Because all the calculations only involves rank-2 matrix multiplication, this method is very fast and stable.

First let us define the system. As shown in Fig. 2.4, light is incident on a stratified structure with an incidence angle θ_i. The incident medium is assumed to be semi-infinite long, with refractive index n_i. The transmission medium (substrate) is also semi-infinite long, with refractive index n_t. The z-direction is the depth direction

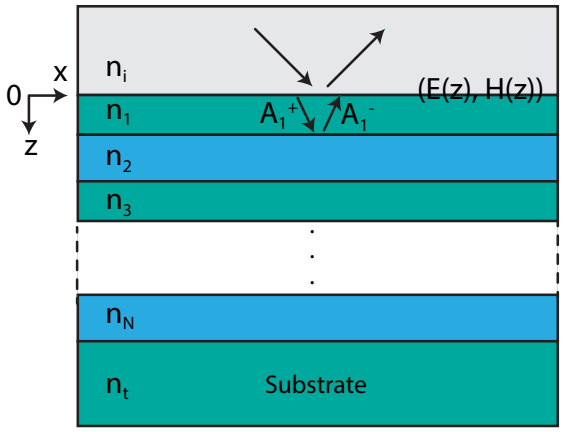

Figure 2.4: The structure to be solved by Transfer Matrix.

with origin at the first layer's upper surface. x-direction is along the incident wave direction, with arbitrary origin. This is a 2D problem.

Due to the symmetry in this problem, the field solution can be decomposed into two independent solutions– transverse electric (TE) polarization and transverse magnetic (TM) polarization. In TE polarization, the electric field is perpendicular to the incidence plane, that is, it only has y-component, no x or z components. It is mathematically simple to choose electric field as the variable to solve. While for TM polarization, the magnetic field has only y-component. It is simple to solve for magnetic field first. Since for optical field, we are primarily interested in the electric field, we need to solve for E-field using Faraday's law, and express the reflection and transmission coefficient with the E-field. In the following, I derive and solve for the two polarizations, which can be easily implemented in computer programs (I used Matlab).

2.2.1 Transfer Matrix for TE Polarization

TE and TM polarization is defined with respect to the incident plane, which is the plane formed by incident k-vector and normal direction of the structrue. TE means transverse electric field, where the electric field **E** is perpendicular to the incident plane. While TM is magnetic field **H** being perpendicular to the incident plane.

In TE polarization, electric field **E** only has one component (y-component), while magnetic field **H** has both x and z component. They are related by Maxwell's equation,

$$\nabla \times \mathbf{E} = -\frac{\partial \mathbf{B}}{\partial t} = -\mu \frac{\partial \mathbf{H}}{\partial t} \tag{2.4}$$

All the field here is assumed to be time-harmonic, which has time dependence of $e^{j\omega t}$. Under this convention, we can make substitution $\frac{\partial}{\partial t} \rightarrow j\omega$.

$$\nabla \times \mathbf{E} = -j\mu\omega\mathbf{H} \tag{2.5}$$

Working with the components, we have

$$H_x = -\frac{j}{\mu\omega}\frac{\partial E_y}{\partial z} \tag{2.6}$$

$$H_z = \frac{j}{\mu\omega}\frac{\partial E_y}{\partial x} \tag{2.7}$$

In **i-th** layer, we assume the electric field E_y consists of two plane wave components

$$E_{yi} = A_i^+ e^{-j(k_x x + \beta_i(z - z_i))} + A_i^- e^{-j(k_x x - \beta_i(z - z_i))} \tag{2.8}$$

A_i^+ term is the +z propagating wave and A_i^- term is the -z propagating wave. The minus sign in the exponent is consistent with the plane wave $e^{j(\omega t - \mathbf{k}\cdot\mathbf{r})}$ convention. k_x conserves over all layers because of phase matching in the tangential direction on the boundary of two layers (or can be explained by the translational symmetry of the system), which can be written as

$$k_x = k_0 sin\,\theta_0 \tag{2.9}$$

The entry semi-infinite medium is layer 1. k_0 is just the frequency ω/c, θ_0 is the oblique angle in vacuum. k_z is denoted as β here to emphasize that z-direction

is the propagation direction over layers, which is used by many literatures. $\beta_i = \sqrt{k_i^2 - k_x^2}$. Finally, it worths to note z_i marks the starting position of i-th layer (the entry medium's starting position is set to be same as z_2). In this definition, the field expression is independent to the definition of the origin.

Now we can use 2.6 to get H_x, then boundary conditions on the tangential field E_y and H_x can be used to relate the field between two adjacent layers. Before we do that, it is advisable to choose proper units for all the physical quantities. For our application in optics, we are mainly interested in visible range of wavelengths. So all lengths are better to have 'nm' as the unit, whereas k-vectors should have unit of 'nmˆ-1'. The field **E** and **H** should be normalized to the incident field, in other words, the incident field is set to be '1'. But because we used the SI unit system, **E** and **H** still have different units and in vacuum $|\mathbf{E}|/|\mathbf{H}| = \eta_0 = \sqrt{\mu_0/\epsilon_0} = 377\Omega$. I developed a trick that multiplies an η_0 to all **H** to make it have the same unit with **E**, which makes 2.6 clean:

$$\eta_0 H_x = -\frac{j}{k_0}\frac{\partial E_y}{\partial z} \tag{2.10}$$

here I assumes all media are non-magnetic media, that is $\mu = \mu_0$. k_0 is the k-vector in vacuum. In i-th layer, the magnetic field becomes

$$\begin{aligned} \eta_0 H_{xi} &= \frac{1}{k_0}[-\beta_i A_i^+ e^{-j(k_x x+\beta_i(z-z_i))} + \beta_i A_i^- e^{-j(k_x x-\beta_i(z-z_i))}] \\ &= n_i cos\ \theta_i[-A_i^+ e^{-j(k_x x+\beta_i(z-z_i))} + A_i^- e^{-j(k_x x-\beta_i(z-z_i))}] \end{aligned}$$

where $\beta_i = n_i k_0\sqrt{1 - k_x^2/(n_i k_0)^2}$, $n_i = \sqrt{\epsilon_{ri}}$ is the refractive index. From now on we will denote dimensionless parameter $n_i\sqrt{1 - k_x^2/(n_i k_0)^2} = \sqrt{n_i^2 - k_x^2/k_0^2}$ as p_i, so that $\beta_i = p_i k_0$

As for transfer matrix, one approach is to obtain the transfer matrix between A_i^+, $A_i^-$and A_{i+1}^+, A_{i+1}^- by matching the boundary condition at the $z = z_i + d_i$ plane.

Another approach, instead of obtaining the relation of field amplitudes, is to obtain the transfer matrix of fields **E** and **H** themselves from one interface to the next interface. Because the tangential fields are continuous across the interface, the boundary condition is implicitly satisfied. We will apply the second approach. From now on we will set $x = 0$.

$$
\begin{aligned}
z = z_i \quad &: \qquad E_{yi} = A_i^+ + A_i^-, \quad \eta_0 H_{xi} = p_i(-A_i^+ + A_i^-) \\
z = z_i + d_i \quad &: \qquad E_{yi} = A_i^+ e^{-j\beta_i d_i} + A_i^- e^{j\beta_i d_i}, \quad \eta_0 H_{xi} = p_i(-A_i^+ e^{-j\beta_i d_i} + A_i^- e^{j\beta_i d_i})
\end{aligned}
$$

By eliminating $A_i^+$and A_i^-, we get a matrix equation

$$
\begin{pmatrix} E_{yi}(z_i + d_i) \\ \eta_0 H_{xi}(z_i + d_i) \end{pmatrix} = \begin{pmatrix} cos(\beta_i d_i) & j\, sin(\beta_i d_i)/p_i \\ jp_i\, sin(\beta_i d_i) & cos(\beta_i d_i) \end{pmatrix} \begin{pmatrix} E_{yi}(z_i) \\ \eta_0 H_{xi}(z_i) \end{pmatrix}
$$

where matrix $M_i = \begin{pmatrix} cos(\beta_i d_i) & j\, sin(\beta_i d_i)/p_i \\ jp_i\, sin(\beta_i d_i) & cos(\beta_i d_i) \end{pmatrix}$ is the transfer matrix. Therefore, from the first interface to the last interface, the total transfer matrix $M_{tot} = M_n \cdot M_{n-1} \cdots M_2 \cdot M_1$(Warning: the order of multiplication matters!).

In the most cases, we are first interested in the reflectivity $r \equiv E_y^{(r)}/E_y^{(i)}$ and transmittivity $t \equiv E_y^{(t)}/E_y^{(i)}$. Consider the field in the entry medium (layer 1) and exit medium (layer 3, here use the convention of layer naming in RCWA),

$$
\begin{aligned}
E_{y,1} &= E_y^{(i)} e^{-j\beta_1(z-z_1)} + E_y^{(r)} e^{j\beta_1(z-z_1)} \\
\eta_0 H_{x,1} &= p_1(-E_y^{(i)} e^{-j\beta_1(z-z_1)} + E_y^{(r)} e^{j\beta_1(z-z_1)}) \\
E_{y,3} &= E_y^{(t)} e^{-j\beta_3(z-z_3)} \\
\eta_0 H_{x,3} &= -p_3 E_y^{(t)} e^{-j\beta_3(z-z_3)}
\end{aligned}
$$

Set z at the entry interface z=z1 and exit interface z=z3, write in the matrix form,

$$\begin{pmatrix} t \\ -p_3 t \end{pmatrix} = (M_{tot}) \begin{pmatrix} 1+r \\ p_1(-1+r) \end{pmatrix}$$

where we can calculate

$$\begin{aligned} r &= \frac{-p_3 M_{11} + p_1 p_3 M_{12} - M_{21} + p_1 M_{22}}{p_3 M_{11} + p_1 p_3 M_{12} + M_{21} + p_1 M_{22}} \\ t &= M_{11}(1+r) + p_1 M_{12}(r-1) \end{aligned}$$

where M_{ij} is the matrix element of M_{tot}. Once obtained r and t, one can easily calculate the field at any point z inside the structure by setting the E-field at the first interface to be $(1+r)$, then multiply by corresponding transfer matrix.

2.2.2 Transfer Matrix for TM Polarization

TM polarization is very similar to TE polarization. The magnet field **H** now act like the electric field **E** in TE. **E** can be calculated through **H** by Maxwell's equation

$$\nabla \times \mathbf{H} = \epsilon \frac{\partial \mathbf{E}}{\partial t} = j\omega\epsilon \mathbf{E}$$

Working with components, we have

$$\begin{aligned} E_x &= \frac{j}{\omega\epsilon} \frac{\partial H_y}{\partial z} \\ E_z &= \frac{-j}{\omega\epsilon} \frac{\partial H_y}{\partial x} \end{aligned}$$

In i-th layer, magnetic field $\eta_0 H_y$ is assumed to be

$$\eta_0 H_{yi} = A_i^+ e^{-j(k_x x + \beta_i (z - z_i))} + A_i^- e^{-j(k_x x - \beta_i (z - z_i))}$$

Electric field can be found to be

$$E_{xi} = \frac{1}{n_i}\sqrt{1 - k_x^2/(n_i k_0)^2}[A_i^+ e^{-j(k_x x + \beta_i(z - z_i))} - A_i^- e^{-j(k_x x - \beta_i(z - z_i))}]$$

From now on, we will define $q_i = \sqrt{1 - k_x^2/(n_i k_0)^2}/n_i = p_i/n_i^2$. Similarly by looking into the fields on the two interfaces of i-th layer, we obtain the transfer matrix of i-th layer:

$$\begin{pmatrix} \eta_0 H_{yi}(z_i + d_i) \\ E_x(z_i + d_i) \end{pmatrix} = \begin{pmatrix} cos(\beta_i d_i) & -j\, sin(\beta_i d_i)/q_i \\ -j q_i\, sin(\beta_i d_i) & cos(\beta_i d_i) \end{pmatrix} \begin{pmatrix} \eta_0 H_{yi}(z_i) \\ E_x(z_i) \end{pmatrix}$$

where $\beta_i = k_0 p_i$, $p_i = \sqrt{n_i^2 - k_x^2/k_0^2}$ same as above.

Fields in the entry and exit medium are

$$\begin{aligned} \eta_0 H_{y,1} &= \eta_0 H_y^{(i)} e^{-j\beta_1(z - z_1)} + \eta_0 H_y^{(r)} e^{j\beta_1(z - z_1)} \\ E_{x,1} &= q_1(\eta_0 H_y^{(i)} e^{-j\beta_1(z - z_1)} - \eta_0 H_y^{(r)} e^{j\beta_1(z - z_1)}) \\ \eta_0 H_{y,3} &= \eta_0 H_y^{(t)} e^{-j\beta_3(z - z_3)} \\ E_{x,3} &= q_3 \eta_0 H_y^{(t)} e^{-j\beta_3(z - z_3)} \end{aligned}$$

The matrix equation of the whole structrue becomes

$$\begin{pmatrix} t \\ q_3 t \end{pmatrix} = (M_{tot}) \begin{pmatrix} 1 + r \\ q_1(1 - r) \end{pmatrix}$$

then

$$\begin{aligned} r &= \frac{-q_3 M_{11} - q_1 q_3 M_{12} + M_{21} + q_1 M_{22}}{q_3 M_{11} - q_1 q_3 M_{12} - M_{21} + q_1 M_{22}} \\ t &= M_{11}(1 + r) + q_1 M_{12}(1 - r) \end{aligned}$$

Note here $r \equiv H_y^{(r)}/H_y^{(i)}$ and $t \equiv H_y^{(t)}/H_y^{(i)}$. If we are interested in the reflectivity and transmittivity of E-field, a relation can be easily derived:

$$\begin{aligned} r_E &= -r_H \\ t_E &= \frac{q_3}{q_1} t_H \end{aligned}$$

2.3 Energy Dispersion of Cavity Photons

With transfer matrix computer program, we can answer the first question posed in last section– how the resonance changes with the incidence angle. Because the incidence angle determines the wave vector in the transverse direction, the functional relation $\omega(k)$ is also known the dispersion relation of the cavity photon. It determines the fundamental properties of any particle.

Before we numerically solve for the dispersion using transfer matrix, it is beneficial to try to solve the dispersion analytically. Analytical solution can give us more physical insights than the numerical one. Given the fact that frequency ω and in-plane k-vector $k_{||}$ conserve over layers, for each layer we have the dispersion relation for any homogeneous medium

$$\omega = \frac{c}{n}k = \frac{c}{n}\sqrt{k_\perp^2 + k_{||}^2}, \tag{2.11}$$

where $k_{||}$ is determined by the incident angle in vacuum, $k_{||} = \frac{\omega}{c}\sin\theta_0$, while $k_\perp$ sets the spatial periodicity of waves in the perpendicular direction of each layer. As discussed in Section 2.1, the standing wave condition requires $l_c = \pi/k_\perp$, where l_c is the real cavity thickness. So the cavity resonance is reached when

$$k_\perp = \frac{\pi}{l_c}. \tag{2.12}$$

As we vary the incidence angle, thus the $k_{||}$, but fixing $k_\perp$ at the above resonance condition value in the cavity layer, we can solve for the resonance frequency

$$\omega_{res} = \frac{c}{n_c} k_\perp \sqrt{1 + k_{||}^2/k_\perp^2} \approx \frac{c}{n_c} k_\perp (1 + k_{||}^2/2k_\perp^2) \tag{2.13}$$

where the approximation is based on we are interested in $k_{||}^2 \ll k_\perp^2$ situation. Therefore we obtain an approximately parabolic dispersion relation. The photon energy can be found as $E_{cav} = \hbar\omega_{res}$ and momentum $\hbar k_{||}$. So the effective mass of the photon can be obtained by

$$m_{ph}^* = (\frac{d^2 E_{cav}}{d(\hbar k_{||})^2})^{-1} = \frac{\hbar n_c k_\perp}{c} = \frac{\hbar n_c \pi}{c l_c}. \tag{2.14}$$

Usually the cavity layer thickness is designed to be $\lambda_{des}/2$ OPL, which means $l_c = \lambda_{des}/2n_c$. Finally we have

$$m_{ph}^* = \frac{2\pi\hbar n_c^2}{c\lambda_{des}}. \tag{2.15}$$

Here I note the square dependence of the refractive index of the cavity layer. For normally used AlAs (n=3.0) cavity, this could mean a factor of 9.

Actually, there is one bug in the above derivation. We used the cavity resonance is reached when the "standing wave" condition is satisfied in the cavity layer. Is it true? Well, for Fabry-Perot cavity with two mirrors all with constant π reflection phase, it is true. But DBR is not such mirror, its reflection phase depends on the incidence angle. It will deviate from π, when the angle deviates from normal. So the resonance condition is actually slightly changed. To get an intuitive understanding of this issue, one can think that when the standing wave condition in the cavity layer is satisfied, the $\lambda/4$ condition in the DBR layers may not be met, unless they have the same refractive index with n_c. As discussed in Section 2.1, any deviation from the ideal DBR thickness $\lambda/4$ will result in a deviation from the perfect constructive interference. In reality, for GaAs based system, the DBR low index could be the same with the cavity layer (all AlAs, n = 3.0), but the high index layer is different. We

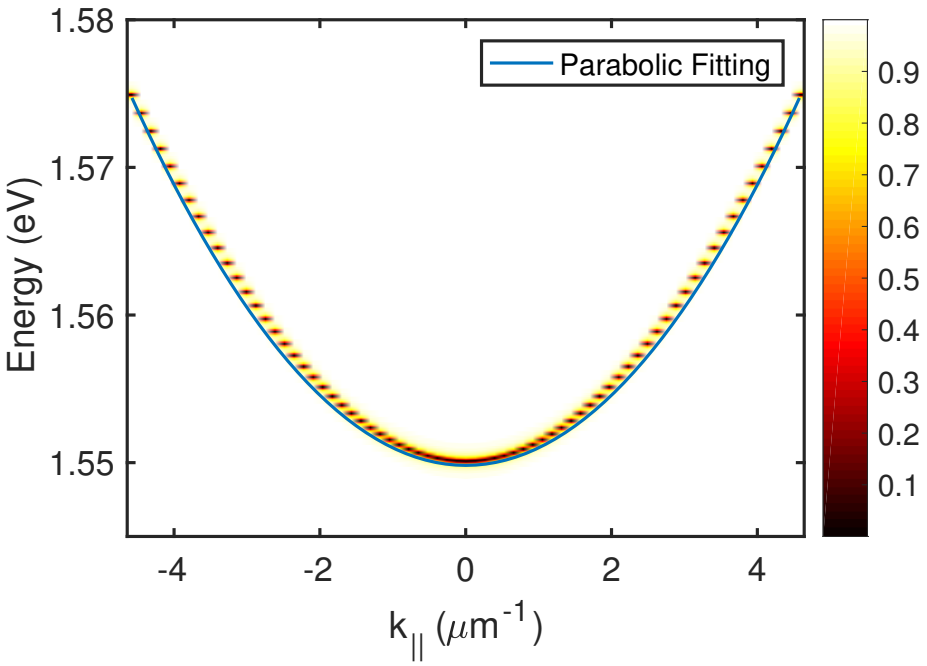

Figure 2.5: Example of DBR cavity dispersion. The color represents the reflection of the cavity. 16.5-pair top DBR and 20-pair bottom DBR are used. The DBR consist of $Al_0.15GaAs$ (n= 3.58) and AlAs (n=3.02) as the high low index layer. $\lambda/2$ cavity layer is also AlAs (n=3.02). This material combination will be used throughout this thesis.

use $Al_{0.15}GaAs$, the refractive index is 3.6, which is slightly larger, but not too bad. We will see the relation Eq. 2.15 is approximately correct. We can define an effective cavity refractive index, whose value will be between 3.0 and 3.6.

In Fig. 2.5, I show an example a DBR cavity dispersion. It is obtained by transfer matrix calculation of reflection of the cavity for incident angle swept from $-35°$ to $35°$. The black and yellow edge dotted line actually represents the reflectance dip of the cavity. Other than the color region, the reflectance is almost 1.0, so displayed as white with the 'hot' colormap. As can be seen, the parabolic approximation is approximately correct with a little underestimation of the curvature at the bottom. The effective mass of the photon at the dispersion bottom (ground state) is found to be $3.2 \times 10^{-5} m_e$. We can test whether the approximated formula Eq. 2.15 hold by calculating the effective cavity index. In this case, the effective cavity index is

$\sim$ 3.25. It is between the real cavity index 3.02 and the high DBR 3.58, which verifies the previous conclusion. The cavity layer's index will be more important in the Fabry-Perot resonance condition than the DBR.

2.4 QW Excitons under Oscillator Model

In this section I aim to use the simplest model to decribe QW excitons, the matter part of microcavity polaritons. As it turns out the simple classical oscillator model is extremely powerful, general enough to be applied to atomic and solid medium with slight quantum mechincal modification and re-inteprettation.

2.4.1 Lorentz Model and Oscillator Strength

In the original pioneering work by Lorentz, Planck and Einstein, atoms are simply treated as one negatively charged electron connected with the positively charged ion (or positive-charge center) via a spring. The simple harmonic oscillator has a natural frequency of ω_0 and damping rate γ. External electric field $\mathcal{E}$ can drive the oscillator away from its equilibrium position. The displacement x follows the Newton's equation of motion

$$m_0\frac{d^2x}{dt^2} + 2m_0\gamma\frac{dx}{dt} + m_0\omega_0^2 x = e\mathcal{E}(t), \tag{2.16}$$

where m_0 is the mass of the oscillator and $e = -1.6 \times 10^{-19}$ C or $e = -4.8 \times 10^{-10}$ esu. The electric field is assumed to be monochromatic with a frequency ω, i.e., $\mathcal{E}(t) = \mathcal{E}_0\cos(\omega t)$. Often it is convenient to consider a complex field

$$\mathcal{E}(t) = \mathcal{E}(\omega)e^{-i\omega t} \tag{2.17}$$

and take the real part of it whenever a final physical result is calculated. With the ansatz

$$x(t) = x(\omega)e^{-i\omega t}, \tag{2.18}$$

we obtain a frequency domain equation

$$m_0(\omega^2 + i2\gamma\omega - \omega_0^2)x(\omega) = -e\mathcal{E}(\omega). \tag{2.19}$$

If we consider a medium consisting of such oscillators, the electric field can induce macroscopic polarization P from the microscopic dipole moments defined as ex. The resulting polarization, defined as dipole moment per unit volume, is

$$\mathcal{P} = P/L^3 = n_0 ex = n_0 d, \tag{2.20}$$

where $L^3 = V$ is the volume, $d = ex$ is the electric dipole moment, and n_0 is the electron density per unit volume. Using the solution for the displacement above, we obtain the polarization in frequency domain

$$\mathcal{P} = -\frac{n_0 e^2}{m_0}\frac{1}{\omega^2 + i2\gamma\omega - \omega_0^2}\mathcal{E}(\omega). \tag{2.21}$$

The complex coefficient between $\mathcal{P}(\omega)$ and $\mathcal{E}(\omega)$ is defined as the optical susceptibility $\chi(\omega)$, representing the ability of a medium being polarized by the E-field. This is an important material property. We obtain it as

$$\chi(\omega) = -\frac{n_0 e^2}{2m_0\omega_0'}\left(\frac{1}{\omega - \omega_0' + i\gamma} - \frac{1}{\omega + \omega_0' + i\gamma}\right) \tag{2.22}$$

Here $\omega_0' = \sqrt{\omega_0^2 - \gamma^2}$ is the resonance frequency that is renormalized (shifted) due to the damping. An important feature is that $\chi(\omega)$ becomes singular at $\omega = -i\gamma \pm \omega_0'$. This relation can only be satisfied if we formally consider complex frequency $\omega = \omega' + i\omega''$.

By far, I have not explained the origin of the resonance frequency ω_0. It actually can be obtained quantum mechanically. For a single atom, one can solve stationary

Schrödinger equation

$$\mathcal{H}_0\psi_n(r) = \hbar\epsilon_n\psi_n(r), \tag{2.23}$$

to for all the energy levels $\hbar\epsilon_n$ and their associated wavefunctions. When the driving field frequency matches with the difference between two energy levels, optical transitions will happen (for details, refer to any quantum mechanics textbook, I use Merzbacher[63]). So the resonance frequency in the oscillator model is simply the energy difference between two energy levels. Following Ref. [7], the atomic optical susceptibility can be written as

$$\chi(\omega) = -\frac{n_0}{\hbar}\sum_n |\mathbf{d}_{ln}|^2\left(\frac{1}{\omega + \epsilon_{ln} + i\gamma} - \frac{1}{\omega - \epsilon_{ln} + i\gamma}\right) \quad \text{Atomic Optical Susceptibility} \tag{2.24}$$

Here $\mathbf{d}_{ln}$ is the dipole matrix element relating the initial state l and final state n.

If we compare above with eq. 2.22, we see both expressions have similar structures. However, in comparison with the oscillator model the atom is represented not by one but by many oscillators with diffent transition frequencites ϵ_{ln}. To see this, we rewrite the above expression, pulling out the same factors which appear in the oscillator result,

$$\chi(\omega) = \frac{n_0 e^2}{2m_0}\sum_n \frac{f_{nl}}{\epsilon_{nl}}\left(\frac{1}{\omega - \epsilon_{ln} + i\gamma} - \frac{1}{\omega + \epsilon_{ln} + i\gamma}\right) \tag{2.25}$$

Hence, each partial oscillator has the strength of

$$f_{nl} = \frac{2m_0}{\hbar e^2}|\mathbf{d}_{nl}|^2\epsilon_{nl}. \quad \text{Oscillator Strength} \tag{2.26}$$

As can be seen, oscillator strength is just the dipole moment matrix element times some constant factor. It is the language used in the oscillator model, but can be conveniently related to its quantum mechenical counterpart. It is dimensionless which is nicer to use than the dipole moment. There is another nice property of oscillator

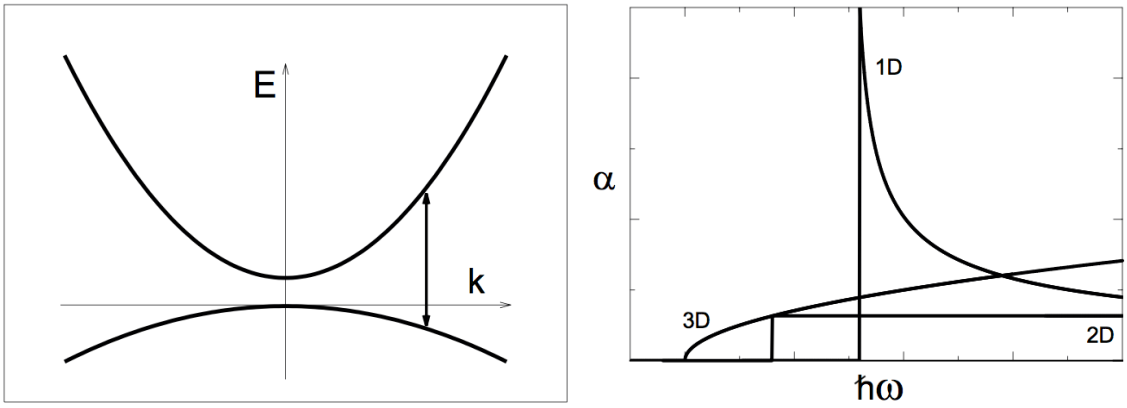

Figure 2.6: Schematic drawing of conduction and valence bands and an optical dipole transition connecting identical **k**-points in both bands (left). Free carrier absorption spectra in three, two and one dimension semiconductors (right). Taken from Ref. [7]

strength, as discussed below.

Adding the stengths of all oscillators by summing over all the final states n, we find

$$\sum_n f_{nl} = \frac{2m_0}{\hbar} \sum_n \langle n|x|l\rangle \langle l|x|n\rangle (\epsilon_n - \epsilon_l). \tag{2.27}$$

By using $\langle n|x|l\rangle (\epsilon_n - \epsilon_l) = \langle n|[\mathcal{H}_0, x]|l\rangle$ and working with the commutators, we finally get a nice result

$$\sum_n f_{nl} = 1 \quad \text{Oscillator Strength Sum Rule} \tag{2.28}$$

The sum rule shows that total transition strength in an atom can be viewed as that of one oscillator which is distributed over many partial oscillators, each having the strength f_{nl}.

In semiconductor, the atomic energy levels become energy bands and Bloch states. If we only consider the interband transition between the conduction band and valence band, the optical dipole matrix element can be written as

$$\mathbf{d}_{cv}(k', k) = \delta_{k,k'} \mathbf{d}_{cv}(0) \frac{\epsilon_0^c - \epsilon_0^v}{\epsilon_k^c - \epsilon_k^v} \tag{2.29}$$

where all the constants has been lumped into the zero-k dipole moment $d_{cv}(0)$. The $\delta_{k,k'}$ represents the momentum conservation under the dipole approximation– photon's linear momentum can be neglected. The numerator is the energy difference at the zero-k, which is the bandgap E_g, while the denominator is $E_g + \hbar^2k^2/(2m_c) + \hbar^2k^2/(2m_v)$. The interband transition is illustrated in Fig. 2.6 left. The interband transition is actually a continuum of transitions at different k-points. Therefore the absorption spectra (at thermal equilibrium) look like a band starting from the bandgap energy. I illustrate the absorption spectra in different dimensions in Fig. 2.6 right.

2.4.2 Excitonic Effect

In the above treatment, the Coulomb interaction between electrons is neglected. That is a so-called free-carrier optical transition. When the Coulomb interaction is turned on, excitonic effect arises. The exciton states can be solved by Wannier equation for the electron and hole relative motion in real space,

$$-\left[\frac{\hbar^2\nabla_r^2}{2m_r} + V(r)\right]\psi_n\nu(r) = E_\nu\psi_\nu(r). \quad \text{Wannier equation} \tag{2.30}$$

where m_r is the reduced mass of electron and hole $m_em_h/(m_e + m_h)$ and $V(r)$ is the dielectric-screened Coulomb potential in the semiconductor medium. The equation is identical to the hydrogen atom equation. The solution is similar

$$\begin{aligned} E_n &= -E_0\frac{1}{n^2} \quad \text{with } n = 1, 2, ... \text{ (3D)} \\ E_n &= -E_0\frac{1}{(n+1/2)^2} \quad \text{with } n = 1, 2, ... \text{ (2D)} \end{aligned} \tag{2.31}$$

The binding energy of the exciton ground state is E_0 in 3D and $4E_0$ in 2D, respectively. The larger binding energy in 2D can be understood by considering quantum well structures with decreasing width. The wavefunction tries to conserve its spherical

symmetry as much as possible since the admixture of p-wave functions is energetically unfavorable. Confinement parallel to the quantum wells is therefore accompanied by a decrease in the Bohr radius perpendicular to the wells. In the ground state, the 3D exciton radius is thus simply the exciton Bohr radius a_0, but it is only $a_0/2$ in 2D [7].

Excitonic Oscillator Strength

Although an exciton has a similar internal structure to a hydrogen atom, a Wannier exciton has much larger Bohr radius and much smaller binding energy than a hydrogen atom, owing to the small effective mass of electrons and the large dielectric constant in semiconductors[64]. For instance, in the ground (1s) state, the electron and hole in a Wannier exciton are much more loosely bound than the electron and proton in a hydrogen atom. On the other hand, since the excitons wavefunction is extended over many lattice sites of the crystal, the exciton collects the dipole oscillator strength of many atoms. More rigorously, the excitonic oscillator strength can be derived as follows[65]:

$$f_{exc} = \frac{2}{m_0 \hbar \omega} |\langle u_v | \hat{\mathbf{e}} \cdot \mathbf{p} | u_c \rangle|^2 V 2 |\psi_n(r=0)|^2 \delta_{k_{exc},0}, \tag{2.32}$$

where u_v and u_c represent the Bloch wavefunctions of the valence band and conduction band, V is the crystal volume, $\psi_n(r)$ is the exciton envelope function, and m_0 is free-electron mass.

For the 1s state,

$$|\psi_{1s}(r=0)|^2 = \frac{1}{\pi (a_B^*)^3}. \tag{2.33}$$

Therefore,

$$f_{exc} = f_{atom} \times \frac{V}{\pi (a_B^*)^3}, \tag{2.34}$$

where f_{atom} is the oscillator strength for a delocalized electron-hole pair (no coulomb bonding). This indicates that the strong electron-hole correlation in an exciton en-

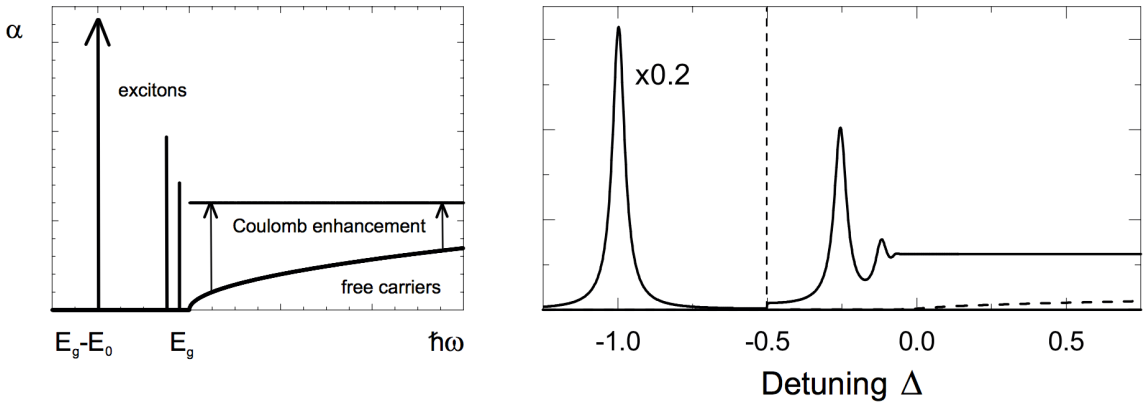

Figure 2.7: Schematic (left figure) and calculated (right figure) band edge absorption spectrum for a 3D semiconductor. Shown are the results obtained with and without including the Coulomb interaction. The 1s-exciton part of the computed absorption spectra has been scaled by a factor of 0.2 . Taken from Ref. [7]

hances its oscillator strength by a factor of $V/\pi(a_B^*)^3$ as compared with the uncorrelated electron-hole pair.

Equation 2.34 shows that the dimensionless oscillator strength is proportional to the crystal volume. This is due to the fact that the exciton center-of-mass wavefunction extends over the whole crystal. The meaningful quantity is the oscillator strength per unit volume, which is related to the absorption coefficient $\alpha(\omega)$ by

$$\int \alpha(\omega)d\omega = \frac{2\pi^2 e^2}{nm_0 c}\frac{f}{V}. \tag{2.35}$$

The excitonic effect introduces discrete absorption lines below the bandgap. Above the bandgap, excitonic effects give a correlation in the electron and hole of the unbound electron-hole pair, leading to an enhanced absorption, as illustrated in Fig. 2.7.

In QW, exciton wavefunction is modified by the quantum confinement in the z-direction. Specifically, the exciton wavefunction can be written as

$$\psi = u_c u_v f_c(z) f_v(z) F_{exc}(\mathbf{r}_\parallel) e^{-i\mathbf{k}_\parallel \cdot \mathbf{R}} \tag{2.36}$$

where the u is a central cell part of the Bloch wavefunction, f is a QW envelope functions, F_{exc} describes the relative electron-hole motion (1s hydrogenic wavefunction), and $\mathbf{R}$ is te center-of-mass coordinate.

The oscillator strength of a QW exciton is proportional to the area S of the sample. Hence the oscillator strength per unit area is introduced:

$$\frac{f}{S} = \frac{2}{m_0\hbar\omega}|\left\langle u_v|\hat{\mathbf{e}}\cdot\mathbf{p}|u_c\right\rangle|^2\frac{2}{\pi a_B^2}|\int c(z)v(z)dz|^2. \tag{2.37}$$

As the quantum well thickness decreases, f/S increases because the exciton radius a_B decreases. For example, $f/S \sim 6\times10^{-4}\mathring{A}^{-2}$ for 10nm GaAs QW with AlAs barrier [66].

Using the above oscillator strength one can obtain a dielectric constant for the QW under the Lorentz oscillator model [67]:

$$\epsilon(e) = n^2(e) = \epsilon_\infty + \frac{fq^2\hbar^2}{m\epsilon_0 L_z}\frac{1}{e_0^2 - e^2 - i\gamma e}, \tag{2.38}$$

where f is the oscillator strength per unit area, q and m are the charge and mass of the electron respectively, L_z is the QW thickness, e_0 is the exciton energy, and γ is the exciton linewidth.

2.5 Polaritons in DBR Cavity

Polaritons as introduced in Chap. 1 is considered to be a quantum phenomenon, since the exciton is coupled with vacuum field fluctuation, which only appear after fully quantization of the photon. Nevertheless, it is well known that quantum theory of the interaction of an electromagnetic field with an atom is entirely equivalent to the Lorentz model for a classical oscillator when the atomic excitation remains weak [8], i.e. the atom remains mainly in its ground state (see Milonni and Eberly (1988) for

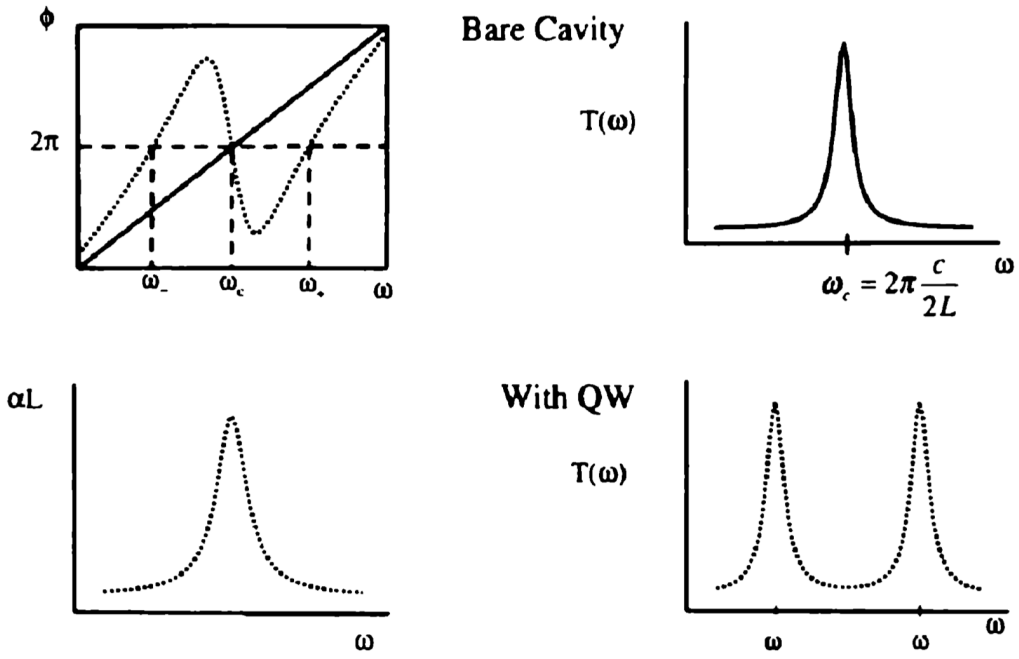

Figure 2.8: (Left) Phase advance vs. frequency. showing the orgin of the two normal modes at ω_- and ω_+. (Right) Cavity transmission vs. frequency; transmission at $omega_c$ is suppressed due to the presence of the absorber in the cavity. Taken from Ref. [8]

a proof). As Zhu, et al first demonstrated [68], the vacuum Rabi splitting (VRS) can actually show up as a feature of a linear-dispersion theory. In his model, N classical (Lorentzian) dipole absorbers are assumed to interact equally with a single cavity mode. The transmission spectra $T_c(\omega)$, reflectance $R_c(\omega)$, and absorption $A_c(\omega) = 1 - R_c(\omega) - T_c(\omega)$ are calculated by applying multi-beam interference analysis of a Fabry-Perot interferometer. Both the absorption $\alpha(\omega)$ and the associated dispersion $n(\omega)$ (so the name linear-dispersion theory) of the Lorentzian absorber are taken into account in calculating the amplitude and phase of the waves propagating through the cavity. This model reproduces results obtained from the Jaynes-Cummings model: if the atom-field coupling g (or $\hbar\Omega$ under different notation) is strong compared to the cavity and exciton damping rates, then the cavity absorption (or transmission, reflection) displays a splitting equivalent to the VRS.

This splitting in the transmission/reflection spectra can be understood from a

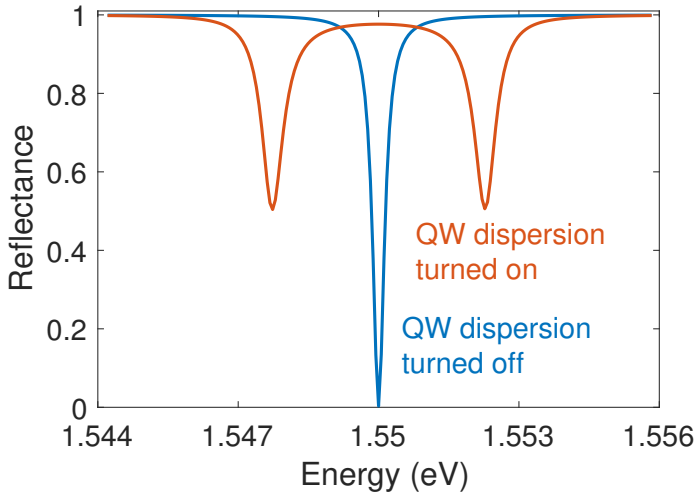

Figure 2.9: Example of transfer matrix calculation of a 12nm GaAs QW in a DBR cavity center. The oscillator strength of GaAs QW is chosen as $f = 6 \times 10^{-4} \mathring{A}^{-2}$ in Eq. 2.38 and damping rate $\gamma = 0.8$meV.

graphical argument. The phase advance of a wave propagating through a cavity is just ω/c times the optical path length (OPL), and the transmission maxima occur when the phase advance is 2π. The phase advance can be written as $\phi = (2L\omega/c)(n_\infty + \Delta n)$, where n_∞ is the background dielectric constant and Δn is the index of refraction due to the Lorentzian absorber (the real part of the susceptibility). The two contributions to the phase shift are shown in Fig. 2.8. The background index has no dispersion and thus the phase advance is linear versus ω; ω_c is the "bare-cavity" resonance (i.e. the resonance without the absorber in the cavity). The dispersion of the absorber can be seen to give rise to two additional frequencies at which $\phi = 2\pi$. Thus one might expect the cavity with the absorber to exhibit there transmission maxima, at ω_-, ω_c and ω_+. However, the absorber prevents the buildup of any substantial field amplitude at ω_c, so transmission peaks actually occur only at ω_- and ω_+ as shown in Fig. 2.8 lower right. A complete analysis shows that the splitting is the same from the classical dispersion and quantum-mechanical models.

The above analysis is mostly correct, except it neglected the reflections from the QW, since QW is generally made of material with a different refractive index from

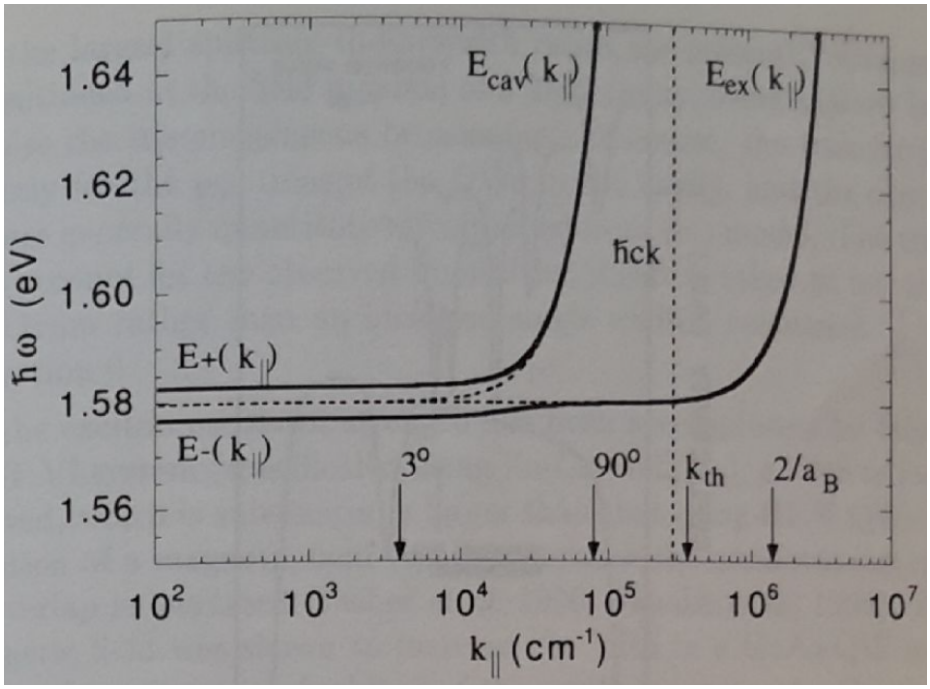

Figure 2.10: Calculated dispersion of the cavity polariton modes. The dotted lines are the exciton and cavity dispersions without coupling; the solid lines are the dispersions when the modes are coupled. Taken from Ref.[8]

the barrier. The most complete model would be, use transfer matrix to include every single layer in the DBR cavity including the QW with a complex dielectric constant (Eq. 2.38). In Fig. 2.9, I show an example of my transfer matrix calculation to produce polariton modes in a DBR cavity.

Transfer matrix combined with the Lorentz model of the QW provides a powerful and simple tool to simulate polariton modes. It even provides a direct experimental observable– the reflectance (or transmittance).

A final comment goes to the experimental observables. One can directly measure the polariton dispersion via the angle resolved reflectance. There is a one-to-one correspondence between the polariton mode and the out-coupled photon. The physics behind this well-known property is well summarized by [64]: In a QW, the lack of full translational invariance relaxes the requirement of momentum conservation in the growth direction, $\hat{e}_z$. In contrast to bulk excitons, a QW exciton with transverse (in-

plane) momentum $\hbar\mathbf{k}_{\|}$ interacts with a continuum of photon modes with the same transverse momentum $\hbar\mathbf{k}_{\|}$ but arbitrary longitudinal momentum $\hbar k_z$. This gives rise to an unassisted radiative decay. From the simplest viewpoint, the radiation emitted by the QW exciton has an escape route from the crystal. From a somewhat more sophisticated viewpoint, the oscillator describing the exciton (or polariton) is **coupled to a continuum** of oscillators describing the optical modes, which acts on the exciton as a dissipative bath and leads to an irreversible decay. Only excitons lying within the light cone, i.e. $k_{\|} \leq E_{exc}/\hbar c$, can decay radiatively [69, 70]. Energy-momentum conservation prohibits radiative decay of excitons with $k_{\|} > E_{exc}/\hbar c$. A picture of polariton in the entire k-space is shown in Fig. 2.10.

CHAPTER III

Design of SWG based Microcavity

As seen in previous chapter, conventional DBR cavities, although can be made very high quality (high-Q), is a very rigid structure. The DBR mirror, usually made of 20–40 pairs of high/low index layers, is about $4\mu m$ in thickness, making the electrical integration and electromechanical tuning challenging. The DBR layers have to be made exactly $\lambda/4$ OPL. Once the semiconductor material is chosen, the structure has few free parameters to tune. The photon dispersion is set as a parabolic shape with effective mass fixed by the cavity refractive index. The only parameter one can tune is the cavity resonance through the tapering of the sample (so the cavity length changes). Moreover, DBR is particularly difficult to create lateral confinement for lower dimensional systems. Most existing methods for confining polaritons lead to a weak modulation potential that modifies the system's properties without reducing its dimensionality from 2D to 1D or 0D. Examples include weak confinement of excitons via mechanical strain[15] and periodic modulation of the optical modes via surface patterning[50] [71]. More intrusive techniques have been developed to dramatically change the lateral mode, for example, embedding apertures inside the cavity,[55, 72] which have led to 0D polariton cells. However, due to the intrinsic defects for the MBE re-growth, polariton lasing or condensation has not been observed until very recent [56]. This is also a difficult technique that involves with very long turn-around

time. The most successful method so far, is direct etching of the vertical cavity into micro-pillars. Using this method, two groups have recently achieved polariton lasing in pillars,[57, 73, 45]. However, despite the technological difficulty that this approach requires plasma etching deep through the 4–8μm structure, it destructs the active media (i.e. QW), introducing unnecessary surface recombination centers. It is also unclear whether further control of the polariton modes in each pillar would be possible.

Considering all above limitation of DBR cavity, different cavity reflectors are worth exploration. Recently, a single layer subwavelength high-index-contrast grating (SWG or HCG) has been demonstrated as a light-weight, controllable mirror, which exhibits desirable features such as broadband high-reflectance[74], polarization selectivity [75], and electro-mechanical tuneability[76]. Its successful application in VCSEL [77] is very encouraging for us to apply it in polariton system, since the two systems share very similar vertical cavity structure in research.

This chapter talks about how I design and optimize a SWG-based vertical cavity for polariton application.

3.1 Subwavelength High Contrast Grating

3.1.1 General Diffraction Gratings

Diffraction grating is an optical component with a periodic structure usually in one dimension that splits and diffracts light into several beams traveling in different directions. The most common grating is 1D long stripes on the surface of either dielectric or metal. Examples of typical grating shapes (cross-section) are illustrated in the Figure 3.1 upper panel.

Taking a general triangle grating as an example (3.1 lower panel), the diffraction directions can be determined by calculating the optical path length (OPL) difference

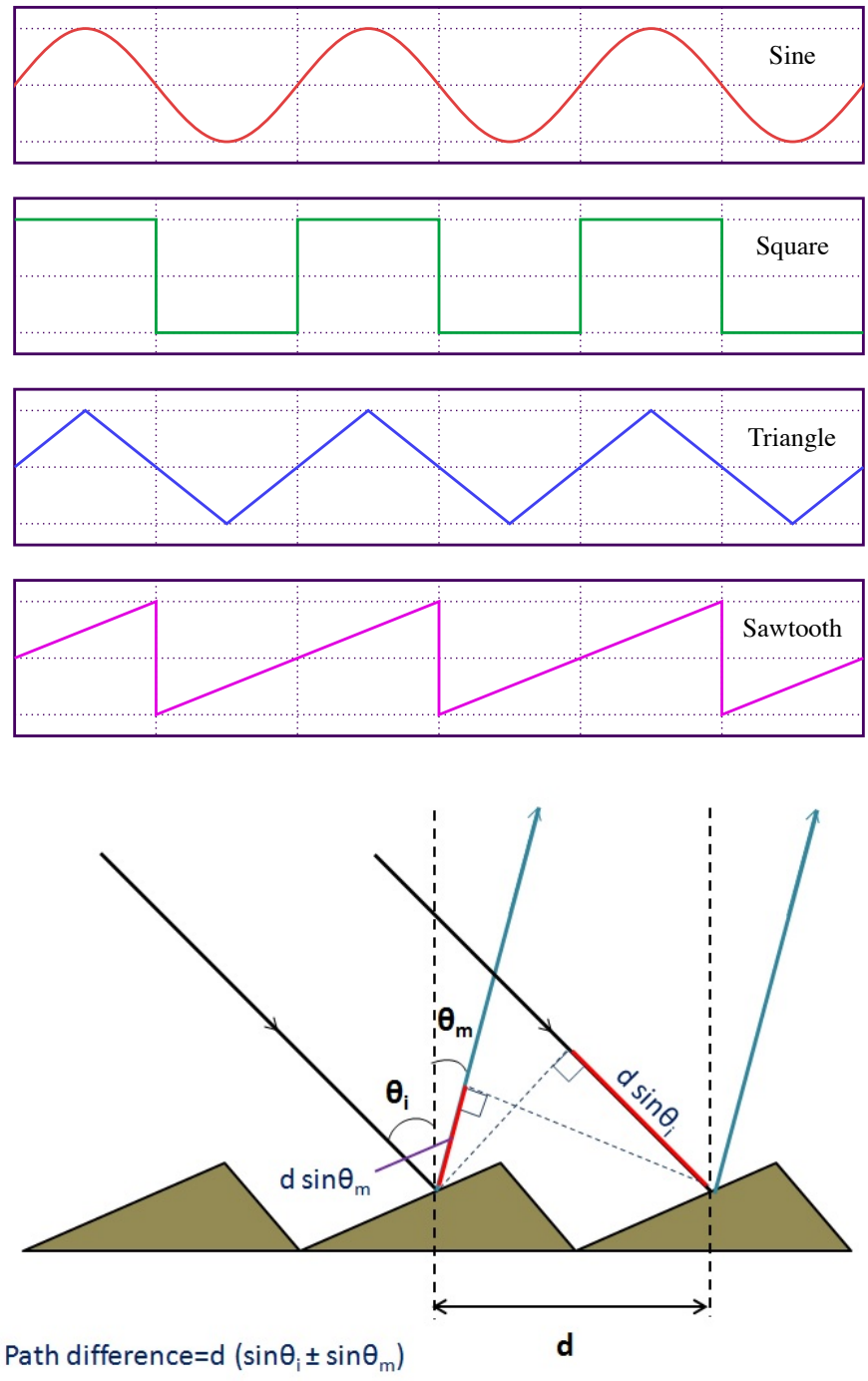

Figure 3.1: Schematics of diffraction gratings with different corrugated surface patterns (upper panel) and the wavefront analysis for an general triangle grating (lower panel). Taken from Wikipedia.

of adjacent rays. A plane wave is incident with an angle θ_i from the normal direction. Two rays among the infinite-many parallel rays are shown. The two rays are hitting on the grating with d apart. d is the period of the grating. The diffracted wave can only propagate with specific discrete angles θ_m (m is the diffraction order), which meet the following **grating equation**

$$d\left(\sin\theta_i + \sin\theta_m\right) = m\lambda, \tag{3.1}$$

where λ is the wavelength. The left-hand-side is the OPL difference of the two points on the same wavefront. Note θ_m can be negative. Eq. 3.1 means, only when the OPL difference is integer number of the wavelength, the two rays will constructively superpose and propagate in the given direction. All other directions are suppressed because the infinite-many rays cannot constructively add up. One can show waves with even slightly mismatched phase will tend to add up to zero. When $m = 0$, we have $\theta_i = -\theta_m$. That means, the zeroth order diffraction is just a specular reflection.

It is deceiving to draw rays reflecting from the flat surfaces of the triangle grating, because one might think the rays would reflect as the Snell's law dictates, i.e., the reflected ray should be symmetric about the normal vector of that surface. However, this is not the case for gratings. The geometric optics breaks down here and is replaced by wave optics. According to Huygens-Fresnel principle, each point on the grating excited by the incident wavefronts acts like a secondary wave source, emitting spherical wave. Microscopically, one can think the atoms or molecules are polarized by the incident wave and oscillate with the same frequency. They act like small antennas with fixed phase relation. These wave sources inherit the phase of the wavefront of the incident wave and can constructively or destructively interfere. So the propagation directions of the diffracted wave are not determined by the slope of the grating "teeth", but the period of the grating d via Eq. 3.1. It is general

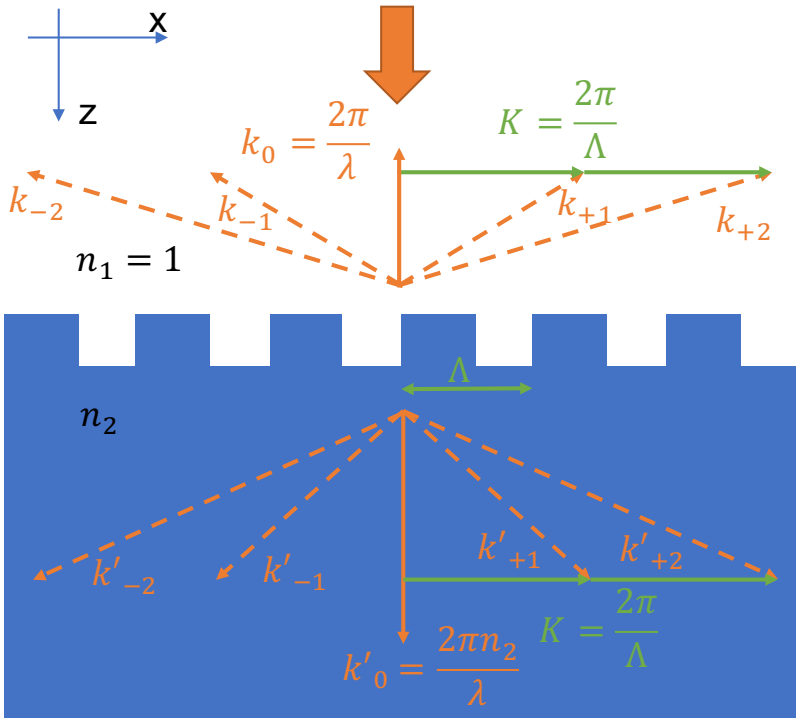

Figure 3.2: Wavevector view of the reflected and transmitted diffraction waves from a subwavelength dielectric grating.

for any periodic surface pattern. The specific grating shape only affects the energy distribution over each diffraction order, or the diffraction efficiency of each order. I will talk about how to quantitatively calculate the diffraction efficiencies after the next subsection.

3.1.2 Subwavelength Gratings

It is interesting to let the grating spacing $d < \lambda$, which we call the grating a subwavelength grating. The first order diffraction will have an angle $\sin\theta_m = \lambda/d - \sin\theta_i$. For normal incident wave, $\theta_i = 0$, we have $\sin\theta_m = \lambda/d > 1$, which has no solution for θ_m in the real domain. That means the subwavelength grating cannot be described by diffraction angles, but it can be well described by complex wave vectors.

In Fig. 3.2, I show a simple dielectric grating formed by alternating rectangle ridges

and grooves. The ridges are assumed to consist of the same material (refractive index n_2) of the underneath substrate. A normal-incident wave has vacuum-wavelength λ and the wavevector is therefore $k_0 = 2\pi/\lambda$. The homogeneous dielectric region above and below the grating can support plane waves of the form (in 2D)

$$E_0 e^{i(k_x x + k_z z)}, \tag{3.2}$$

where the wavenumbers k_x and k_z can be real or purely imaginary, and they satisfy the dispersion relation

$$k_x^2 + k_z^2 = (2\pi n/\lambda)^2 \tag{3.3}$$

where n is the refraction index of the dielectric. Required by the periodic boundary condition of the grating region, the complex E-field is also periodic in the x-direction. That is, the E-field has a factor of

$$e^{i\, m \frac{2\pi}{\Lambda} x}, \tag{3.4}$$

where $2\pi/\Lambda$ is the reciprocal wavevector of the grating, m is an integer. Comparing Eq. 3.2 and Eq. 3.4, k_x can only take discrete values given by

$$k_x = m\frac{2\pi}{\Lambda}, \tag{3.5}$$

which corresponds to the m-th diffraction order. These discrete wavevector plane waves are called Rayleigh diffraction waves. The quantity

$$K = \frac{2\pi}{\Lambda} \tag{3.6}$$

is called the grating wave number (or grating vector).

When the subwavelength condition $\Lambda < \lambda$ is met, the first order diffracted wave

with $k_x = \pm K$ starts to have a purely imaginary k_z, which makes the first order diffraction wave evanescent in air/vacuum. Note that it may not be evanescent in the substrate due to the higher refractive index n_2. Because evanescent wave does not carry energy, the incident energy are restricted in the 0-th order reflection and transmission. Under certain resonance condition, the subwavelength grating may be designed to have strong reflection and little transmission, which make it suitable as a cavity mirror.

3.1.3 Rigorous Coupled Wave Analysis

To be able to quantitatively calculate the reflection and transmission coefficients of the subwavelength grating, many methods have been developed. Major ones include Rayleigh's Theory [78], Integral Method [79], Differential Theory [80], Rigorous Coupled Wave Analysis (RCWA) [81, 82], and Theory of Coordinate Transformation (or C-method) [83, 84]. Among all these methods, RCWA is the most widely used one. It is initialized by Gaylord and Moharam, et al [81, 82] and improved by the same group and other groups [9, 85, 86, 87, 88] in the 90s. It is general enough to analyze the diffraction of electromagnetic waves by any period structure. That includes the multilayer structure consisting of both periodic-modulated and uniform components.

In the following I will give a brief overview of how RCWA works. Detailed formulation can be found in Ref. [9, 85]. Let us again take the simple binary grating (Fig. 3.3) as an example. The space is divided into three regions– Grating Region, Region I (above the grating) and Region II (below the grating). Although the grating is 2D, the incident wave can be in a 3D configuration, as shown by the conical k-vector. For simplicity, let us consider the transverse electric (TE) polarization case, where the k-vector lies in the x-z plane and the electric field has only the y-component.

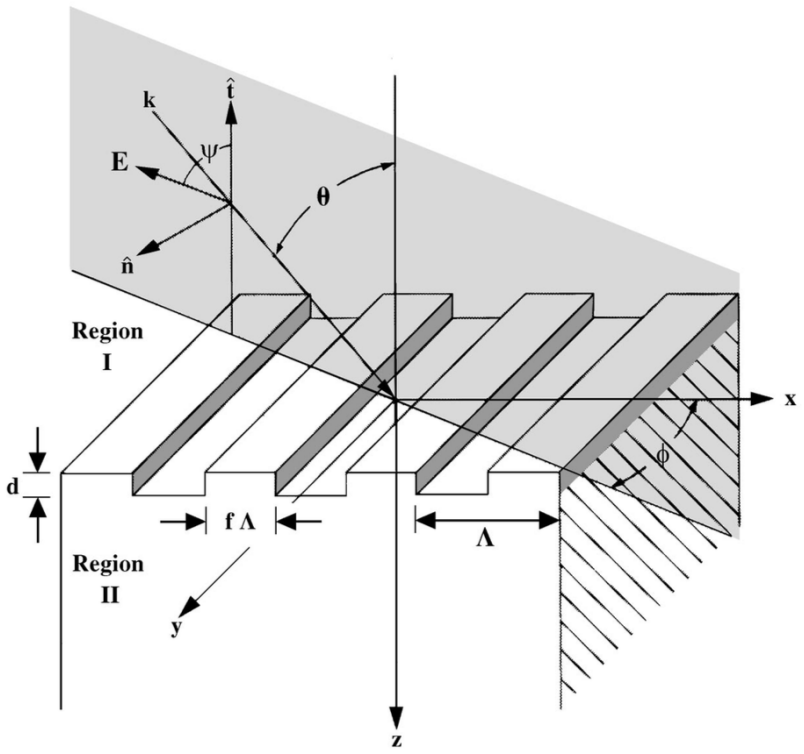

Figure 3.3: Schematic of a simple binary grating problem that RCWA aims to solve. Taken from Ref. [9].

The E-field in region I and II are well described by the Rayleigh diffraction modes:

$$E_{I,y} = E_{inc,y} + \sum_i R_i \exp[-j(k_{xi}x - k_{I,zi}z)], \tag{3.7}$$

$$E_{II,y} = \sum_i T_i \, exp\{-j[(k_{xi}x + k_{II,zi}(z-d)]\}, \tag{3.8}$$

where the region I has two contributions– incident plane wave $E_{inc,y}$ with k-vector $(k_0 n_I \sin\theta,\ k_0 n_I \cos\theta)$ and the reflected waves with a series of k-vectors $(k_{xi},\ k_{I,zi})$. As discussed above, k_{xi} is determined from the Floquet condition and is given by

$$k_{xi} = k_0[n_I \sin\theta - i(\lambda_0/\Lambda)]. \tag{3.9}$$

$k_{I,zi}$ is then determined by the dispersion relation Eq. 3.3. The coefficients R_i and T_i are the complex amplitudes of the reflected and transmitted diffraction waves. We strive to solve for them by matching the boundary conditions of the three regions. The only region left out of description is the grating region, which we will apply Fourier analysis in the following.

Due to the periodicity of the Grating Region, the spatial-dependent field can be expanded into Fourier series, which resembles the solutions in Region I and II:

$$E_{g,y} = \sum_i S_{yi}(z) \exp(-jk_{xi}x), \tag{3.10}$$

$$H_{g,x} = -j(\epsilon_0/\mu_0)^{1/2} \sum_i U_{xi}(z) \exp(-jk_{xi}x), \tag{3.11}$$

where ϵ_0 is the permittivity of free space. Note the k_{xi} is just given by Eq. 3.9. $S_{yi}(z)$ and $U_{xi}(z)$ are the normalized amplitudes of the ith space- harmonic fields such that $E_{g,y}$ and $H_{g,x}$ satisfy Maxwells equation in the grating region. One can obtain that the Maxwell's equations reduce to coupled linear equations between different space-harmonics. The inter-coupling strength between different field space-harmonics are

given by the Fourier coefficient of the permittivity spatial function

$$\epsilon(x) = \sum_h \epsilon_h \exp(j\frac{2\pi h}{\Lambda}x). \tag{3.12}$$

The coupled-wave equations can be then formulated by matrix equations and solved by numerical eigenvalue solvers.

We see that the periodicity of the grating system makes a convenient Fourier expansion discretization possible. The Fourier series is infinite, thus needs to be cutoff in practice. The number N of harmonics included in the Fourier series determines the accuracy of the RCWA calculation. N needs to be pre-determined by convergence test, that is, beyond certain large enough N, the results stay the same. A empirical safe value of N is 41.

We already see the simple binary grating can be solved by RCWA. Actually, an arbitrary shape grating can be approximated by a stack of thin binary gratings and solved by RCWA layer by layer. The way RCWA dealing with multilayer structure is similar to the Transfer Matrix, except the matrices are not 2-by-2, but N-by-N. Therefore, RCWA is a superset of transfer matrix method. It can solve grating combined with multilayer uniform structure like in a SWG-DBR hybrid cavity as will be introduced later.

While RCWA is just a standard Fourier analysis, its implementation in a computer program can be tricky. One need to consider the matrix solver's efficiency, numerical stability, especially for TM polarization and conductive material. A colleague Lei Zhang wrote a Matlab program in 2010 to implement RCWA, which he calls RicWaA (http://www-personal.umich.edu/ zlei/). I used his program in the early years of this thesis (2011-2012) but later I found the program gave inaccurate results (especially in the phases) for TM polarization in spite of how large N I set. Also, the program did not solve for the general 3D conical incident case. Later I started to use another

Matlab program called RCWA-1D, shared by Dr. Pavel Kwiecien as an open-source code in 2012. It is originally written for general grating design. I corrected a few bugs in his program, restructured the program to make it more user friendly and more suit to our needs. All RCWA calculations presented in this thesis is done through RCWA-1D program.

Other RCWA programs available online includes:

* RODIS

(http://photonics.intec.ugent.be/research/facilities/design/rodis/default.htm). It is consequently by several people in UGent University in Europe. It is designed for calculation of 1D, 2D gratings (reflection, transmission, diffraction efficiency of different modes). However, it requires python 2.2, which is too old version for convenient coding. A lot of packages are not supported, eg, the most important one, numpy for scientific computing. It passed the non-conical case test, but does not work for conical incident waves.

* CAMFR

It is a more comprehensive program, from the same university of RODIS, by Peter Bienstman. The code is based on RCWA, but integrated with PML, PEC, boundary condition. It is powerful, not only for periodic structure. However, the periodic grating, which is to our interest, is not documented. It is not an easy-to-use program.

* S4 from Fan group in Stanford

It should be a reliable choice. Fan group published many papers in photonic crystals using the code. I know people from Norris group in Michigan had successful experience with it, although I didn't try it out.

It worths note that finite difference time domain (FDTD) method can also solve grating problems, since it basically solves the Maxwell's equations. Compared to the frequency domain method RCWA, FDTD is more capable and general purpose method. For example, FDTD can solve for different types of excitation (plane wave,

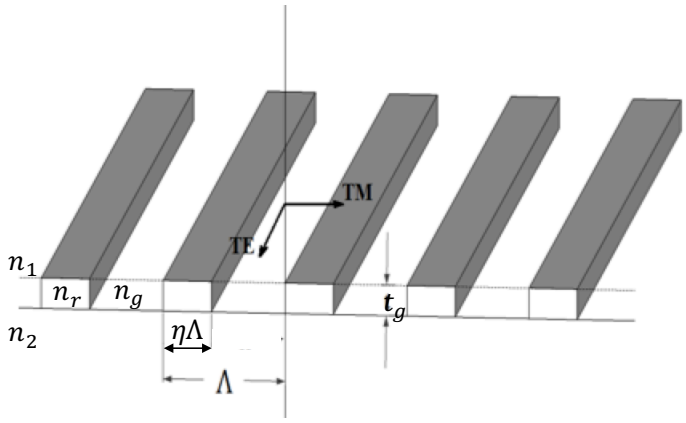

Figure 3.4: A schematic of high contrast gratings (HCG)

gaussian wave, dipole, etc) while RCWA can only deal with plane wave excitation, although gaussian or arbitrary incident waves can be decomposed into planes waves and solved by RCWA. FDTD can also apply different boundary conditions (periodic, radiation, PML, etc). Finally FDTD as a time-domain method can see the evolution of the fields over time. However, FDTD is considered to be more expensive method, both in time and memory requirement. We used Lumerical FDTD Solution, a commercial program to compute some of the structure presented in this thesis. But it is mainly assisting RCWA in designing and simulating the experimental devices.

3.1.4 High Contrast Gratings

A high contrast grating (HCG) is a subwavelength grating with high refractive index "ridge" surrounded by much lower refractive index materials, so the name "high contrast". It debuts in 2004 as a promising broadband high reflectance mirror [89]. A schematic of a typical rectangular shaped HCG is shown in Figure 3.4. The grating bars are made of material with refractive index n_r, r stands for 'ridge'. The groove region has refractive index n_g. The upper space is filled with material of index n_1 and the lower space filled with n_2. The high contrast requires that n_r is much greater than all n_1, n_2, n_g. In practice, the grating bars can be made of Si or GaAs (refractive index

3.7 and 3.6 at 800nm respectively). n_1 and n_g are commonly made of air (n=1.0). n_2 can be metal oxides such as SiO2 or Al2O3 (n = 1.45 and 1.67 respectively), or simply air. In this later case, the grating is fully suspended in air, which means one has to design a tethering structure to hold the grating bars at the two sides.

The HCG has more designable geometric parameters than DBR. The period of the grating is Λ; the grating bar width is $\eta\Lambda$, where η is the grating duty cycle; the thickness of the grating is t_g. We define the TE polarization as the electric field has only one component along the grating bars, and TM polarization as the electric field is perpendicular to the bars' direction.

HCGs have many good properties. In the following I will give an overview of those properties.

Scalability

The first nice property is HCG's scalability with wavelength. That is, HCG's reflection and transmission coefficients are invariant from one wavelength to another if one scale all the dimensions of the HCG by the same factor with the wavelength. Actually, this property is not unique to HCG, but universal for any mild dispersive dielectric structure. This property stems from the invariance of Maxwell's equation under linear scaling. Specifically, consider the following Maxwell's equations relating the electric and magnetic field,

$$\nabla \times \mathbf{E}(\mathbf{r}) = -\frac{\partial \mathbf{B}}{\partial t} = -j\omega\mu(\mathbf{r})\mathbf{H}(\mathbf{r}) \tag{3.13}$$

$$\nabla \times \mathbf{H}(\mathbf{r}) = \epsilon\frac{\partial \mathbf{E}}{\partial t} = j\omega\epsilon(\mathbf{r})\mathbf{E}(\mathbf{r}) \tag{3.14}$$

where the field is assumed to be time-harmonic with frequency ω, and μ and ϵ are assumed to be independent of ω. Because of the spatial derivatives, the LHS of the two equations are proportional to r^{-1}, where r can represent any spatial coordinate.

The RHS contains the angular frequency ω which is proportional to λ^{-1}. Under the transformation $\mathbf{r} \to \alpha\mathbf{r}$ (α is a constant factor), if λ scales the same factor as $\alpha\lambda$, the Maxwell's equation will have the same solutions for $\mathbf{E}(\mathbf{r}), \mathbf{H}(\mathbf{r})$. The electromagnetic fields and thus the reflection and transmission coefficients of a given incident field are the same under the new wavelength. The scaling in $\epsilon(\mathbf{r})$ means a dielectric region with permittivity ϵ expands α times in space.

The scalability is a very convenient feature of HCG. One can design HCG for one wavelength for example infrared and later easily extend all conclusions to a new wavelength such as visible. More generally, one can normalize all relevant physical quantities with 'Length' dimension to some characteristic length, for example, the period of the grating, which will help reduce the number of parameters we study. Of course, the premise is the permittivity ϵ of the material used is non-dispersive. Although semiconductors such as GaAs and Si all have dispersions (refractive index decreases with increasing wavelength), the slope of the dispersion becomes mild when the wavelength goes beyond the bandgap wavelength and approaches the long-wave limit. It is a good approximation to treat mild dispersive media as scale invariant. HCG is not sensitive to the mild change of refractive index.

Broadband High Reflectance

The most important feature of the HCG is that it can provide very high reflectivity over a wide wavelength range. In the following, I will use example HCGs made of $Al_xGa_{1-x}As$-based materials to discuss this point. Specifically, grating ridge is assumed to be $Al_{0.15}Ga_{0.85}As$ with $n_r = 3.58$ (at 800nm, no absorption). The grating is surrounded all by air, that is, $n_1 = n_2 = n_g = 1.0$ (see Fig. 3.4).

In Fig. 3.5, I show the reflectance of the HCG under TE and TM polarized normal-incident waves. The duty cycle is fixed at 50%, while the thickness of grating t_g and wavelength λ are varied to cover the designable parameter space. As discussed above,

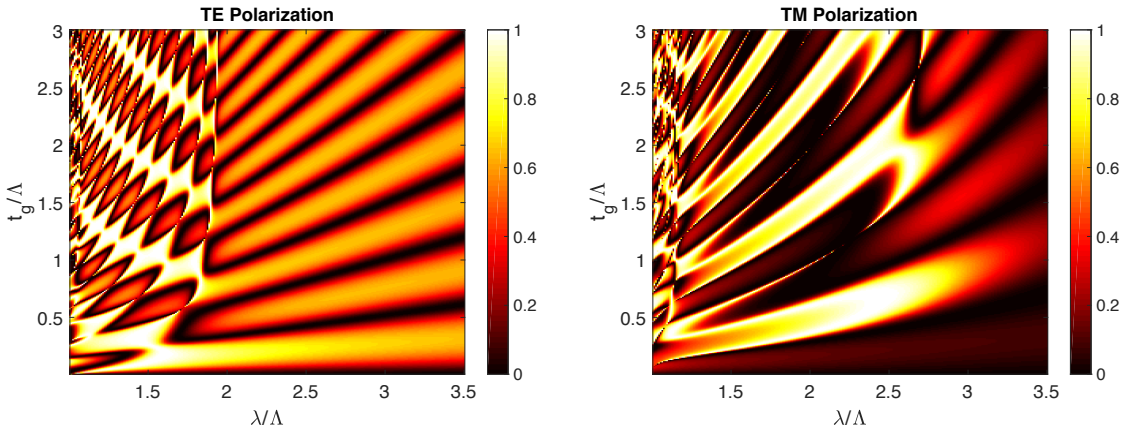

Figure 3.5: Reflectance maps for HCG, with TE polarized normal-incident light (left), and TM polarized normal-incident light (right). The x-axis is wavelength normalized by period of grating and y-axis is the thickness of grating normalized by period of grating. Duty cycle is fixed to 50% for both cases.

t_g and λ can all be scaled to the period of the grating Λ without losing any information. Only the subwavelength regime $\lambda/\Lambda > 1$ is shown. The most eye-grabbing feature of the reflectance maps is the "checker-board" like pattern. There are straight stripes radiating into the long wavelength. On top of those are a series of parabola-like lines superposing. We will learn in the next section these two sets of lines/stripes come from the internal modes inside the HCG. In the crossing regions, high reflectance (high-R) regions are formed alternatively, giving a nice looking checkerboard pattern.

Although any high-R region (white in the figures) can potentially serve as a high-reflective cavity mirror, one would prefer large continuous high-R regions because gratings with parameters in those regions have broad working wavelength range and more robust against fabrication error in t_g. We see from Fig. 3.5 that as t_g increases, the high-R regions become choppy. The best broad high-R regions generally have short t_g, or more precisely, the lowest order longitudinal mode, since the t_g controls the longitudinal feedback between the grating's upper and lower boundary.

There are some qualitative difference between the TE and TM polarization. First,

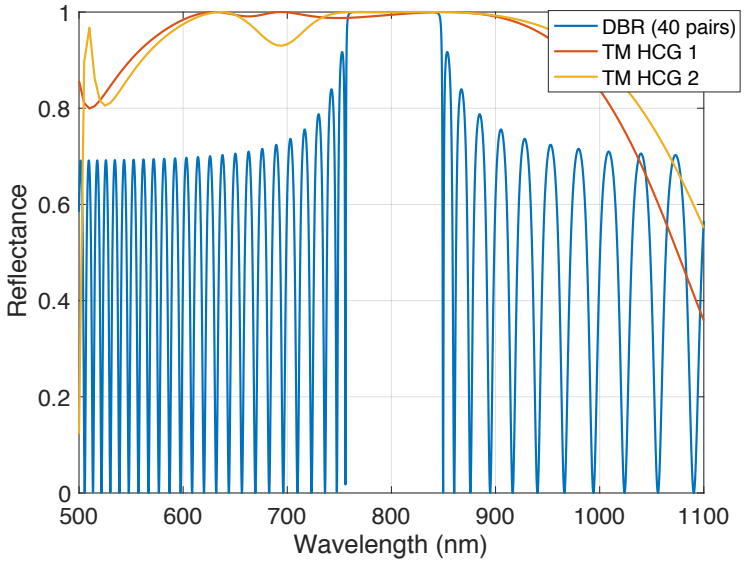

Figure 3.6: Broadband high reflectance of HCG mirror compared to DBR. The TM HCG1 has period 350nm, $t_g = 200$nm, duty cycle $\eta = 75\%$, while the TM HCG2 has slightly different $t_g = 210$nm and $\eta = 76\%$. TM HCG1 enables $\Delta\lambda/\lambda = 40\%$ for high reflectance over 99%. TM HCG2 is tweaked to enable ultra-high reflectance ($R > 0.995$) for cavity application, which is better than 40 pairs of DBR ($Al_{0.15}Ga_{0.85}As$ /AlAs).

the long wavelength stripes from TM is more curved than TE's, which makes the shorter wavelength stripes almost parallel with them so that the checkerboard is not very obvious. Second, the stripes from TM are more sparse; have larger spacing between each other. These two difference makes the high-R region in TM broader in wavelength and t_g than TE. An optimized TM grating can have $\Delta\lambda/\lambda > 40\%$ where $\Delta\lambda$ is the band with $> 99\%$ reflectance. This may be very useful for broadband high-R mirror applications. However, the lowest order high-R region from TM has a thicker t_g than TE's. This may not be beneficial to achieve thinner gratings, which are generally easier to electro-mechanically tune and to integrate with electrical injection.

To give a real sense of the grating dimensions used for cavities operating around 800nm, when the lowest t_g lobe is used, TE grating has a period $\Lambda \sim 500$nm and $t_g \sim 100$nm, TM grating has a $\Lambda \sim 330$nm and $t_g \sim 240$nm (greater than the bar width). Duty cycle in this case is fixed to 50%, but can be tuned to move the high-R

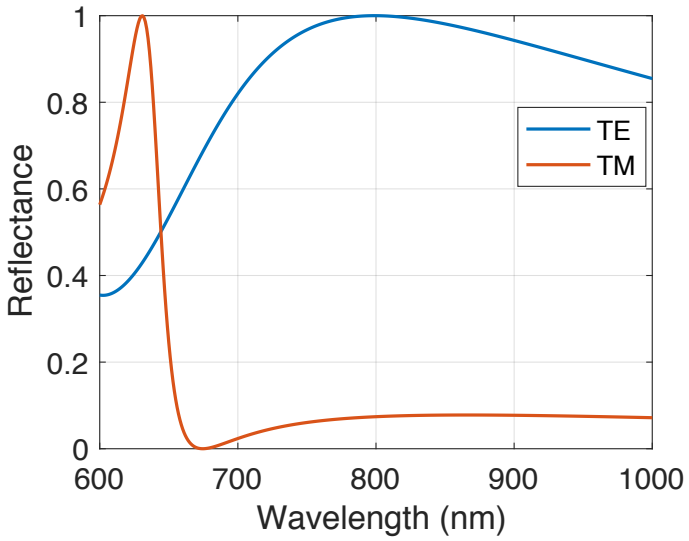

Figure 3.7: Reflection spectra for two polarizations TE and TM. The HCG parameters are $\Lambda = 510$nm, $t_g = 90$nm and $\eta = 0.4$. The HCG is optimized as a good cavity mirror centered at 800nm.

region to the left or right, and possibly merge two lobes of high-R region to be a bigger one.

The broadest stop-band (reflectance > 0.99) is achieved by using duty cycle 75%, as shown in Fig. 3.6, the TM HCG1 curve. The stop-band width is $\Delta\lambda/\lambda \sim 40\%$, which is much broader than 40-pair DBR ($\Delta\lambda/\lambda = 10\%$), while the thickness of the HCG is only 200nm, 4% of the DBR's thickness $\sim 5\mu$m. However, the HCG1's reflectance at around 750nm is not enough for constructing high quality cavity. To improve the overall reflectance within the stop-band, I tweaked the HCG parameters, which is shown as the TM HCG2 curve. As can been seen, although there is a 'dent' at around 700nm that breaks the broad stop band, the reflectance at around 800nm is improved to the same level of the DBR's. Even though, the HCG2 still has a much broader stop-band $\Delta\lambda/\lambda = 20\%$ than the 40-pair DBR.

Polarization Selectivity

Another important feature for the HCG is that it can provide polarization selectivity by exhibiting very high reflectance for one polarization but minimal reflectance in the orthogonal polarization. In Fig. 3.7, I show an example HCG optimized as a high-R cavity mirror centered at 800nm. The TM reflectance (~ 0.08) is much lower than the TE reflectance around 800nm.

One can see this conclusion easily from the reflectance map Fig. 3.5. The TE design parameters comes from the lowest t_g lobe in the TE R-map. Correspondingly, the TM map is very dark around the same wavelength of the lobe. The grating is in the effective-medium regime for TM polarization. The grating can be treated as an effective slab of dielectric with index ~ 2.0 (weighted average of the AlGaAs and air, see Ref. [83] for how to weight the refractive index). The reflectance from such an effective medium is $((n-1)/(n+1))^2 \sim 0.09$, roughly agreed with the RCWA calculation.

Although the polarization selectivity is desirable for building laser cavity (single-mode operation) and polarization filter, there are some applications requiring mirrors insensitive to polarization. Because of the symmetry breaking in the along-bar and cross-bar direction, the HCG usually has large reflectance asymmetry for the two polarizations. However, the large parameters space of HCGs make it very flexible to design for polarization-insensitive purpose. One can find some narrow region that TE and TM has both high reflectance. Alternatively, 2D photonic crystal slab (also high index contrast) can help to reduce the asymmetry, and produce highly even performance for both polarization[90].

3.1.5 Physics Origin of High Reflectance

It is surprising to see such a high reflectance coming from a very thin layer of HCG. After all, we learn from basic optics that a thin slab of dielectric can only

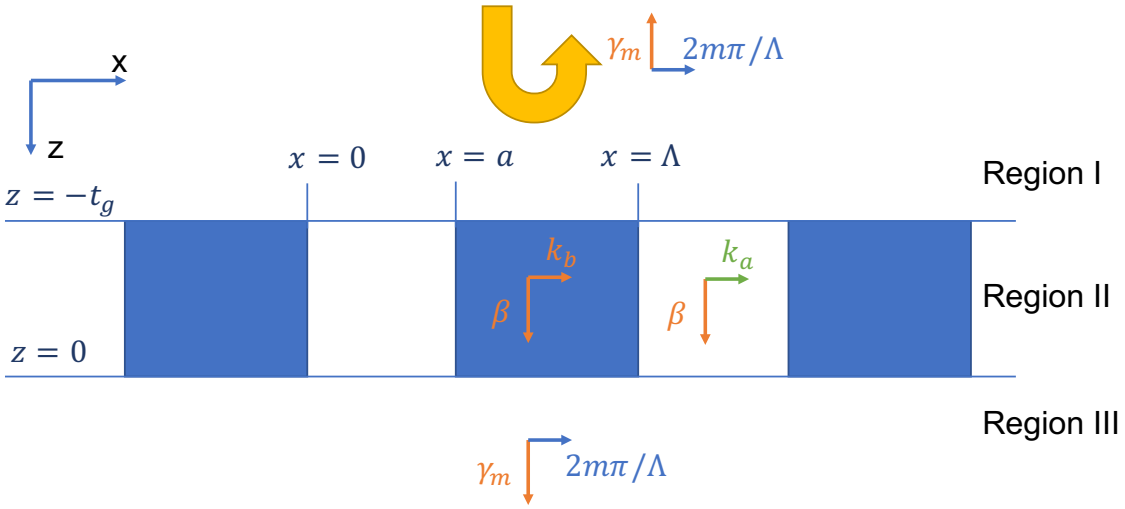

Figure 3.8: Schematic for solving waveguide array (WGA) modes inside the grating to explain the broad near-100% reflectance.

provide a reflectance proportional to the index contrast $(n-1)/(n+1)$, which is quite limited for all semiconductors in the optical frequency domain. However, one can easily get 100% transmission from a dielectric slab of OPL $\lambda/4$, by the Fabry-Perot resonance where the multiple reflections between the two interfaces of the slab completely cancel out. Similarly, we will see HCG can form an internal resonance that cancels the transmitted waves at the output plane of the grating.

Unlike dielectric slabs where the internal modes are counter-propagating plane waves, HCGs have more complex internal mode due to the transverse modulation. Consider the HCG illustrated in Fig. 3.8, a plane wave is incident with normal angle; the reflected and transmitted waves in Region I and III have discrete transverse wavenumber defined by the inverse of the period $2\pi/\Lambda$. The grating region (Region II) has two homogeneous regions– grating bars and air gaps. The solutions to the field in these regions can be expanded using plane waves basis, with propagating constant (along z) β and transverse wavevector k_b and k_a for 'bar' and 'air' respectively. Because the phase matching condition at the interface of the bars and air gap, propagating constants are the same in both region. The idea is to apply the boundary

conditions for E and H field at the region boundaries to obtain the dispersion relation between these wavevectors.

Ref. [10] gives the full derivation of the mode dispersion inside the HCG. The basic conclusion is, the HCG can be considered as a waveguide array (WGA) with propagation direction in the z-direction. For a given frequency, the WGA modes are also discrete, that is, β, k_a and k_b can only take discrete values. For normal incidence, the excited modes are restricted to the even modes, so the field in the grating bars and air gaps can be expressed as cosine functions,

$$H_{y,m}(0 < x < a) = \cos(k_{b,m}b/2)\cos[k_{a,m}(x - a/2)] \quad \text{–inside air gaps} \tag{3.15}$$

$$H_{y,m}(a < x < \Lambda) = \cos(k_{a,m}a/2)\cos[k_{b,m}(x - (a + \Lambda)/2)] \quad \text{–inside grating bars} \tag{3.16}$$

Here I consider the TM polarization where magnetic field has only y-component thus easier to solve first. The dispersion relation between k_a and k_b can obtained by matching the boundary condition at the bar and air interface,

$$n_{bar}^{-2} k_{b,m} \tan(k_{b,m}s/2) = -k_{a,m} \tan(k_{a,m}a/2). \tag{3.17}$$

We have additional constraint relating β and k_a, k_b

$$\beta_m^2 = (2\pi/\lambda)^2 - k_{a,m}^2 = (2\pi n_{bar}/\lambda)^2 - k_{b,m}^2 \tag{3.18}$$

Above can be solved graphically or numerically.

High reflectance HCG is operating in the dual-mode regime. We can see the dispersions of the lowest two modes manifest in the reflectance map shown in Fig. 3.9, the orange and light green lines. The long wavelength stripes (zero transmission, blue region) comes from the Fabry-Perot resonance of the lowest WGA mode between the two grating interfaces. The second WGA mode kicks in at a cutoff wavelength

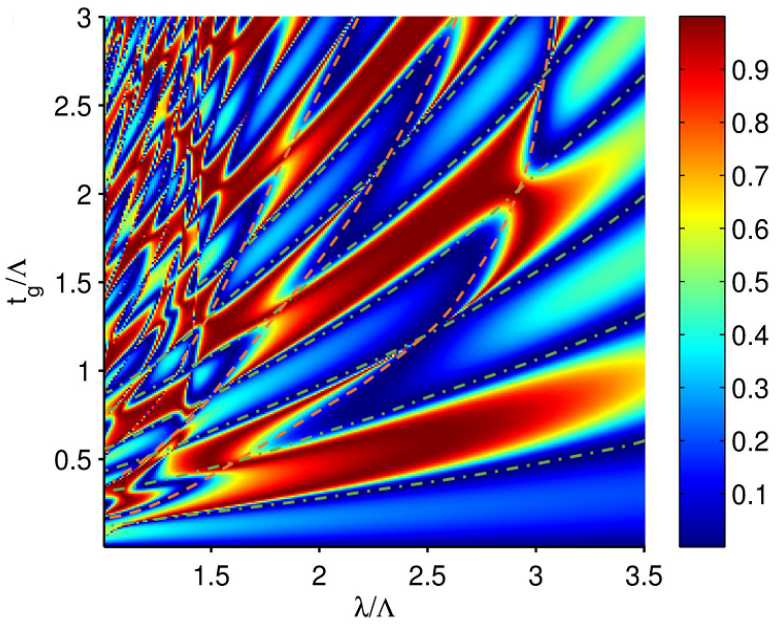

Figure 3.9: Reflectance map for a HCG under TM wave incidence. The HCG $\eta = 0.65$. The orange and green dash-dotted lines comes from the WGA mode dispersion.

$\lambda/\Lambda \sim 3$. They cross and anti-cross each other depending on the phase relations. The two-mode interaction determines the reflectance of the HCG. Ref. [10] calculated the two modes' field profile, amplitude and phase of the dc-component, as shown in Fig. 3.10.

The field profile of the lowest two modes inside the grating is piecewise cosine functions (3.16) as shown in 3.10 (b) left. When the internal modes couple out to the Rayleigh diffraction modes in Region I and III, the conversion efficiency (determines the reflection and transmission coefficients) is determined by the overlap integral between the mode profile and the zeroth order diffraction, since only the zeroth order carries energy. That is, the dc-component that matters for the reflection and transmission behavior. The amplitudes of the dc-component of the first and second WGA modes are around the same in a large wavelength range (Fig. 3.10 (a)) but the phases are opposite. At the output plane $z = 0$, the two modes perfectly cancel out and thus

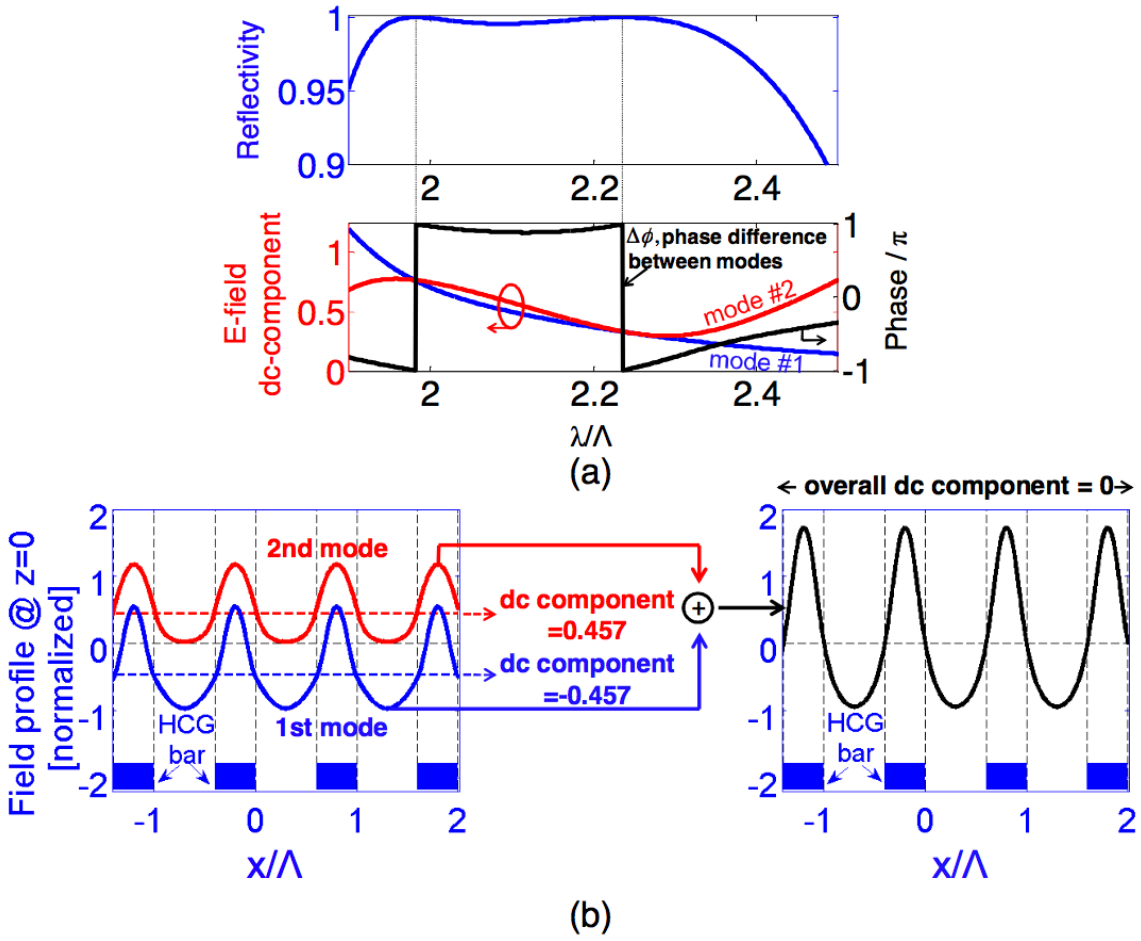

Figure 3.10: The mechanism of 100% reflectance of HCG. Taken from Ref. [10].

.

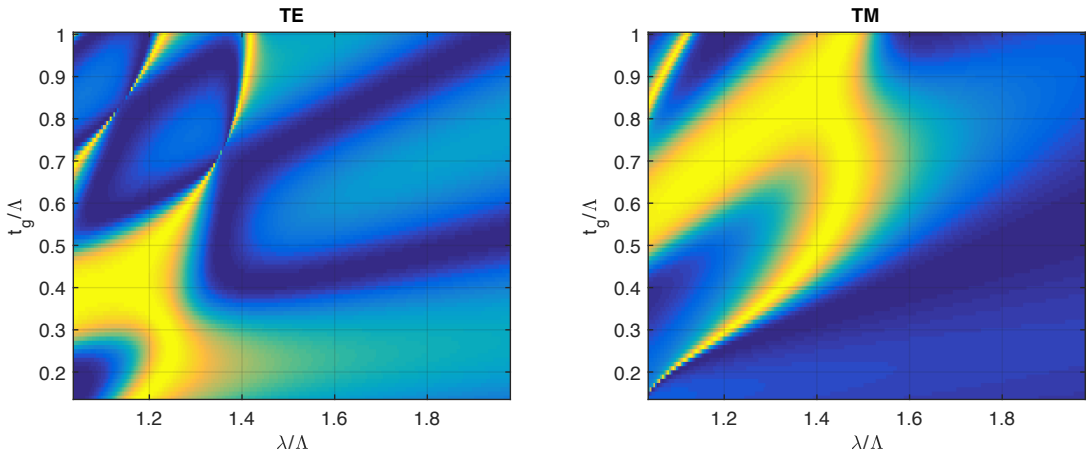

Figure 3.11: The best broadband high reflectance from HCG made of refractive index = 2.3 material. The best duty cycles for TE (53%) and TM(43%) are shown.

.

suppress the transmission. This is the reason of the broad, nearly 100% reflectance in a HCG mirror.

It turns out the two-mode perfect cancellation over a broad wavelength range can only happen for sufficient high refractive index contrast. First, the index contrast between the grating bar and air gap facilitate the formation of the discrete WGA modes (Eq. 3.18). Second, the abrupt change in the refractive index at the exit plane $z = 0$ provides strong feedback to those WGA modes. The WGA mode can form standing waves between the entry and exit plane. These strong standing waves can interact with each other or in other words inter-couple with each other at the exit plane. This is the basis of the perfect cancellation.

To see the detrimental effect of lower index contrast, I show the best reflectance map resulting from a grating made of refractive index of 2.3 (eg. GaN at $1\mu m$), in Fig. 3.11. Although near 100% reflectance can be found through parameter optimization, the stop-band width ($R > 0.99$) is limited at only $\Delta\lambda/\lambda \sim 18\%$ for TE and $\Delta\lambda/\lambda \sim 8\%$ for TM. The optimized design presented here may be largely okay for cavity application, since we still have at least 40nm 0.99 stopband or 30nm 0.995

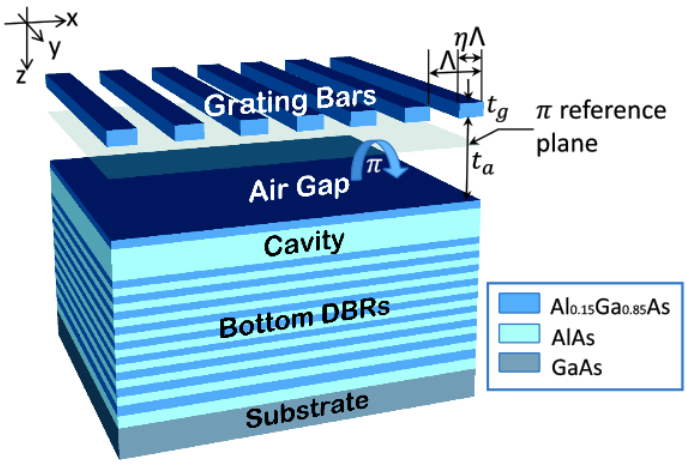

Figure 3.12: Schematic of SWG-DBR hybrid cavity.

stopband to work with. However, $n = 2.0$ will make high-R like 0.995 impossible at all.

3.2 Designing the SWG-DBR Hybrid Cavity

To be compatible with current fabrication technology, we implement an SWG-DBR hybrid structure. The sample structure is shown in Fig. 3.12. The goal is to achieve a high-Q cavity which resonates with the QW excitons at an energy pre-defined by material and sample growth (1.550eV or 800nm in this thesis).

3.2.1 HCG Optimization

There are three criteria for a good HCG used for cavity mirror:

1. High-reflectance (> 0.995)
2. Wide (eg. $> 60nm$) reflectance range centered at 800 nm
3. High tolerance on thickness, duty cycle, grating period, grating index and incident angle

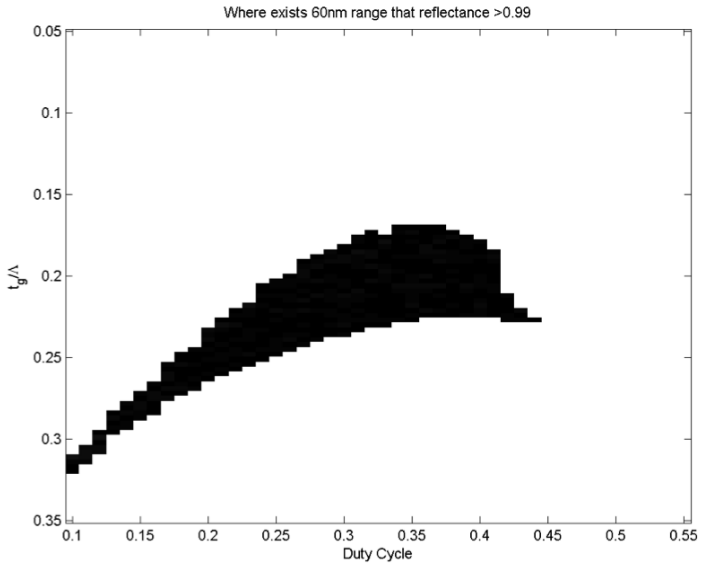

Figure 3.13: HCG reflectance map in the parameter space.

Candidates that meet condition 1) and 2) are shown in dimensionless parameter space (thickness/period and duty cycle) in Fig. 3.13, the black region. I focus on the lowest t_g lobe (Fig. 3.5) and the TE polarization here. The stop-band width are automatically extracted using a Matlab script. Actually I relaxed the criterion (1) and thus plot a larger region in Fig. 3.13, because it may allow one to evaluate how quickly the reflectance of HCG becomes really bad. The ideal design should be chosen at the center of the area, so it will enable larger tolerance.

3.2.2 Tolerance Analysis

In principle, every point in the previous map can be used as a HCG mirror. However, considering the possible fabrication error, one should choose the point most robust against those errors. The scanned map 3.13 already showed some sense of tolerance. One should choose the region in the middle instead of the edge regions. A more systematic tolerance analysis is shown in Fig. 3.14.

Not only the geometry parameters such as the thickness of grating, duty cycle and period is checked, the refractive index is also checked since the epitaxial growth

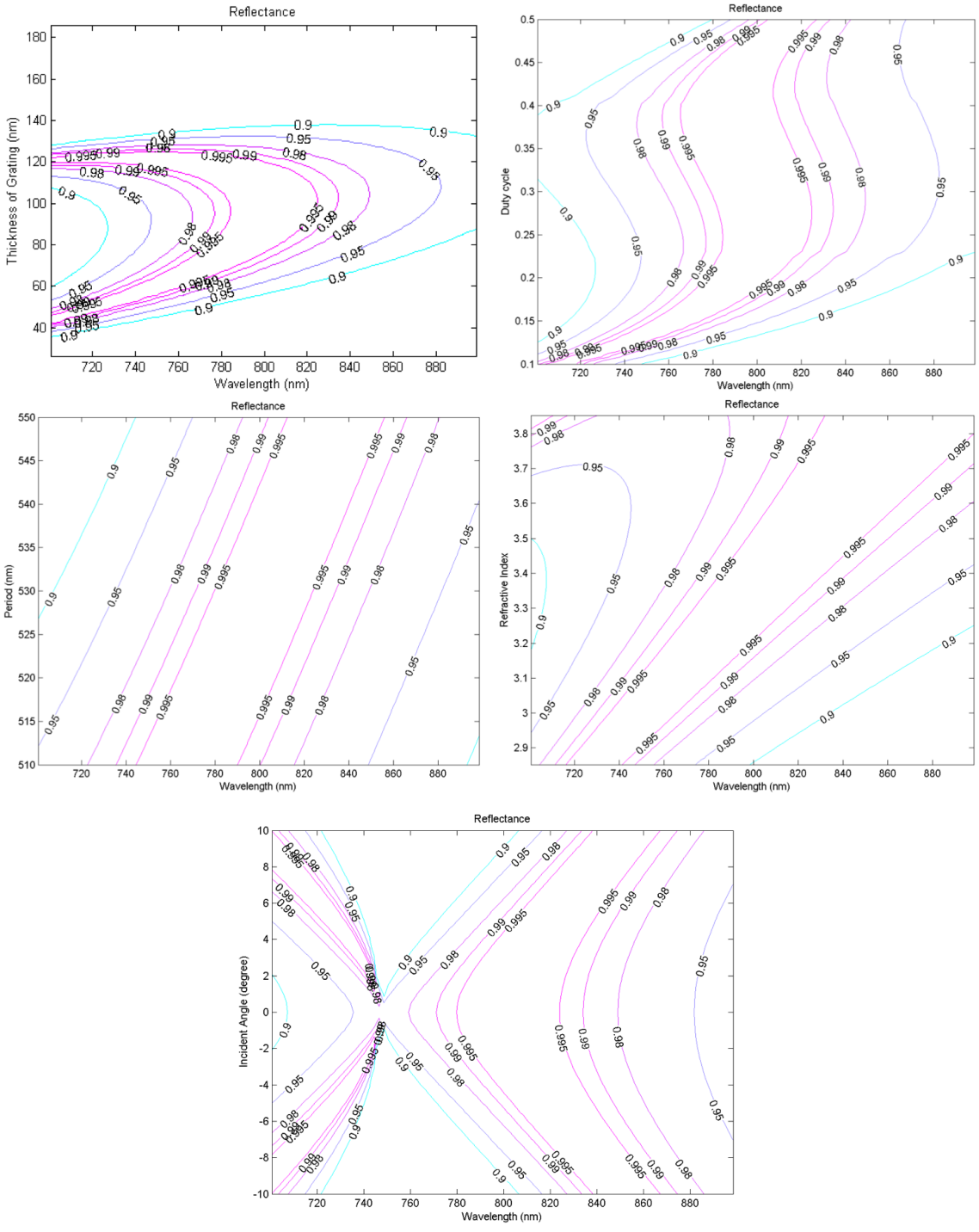

Figure 3.14: HCG tolerance scan for various parameters.

may introduce small variation in the Al-composition in $Al_xGa_{1-x}As$. Fortunately, the variation is negligible in the range of the possible Al fluctuation.

In addition, the angle tolerance is also checked. Comparing to DBR, one downside of the HCG mirror is its limited high-R angle range, especially for TE polarization design. In this design case, the $R > 0.995$ angle range is $\pm 6°$. We will see later in the experimental characterization, this seems to be not a problem, as we mainly care about the near normal-incidence property (ground-state). Note that a high angle tolerance HCG mirror can be designed, if required by certain application. The highest angle tolerance I achieved is $\pm 35°$ using a TM design. If this is not enough, one can stack two HCG mirrors together, forming a double-HCG to enhance the angle tolerance to over $\pm 60°$. However this may increase the fabrication difficulty.

3.2.3 Assembling SWG and DBR

General Principle

After obtaining the optimized SWG, the next step is to assemble it with a bottom DBR and a cavity layer. Here the Fabry-Perot resonance condition is crucial for achieving the desired cavity resonance. Specifically, the round-trip phase in the cavity layer should be integer numbers of 2π. That means the top mirror, albeit using a SWG, should act like a DBR with a high-index layer in contact with the low-index cavity. Because the SWG requires an air gap, I put a high-index $\lambda/4$ DBR layer as the matching layer on top of cavity layer (see Fig. 3.12). Because air gap is a low-index layer, we need the SWG act like a high-index DBR layer. Here I introduce a reference plane where the reflection phase is exactly π. The reflection phase consists of the real reflectance at the grating lower boundary plus the traveling phase between the reference plane and the grating boundary. The buffer layer thickness can be determined by

$$\phi_{SWG} - 2k_0 t_{buffer} = \pi, \tag{3.19}$$

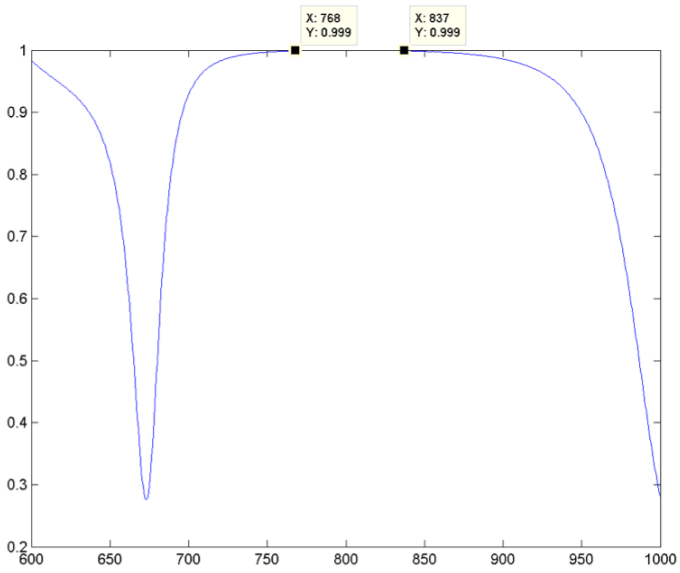

Figure 3.15: Reflection spectra for SWG combined with 1.5 pair of top DBR. Because they are phased matched, the reflectance is improved over the single SWG.

where $k_0 = 2\pi/\lambda$. It is possible t_{buffer} becomes negative. But it would not change the conclusion. After the buffer layer is the $\lambda/4$ low-index air layer in conjunction with the underneath high-index layer. As a whole, all the layers above the cavity is the top mirror in our case. The reflectance of the mirror is shown in Fig. 3.15. Because the additional airgap and one (or more) layers of top DBR layer, the reflectance and the bandwidth are improved over the SWG alone.

One additional caveat, if the cavity is constructed according to the above design rule, it is possible the total air gap is very thin. The first order diffraction (evanescent) may not decay completely before reaching the bottom structure. It results in some coupling into the cavity and DBR layer, because it is not evanescent in those layers. This leakage will lower the quality factor of the cavity, thus should be avoided. One can make the air gap thicker by $\lambda/2$ to circumvent this problem.

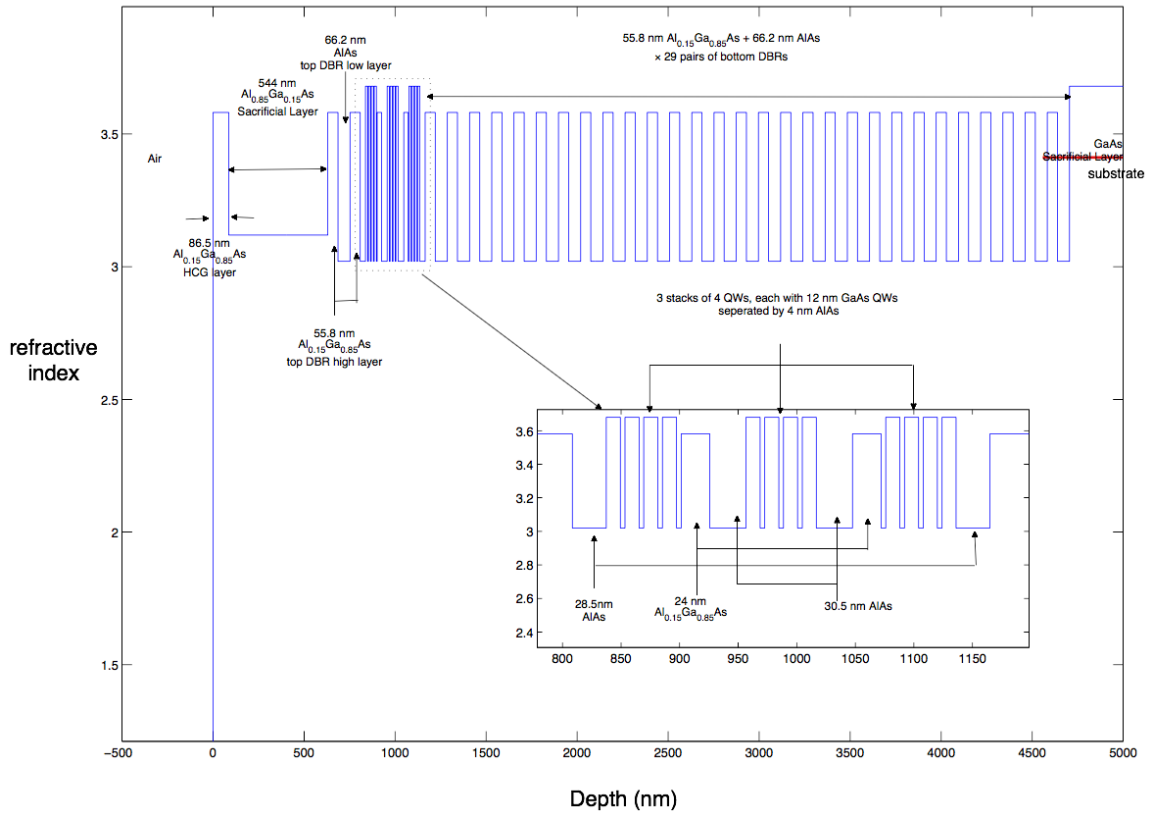

Figure 3.16: Design map for a TE sample.

An Example TE Design

An example design map sent to our collaborator for sample growth is shown in Fig. 3.16. 12 QWs in 3 sets are placed at the anti-nodes of the resonant cavity field, the OPLs of the layers around QWs are compensated for the higher index of GaAs. Actually, keeping the OPL same would not automatically make the correct resonance. The reflections between the QW and the surrounding layers will effectively increase the cavity length. The surrounding layers need to be further shrunk to shift the resonance back. The 86.5nm thick grating layer will need to be etched into period 509nm and duty cycle 0.4.

The reflectance of the sample after growth is simulated for our collaborator to calibrate the MBE parameters, as shown in Fig. 3.17. The reflectance of the sample

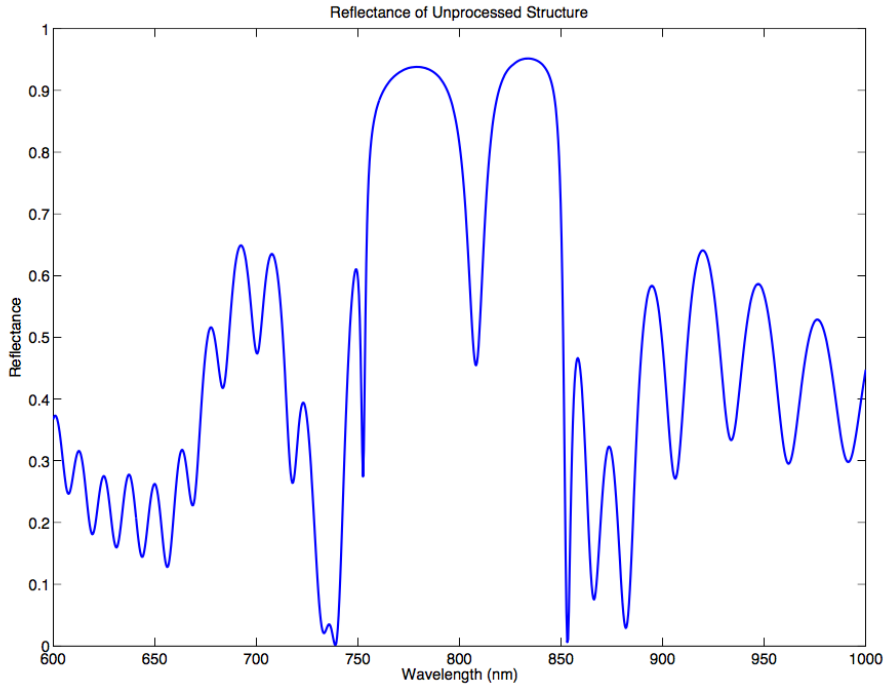

Figure 3.17: Reflectance of the unprocessed sample at room temperature. Only including Al85Ga15As sacrificial layer absorption

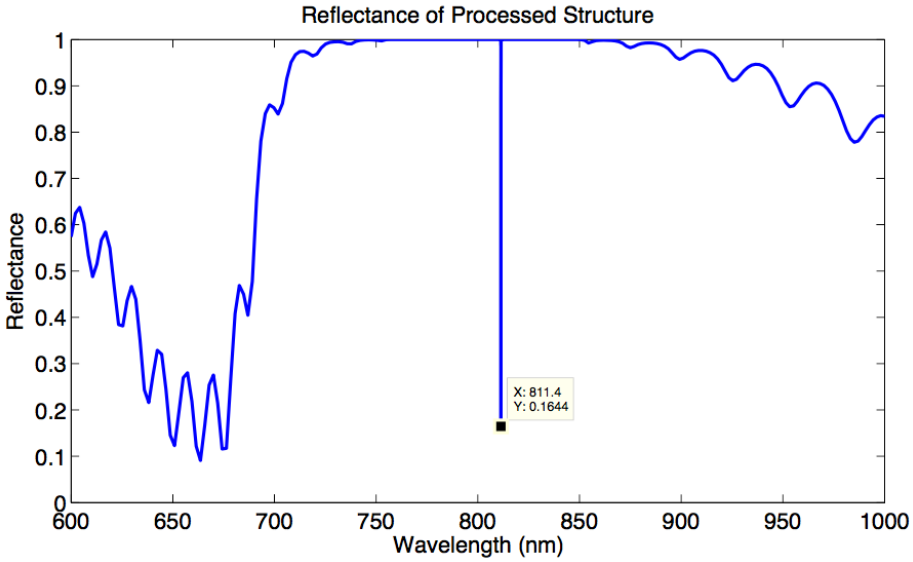

Figure 3.18: Reflectance of the processed sample at room temperature. In this 300K design, the resonance appears at 811.4 nm, which will blue shift 12nm to 800nm when cooled down to 4K. Hence cavity resonance will match exciton resonance in 12nm-QWs.

after etching is also simulated, as shown in Fig. 3.18. A special note, the design should compensate for the cavity resonance shift due to temperature change. This temperature dependence of the cavity resonance is mainly due to refractive index shrinkage when temperature decreases. The thermal expansion/contraction is negligible. The temperature dependence of refractive index can be found in Ref. [91]. From 300K to 4K, GaAs's refractive shrinks $\sim 2\%$, while the linear thermal expansion is only -0.15% (http://www.ioffe.ru/SVA/NSM/Semicond/GaAs/thermal.html).

The E-field distribution of our SWG-DBR cavity at the designed resonance (800nm) is shown in Fig. 3.19. For TE polarization, the field is concentrated at the center of the cavity (z=1000nm). The field enhancement compared to the incident field is around 10 times. As a comparison, with TM polarization, the field is only enhanced by 3 times compared to the incident field. Note the absolute value of the field in Fig. 3.19 should not be directly compared since they are normalized to different quantities for TE and TM polarization. By default, RCWA will normalize E-field to the incident E-field E_y^{inc} for TE polarization (has only y-component), but normalize H-field to incident H-field H_y^{inc} for TM polarization. Because in vacuum $|E|/|H| = 377\Omega$, the field in TM case will be 377 times larger than its counterpart in TE.

An Example TM Design

One drawback we later found for the previous TE design is, the grating thickness is so small that it is easy to break during the fabrication. We succeeded to fabricate 7.5μm long grating but all 10μm and above gratings have snapped. Comparing the thickness 86.5nm with the bar width 204nm, the cross section of the grating bar is very like raw Chinese-style noodle or raw pasta (Linguine). If one makes the pasta long enough and hold it horizontally, it will eventually snap due to self-weight. Even worse, GaAs is more brittle and subject to strain induced force at the tethering structure, which all makes it prone to break (imagine one applies pressure at the two

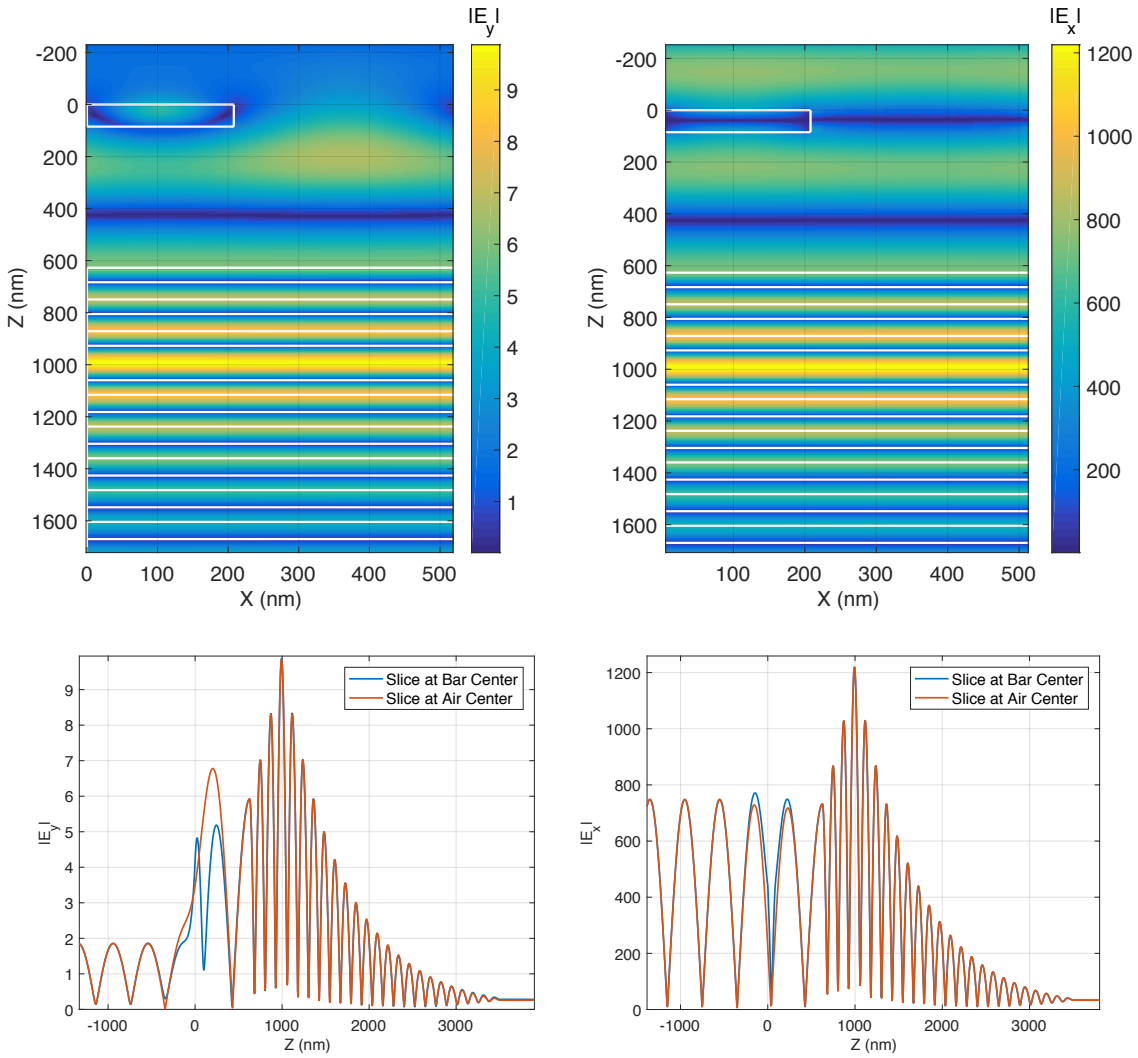

Figure 3.19: Field distribution of the designed cavity with TE and TM excitation waves. The QWs are not integrated into the cavity yet. The field is normalized to E_y^{inc} for TE and H_y^{inc} for TM (the convention in RCWA program). The 1D plots in the lower panel are 1D slices at center of the grating bars and center of air gaps. White lines are the boundary of materials. The cavity center locates at around 1000nm deep from the grating upper surface (z=0).

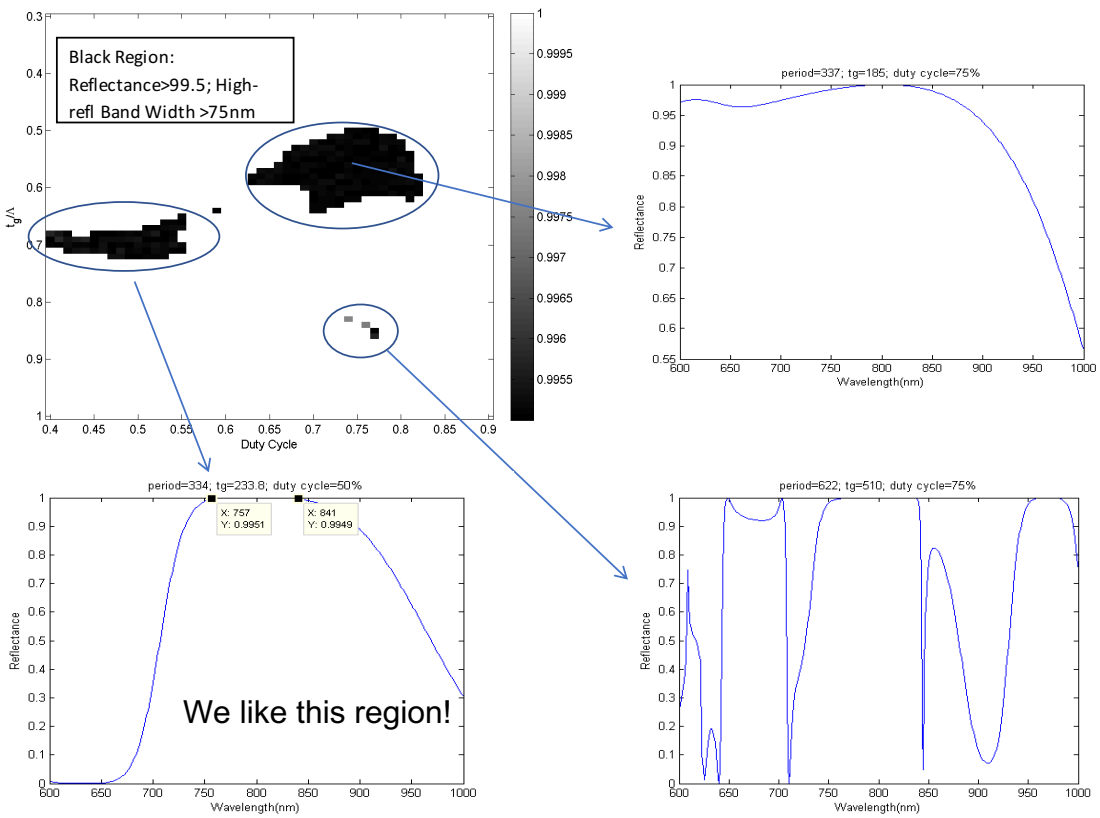

Figure 3.20: HCG optimization for TM polarization.

ends of the pasta).

One way to alleviate the snapping problem is to add more thickness to the rectangle-shape grating bar. As shown in Fig. 3.5, TM design generally has more thickness over TE design. In this subsection, I will introduce a TM design we aim to make longer gratings and improve the success rate of fabrication. In Fig. 3.20, I show the parameter sweep result for a TM grating. The $t_g - \eta$ parameter space has two major high-R region– one at around 50% duty cycle is smaller, another one at around 75% duty cycle is larger. However, the actual dimension of the grating for the larger region is about 253nm wide and 185nm thick. The air spacing of the grating bars is only 84nm, which may be hard to accurately control during the etching (usually the etching precision is about 5nm). It is preferable to have a larger air spacing. Therefore we chose the region around 50% duty cycle to do further design. The lower

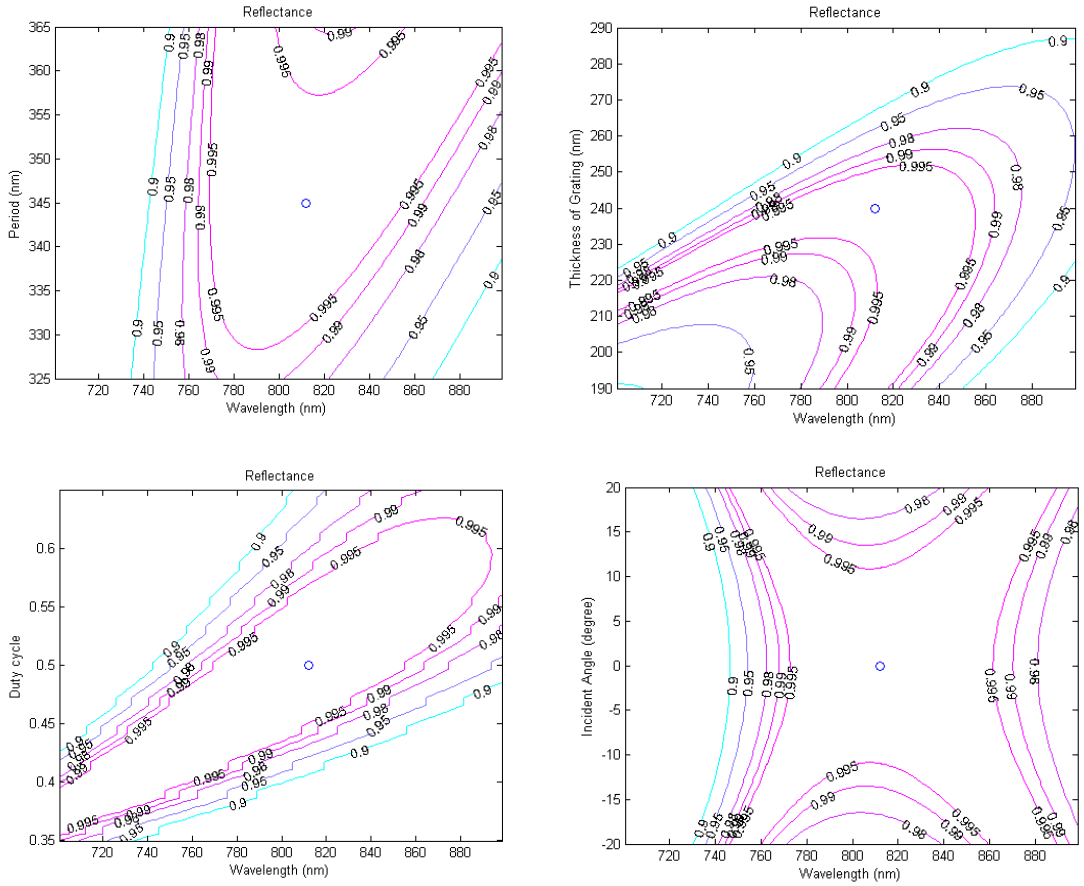

Figure 3.21: Tolerance Analysis for TM grating. The grating is again assumed to be $Al_{0.15}Ga_{0.85}As$ (n=3.58)

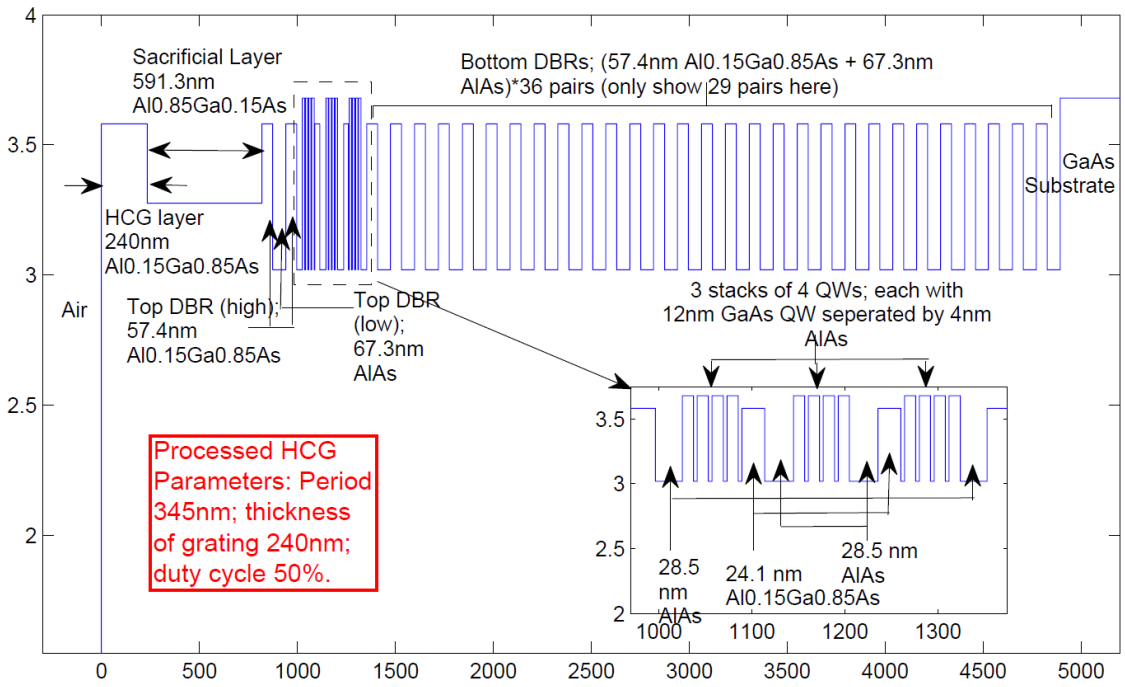

Figure 3.22: The design map for a TM sample.

left spectrum of Fig. 3.20 shows the $> 99.5\%$ reflectance band can be as wide as 84nm around design wavelength 800nm.

The best design parameters for the TM HCG we chose are, $\Lambda = 345$nm, $t_g = 240$nm and $\eta = 50\%$. The sensitivity of each parameter around the designed value is shown in the tolerance analysis Fig. 3.21. The error tolerance is generally better than the TE design. Especially, the angle tolerance range is improved from $\pm 6^\circ$ to $\pm 12^\circ$. This design is not optimized for angle tolerance. The highest I can achieve is $\pm 35^\circ$.

The final design map is shown in Fig. 3.22. To match the ultra-high reflectance of the TM HCG, we used a 36 pairs of bottom DBR to balance the reflectance from top and bottom, so that the resonance dip in reflectance will go to zero. Similar with before, 12 QWs in 3 sets are placed at the anti-nodes of the resonant cavity field, the OPLs of the layers around QWs is compensated for the higher index of GaAs. The grating thickness is designed to be 240nm, even greater than the grating bar width. Therefore the grating is strengthened in the thickness direction. The weak

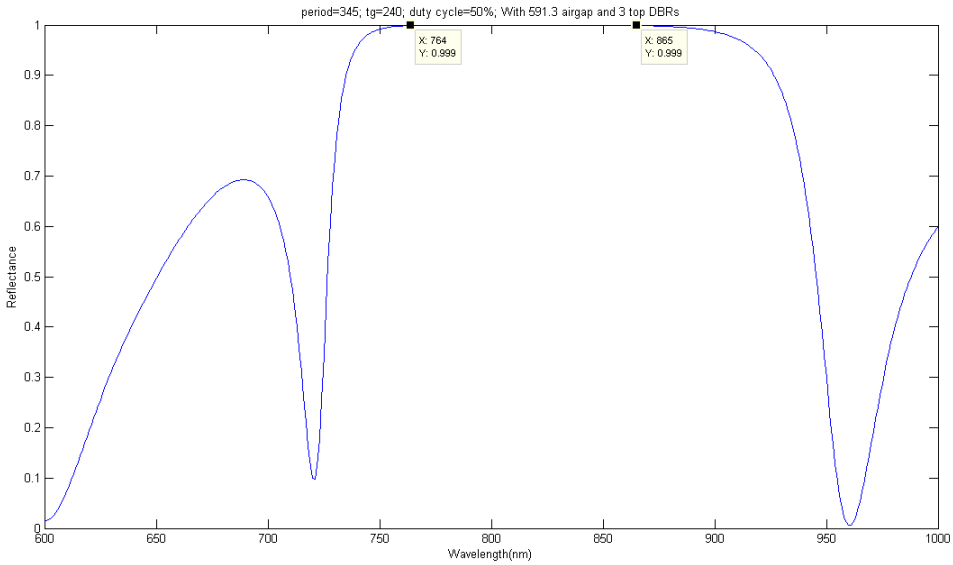

Figure 3.23: The top mirror performance for the TM HCG design.

link now changes to the horizontal direction– the grating is still subject to buckling in the horizontal direction during fabrication.

The grating together with the top DBR exhibits an enhanced reflectance, as shown in Fig. 3.23. The $R > 0.999$ stopband width increases to a very large 100nm.

The sample before processing (after wafer growth) is simulated to feature a reflection spectrum as shown in Fig. 3.24 left. There is no obvious broad cavity dip in the spectrum, in contrast with the TE design. After processing of the grating, the cavity exhibits a resonance dip at 812.002nm and a linewidth 0.001nm. The cavity Q is thus $812/0.001 \sim 8 \times 10^5$.

The field distribution at resonance is shown in Fig. 3.25. Because the phase matching is well designed, the field maximum is exactly at the center of the cavity.

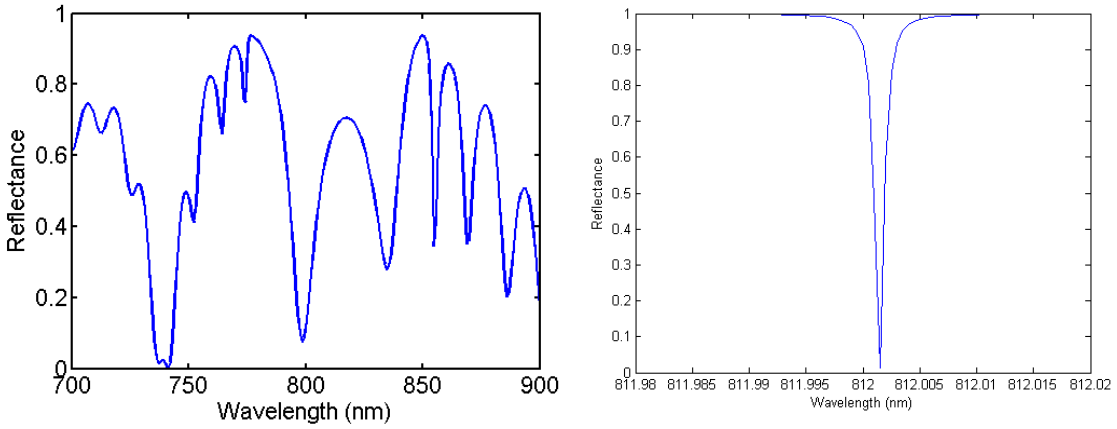

Figure 3.24: The reflection spectra for TM HCG cavity before processing (left) and after processing (right).

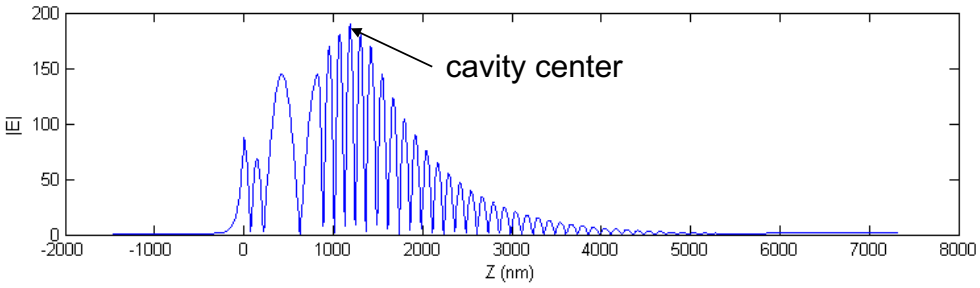

Figure 3.25: Field distribution for TM HCG cavity at resonance.

3.3 Effect of Unmatched Phase

3.3.1 Resonance Shift due to Airgap Thickness Change

Previous design construct the SWG-DBR hybrid cavity using the DBR-cavity phase matching principle. That is, the airgap between the SWG and the underneath DBR structure is designed to be exactly low-index $\lambda/4$ layer (starting from the π reference plane, Fig. 3.12). In this section, I discuss the effect of unmatched phase, which is inevitable because of the fabrication error. Also, later we found the grating may bend because of local strain release is not complete. Intuitively, the raised or lowered grating surface may change the cavity length and thus change the resonance. Consider the extreme case, if the airgap becomes a $\lambda/2$ OPL layer, does it become a low-index cavity? Because the top mirror is high reflective and we have bottom DBR as the bottom mirror. Will the airgap act like another cavity in additional to the real cavity underneath?

To see the effect, let us study a DBR-DBR cavity, which is easier to simulate using transfer matrix. In Fig. 3.26, I replace the SWG with a top DBR. The airgap is kept the same, but count from the π reference plane. In the case of DBR, it is just from the boundary of the top DBR. I call the one to a few layers of DBRs on top of the cavity layer as middle-DBRs.

I swept the number of top and middle DBR of the cavity. I fix the airgap to be$\frac{1}{4}\lambda$, $\frac{1}{2}\lambda$, $\frac{3}{4}\lambda$, λ, and then scan number of topDBR from 1 $\sim$ 20 pairs, number of midDBR from 0.5 $\sim$10.5 pairs.

From field strength in cavity plots Fig. 3.27, odd number of $\lambda/4$ thickness makes airgap as a perfect DBR layer, connecting the top DBR and middle DBR and making them acting like a whole. That is why in left panel only the sum of the number of top and middle DBRs matters, making the iso-height lines straight. However, if the airgap is even number of $\lambda/4$ thick, it will actually act like a cavity layer, which will

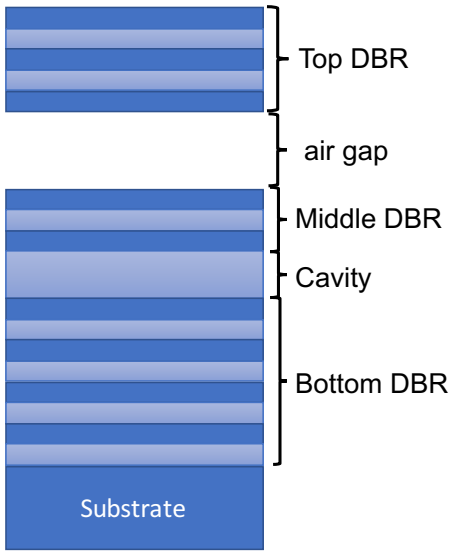

Figure 3.26: Schematic of an equivalent DBR cavity with air gap. Used for study of the airgap effect.

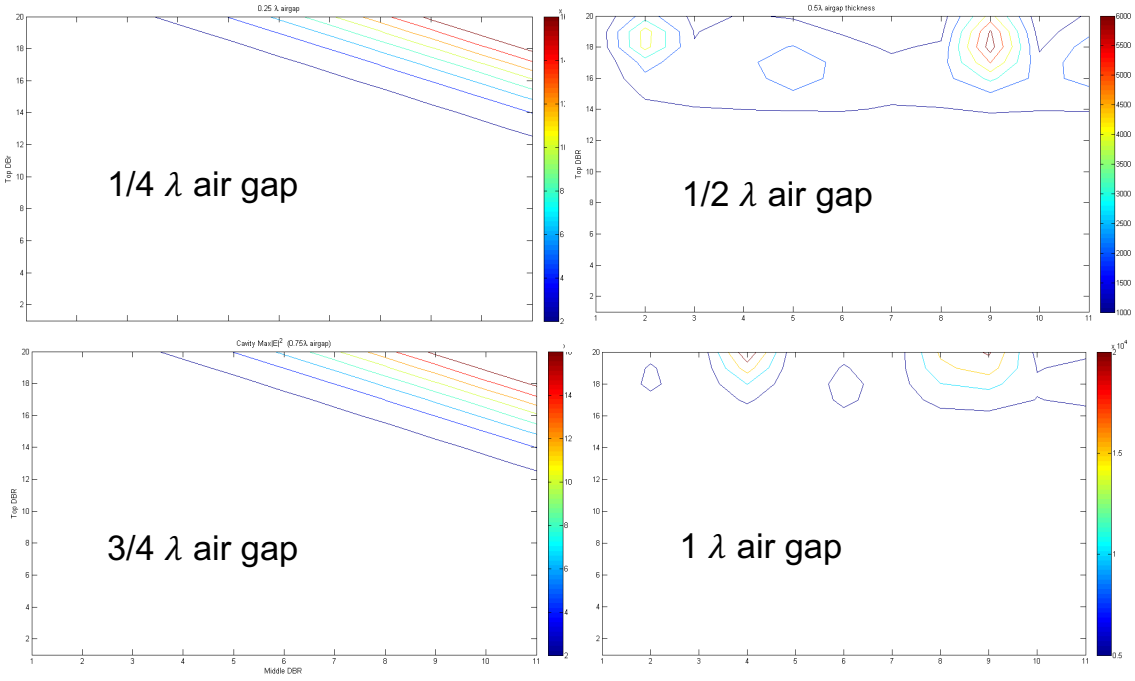

Figure 3.27: Field strength in the cavity as a function of number of top and middle DBRs, with different airgap thicknesses. Only odd number of $\lambda/4$ airgap matches the multi-reflection phase, and bridge the top DBR and middle DBR together. Even number will make airgap act like a cavity and compete with the real cavity.

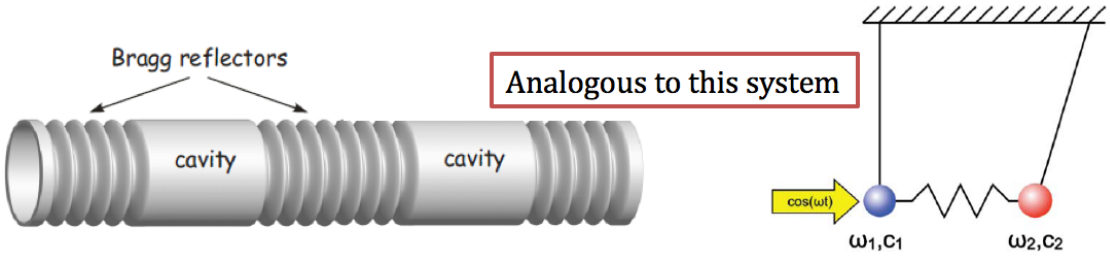

Figure 3.28: Coupled DBR cavity. The number of middle DBR pairs determines the coupling strength of the two cavities.

compete with the real cavity for the field through the a few layers of middle DBR. The coupling between adjacent cavities is well studied, basically can be analogously thought as two coupled harmonic oscillators, as illustrated in Fig. 3.28.

Let us see the same effect for our SWG cavity. Take the TE design as an example. As shown in Fig. 3.29, the original designed airgap thickness is 540nm for resonance around 800nm. If one reduce the airgap by $\lambda/4 = 200$nm, the airgap will act like a second cavity. The coupled cavities will split the resonance into two symmetric resonances around the original one. If one reduce the airgap even more by 40nm, the right mode will dominate the spectrum. And increasing it by 40nm will make the left mode dominate. So from the original airgap thickness 540nm to the limiting case 340nm, the cavity resonance shifts $0.13nm$ per nm of airgap thickness change. Roughly, 20nm airgap change results in 1nm resonance shift.

The energy splitting resulting from the coupled cavity geometry can be engineered and become useful for 2D material applications. An example is shown in Fig. 3.30, which is a cavity design featuring double resonances. The two resonances both have E-field maximum in both of the cavity layers. They are used to couple with the A-exciton and B-exciton in TMD 2D material placed in both of the cavity centers. The energy splitting of the two resonance is tuned by the middle DBR layer. I used only 1.5 pair of DBR as the middle DBR, which gives the largest splitting.

In conclusion, the airgap in SWG-DBR cavity should be kept exactly at $\lambda/4$ OPL

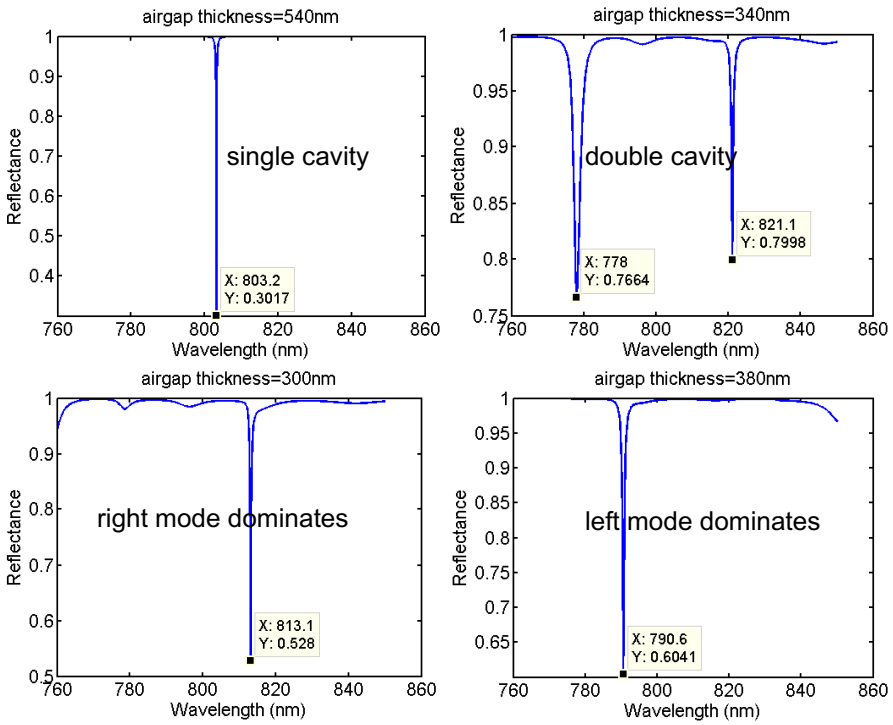

Figure 3.29: The resonance shift/splitting due to airgap thickness change.

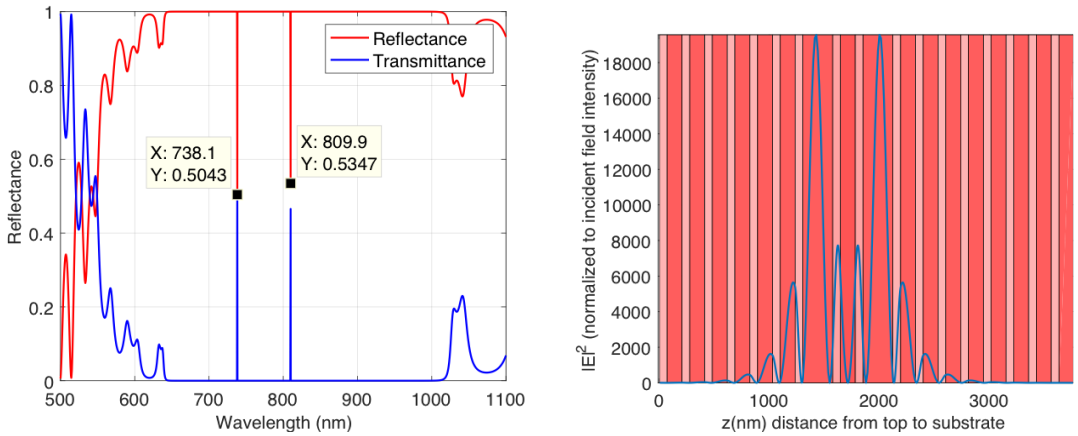

Figure 3.30: Double resonances is created for the coupled cavity structure illustrated in Fig. 3.28. The right figure is the field intensity distribution for the left resonance. The right resonance is very similar. Parameter used: highDBR- TiO2 (n = 2.81), lowDBR and cavity SiO2 (n=1.454). 8-pair topDBR, 1.5-pair midDBR, 10-pair botDBR. Guidline: more coupling (less midDBR) leads to larger splitting.

thick. Any deviation will cause the resonance to shift either to red or blue depending on the direction of the deviation. In the limiting case of a $\lambda/2$ airgap, the resonance will split into two, at the two sides of the original resonance. The energy splitting is determined by the coupling strength, which in our system is determined by the number of pairs of the middle DBR. Less pairs of middle DBR will increase the 'leakage' between the cavity, thus increase the coupling. This phenomenon can be used to tune the cavity resonance, or model the resonance shift due to unexpected fabrication errors.

3.3.2 Resonance Shift due to Grating Dimension Change

Previous subsection discussed the deviation from Fabry-Perot round-trip phase condition because the airgap thickness fluctuation affects the traveling phase. However, there is another term in the round-trip condition– the reflection phase from the HCG. Specifically, the round-trip condition requires that

$$\phi_{HCG}(\lambda) + \phi_{traveling}(\lambda) + \phi_{DBR}(\lambda) = 2m\pi, \tag{3.20}$$

where $\phi_{HCG}(\lambda)$ is the reflection phase from the HCG incident plane, ϕ_{DBR} is the reflection phase from the bottom DBR, which is π at the design wavelength. Suppose the HCG is somehow varied in one dimension, for example, in the thickness t_g, then the reflection phase no longer fulfills the phase condition Eq. 3.20. A new resonance wavelength will take over to fulfill the condition. This is the resonance tuning effect by varying the dimension of the grating.

In Fig. 3.31 upper panel, I show the sensitivity of the resonance wavelength of the TE design on three grating parameters– period, thickness of grating and bar width (or duty cycle). As can be seen, the resonance is not very sensitive to all the grating parameters. The most sensitive one is, 10nm variation in t_g gives 0.5nm difference in

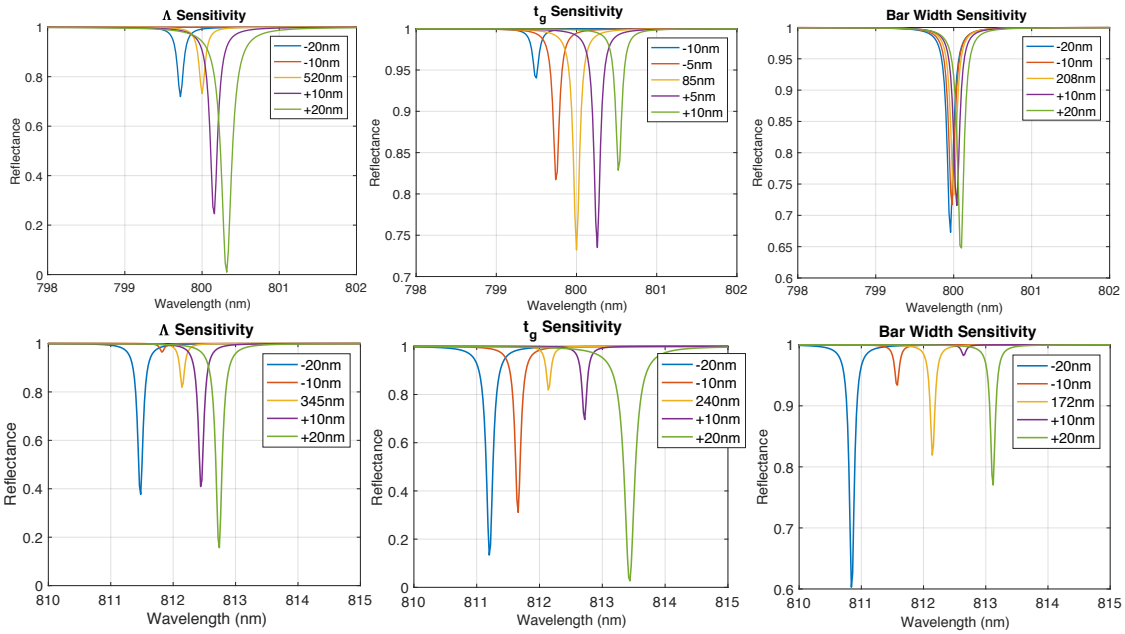

Figure 3.31: The resonance wavelength sensitivity by varying the grating parameters around the design values. Upper panel: TE design; Lower panel: TM design.

resonance. This is comparable to the airgap thickness tunability. The period and bar width have much mild tuning. Therefore, it is usually not realistic to tune the cavity resonance by the grating parameter for TE design, because the workable (high-R) parameter region is relatively small; the range of tuning is rather limited.

In Fig. 3.31 lower panel, I show the sensitivity of the resonance wavelength of the TM design on the grating parameters. The period and thickness of grating sensitivity are similar with the TE design, while the duty cycle or bar width sensitivity is larger. Although the small range of ±20nm is swept, the TM design has a broader high-R region (refer to Fig. 3.20) so that it can withstand more tuning range of the grating parameters.

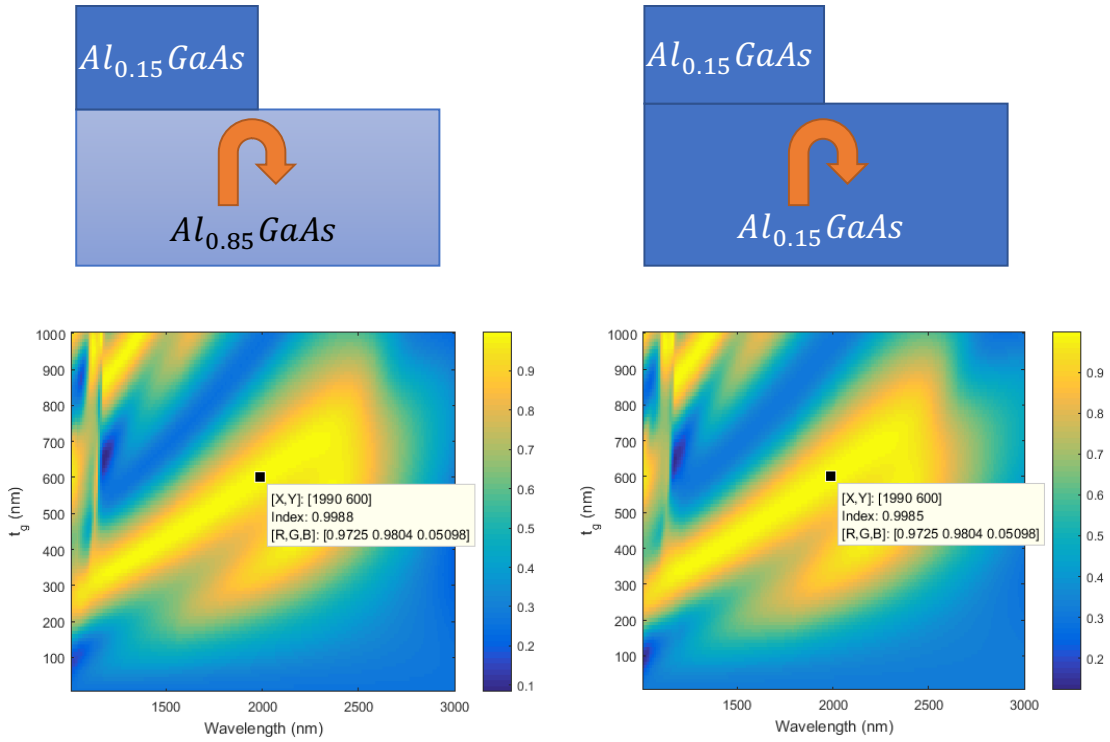

Figure 3.32: Monolithic HCG with two supporting materials. The duty cycle is fixed at 50%. Period of grating is fixed to 1000nm. All lengths can be normalized to the period. The reflectance maps are for waves incident from the bottom material, which is assumed to be semi-infinite.

3.4 Monolithic High Contrast Grating

In past three years, a variant of HCG emerged as an alternative to the traditional HCG suspended in air or surrounded by low-index materials. Instead, the grating directly sits on a similar index material, even on the same index material (Fig. 3.32), creating the so-called zero contrast grating (ZCG)[92, 93]. Because the grating is not detached from the underneath structure, it is also called monolithic high contrast grating (MHCG) [94]. It has been demonstrated that the ZCG or MHCG can exhibit the same broadband high reflectance with HCG. Because it does not require the grating to be suspended, it decreases the risk of grating bending and collapsing in real sample fabrication. This is the main motivation why I develop such gratings to construct a more robust high-Q cavity for polariton research.

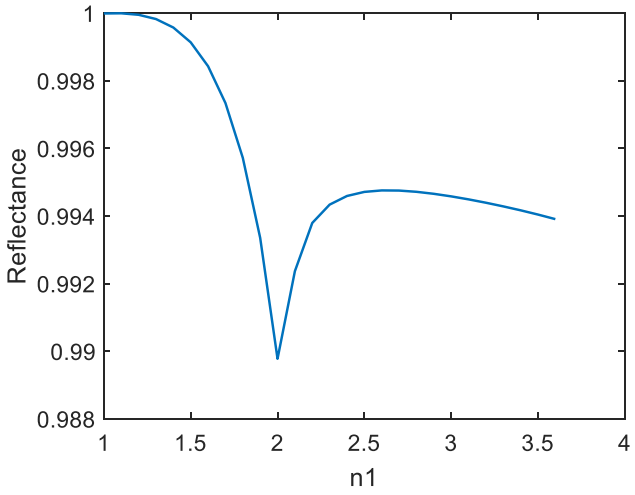

Figure 3.33: Monolithic HCG with incident medium index swept from $n_1 = 1.0$ to 3.6. The duty cycle is fixed at 50%. Period of grating is fixed to 1000nm. The reflectance is taken from the same t_g and λ.

It should be noted that the original ZCG proposed by R. Magnusson [92] still needs a low index substrate under the same-index supporting slab. The feedback from the abrupt index change is still required to create broadband high reflectance. It is just the feedback is delayed from the grating and supporting material interface to the substrate interface. Magnusson et al still considers the wave incident from the top of the grating. However, Gebski et al actually considered waves incident from the bottom, the similar-index substrate. From the cavity standpoint, this is more meaningful because if a cavity is constructed, the grating is reflecting light from the cavity. We mainly discuss Gebski's scheme in this thesis. In the following, I will introduce the major properties of the MHCGs.

3.4.1 Basic Features

Reflectance is almost Independent of Incident Medium

As shown in Fig. 3.32, the incident medium of the MHCG is chosen to be a slight different material $Al_{0.85}Ga_{0.15}As$ (n=3.11) and the exactly same material $Al_{0.15}Ga_{0.85}As$

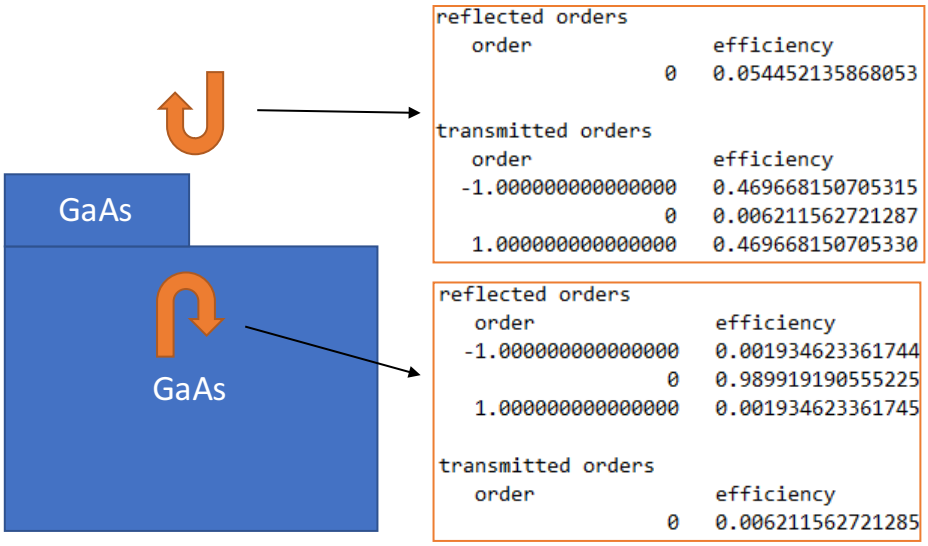

Figure 3.34: The energy distribution over all diffraction order of a MHCG, with waves incident from top and bottom.

(n=3.58). The parameter sweep shows almost identical reflectance map for both cases. An example point in the reflectance map is marked to show that the reflectances only differ at the fourth digit. I also swept the index of the incident medium from 1.0 to 3.6, the reflectance variation is still small, with a minimum at $n = 2.0$, as shown in Fig. 3.33.

Broadband High Reflectance is Attainable

Clearly a high reflectance (> 0.995) region exists for such a MHCG structure. The stop-band width is not as wide as the HCG, but usable for cavity applications. The mechanism of the broadband high reflectance is the same with HCG as discussed in last section. The two-mode-cancelling just needs to be satisfied at the exit plane of HCG. This is why MHCG is almost immune to the material change for the incident medium. This actually inspired me to flip the incident direction to study the reflectance from inside in 2015, without knowing the work done by Gebski et al.

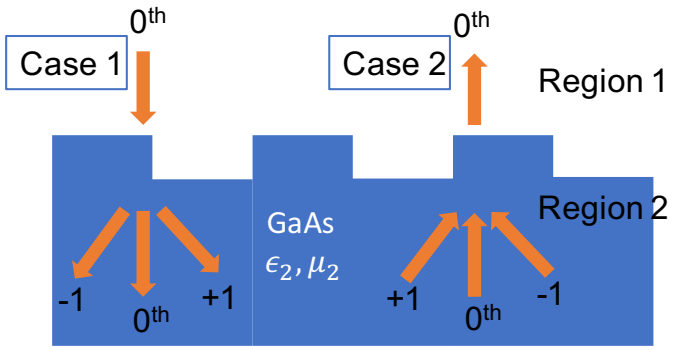

Figure 3.35: Two cases of wave excitations on MHCG that are truly reciprocal.

Seemingly Non-reciprocal Reflectance

A somewhat puzzling feature of the MHCG is, the reflectance is extremely asymmetric for light incident from top and from bottom. In Fig. 3.32 we showed the high-R region is easily achieved for waves incident from the bottom. However, the same grating is a very poor reflector ($R < 0.1$) for all the wavelength. This seems contradict with the reciprocal principle stemming from Maxwell's equation, which says if one swap the source and observation positions, the measured field (in our case the reflected and transmitted waves) stays the same. Usually, non-reciprocity is only possible when there is magnetic materials that break the time-reversal symmetry. The dielectric components in MHCG is simply linear optical material. Why the reciprocal law does not apply here? Or some configuration goes wrong?

The true reason is, by merely switching the incident direction, we are not totally swapping the sources with the observation points. The key difference between a dielectric slab and a grating is, the gratings can create additional diffraction orders other than the zeroth (normal incidence). As shown in Fig. 3.34, except for the zeroth order, the first order mode can also propagate in the GaAs ($k_x = 2\pi/\Lambda < 2n_{GaAs}\pi/\lambda$), although it is evanescent in the air. For waves incident from air, the reflected wave has only the zeroth order carrying energy, which is only 5.4% in this case. Most of the energy gets transmitted, and mainly carried in the ± 1 orders

(92%). In contrast, for waves incident from the bottom GaAs semi-infinite medium, the reflected waves are mainly carried in the zeroth order (99%), very little leaked into the ± 1 order. More importantly, the transmitted wave only carries 0.6% of the energy. And the transmittance is exactly the same with the zeroth transmission from top. That means, for zeroth order transmission, the grating is reciprocal. But the reflection is redistributed into the non-evanescent ± 1 orders. If one wants to be completely reciprocal, he should re-create all the orders including the ± 1 orders from the bottom medium, as depicted in Fig. 3.35. In case 2, all propagating orders are reversed in their propagation direction. The fields of the two cases will be exactly the same if one solves the Maxwell's equation.

This extreme asymmetry in reflectance from two directions has important implications if MHCG is made into a laser cavity. The light coming from the cavity will be strongly reflected, thus forming a high-Q cavity. However, light from the top can easily pass through the MHCG. This is particular useful for near-resonance pumping, which is not possible using a DBR because of its stop band.

3.4.2 Example of a MHCG Cavity Design

To be compatible with our existing wafer grown for air-suspended HCG cavity, I demonstrate in this section a possible MHCG cavity design with $Al_{0.15}Ga_{0.85}As$ as the grating layer, $Al_{0.85}Ga_{0.15}As$ as the incident medium of the MHCG. We are reusing the same wafer where we did the TM design.

MHCG Optimization

Setting the incident medium and grating parameters, the reflectance of the MHCG can be calculated in a $t_g - \lambda - \eta$ parameter space. A few reflectance maps are shown in Fig. 3.36. Only TM polarization is used, because TE polarization cannot give any $R > 99.5\%$ regions. Even with TM polarization, only when $\eta = 0.45 \sim 0.65$ can we

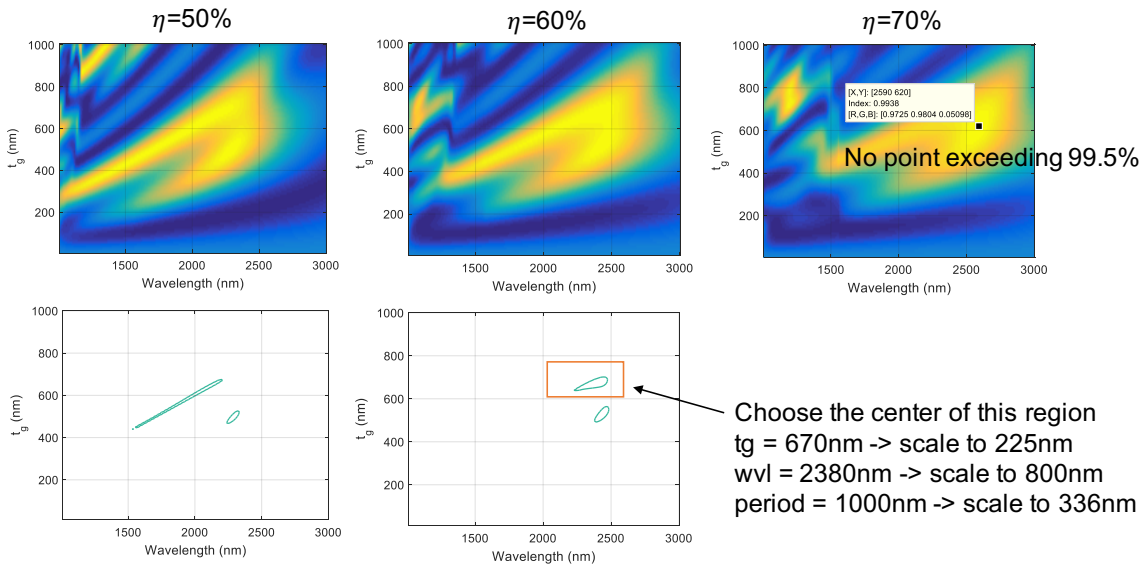

Figure 3.36: Reflectance maps of MHCG under TM polarization. The reflectance is for the 0-th order reflection. The incident medium is $Al_{0.85}GaAs$ and the grating bar is $Al_{0.15}GaAs$. The bottom panel shows the $R_{0-th} > 99.5\%$ regions.

observe $R > 99.5\%$ regions as shown in the bottom figures of Fig. 3.36. The center of one high-R region is chosen as the final design for MHCG.

Assembling MHCG Cavity

The cavity design is shown in Fig. 3.37. The $Al_{0.85}GaAs$ layer needs to be chosen from one of the lengths given in the figure, to ensure perfect phase matching. The 547.6nm (red one) is the closest to one of our existing wafer's thickness for that layer. We use it for further optimization. The simulated reflectance from the cavity is shown in Fig. 3.38. As can be seen, the reflectance from the MHCG cavity is also asymmetric for incident from top and from bottom. Usually in experiment, we have access to the sample top, so we expect to see a reflectance peak instead of a dip in normal Fabry-Perot cavity. The field at resonance is indeed concentrated in the cavity region.

At resonance, the field (both H-field and E-field) in the MHCG are shown in

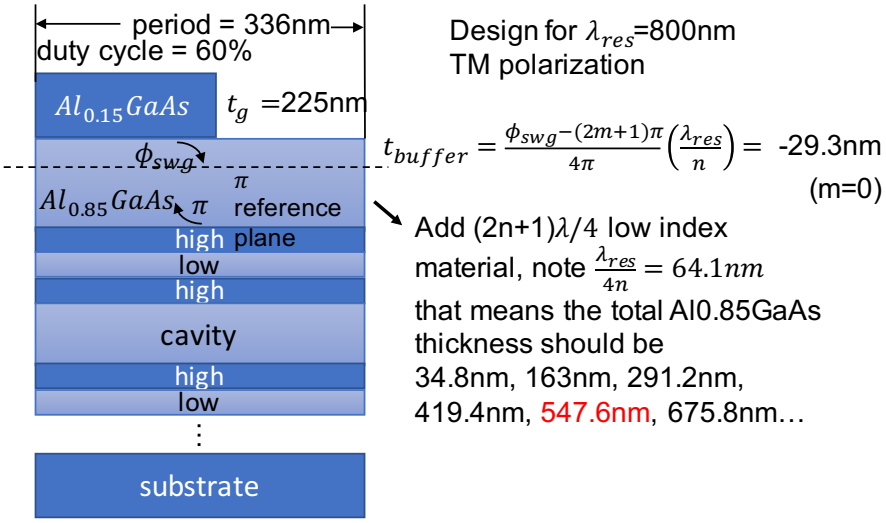

Figure 3.37: The schematic of a MHCG cavity with real parameters.

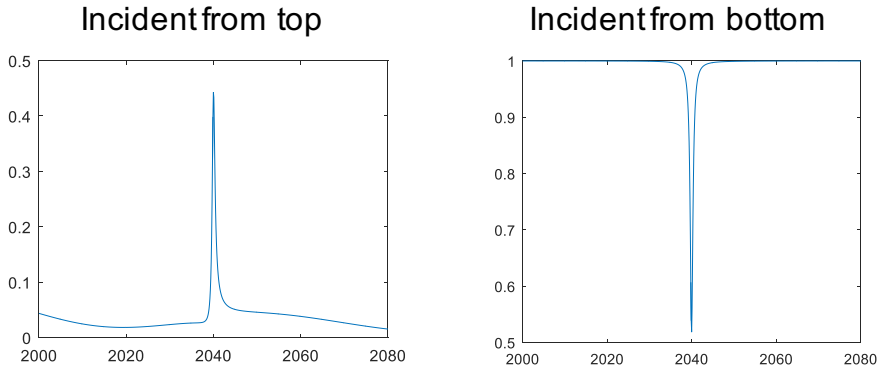

Figure 3.38: The reflectance of a MHCG cavity. Excitation waves are incident from top (left) and bottom(right). The resonance wavelength needs to be scaled to 800nm.

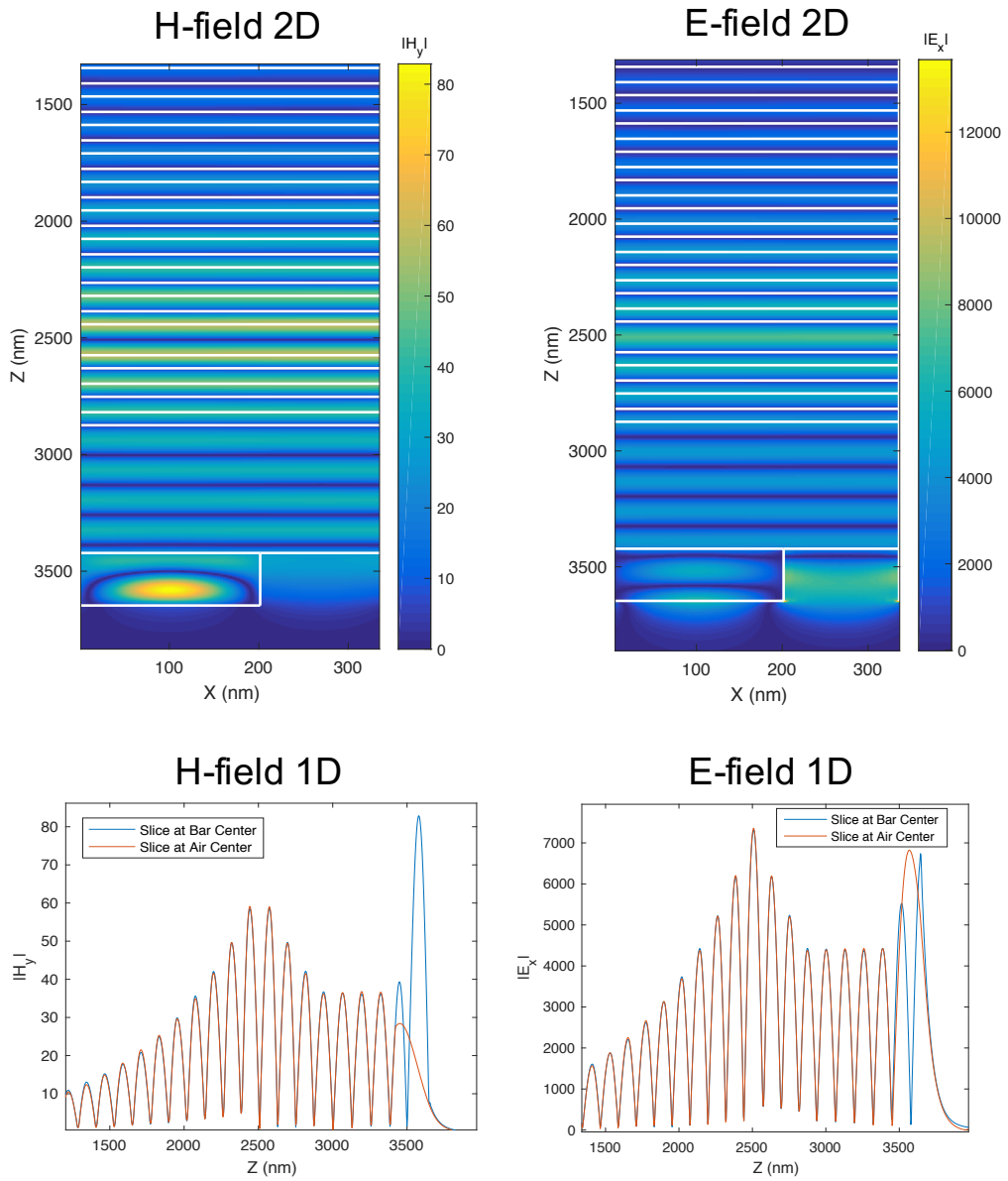

Figure 3.39: The field distribution of a MHCG cavity at resonance. Excitation waves are incident from bottom.

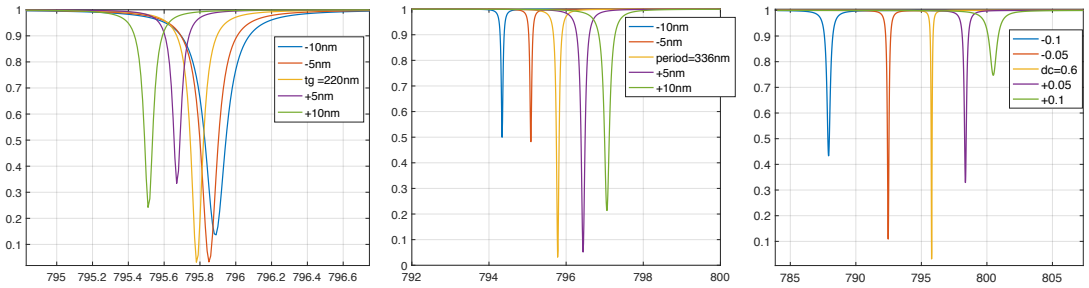

Figure 3.40: Resonance wavelength sensitivity of the MHCG cavity.

Fig. 3.39. The E-field maximum is at the center of the cavity, although the field in the grating is also as large. The sacrificial layer in the wafer (591nm designed for TM HCG) is kept intact in this case. The large OPL gives multi-nodes field inside it. Lastly, the resonance sensitivity on the grating parameters of this design is shown in Fig. 3.40.

To summarize, in this chapter I presented the design methodology of the SWG based cavity. I introduced the unique features of high-contrast SWG, its function as a broadband high reflectance reflector, and compared its advantages and disadvantages to conventional DBR. I discussed the physics origin of its broadband high reflectance, which guided the design of SWG mirrors as shown in a few examples. I also gave the design procedures for a real SWG-DBR hybrid cavity. The phase matching is highlighted to ensure the right cavity resonance. Unmatched phases are shown to tune the resonance. In the end, I introduced the recently emerged monolithic HCG, which eliminates the need of an airgap below the HCG.

CHAPTER IV

Sample Characterization and Polariton Lasing

Previous chapters mainly talk about the SWG cavities on paper. In this chapter, I will start to present the realized experimental system. I will first cover the details of the material and structural parameters of our system. Then I will briefly describe the fabrication procedures, which is a major work done by a colleague Dr. Bo Zhang. With the fabricated devices, I will spend the most space to present their optical properties using various optical characterization methods. Finally, most importantly, I will demonstrate polariton lasing in our device, which is the smoking gun for a real macroscopic quantum device.

The content of this chapter can also be found from our first journal publication [95].

4.1 Device Structure

The new cavity structure replaces the top DBR with a slab of SWG as shown in Fig. 4.1(a). The SWG shown is suspended in air by the surrounding tethering structure. The trenches around the grating are designed to release the surface tension built up during the material processing. The size of the SWG is designable, which enables confinement and control of the polariton modes. In Fig. 4.1(b), a $5\mu m$by $5\mu m$ SWG is shown. We also successfully made $7.5\mu m$, $10\mu m$, $15\mu m$ and $20\mu m$ ones, but

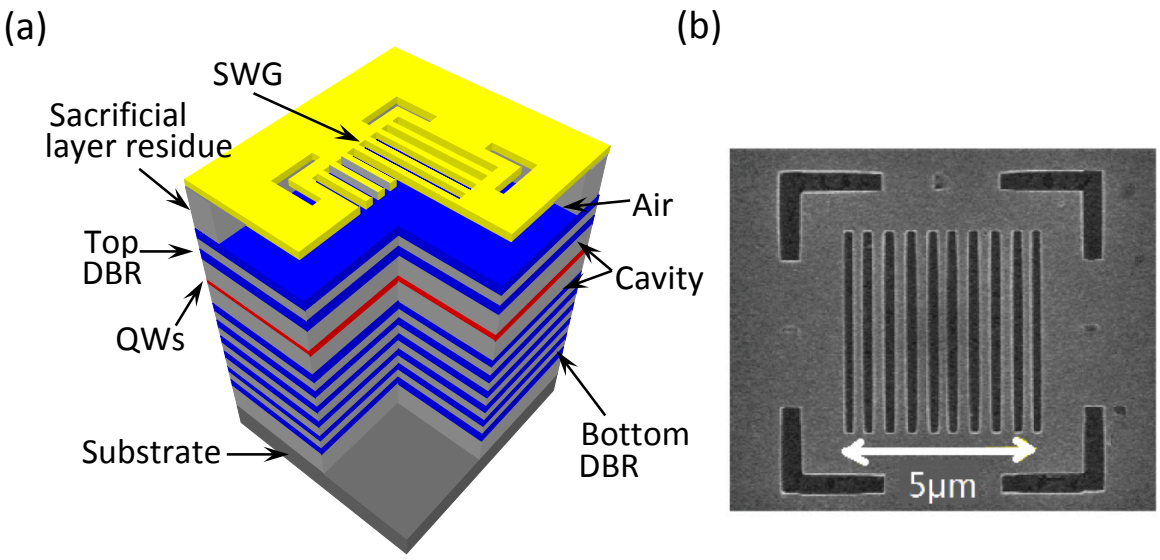

Figure 4.1: Examples of the hybrid cavity.(a)A schematic of a 0D hybrid cavity with a SWG mirror.(b)Top-view SEM image of a fabricated 0D cavity with a SWG of $5\mu \times 5\mu$ in size. 0D, zero-dimensional; SEM, scanning electron microscopy; SWG, subwavelength grating.

not longer gratings, because the large length-to-width ratio makes the grating easy to break. The best performing ones are from the $7.5\mu m$ ones. Under the SWG is a few layers of top DBR. It is mainly designed to protect the active media underneath, since the SWG can already provide sufficient reflectivity. Therefore, there is no destructive interface in the QW layers or the main cavity layers. The cavity Q can be kept very high, and excitons suffer less disorders which forms local traps to restrict exciton motion.

Before the nano-patterning for the device, the molecular beam epitaxy grown GaAs wafer is with the layer by layer structure as following: 30 pairs of bottom DBR, an AlAs $\lambda/2$ cavity layer, 2.5 pairs of top DBR consisting of $Al_{0.15}GaAs/AlAs$, and an $Al_{0.85}GaAs$ sacrificial layer followed by an $Al_{0.15}GaAs$ top layer. There are 12 GaAs quantum wells distributed in the three central antinodes of the cavity.

We created square gratings of different lengths on the top layer via electron-beam

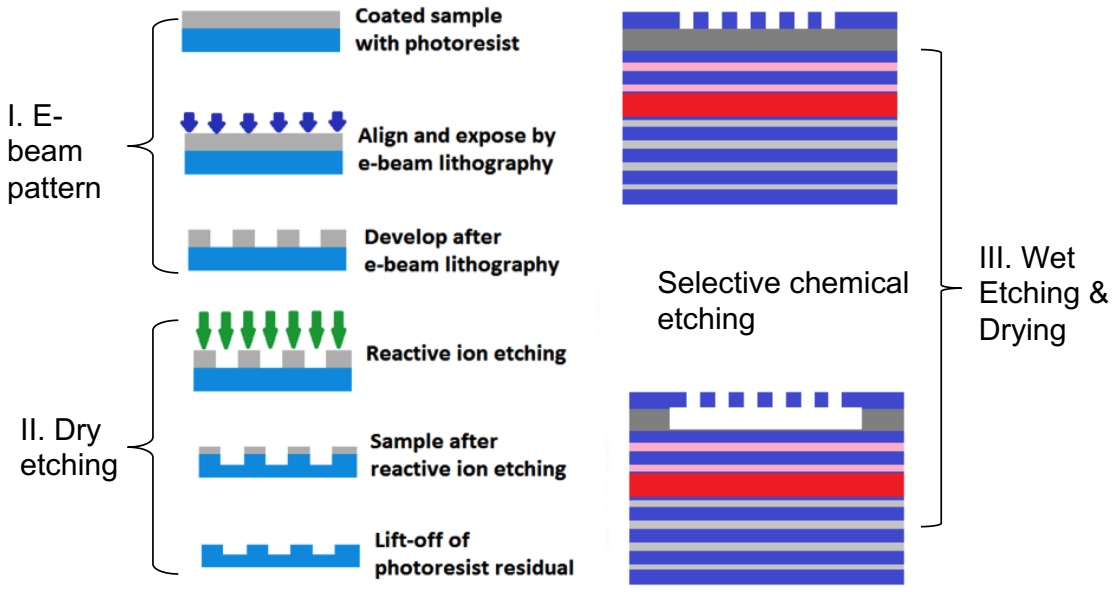

Figure 4.2: Fabrication flow

lithography followed by a short plasma etching step. Hydrochloric acid chemical etching was then applied to remove the sacrificial layer, followed by critical point drying. The fabricated gratings are approximately 80 nm thick, with a period of approximately 520 nm and a duty cycle of approximately 40%, and are suspended over an air gap of approximately 300 nm. The gratings are optimized as a high-reflectance mirror for light polarized along the grating bar direction (transverse electric (TE)-polarization). Figure 4.1 (b) shows a scanning electron microscopy image of the top view of one of the devices.

4.2 Sample Fabrication

To fabricate the sub-wavelength high contrast gratings, the process includes pattern definition by using electron beam (e-beam) lithography, reactive ion etching or dry etching, selective wet chemical etching and critical point drying. The fabrication process is illustrated in the flow chart in Figure 4.2.

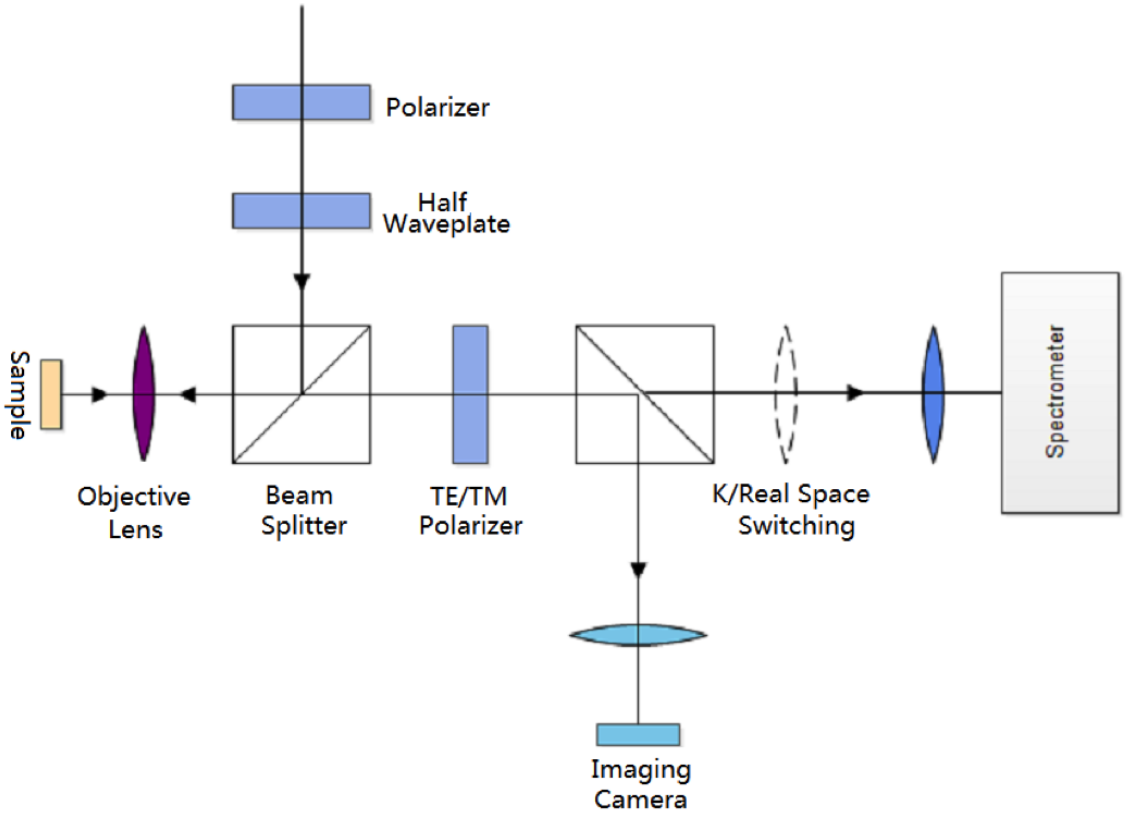

Figure 4.3: Optical characterization set-up for the device.

4.3 Optical Properties of 0D SWG Polariton Device

4.3.1 Optical Characterization Methods

Optical measurements were performed to characterize the pro- perties of the cavity system. For consistency, all data shown were taken on a device of $7.5\mu m \times 7.5\mu m$ in size. The sample was kept at 10∼90 K in a continuous flow liquid-helium cryostat. The optical measurement set-up in shown in Figure 4.3.

For the photoluminescence (PL) measurement characterization: A pulsed Ti:sapphire laser at 740nm was used as the excitation laser, with an 80-MHz repetition rate and

a 100-fs pulse duration. The laser was focused to a spot size of approximately $2\mu m$ in diameter on the device from the normal direction using an objective lens with a numerical aperture of 0.55. The photoluminescence signal was collected with same objective lens, followed by real space for Fourier space imaging optics, and then sent to a 0.5-m spectrometer with an attached nitrogen-cooled charge coupled device (CCD).

The spectrally resolved real space and Fourier space distributions were measured by selecting a strip across the center of the Fourier space and real space distributions using the spectrometer's entrance slit. The resolution of the measurements was limited by the charge-coupled device pixel size to $0.3\mu m^{-1}$ for Fourier space imaging and by the diffraction limit to 0.4 mm for real space imaging.

For the reflection measurement characterization, we are using a similar set-up. The same Ti:sapphire pulsed laser with 100 - fs pulse duration was focused on the device. Instead of using the wavelength of $740nm$, we use central wavelength of 800nm with spectrally line width of 15nm. Similarly, the signal collected by the objective lens was directed into the spectrometer in momentum space. As for the reference reflection, we replace the sample with a silver mirror at the exact same position. Dividing the signal intensity from the device by the reference reflection from the mirror, we will get the reflectance of the device.

4.3.2 Spectral Properties of 0D SWG Polariton Device

Strong coupling between the excitons and TE cavity modes was evident in the momentum space images of the emission from within the cavity, as shown in Figure 4.4 (a). Discrete lower polariton (LP) modes and a faint upper polariton (UP) branch were observed below and above the exciton energy, respectively, with dispersions distinct from that of the cavity photon (the red solid line). In contrast, the emission from outside the hybrid cavity region shows a flat, broad exciton band at the heavy hole exciton energy of $E_{exc} = 1.551eV$ (Figure 4.4 (b)). The energies of the polariton

modes can be described as follows in the rotating wave approximation:

$$E_{LP,UP}(k) = \frac{1}{2}[E_{exc}(k) + E_{cav}(k) \pm \sqrt{(E_{exc}(k) - E_{cav}(k))^2 + 4\hbar^2\Omega^2}] \tag{4.1}$$

Here, k is the in-plane wavenumber, E_{cav} is the uncoupled cavity energy and $2\hbar\Omega$ is the exciton-photon coupling strength, corresponding to LP-UP splitting at zero exciton-photon detuning. Using Equation 4.1 and the measured $E_{exc}(k = 0) = 1.551eV, E_{LP}(k = 0) = 1.543eV$and $E_{UP}(k = 0) = 1.556eV$, we obtain $E_{cav}(k = 0) = 1.548eV$ and $2\hbar\Omega = 12meV$.

The discrete LP modes show full three-dimensional confinement of the polaritons. The lateral size of the hybrid cavity is determined by the size of the high-reflectance subwavelength grating (SWG). Outside the SWG, there is no cavity resonance, and the excitons are eigen-excitations. Inside the SWG region, the TE-polarized cavity modes strongly couple to the excitons, leading to laterally confined TE-polarized polariton modes. The transverse magnetic (TM)-polarized excitons remain in the weak coupling regime. Because there is not a sharp lateral boundary at which the cavity mode disappears, we phenomenologically modeled the effective confinement potential as an infinite harmonic potential. The calculated energies of the LP modes are indicated by the dashed lines in Figure 4.4 (a), which agree very well with the measured LP resonances. For comparison, the confined cavity modes (crosses) and corresponding 2D dispersions of the LP, UP and cavity modes are also shown (solid lines).

The spatial profiles of the confined LP modes were also measured via spectrally resolved real space imaging, as shown in Figure 4.4(c). The four lowest LP modes are well confined within the SWG region, while the higher excited states are spread outside and form a continuous band. The variances of the k-space and x-space wave-

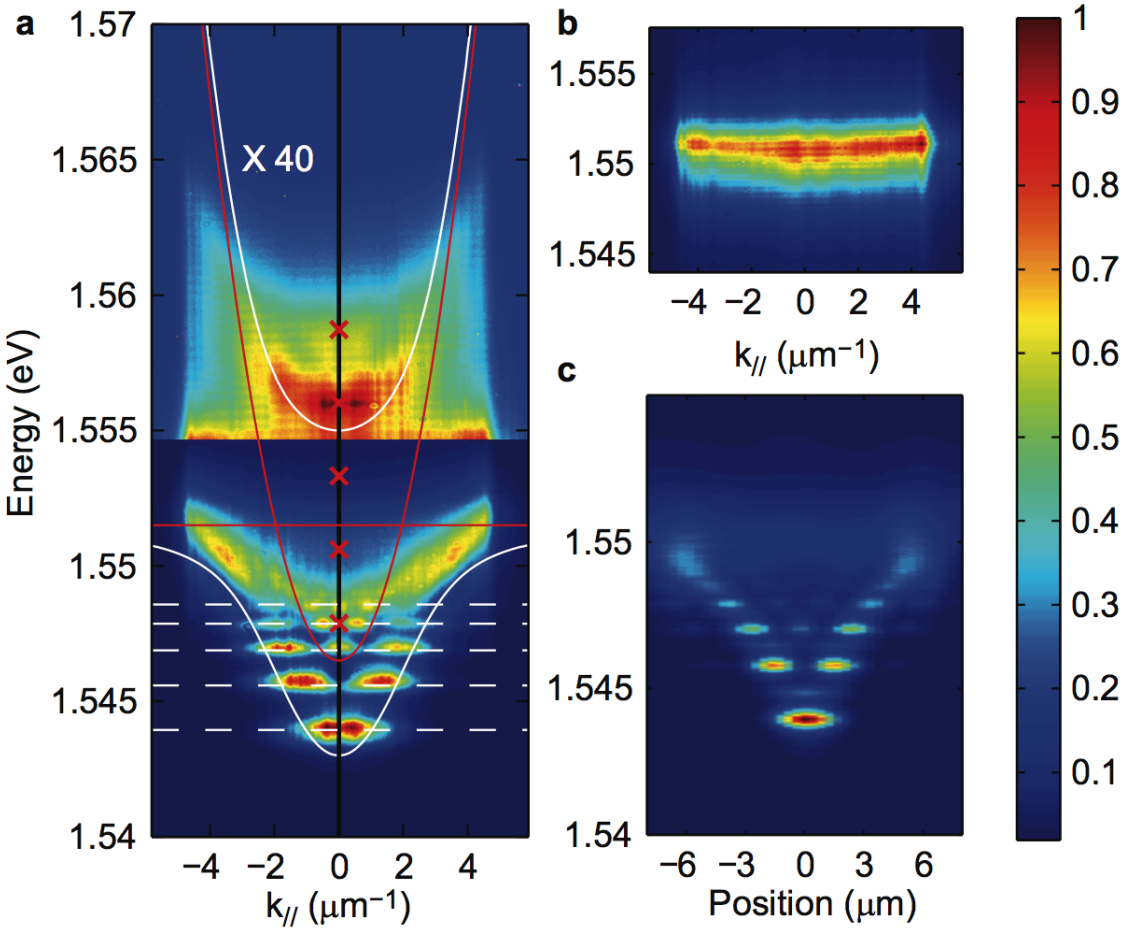

Figure 4.4: Spectral properties of a 0D polariton device.(a)Spectrally resolved momentum space image of the PL from a 0D cavity,which shows discrete LP modes and an UP mode. To clearly show the UP mode, the intensity of the upper panel is magnified by 40× compared to the lower panel. The straight red line at 1.551 eV corresponds to the independently measured exciton energy. The other solid lines are the calculated dispersions of the LP, UP and uncoupled cavity. The white dashed lines and the crosses (×) mark the position of the calculated discrete LP and cavity energies, respectively. (b) Spectrally resolved momentum space images of the exciton PL, measured from the unprocessed part next to the SWG-DBR cavity. (c) Spectrally resolved real space image of the PL from the 0D cavity, showing the spatial profile of the discrete LP modes.

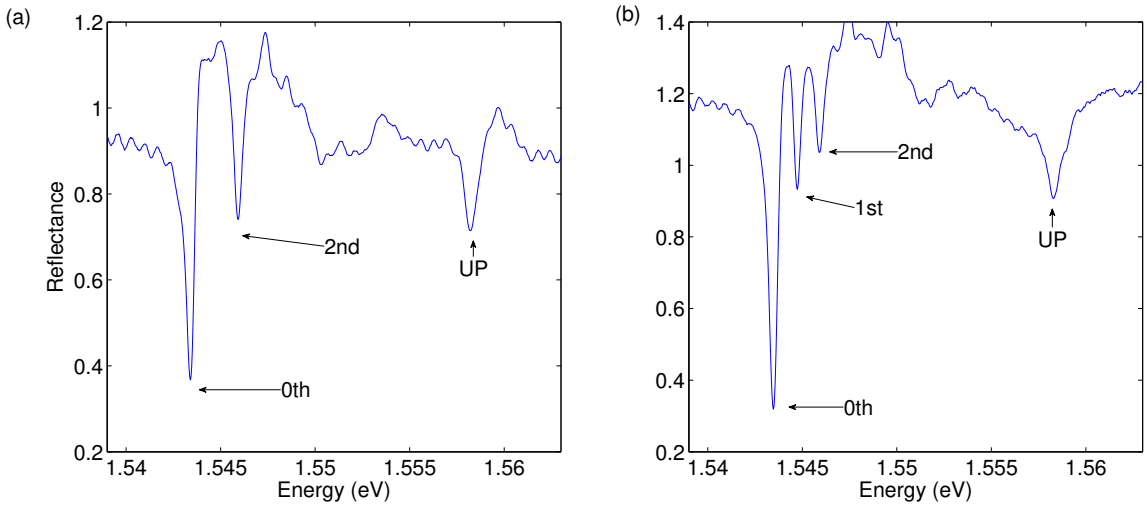

Figure 4.5: Reflectance spectra of the 0D cavity measured from (a) the normal direction and (b) 3.5 degree from the normal direction, both with an angular resolution of 0.276 degree.

functions along the detected direction are $\Delta k = 0.85\mu m$ and $\Delta x = 1.01\mu m$. Their product is $\Delta x \times \Delta k = 0.86$, slightly larger than the uncertainty limit of 0.5, which may be due to the diffusion of the LPs.

The absorption spectra of the modes were obtained via reflectance measurements. The spectrum measured normal to the sample (Figure 4.5 (a)) shows the three symmetric modes with the lowest mean in-plane wavenumber: the UP ground state, the LP ground state and the second LP excited states. The spectral weights of the other polar- iton states are too small to be measured in reflectance. When measured at 3.56 from the sample normal, the first excited state of the LPs was also observed (Figure 4.5 (b)).

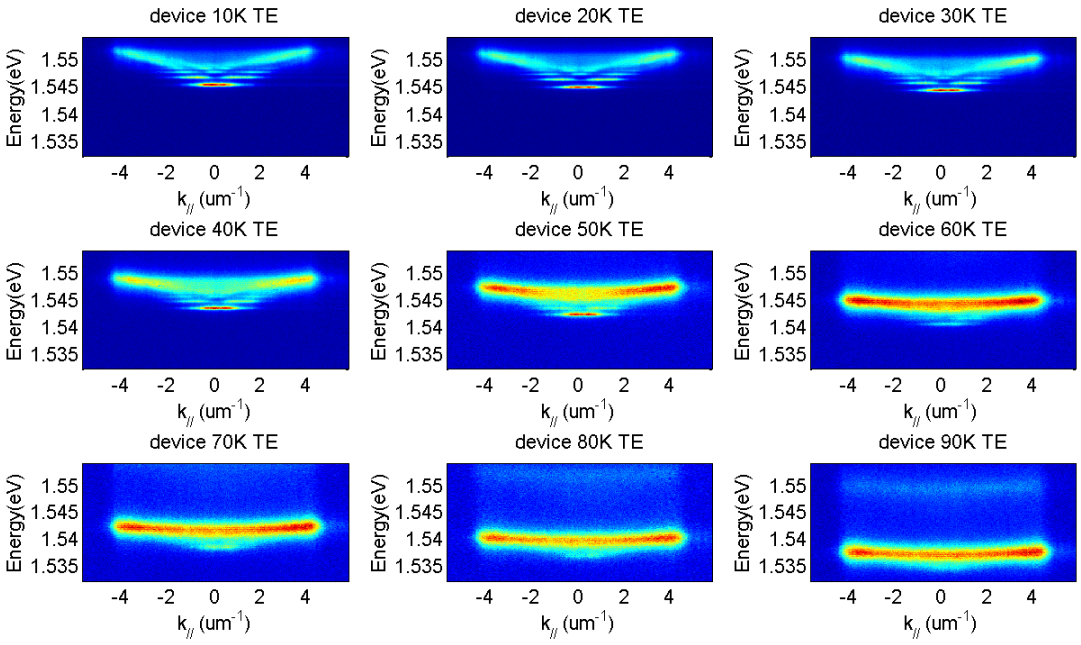

Figure 4.6: The PL signals of LP from the 0D device at temperatures from 10K to 90K

4.3.3 Temperature Dependence of SWG Polariton Device

A further confirmation of the strong-coupling regime is the anti-crossing behavior by temperature tuning of the resonances.

The PL signals of the LP from the device and exciton from the planar part of the sample are measured at different temperatures from 10K to 90K. These measurement results are shown in Figure 4.6 and Figure 4.7.

Since we can not directly measure the cavity resonance due to the strong coupling effect between the exciton and the cavity photon, we measured the side-dips energy shift as a function of the temperature. It is an direct indicator for the cavity resonance shift due to the same shifting trend between the cavity resonance and the side-dips in the reflection spectrum. The temperature dependent reflection measurement results

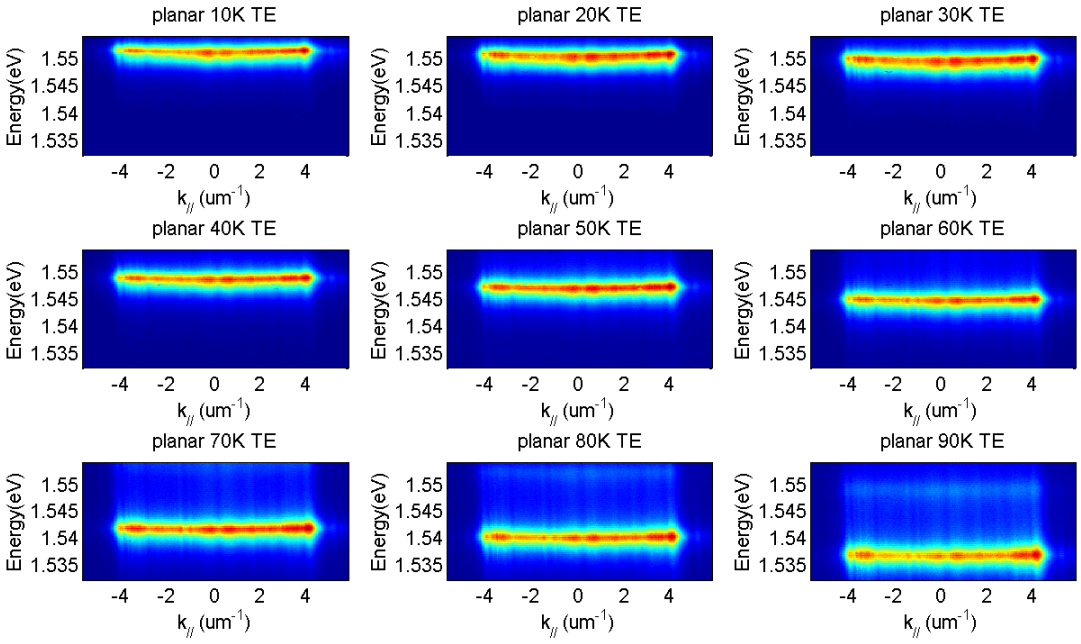

Figure 4.7: The PL signals of excitons from the planar part (non-SWG region) of the sample at temperatures from 10K to 90K

are shown in Figure 4.8.

For LP energy, we use the ground state energy throughout the temperature variation from Figure 4.6; For the cavity resonance dependence, we use the energy of the cavity resonance at 10K plus the energy shifting from the side-dips at various temperatures in Figure 4.8. Also we convert the wavelength in Figure 4.8 to energy unit eV in Figure 4.9.

The summary of graph of the temperature dependence for LP, exciton and cavity resonance is shown in Figure 4.9. As the temperature increased, the LP and UP ground state energies were redshifted and were measured via k - space photoluminescence. The exciton energy was directly measured in the planar region outside the SWG. The shift of the cavity photon energy was obtained from the shift of the first low-energy side minimum of the stopband. Anticrossing of the LP and UP modes is evident.

The calculated the coupling strengths at difference temperatures are also shown in Figure 4.10. From the LP, exciton and cavity energies, we obtain a coupling strength of $2\hbar\Omega(T) \sim 10meV$ from 10 K to 80 K, showing that strong coupling persists to the liquid nitrogen temperature and higher.

4.3.4 Polarization Property of the SWG Polariton Device

Unlike planar DBRs, the grating breaks the in-plane rotational symmetry. As a result, the SWG mirrors can have high polarization selectivity. We optimized our SWG to have high reflectance for the TE mode and low reflectance for the orthogonal TM mode. Correspondingly, the polaritons are TE-polarized, while the TM-polarized excitons remain in the weak coupling regime. Figure 4.11 shows the photoluminescence intensity vs. the angle of linear polarization for the LPs and excitons at $k \sim 0$ within the SWG region, normalized by the maximum intensity. We fit the data with,

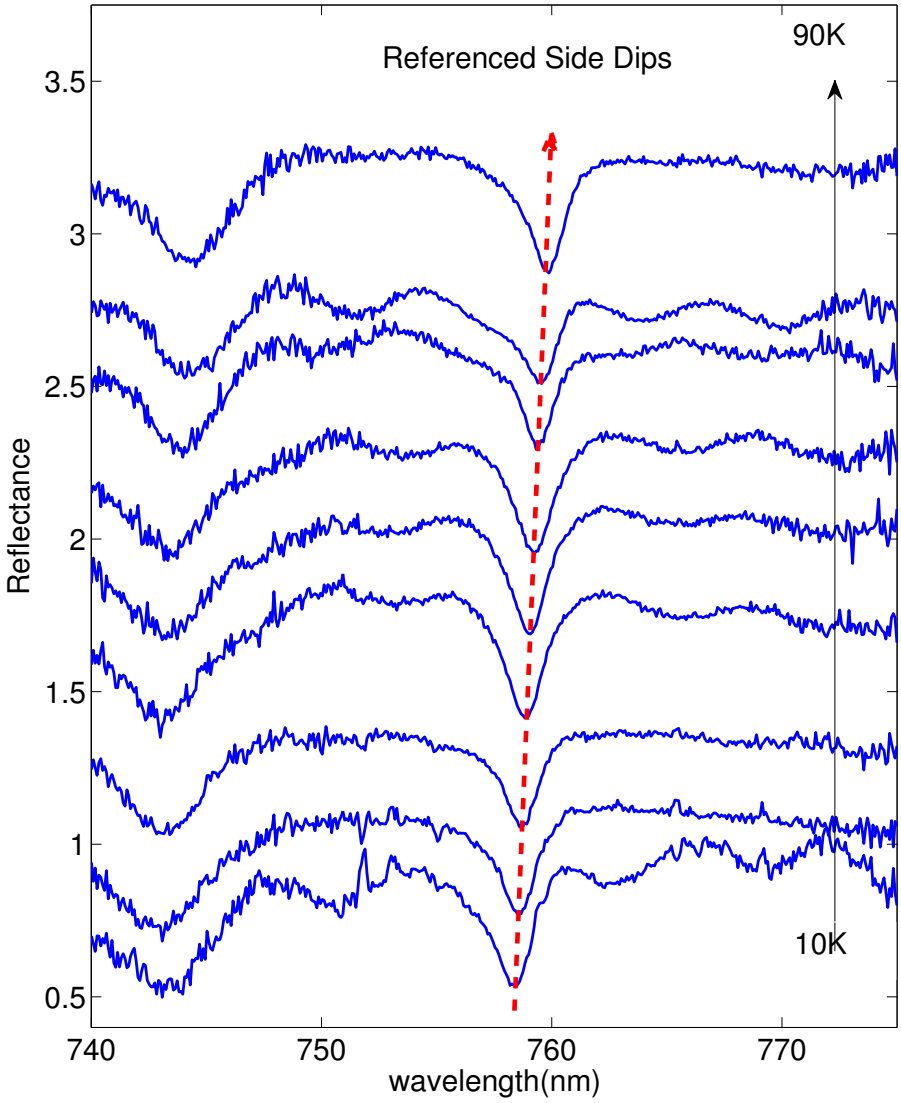

Figure 4.8: The reflection spectra from the planar part of the sample at temperatures from 10K to 90K

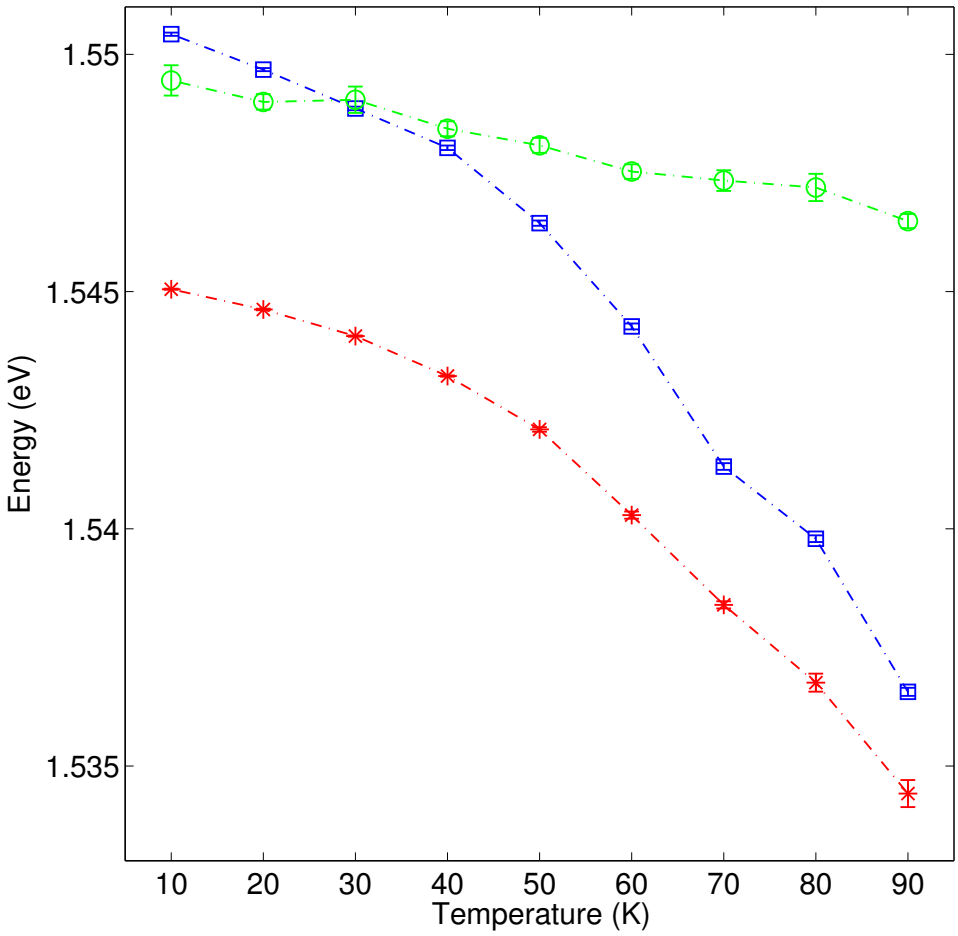

Figure 4.9: The summary graph of temperature dependence of the LP (stars), exciton (squares) and cavity resonances (circles).

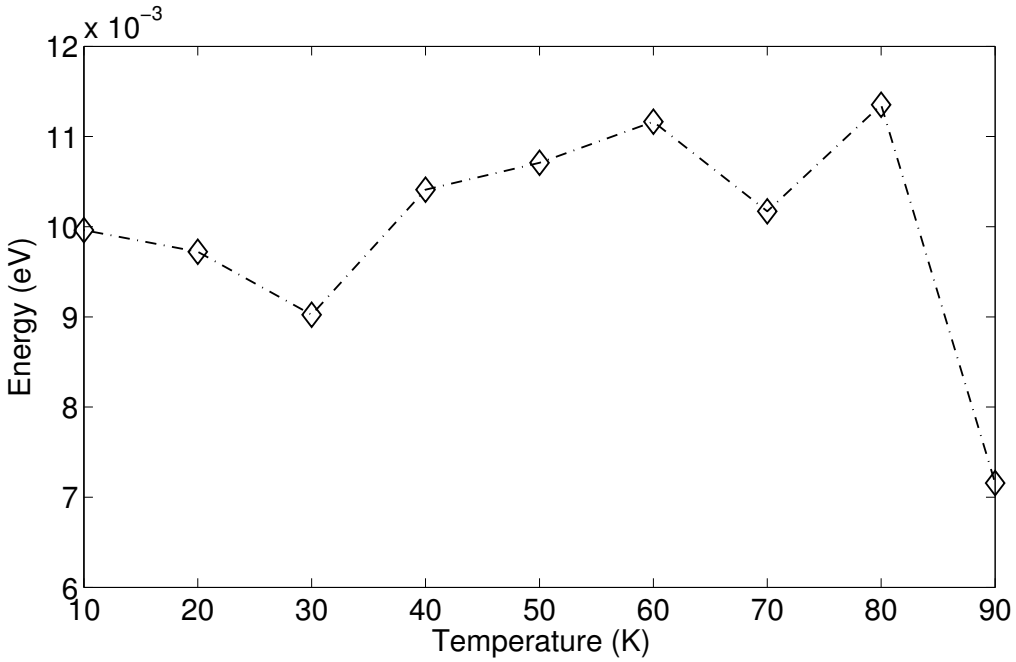

Figure 4.10: The calculated coupling strength at various temperatures from 10K to 90K

$$I = Acos(\theta - \Phi)^2 + B \tag{4.2}$$

where the fitting parameter w depends on the orientation of the device, A corresponds to linearly polarized light, and B corresponds to a nonpolarized background. Correspondingly, the degree of linear polarization is:

$$DOP = \frac{I_{max} - I_{min}}{I_{max} - I_{min}} = \frac{A}{A + 2B}. \tag{4.3}$$

We obtained $A_{LP} = 1.04 \pm 0.04$, $B_{LP} = 0.05 \pm 0.01$, $\Phi_{LP} = 71 \pm 1$ and $DOP = 91.9\%$ for the LPs, confirming that the LPs are highly TE-polarized. For the excitons, we obtained $A_{exc} = 0.891 \pm 0.001$, $B_{exc} = 0.0081 \pm 0.0002$, $\Phi_{exc} = 161 \pm 1 = \Phi_{LP} + 90$, $DOP = 98.2\%$, showing that the excitons are polarized orthogonal to the LPs.

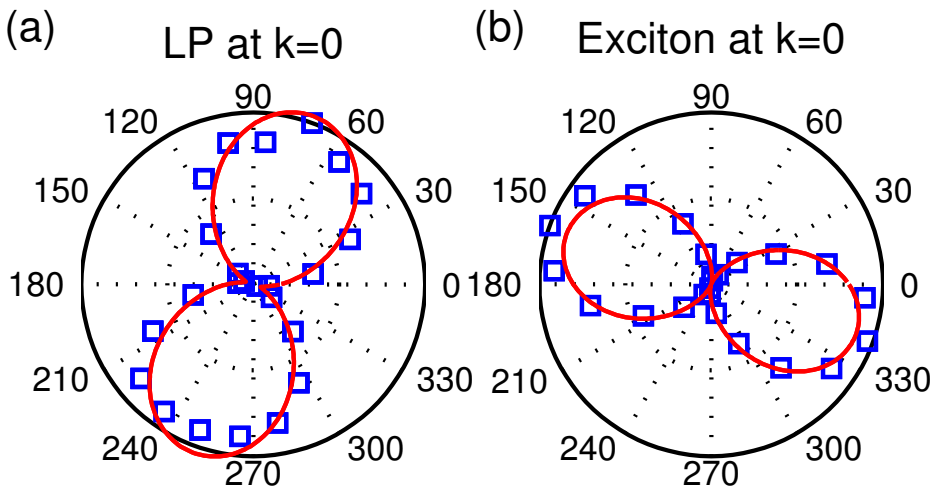

Figure 4.11: Polarizations of the polaritons and excitons in the hybrid-cavity polariton system. (a) Polar plots of the LP ground state intensity as a function of the angle of the linear polarization analyzer. The symbols represent the data. The solid lines fit to Equation 4.2, with a corresponding fitted linear degree of polarization of 91.9%. (b) Polar plot for the exciton emission intensity from within the SWG, corresponding to a fitted linear degree of polarization of 98.2%, with orthogonal polarization compared to (a)

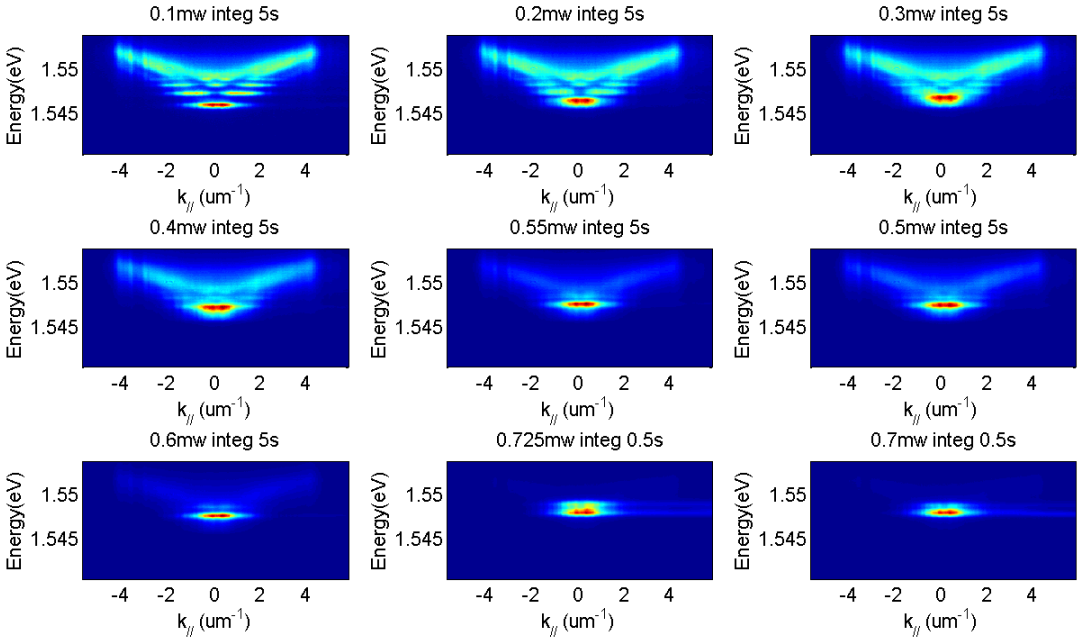

Figure 4.12: 0D SWG polariton device spectra with excitation power from 0.1mW to 0.7mW

Such control of the polariton polarization has not been possible with conventional DBRDBR cavities and is unique to the SWG-based cavity.

4.4 Lasing in 0D SWG Polariton Device

In this section, we show that polariton lasing was achieved in the 0D hybrid cavity. We continued to use the same pumping condition as the previous PL optical characterization and continuously increased the excitation power. The PL signal from the device shifts from multiple discrete modes to single mode accompanying the increased PL intensity. This phenomena was captured in the following spectra figure at nine different pumping powers. (Figure 4.12)

The summary and analysis of the the lasing phenomena are presented in Figure

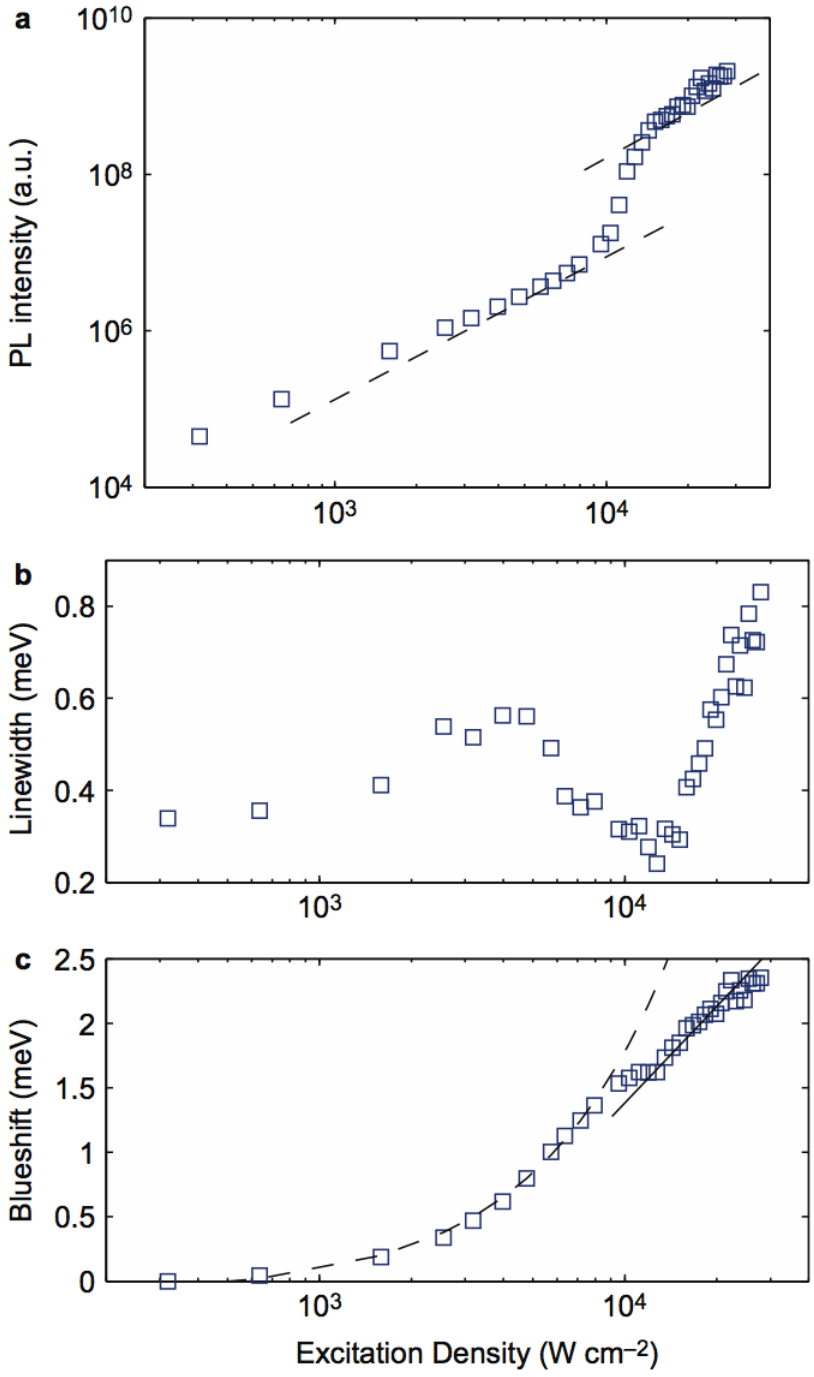

Figure 4.13: Lasing properties of the 0D polaritons. (a) Integrated intensity, (b) linewidth and (c) corresponding energy blueshift of the LP ground state vs. the excitation density. The dashed lines in (a) provide a comparison with quadratic dependence. The dashed lines in (c) display comparisons with the linear dependence below the threshold and logarithmic dependence above the threshold. 0D, zero-dimensional; LP, lower polariton; PL, photoluminescence.

4.13. As shown in Figure 4.13(a), the emission intensity I from the LP ground state increases sharply with the excitation power P at a threshold of $P_{th} =\sim 5kW/cm^{-2}$, characteristic of the onset of lasing. Interestingly, the emission intensity I varies with P quadratically both below and well above the threshold, except at very low excitation densities. This result may arise because the energy separation between the discrete modes is larger than $k_BT \sim 0.8meV$. As a result, relaxation to the ground state through LP- phonon scattering is suppressed compared to LP - LP scattering.

Accompanying the transition, a sharp decrease in the LP ground state linewidth was measured. The minimum linewidth of 0.24 meV may be primarily limited by the intensity fluctuation of the pulsed excitation laser [96]. The LP energy increased continuously with the excitation density due to excitonexciton interactions. The blueshift shows a linear dependence below the threshold, is suppressed near the threshold, and shows a logarithmic dependence above the threshold [57] [47]. The discrete energy levels are maintained across the threshold and remain distinct below the uncoupled cavity energy.

The establishment of polariton lasing confirms the quality of the 0D polariton system. The threshold density is smaller than or comparable to those measured in DBR - DBR pillar cavities [57] [73]. The linewidth reduction and blueshift are all within an order of magnitude of reported values in DBR - DBR planar or pillar microcavities [97] [57] [73]. Unlike DBR - DBR cavities, however, the polariton lasing demonstrated herein occurs with a *priori* defined polarization, independent of the excitation conditions.

CHAPTER V

Nonlinear Regime of SWG Cavity

Having polariton lasing established, our SWG cavity system is ready for more in-depth study that enhances people's understanding in polariton community. I will show in this chapter, the SWG cavity platform actually provides unique venues to explore the nonlinearity of polaritons.

5.1 Introduction

Microcavity polaritons, which are strongly coupled modes between quantum well (QW) excitons and microcavity photons, interact through their exciton components. The excitonic interaction or nonlinearity plays a key role in assisting the polariton energy relaxation and stimulated scattering [98, 99, 100, 101], which finally leads to polariton condensation in the ground state [13, 14, 15]. After condensation threshold, the excitonic interaction continues to influence the temperal [13, 102, 103, 104, 105, 96] and spatial [14, 15, 106] coherence properties of the polariton condensate and governs the superfluidity and other manybody phases of the condensate [16, 107, 108]. As the exciton density increases, the possible cross-over between the BEC and BCS state of polaritons is also an active research area [34, 6, 5]. Many novel applications also rely on the strong nonlinearity resulted from the polariton interaction, for example, optical parametric oscillator [100, 109, 110] and polariton circuits [111, 23, 112, 26].

Understanding the origin of the polariton nonlinearity is thus one of the central issues of the microcavity polariton research.

The present understanding mainly comes from the interacting bosonic picture of polaritons. Two major physical processes resulting in polariton nonlinearities has been identified: the exchange interaction between excitons and phase space filling (PSF), both due to the fermionic nature of the constituent electrons and holes [113, 114]. They lead to different polariton renormalizations at elevated densities. The repulsive exchange interaction tends to blueshift the exciton resonance, changing the energy detuning between the photons and excitons. While the PSF saturates the oscillator strength of the exciton, leading to a shrinking Rabi splitting. It is commonly assumed the exchange interaction makes larger contribution while the PSF induced saturation effect can be neglected in many conventional microcavity systems– CdTe [115, 116] and GaAs [57, 108, 58]. This view is backed up by an early theoretical work studying bottle-neck effect in samples where Rabi-splitting is less than the binding energy [99]. However, for state-of-the-art microcavity samples exhibiting nonlinear emissions, the Rabi-splitting usually exceeds binding energy, the saturation effect is expected to be more prominent. The impact of saturation in polariton interaction has been demonstrated both theoretically [117, 118] and experimentally in early normal-mode coupling (NMC) samples [119, 120], and later in strong coupling samples such as CdTe[14], GaN [121, 122] and organic samples [123]. Those early NMC samples, though gave clear signature of saturation– shrinking splitting, were not able to reach polariton condensation before the Rabi splitting collapses. Later strong coupling samples are mostly subject to strong disorder or obscuring effects like quantum confined stark effect (QCSE) [Ref.40 of [122]]. A clear signature of saturation effect across condensation threshold in a cleaner GaAs-based system is lacking.

In this chapter, I aim to provide unambiguous experimental evidences for prominent saturation effects in a specially designed GaAs-based microcavity below the

lasing threshold, while deviation from either the saturation or excitonic blueshift picture after lasing threshold. Our cavity allows simultaneous observation of strong-coupled polaritons in one linear polarization and bare excitons in the orthogonal polarization from the same excited region. We will show that lower polaritons exhibit large blueshift (2meV) up to the condensation threshold, which cannot be accounted solely by the mild exciton energy shift measured. Instead, with a carefully calibrated exciton density the polariton blueshift can be modeled by a saturation model with a saturation density matched well with theoretical predictions [113, 118]. Through power-dependent reflection measurements, we discovered a surprising coexistence of Mott-transitioned exciton and robust polariton modes. Our finding reveals the non-negligible role of excitonic saturation in polariton renormalization. It will revise the key parameters in the Gross-Pitaevskii description of the polariton condensate, including the density-dependent and spatial-dependent effective mass and interaction constant g. The revised interaction constant may ultimately change the phase diagram of a polariton gas [108]. Further, the final deviation from the saturation model and the well-observed polaritons under the bleached exciton reservoir provokes the need of a more expressive Fermionic theory to fully explain the experimental results.

5.2 Sample and Experiment Details

A schematic of the cavity structure we use is shown in Fig. 5.1(a). Different from conventional distributed Bragg reflector (DBR) cavities, the confinement from top is provided by a high-index-contrast subwavelength grating (SWG) suspended in air [124]. The SWG is designed to have high reflectance (> 0.995) for TE polarization, but low reflectance (~ 0.1) for TM polarization. The cavity thus supports strongly coupled polaritons in the TE polarization but only bare excitons in the TM polarization due to the poor cavity mode. Three groups of four GaAs QWs are placed at the antinodes of the cavity field. The bottom confinement is provided by 30 pairs of

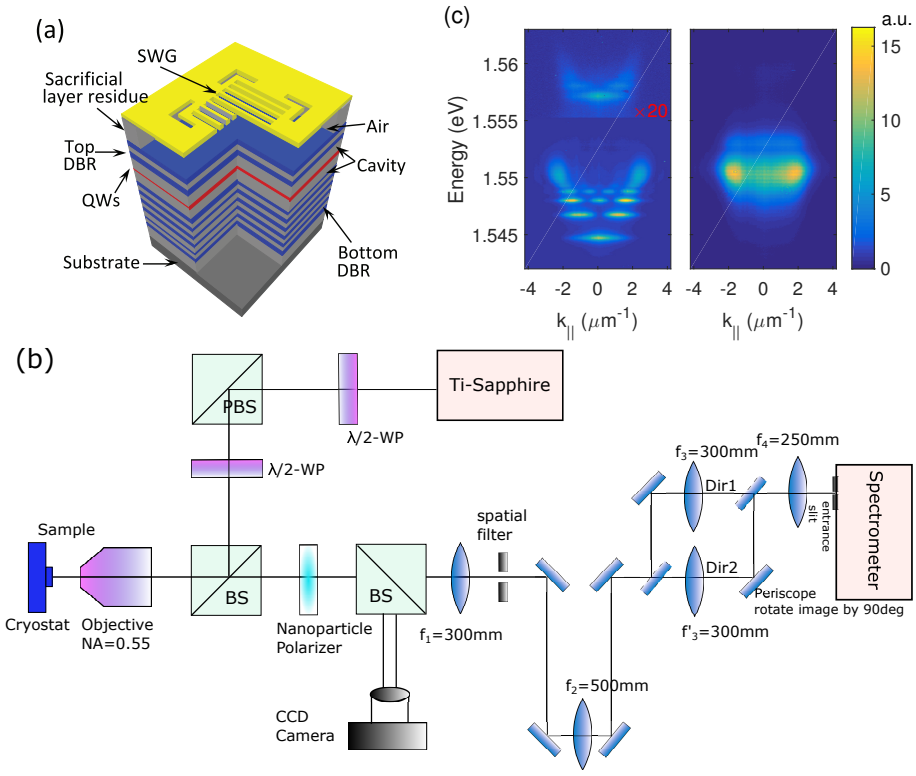

Figure 5.1: Sample and Experiment Details. (a) A schematic of a SWG-based microcavity. Grating and high-index DBRs are made of $Al_{0.15}Ga_{0.85}As$, cavity and low-index DBRs are made of AlAs. 12 QWs made of GaAs are placed in the 3 antinodes of the cavity. (b) The schematic of our experimental set-up. The four-lens confocal relay together with the objective image the k-space of sample emission onto the entrance slit of the spectrometer. The Dir1 and Dir2 branches switch between the two orthogonal directions of the k-space image at the slit. (c) PL intensity of TE polaritons (left panel) and TM excitons (right panel) at pump power of 1 μW. In the left panel, the intensity at an energy above 1.555 eV is magnified by 20 times to show the weak upper polaritons. The excitons are inhomogeneously broadened because of disorders present in the system.

AlGaAs/AlAs DBR. More sample details can be found in [95].

The sample was kept in a cryostat at temperature $\sim 5.5\,\mathrm{K}$. The cavity is pumped with a continuous-wave (CW) Ti-Sapphire laser with TM polarization at energy of $\sim 1.581\,\mathrm{eV}$, above the GaAs quantum well (QW) exciton resonance at $\sim 1.550\,\mathrm{eV}$. The pump laser is focused by an objective lens (numeric aperture ~ 0.55) at the center of the device with a spot size of $\sim 2\,\mu\mathrm{m}$ and chopped by an electro-optical modulator (EOM) with 1MHz and 10% duty cycle to reduce sample heating. Photoluminescence

(PL) of both TE and TM polarization from the sample are collected by the same objective and passed through a k-space imaging set-up, as shown in the Fig. 5.1(b).

An example of the k-space PL is shown in Fig. 5.1(c) for both TE (left panel) and TM (right panel) polarizations. The TE polarization PL clearly shows upper and lower polaritons above and below the exciton energy of $\sim 1.55\,\mathrm{eV}$. The discreteness of the TE polariton modes is due to the effective lateral confinement of the finite-size ($7.5\,\mu\mathrm{m} \times 7.5\,\mu\mathrm{m}$) grating. In contrast, the TM excitons do not couple to the discrete TE photon mode, thus show a flat continuous dispersion resulting from its relatively large effective mass ($\sim 0.1 m_e$). The reason of a shoulder appearing at the high energy side is not yet clear. We do not observe it in the non-patterned part of the sample. But the shoulder will quickly disappear with increasing pumping power.

5.3 Monitoring Exciton Reservoir via TM Exciton

A unique advantage of our single-polarization cavity system is the PL of the TM excitons can be used to infer the information of the whole exciton population, including those large-k states and dark states. Owing to the long lifetime ($\sim 1\,\mathrm{ns}$), these exciton states are usually assumed to form a thermalized exciton reservoir that appears in many literatures [58, 125, 126]. In this section, I will first check the validity of this basic assumption. Then the total exciton density, a fundamental control parameter of excitonic nonlinearity, will be calibrated using the PL intensity of the TM excitons. It will be shown to agree well with the density calculated from the absorbed pump density. The exciton density calibrated here will be used in later sections to model the polariton renormalization.

5.3.1 Quasi-equilibrium between TM Exciton and Exciton Reservoir

The assumption of a thermalized exciton reservoir is valid when the lifetime of exciton is much longer than the relaxation time. It can be checked by a time-resolved

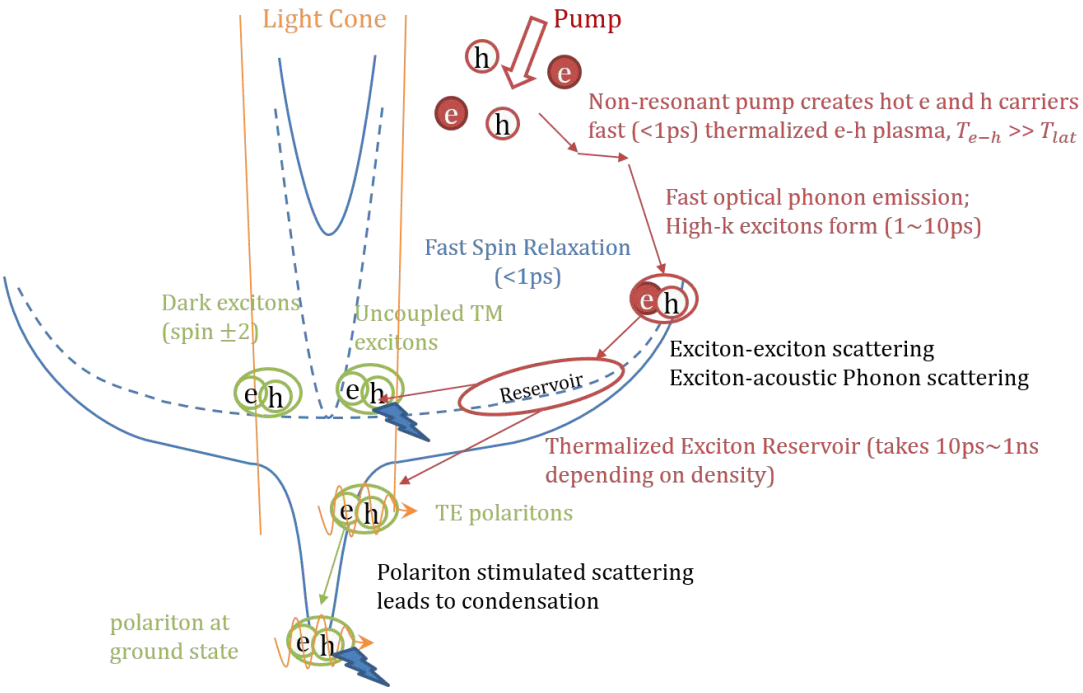

Figure 5.2: Energy relaxation diagram for our SWG based cavity system. The continuous polariton band shown here is for simplicity, not representing the real discrete photon modes in our cavity. Although the relaxation rate of the lowest polariton states needs to be modified by the discrete energy levels, the basic picture is unchanged.

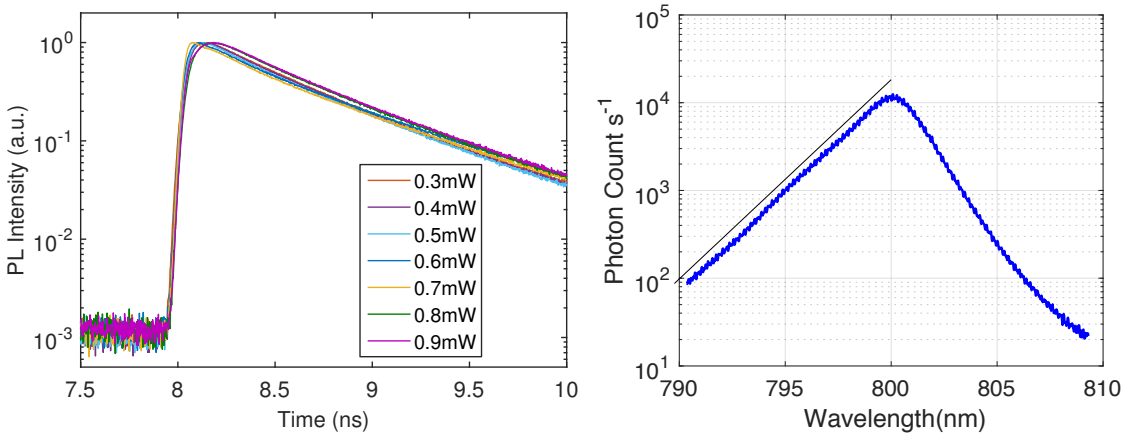

Figure 5.3: Time-resolved PL of TM excitons with different pump powers (left) and the temperature extraction from the exciton PL emission (right). A fs-pulsed excitation at 740nm was used. The PL intensity is normalized to their maximum value. 0.5 mW is the condensation threshold. The right figure is taken at the lasing threshold.

PL (TRPL) measurement of the TM exciton, as shown in Fig. 5.3(a). First, the excitons exhibit an exponential decay, by which the lifetime of the excitons is determined to be around 560 ps, nearly invariant with pump power. The rise time (defined as the time during intensity rising to half of the maximum), representing the relaxation time from the injected carriers to the bottom of exciton band, vary from 90 ps to 120 ps. They are all much shorter than the exciton lifetime, evidencing that excitons have enough time to thermalize among themselves. Therefore it is safe to assume the reservoir is thermalized, and the detected TM excitons at the center of the Brillouin zone are in thermal equilibrium with the reservoir with a much larger k-extent.

Based on the assumption of thermalized exciton reservoir, we can estimate the temperature of the reservoir. By assuming a Boltzmann distribution and a constant density of state (DOS) of the excitons, the high-energy tail of the exciton PL is proportional to the Boltzmann distribution $\exp(-E/k_BT)$. In Fig. 5.3 (right figure) we fit the logarithmic slopes of the high-energy tails of the exciton PL at different pumping power. We obtained exciton temperatures ranging from 10K to 25K in the

power range we applied. Note that the real DOS is a smoother step function due to the localized states formed by disorder, which will make the estimated temperature a little higher than the real temperature.

The second major assumption is regarding the spin relaxation of the exciton population. During the thermalization process, the excitons also undergo a fast spin relaxation ($\sim 5\,\mathrm{ps}$ at $7 \times 10^{10}\,\mathrm{cm}^{-2}$ [127]. We assume in our system the spin relaxation equalize the population of the degenerate bright states (spin ± 1) and the dark states (spin ± 2) [99] in the reservoir. Except in the small $k_{\|} \sim 0$ region, the exciton dispersion is radically modified by the TE cavity dispersion, so the excitons can have unequal spin components. But this region is so small compared to the large k region of the reservoir. It will not change this basic assumption especially in calculating the total exciton density.

5.3.2 Reservoir Depletion by Polariton Condensate Observed

Based on above validated assumptions, the PL from TM excitons detected within the numerical aperture (NA) of our apparatus can be a useful probe for the exciton reservoir. In Fig. 5.4, we first show the power-dependent PL intensities of the TM excitons together with TE polaritons across the lasing threshold of the later. The PL intensities are expressed in photon fluxes, i.e., how many photons emitted from certain states per second. This is advantageous in comparing the absolute emission intensity of different states. The polariton ground state (shown as a blue curve), with a finite size both in real space ($\sim 2.2\,\mu\mathrm{m}$) and k-space ($\sim 1.8\,\mu\mathrm{m}^{-1}$), can be fully detected within the objective NA (=0.55). In contrast, the exciton emission is only partially collected due to its large extent in k-space. Here we plot exciton emission within the aperture of the objective (square marker), and multiply a common factor to obtain the total exciton emission within the light cone defined by $k_0 = 2\pi/\lambda$ (circle marker). The polaritons PL exhibits a sharp nonlinear increase at a threshold of $\sim 3\,\mathrm{mW}$,

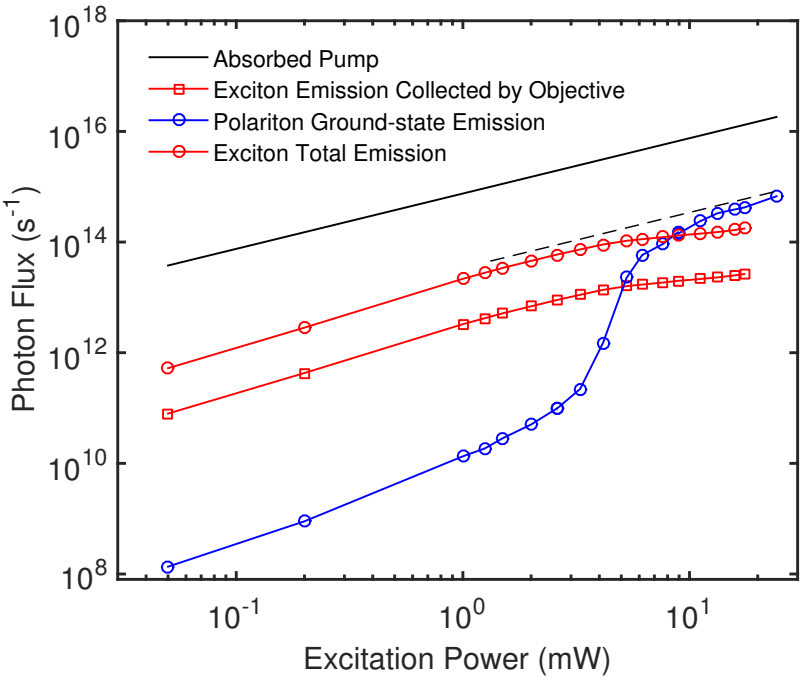

Figure 5.4: Flux balance of our system. The absorbed photon flux from pump (black line) uses a constant absorption of 0.3 measured by a reflection spectroscopy.

evidencing the onset of polariton lasing. In contrast, excitons PL exhibits a first super-linear then a sub-linear increase before and after the lasing threshold. The super-linear part is probably due to increased exciton-exciton scattering in the relaxation process. The sub-linear emission of the excitons after the threshold is clearly compensated by the polariton emission flux. The dashed line with a linear slope acts as a guide of eyes. In steady state, the input flux of the reservoir from the carrier relaxation, assumed to be a constant fraction of the absorbed pump flux (black line), should be balanced by the output flux through the radiative states. In our system, the bright excitons within the light cone and TE polaritons (ground state dominates after threshold) are the two major radiative sinks. The clear compensation between the two sinks suggests that the exciton reservoir is drained by the polariton ground state, via a stimulated scattering process after threshold. The exciton reservoir is directly observed to be clamped by this nonlinear process, in line with many literature [99, 128, 122].

5.3.3 Exciton Density Calibration via Exciton Emission

The total density of exciton reservoir, a key parameter determining exciton saturation and Mott transition, can be estimated from the emission of the TM excitons. The population of excitons in radiative states can be obtained by $\Phi_{PL}\tau_X^r$, where the Φ_{PL} is the PL emission flux of the considered exciton states and τ_X^r is the radiative lifetime of the states. However, to relate the radiative exciton population to the total exciton population, a common challenge is that the observable exciton PL represents only a very small fraction of the total exciton population. In a disorder-free QW, excitons distribute along their continuous energy-momentum dispersion with occupation factors given by Bose statistics or approximately by Boltzmann statistics at low density. So the population at larger momentum thus higher energy states can be well related to the detected exciton population from the small momentum thus low energy states by a Boltzmann factor. However, disorders of QWs are inevitable even for the relatively clean GaAs-based system. In situations where the thermal energy is not enough to overcome the disorder potential barriers, this simple relation will break down. The disorder strength of our sample can be inferred by the inhomogeneous linewidth of the TM exciton $\sim 3\,\text{meV}$ at low density, which is larger than the exciton temperature $\sim 10\ K$ or $1\,\text{meV}$. Due to the scattering by the disorder potential, the excitons' energy eigen-states are no longer well defined by their momentum. We need to calculate the new eigen-states of our system under disorder potentials.

2D wavefunctions of excitons in disorder potential

Disorder in QW is described by an effective potential. In GaAs QW, the major disorder is the mono-layer variation of the well. Adopting the analysis given by Runge et al [129], the disorder potential can be described by two parameters– the confinement

potential depth δE_{conf} and width l_c. The potential depth can be estimated through

$$\frac{\delta E_{conf}}{\delta L} \approx -\frac{\hbar^2 \pi^2}{m L_{eff}}, \tag{5.1}$$

where δL is the monolayer thickness (fluctuation) and L_{eff} is the effective width of the QW. For GaAs QW, $\delta L = 0.56$nm and I just use the QW thickness 12 nm as the L_{eff} since the confinement of GaAs/AlAs is sharp. I obtain $\delta E_{conf} = 3$ meV, matched well with the inhomogeneous linewidth. One can understand the disorder potential as a Gaussian random variable at each position, δE_{conf} is its standard error around its mean.

Further, the random confinement potentials are correlated. Assuming a Gaussian correlation kernel,

$$k(x, x') = E(U(x)U(x')) = \exp(-|x - x'|^2/2l_c^2) \tag{5.2}$$

The potential width l_c manifests as the correlation length in the Gaussian exponent. One can generate a Gaussian random field with some advanced algorithm, for example `stationary_Gaussian_process(x, y, rho)` in MathWorks File Exchange. `rho` is correlation length, which is set to be 6 nm, the Bohr radius of GaAs QW exciton, according to Runge et al [129]. The wavefunctions in a time-independent 2D disorder potential U(x, y) can be solved by the following eigenvalue equation:

$$(\frac{\hbar^2}{2m}\nabla^2 + U(x, y))\psi(x, y) = E\psi(x, y). \tag{5.3}$$

The computation domain is set to be 1um size, much larger than the disorder correlation length 6nm. Periodic boundary condition is used. The spatial resolution is set to be 2nm, to reduce the computation time.

To give a sense of what the wavefunctions look like, I first show the lowest 6

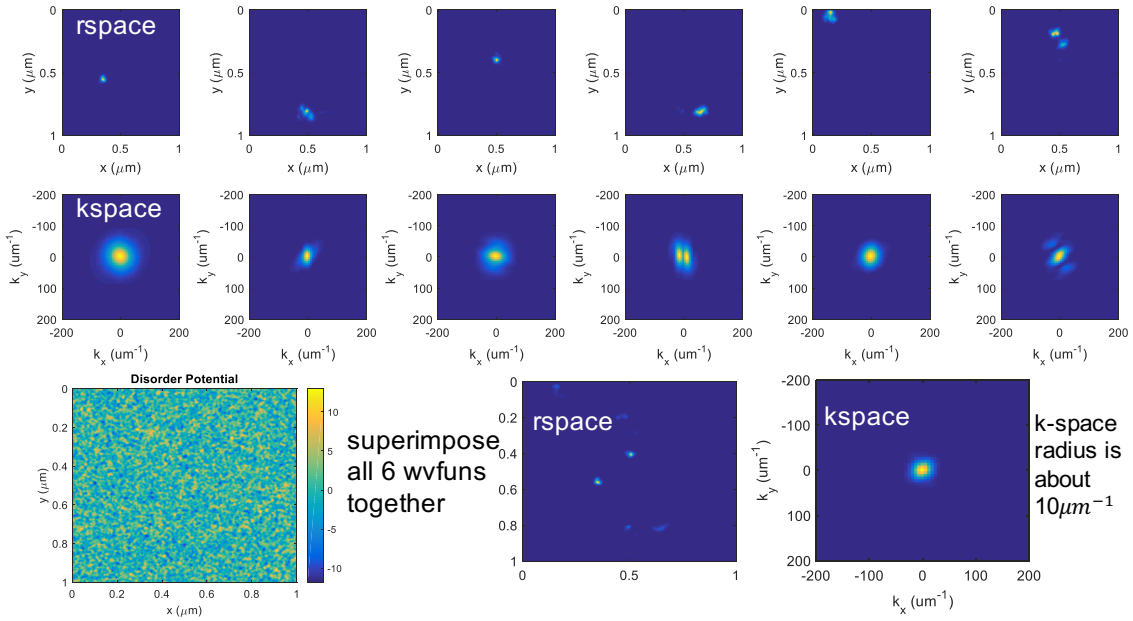

Figure 5.5: The lowest 6 energy states (upper two rows) in a random generated disorder potential (lower left).

energy states in Fig. 5.5. Not surprising, the lowest energy states are trapped states. The wavefunctions are localized at some random positions. However, the k-space wavefunction is centered at zero and has an extent of $10\mu m^{-1}$.

However, the higher energy states are more extended rather than localized, as shown in Fig. 5.6. The k-space function looks like a ring instead of a spot. That means, although the wavefunction covers all the k, the k-distribution is more concentrated at some higher k. Fig. 5.7 shows the first 500 wavefunctions spaced with their eigen-energies. Only one dimension is shown for visualization purpose. As can be seen, although with some spread in k, the k-space wavefunctions lie roughly on the parabolic dispersion curve of excitons. Here I used $m_{exc} = 0.06m_e$.

Summing over the k-space wavefunctions weighted by the Boltzmann occupation factor, we obtained the k-space distribution of the excitons as shown in the inset of Fig. 5.10. Note that the radius at the half maximum of the distribution is $33\,\mu\text{m}^{-1}$. Comparing with the measurements, this is much larger than the detected k-space

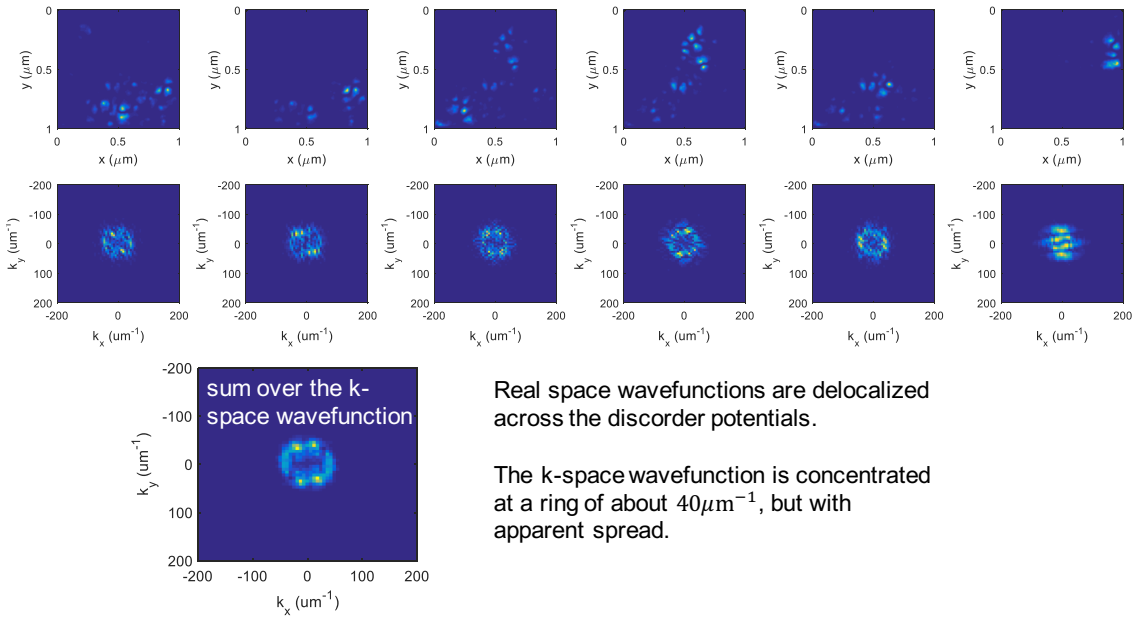

Figure 5.6: The 91st to 96th energy states (upper two rows) and the superimposed wavefunction of them.

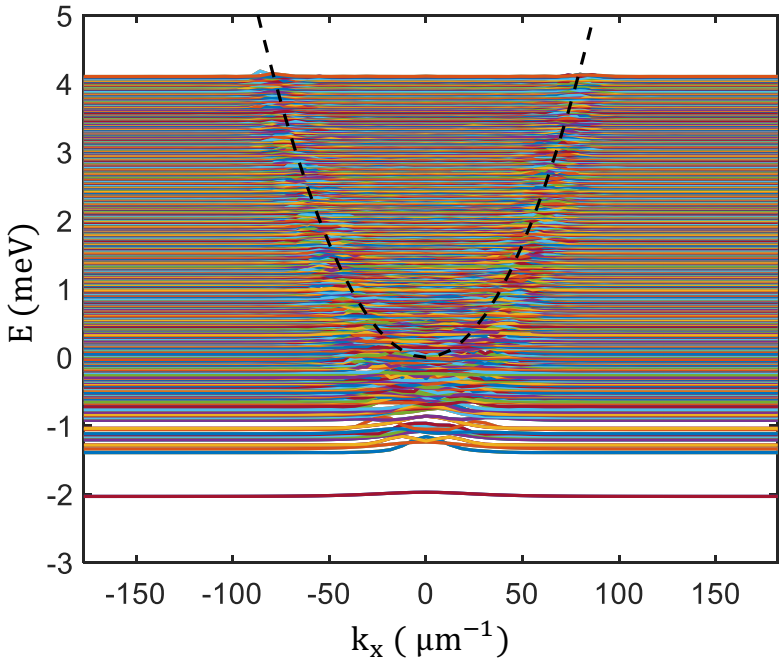

Figure 5.7: The lowest 500 k-space wavefunctions positioned at their eigen-energies in the y-axis.

radius of $4\,\mu\text{m}^{-1}$, but smaller than the radius defined by $k_B T_X$. Using the k-space area ratio, the total exciton density can be calculated via the following,

$$n_{tot} = 2\Phi_{det}\tau_{exc}(A_{tot}/A_{det})/S_X N_{QW}, \tag{5.4}$$

where n_{tot} is the total exciton density. Φ_{det} is the detected exciton emission flux within the objective aperture. τ_{exc} is the exciton lifetime. A_{tot} and A_{det} are the total and detected k-space areas respectively. N_{QW} is the number of quantum wells. The factor of 2 is to account for the TE and TM polarization.

Exciton Spot Area

The unknown quantity left out in Eq. 5.4 is the exciton spot area S_X. It is determined by the exciton diffusion length from the pump spot center (the pump spot itself is small). We can directly measure the bright exciton spot diameter ($\sim 5\,\mu$m) by imaging the TM excitons in real space. However, this underestimates the diffusion length of dark excitons and the high-k excitons outside of the light-cone. To determine the real exciton spot area, we also did large pump spot check. In a later experiment, I used a large Gaussian pump spot with a diameter of $38\,\mu$m (Fig. 5.8 left), which is supposedly much larger than the exciton diffusion length. The exciton extent is set by the pump spot instead of the diffusion length.

From the power dependent PL intensity, we can find the threshold power for both small and large pump spot on the device. Assuming at threshold, the e-h pair density is roughly the same. We can solve for S_X through,

$$n_{pair} = \alpha\Phi_{pump,small}\tau_X/S_X = \alpha\Phi_{pump,large}\tau_X/S_{pump,large}, \tag{5.5}$$

where α is the device's absorption coefficient at the pump wavelength, Φ_{pump} is the pump photon flux (Pump power P over photon energy $E = \hbar\omega$), τ_X is the averaged

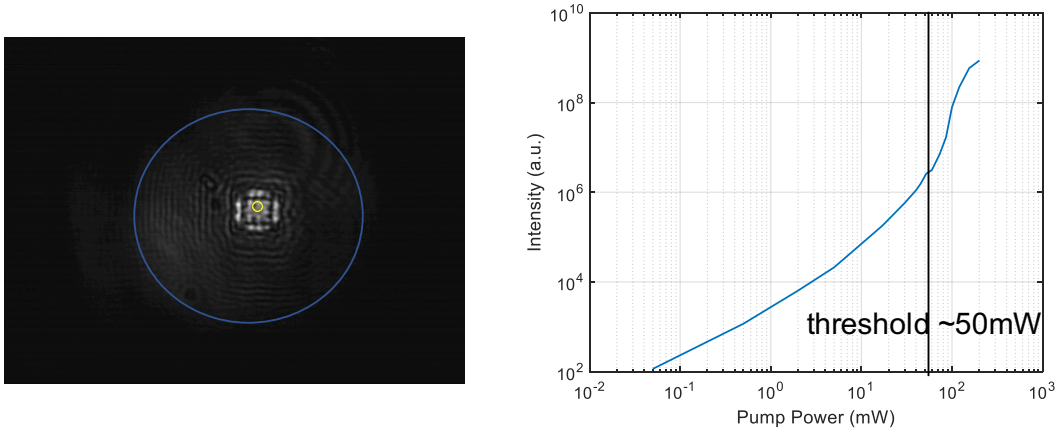

Figure 5.8: The large pump spot shown in monitoring camera (left) and polariton power dependent PL intensity (right). The bright square in the left figure is the SWG device.

lifetime for e-h pairs in all the states. Assuming α and τ_X are not changing with the small and large pumping condition, we can obtain $S_X = S_{pump,large} * P_{small}/P_{large}$. Given $P_{small} = 3\text{mW}$ and $P_{large} = 50\text{mW}$ at threshold, $S_X \simeq S_{pump,large}/16$. So the diameter of the exciton spot is thus $d_{pump,large}/4 \simeq 10\mu m$, which is 2 times larger than the measured bright exciton spot diameter $\sim 5\,\mu\text{m}$.

The above estimated S_X completes the equation Eq. 5.4 and we obtain the total exciton density with pump power shown in Fig. 5.10.

As another sanity check, we also calculate the e-h pair density through the absorption (see the first half in Eq. 5.5), also overlaid in Fig. 5.10. We assume the absorption α and τ_X are constant with pump power, so the curve is linear. We determined through measurement $\alpha = 1 - R - T = 0.3$ (see Fig. 5.9), where $R = 0.7$ is the reflectance of the sample at the pump wavelength obtained by a reflection spectroscopy at low excitation. T is the transmission through the sample, which can be set to be zero because the bottom DBR is a good mirror (reflectance > 0.995) at our pump wavelength. The average e-h pair lifetime τ_X should in principle be different from the radiative lifetime τ_X^r of the TM excitons we measured. In Appendix A, I

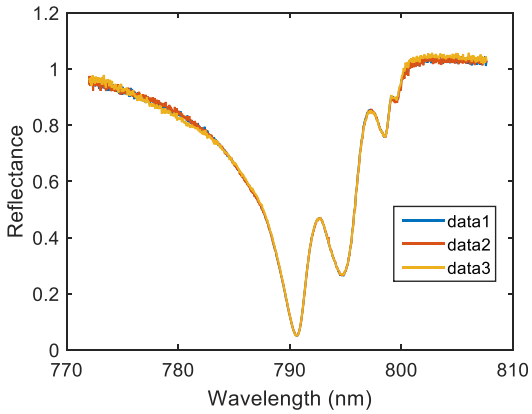

Figure 5.9: Reflection measurement to calibrate the absorption of pump at 784 nm. The measurement shows good repeatability among three trials.

derived the averaged lifetime $\tau_X = 2\tau_X^r$ from simple rate equations. A full rate equation modeling is also given, where I reproduced the nonlinear increase of the polariton condensate.

As can be seen, the two independent density calibrations agree well with each other. Indeed, the calibration from absorption gives a little higher density than the calibration from emission, due to the e-h plasma portion that is not accounted in emission calibration. The obvious deviation in the low power range is because the e-h pairs are not efficiently relaxed to the exciton branch. And the deviation in the high power range is due to the drainage from polariton condensate, which has a much smaller radiative lifetime.

5.4 Density-dependent Energy Shifts

The density-dependent energy shifts of the TE polaritons and TM excitons are shown in Fig. 5.11. The condensation threshold divides the figure into two regions. Before the threshold, the lower polariton undergoes a large blueshift $\sim 2\,\text{meV}$ while the excitons keep a nearly constant energy. The polariton shift obviously does not follow the exciton shift, making the exciton-shift dominated view unsuitable here. In

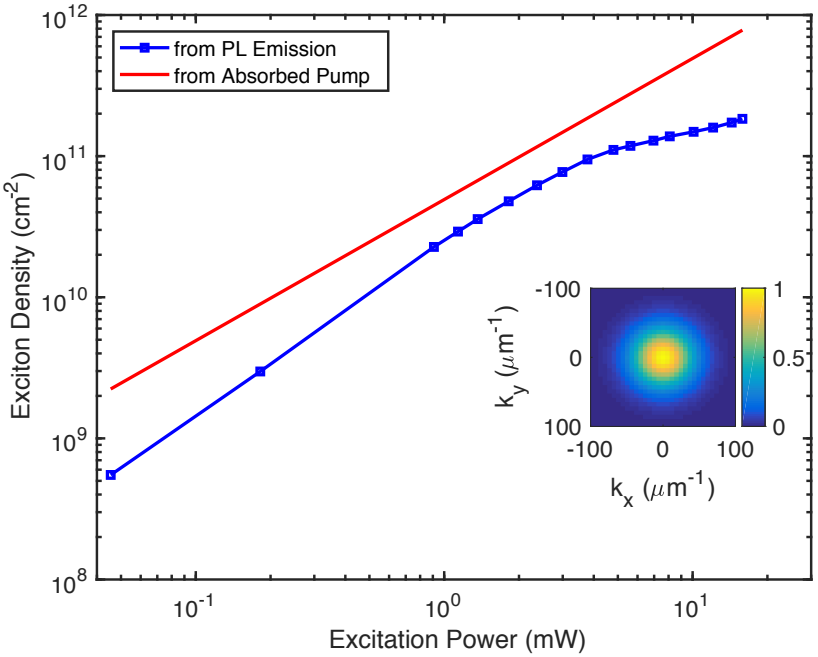

Figure 5.10: Exciton density as a function of excitation power calibrated using PL of TM exciton (blue line) and absorbed pump (red line).

addition, the upper polaritons keep a constant energy, resulting in a shrinking Rabi splitting. It indicates a possible saturation of oscillator strength. We try to model the saturation effect through a conventional saturation model by introducing a saturation density n_s [113]:

$$f_{osc} = f_0/(1 + n/n_s) \tag{5.6}$$

Here f_0 is the areal oscillator strength in the linear regime and n is the exciton density. Because Rabi splitting $\Omega \propto \sqrt{f_{osc}}$, the Rabi splitting relates to the density via

$$\hbar\Omega = \hbar\Omega_0/\sqrt{(1 + n/n_s)} \tag{5.7}$$

where Ω_0 is the Rabi splitting in the linear regime, which amounts to 12.4 meV for our system.

With this density-dependent Rabi splitting, we can fit the lower polariton energy

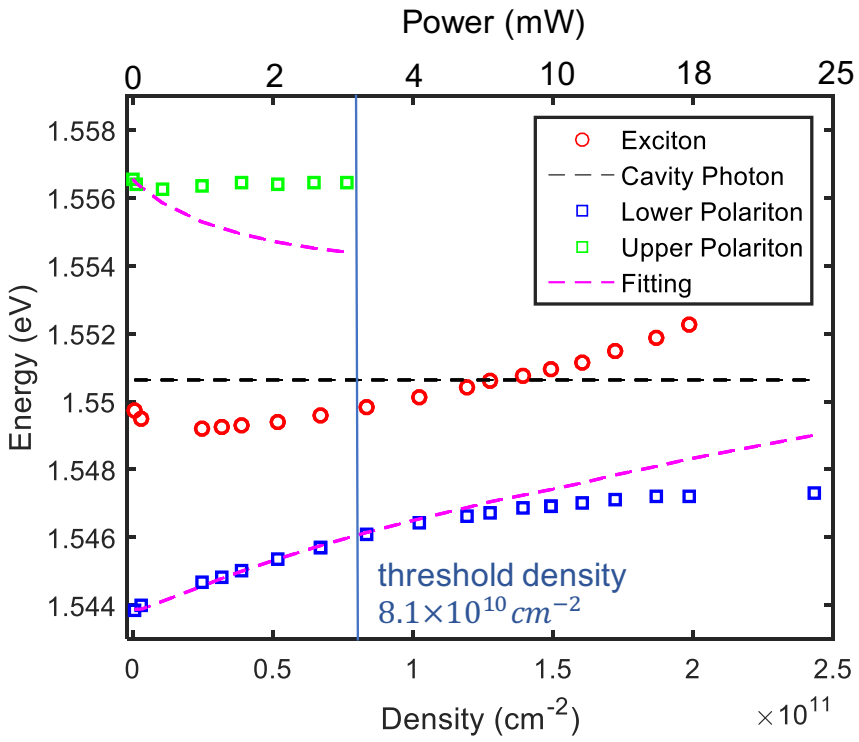

Figure 5.11: Density-dependent energy of upper polariton, lower polariton (square marker) and TM excitons at $k_{\parallel} \sim 0$. The cavity photon line (dash-dotted) is calculated via coupled oscillator model using the energies of polaritons and excitons at lowest power.

shift before threshold via the coupled oscillator model (COM),

$$E_{LP,UP} = (E_{cav} + E_{exc})/2 \pm \sqrt{\Omega^2 + (E_{cav} - E_{exc})^2}/2, \tag{5.8}$$

where $E_{LP,UP}$ are the energies of lower and upper polariton, E_{exc} is the energy of the excitons using the measured value, and E_{cav} is the energy of cavity photon (shown as black dash-dotted line) evaluated at low density. Before threshold the lower polariton fits well with the COM, using a saturation density of $6.0 \times 10^{10}\,\mathrm{cm}^{-2}$. However, the upper polariton does not fit with the COM. Also after threshold, albeit the exciton undergoes a continuous blueshift, the polaritons seem to plateau more than the COM predicts. These discrepancies may be attributed to the many-body effects of the polariton condensate that needs further investigation.

Our saturation density matches well with theoretical predictions. A theory given by Schmitt-Rink, et al [113], predicts the excitonic PSF and exchange interaction contributes $4.57\pi a_{2D}^2$ and $3.94\pi a_{2D}^2$ respectively to the inverse of saturation density. The total saturation density is thus given by $n_s = 0.117/\pi a_{2D}^2$, where $a_{2D} = a_{3D}/2 \sim 8.5\,\mathrm{nm}$ is the 2D Bohr radius for GaAs/AlAs QW. We thus obtain $n_s = 7.7 \times 10^{10}\,\mathrm{cm}^{-2}$. A work by Rochat, et al [118], predicts a saturation density $n_s = 0.139/a_{2D}^2 \approx 9.1 \times 10^{10}\,\mathrm{cm}^{-2}$. Our experimental-extracted value is close to these theoretical predictions.

The density-dependent polariton energy shift can be used to calculate the polariton interaction constant g, a key parameter in the Gross-Pitaevskii (G-P) descripition of the polariton condensate:

$$(-\frac{\hbar^2}{2m}\nabla^2 + V_{confine}(r) + g_{res}n_{res}(r) + g|\psi(r)|^2)\psi(r) = \mu\psi(r) \tag{5.9}$$

where $\psi(r)$ is the polariton wavefunction, m is the polariton effective mass, $V_{confine}$ is the confining external potential, g_{res} is a constant describing polariton interaction

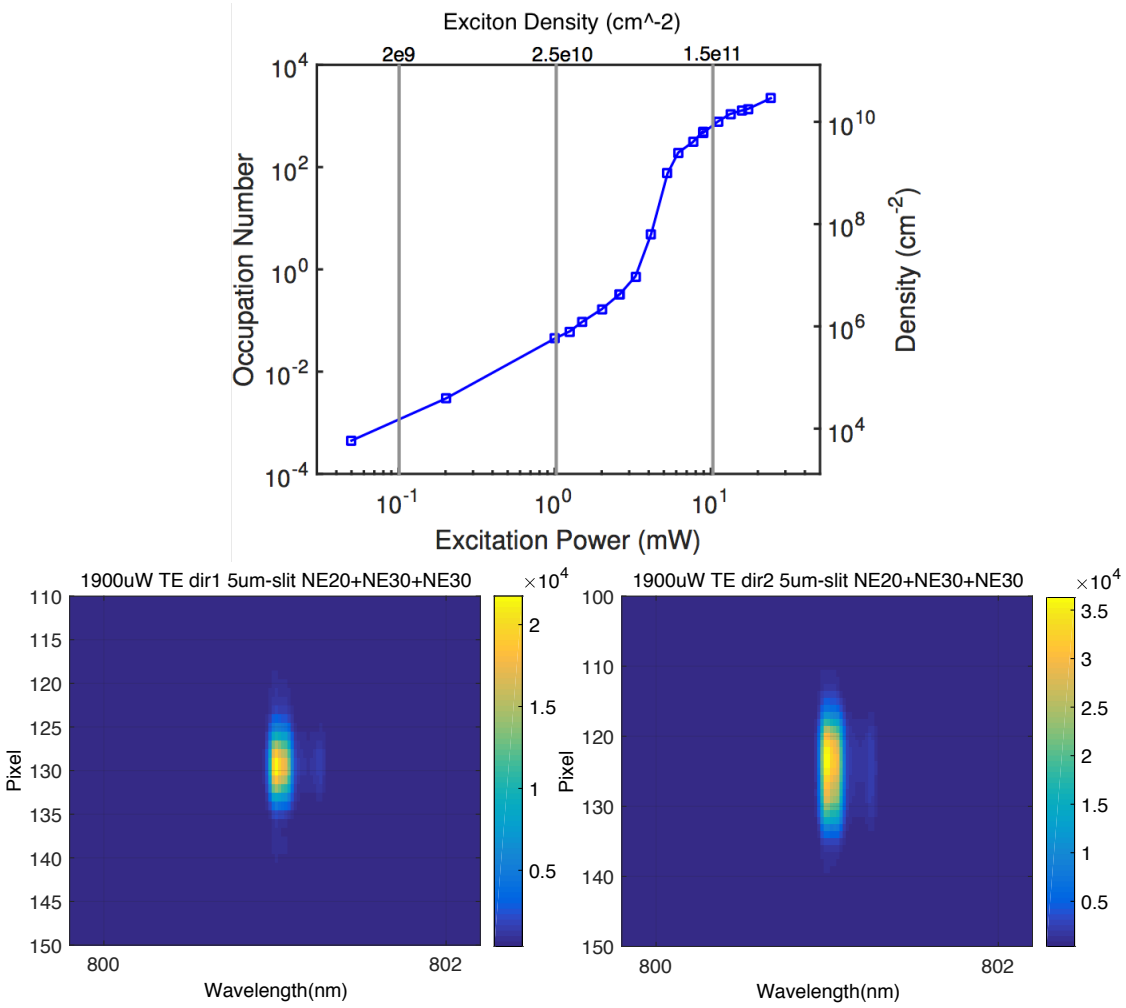

Figure 5.12: Occupation number of polariton ground-state as a function of the excitation power. The density of the polariton ground-state is also shown on the right-axis, via dividing the occupation number by the mode area $\sim 6\,\mu\text{m}^2$ determined by the real space images of the polariton mode (above lasing threshold) sliced in the along-grating-bar and cross-grating-bar directions. Each pixel is 26 μm square and the magnification is 104. The polariton mode measures FWHM 7pixel (1.75 μm) and 14pixel (3.5 μm) in the two directions respectively. So the mode shape is not round but elliptical.

with exciton reservoir, μ is the chemical potential [116, 58]. Polariton-polariton interaction constant g and g_{res} have the same origin, that is, the excitonic interaction and saturation. So they only differ a factor of the exciton fraction $|X_k|^2$, where X_k is the Hopfield coefficient of a polariton at momentum k [117]. Since our system is close to zero-detuning, the polariton ground state has a $|X_{k\sim 0}|^2 = 1/2$, which gives $g \sim \frac{1}{2} g_{res}$. Because the ground-state polariton density is more than one order of magnitude smaller than the exciton density (Fig. 5.12), we attribute the energy shift of polaritons exclusively to the exciton reservoir, i.e., $\Delta E_{LP} = g_{res} \Delta n_{res}$. By taking the derivative of the density-dependent energy of LP ground-state from Fig. 5.11, we obtain $g_{res} \simeq 4\,\mu\text{eV}\mu\text{m}^2$ at low-density and continuously decrease at higher density.

The highest polariton-polariton interaction constant g is thus $2\,\mu\text{eV}\mu\text{m}^2$ and decrease at higher density. Comparing to other g values reported [58], $g = 2\,\mu\text{eV}\mu\text{m}^2$ in optical trap and $9\,\mu\text{eV}\mu\text{m}^2$ in $10\,\mu$m pillar, our g value matches very well with the optical trap one, but lower than the pillar one. It may be due to the lower interaction constant for the linear polarization of our polaritons. Another independent determination of the g-value for our device is done by the fitting of the first-order temporal coherence function to theoretical model [130]. The g value obtained there is $4\,\mu\text{eV}\mu\text{m}^2$, roughly agreed with the value obtained here (density calibration could be easily factor of 2 off). Our result also suggests that density-dependent thus spatial-dependent interaction constant may need to be considered in the G-P equation Eq. 5.9, in line with the modeling from Utsunomiya et al [131].

5.5 Evidence of Co-existing Polariton Lasing and Mott-Transitioned Excitons

In previous section, I showed the energy shifts of polaritons and excitons through PL measurement. One important feature not shown is the linewidth of each state,

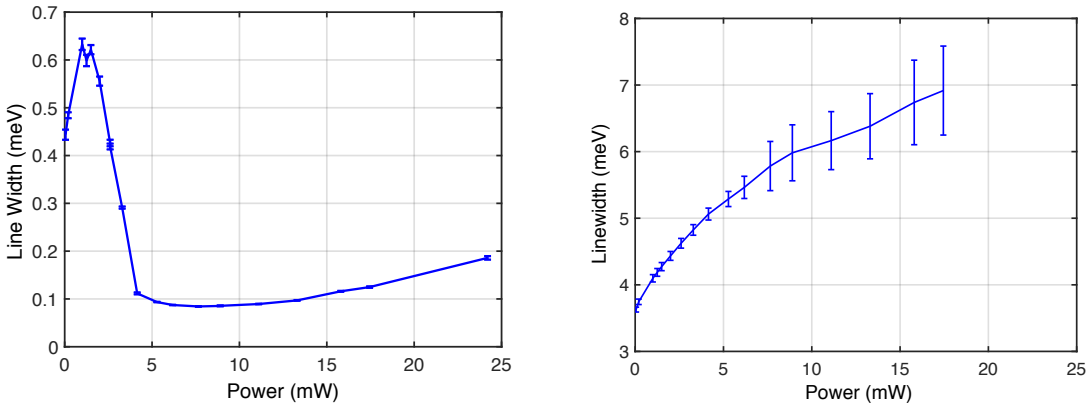

Figure 5.13: Linewidth of polariton ground state and TM exciton measured from PL.

because exciton nonlinearity can be expressed as the change of optical susceptibility

$$\chi(E) \propto \frac{f_{osc,X}}{E - E_X + i\gamma_X} \tag{5.10}$$

with exciton density, where $f_{osc,X}$ is the oscillator strength of exciton state, E_X is the exciton energy and γ_X is the linewidth of exciton. The linewidth can be measured by absorption spectroscopy (the imaginary part of the susceptibility determines the absorption linewidth). PL is not a truthful representation because of the thermalization process. Nevertheless, I first show the PL linewidth of both the polariton ground state and the TM exciton (Fig. 5.13).

As can be seen, the polariton ground state linewidth first experiences a sharp decrease at around the threshold, then goes up slowly because of the polariton interaction within the condensate. In contrast, exciton linewidth goes up continuously, from 3.6meV to very large 7meV. The errorbar is also large, because the Lorentzian fitting no longer capture the PL lineshape. The PL becomes asymmetric– high-energy tail is fatter than the low-energy tail. The large linewidth and asymmetric lineshape suggests a possible exciton bleaching or Mott-transition is undergoing. The exciton becomes less tightly bounded, but evolves into e-h plasmas at high pump power and

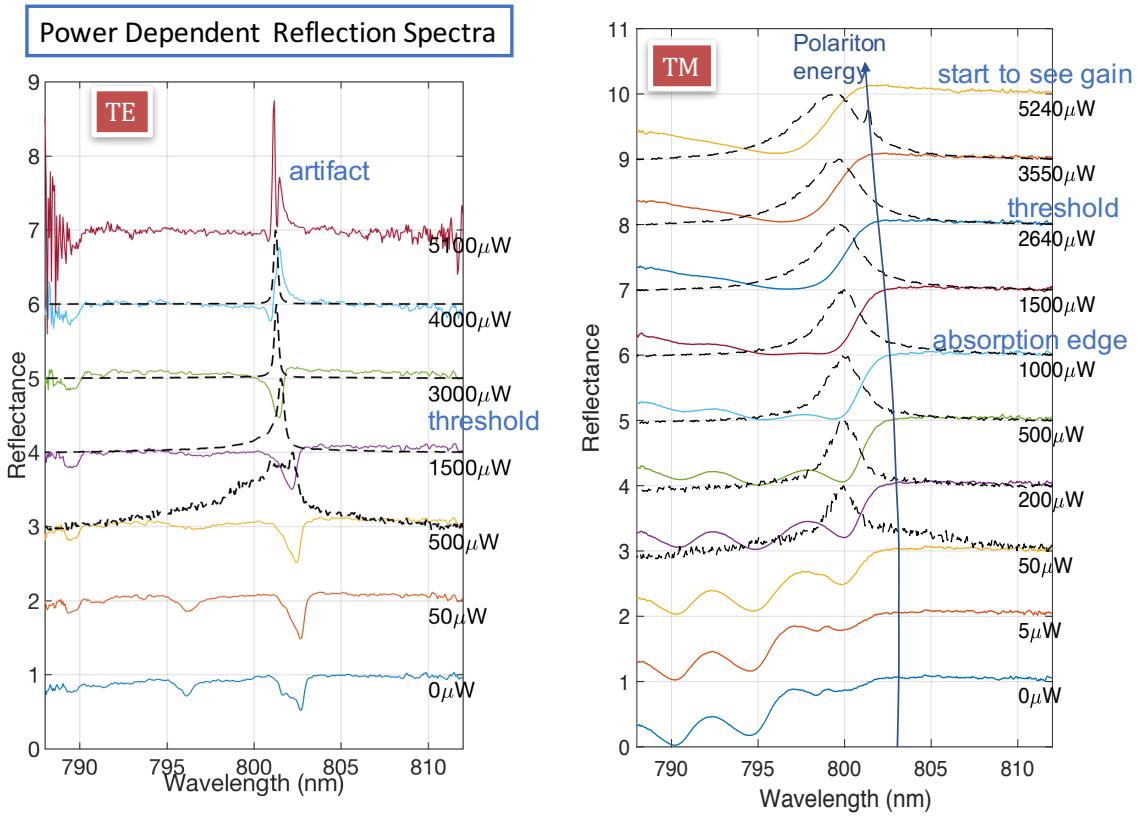

Figure 5.14: Reflection spectra at different pump power from device 4-6-1, TE (left) and TM (right) polarization. The simultaneous PL data are overlaid with the reflectance (black dashed lines, only for high enough powers).

density.

To unambiguously reveal the nonlinear processes happening in the excitons, I conducted a power-dependent reflection measurement (equivalent to absorption measurement for our system). Such measurements require that the same above-band pumping with PL measurements, and a weak pulsed probe covering the polariton and exciton spectral range. It is challenging because it is difficult to separate the weak probe pulse and the strong PL emission (especially when lasing) from the device, thus a poor signal to noise ratio. We adopted the following method: use CW pump and pulsed probe, and separate the CW PL and the pulsed reflected probe in

time domain using streak camera.

The resulting reflection spectra at different pump powers are shown in Fig. 5.14. From bottom to top are the reflection spectra at increasing pump power, shifted by 1.0 for clarity. The lower polariton and upper polariton dips are clearly visible at lower power. At high power, the upper polariton becomes indistinguishable, but seemingly red-shifted to converge with the blueshifted lower polariton, indicating a saturation of the oscillator strength. After the threshold, the lasing is so strong that even the streak camera cannot separate the CW PL from the pulsed reflection. Although I have subtracted the CW PL background, the pulsed PL caused by the pulsed probe contributes a considerable amount of the signal. The peak at $4mW$ and $5.1mW$ is possibly the pulsed PL contribution, or optical gain, which currently cannot be concluded. The sharp dip in $5.1mW$ is an artifact from the curvature correction by streak camera, should be ignored. Although the polariton resonance cannot be distinguished in the reflection spectrum due to the artifact, the PL peak can provide such information instead. The overlaid normalized PL is helpful in tracking the polariton blueshift, especially after lasing threshold 3mW.

The TM reflection spectra shows the evolution of the TM exciton resonance. At zero pump power, the heavy hole exciton actually splits into two small dips at around 799nm, whereas the heavy hole exciton from the planar part (non-device region) is a single dip at 799nm. This may be due to the wet etching changes the strain for the QWs close to the surface, resulting in inhomogeneity in exciton energy. But it is not conclusive either. The dips at 790 nm and 795 nm are from light hole, again, seemingly split from the planar part light-hole exciton at around 793nm. The heave-hole dip at 800nm gradually takes over at higher pump power. At $200\mu W$, only the dip at 800nm is visible and becomes very deep. At $1000\mu W$ the dip becomes almost an absorption edge, resembling the behavior of a semiconductor band edge. The band edge continuously blueshifts passing the lasing threshold and exhibits some

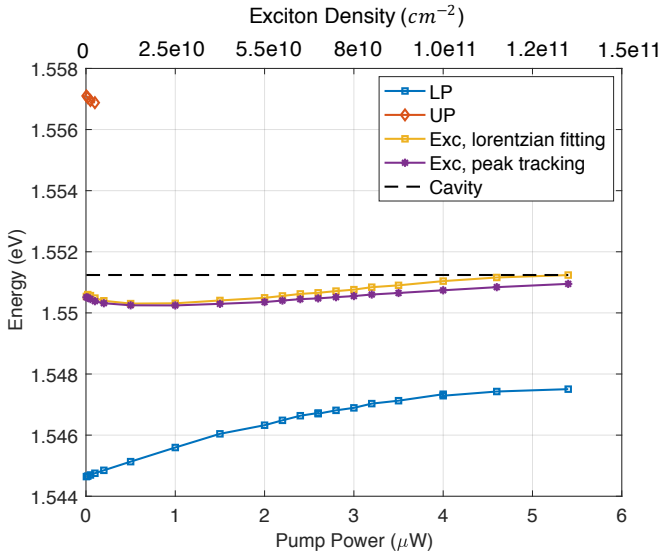

Figure 5.15: Energy shift of TE polariton and TM exciton with density and pump power for device 4-6-1.

optical gain at the edge top, at the highest power reached in this experiment. In this experiment, the pump power only reached twice of the lasing threshold because higher power poses danger of thermal damage to the grating. We didn't applied optical chopping because of the complexity from the streak camera syncing. I have more data from different devices, all confirming the same behavior presented here. I even pushed one device to 10 times of the threshold, where the optical gain from TM polarization is much larger than the gain shown here. But unfortunately the device is found thermally damaged later, making the data questionable. Therefore I don't include it here. As a reference, I tracked the polariton and exciton resonance for this device, as shown in Fig. 5.15. The energy shifts are comparable with the device 2-6-4 I showed in last section. However, this device only reached 2 times of threshold, restricted by the thermal damage limit. The upper polariton also becomes indistinguishable at a much lower pump power.

Evident from the power dependent reflection spectra, the band edge formed at 1/3 of the threshold pump power indicates the exciton starts to undergo a Mott-transition lower than the lasing threshold. At the same time, polariton robustly existed and

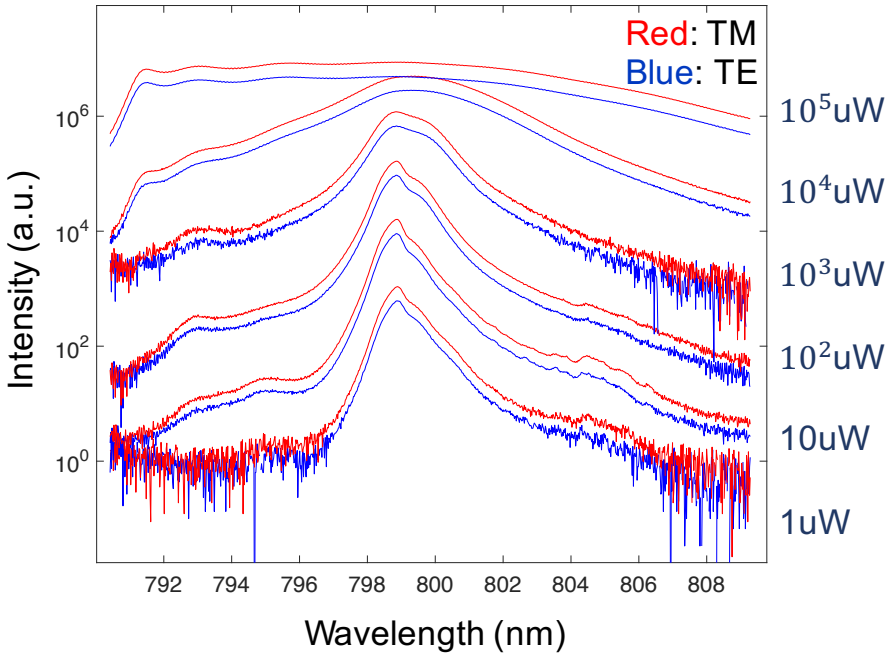

Figure 5.16: The exciton PL from planar part (non-device region of our sample) from low to high pump power, under TE and TM non-resonant pumping at 784nm. There is no lineshape difference betweeen TE and TM pumping. The slight difference in intensity is because of the different responses of our experimental set-up for the two linear polarizations.

lased at a larger pump power. If we assume the TM exciton and the excitonic component in polaritons come from the same reservoir, the co-existing polariton and Mott-transitioned exciton is really puzzling because in the widely accepted picture polariton can only exist when the electron and hole are still bounded as an exciton.

I checked for planar part[1], either TE or TM non-resonant pumped e-h pairs will relax to TE and TM excitons symmetrically. As shown in Fig. 5.16, from low to very high power, the exciton PL evolves into broad plasma PL lineshape. There is no difference in the lineshape for TE and TM pumping, indicating the e-h pairs' polarization are randomized and split into equal TE and TM populations along the relaxation path. In other words, the TE and TM excitons are from the same origin,

[1]It is practically difficult to directly check the device at 784nm pump wavelength because it is still within the TE stop band, it is hard to create the same e-h pair density for the two polarizations.

if one is shown bleached, the other should also be bleached.

This fact may shake the common understanding – polaritons are weakly interacting Bosons. The interaction constant can be obtained by the Coulomb interaction and saturation contribution. Namely, the Hamiltonian of the lower polaritons can be expressed as,

$$H_{LP} = \sum_{k} E_k^{LP} L_k^\dagger L_k + \sum_{k,k',q} V_{k,k',q}^{eff} L_{k+q}^\dagger L_{k'-q} L_{k'} L_k \tag{5.11}$$

where $V_{k,k',q}^{eff}$ contains X-X coulomb interaction term and saturation term (truncated to first-order) [128]. The major limitations of this approach are (i) the perturbative regime $n_{exc} << n_{sat}$ is required, high density regime cannot be described, which is actually more often reached in major experimental platforms. It is just people don't realize it due to lack of ways to calibrate the exciton density. (ii) Effect of disorder is neglected. To solve the (i) limitation, one would resort to full Fermion theory, where the electron, hole and photon correlations are fully included. The key equation is semiconductor Bloch equation. Several ansatz can be made to solve it. The actively researched one is the BCS wavefunction [6, 34], the predicted features of which got confirmed by several experiments [132, 36, 38]. The theory along this line is currently under development by a collaborator of us. To solve the limitation (ii), one would resort to the generalized Dicke model for localized polariton[133], where the disorder effect is emphasized to extreme. The real behavior should lie between the full Fermion model and the generalized Dicke model.

5.6 Summary

In summary, we have studied the polariton nonlinearity in our SWG cavity system. Thanks to the special polarization selectivity of the top mirror of our cavity, we were able to monitor the exciton reservoir through the uncoupled TM exciton emission. The reservoir drainage caused by the polariton condensate is well observed. The

energy of the excitons shows little shift before threshold while the polariton shows a large blueshift. We can partially explain the polariton energy shifts through a coupled oscillator model by introducing a decreasing oscillator strength with a saturation density. The obtained saturation density compares well with theoretical predictions. The prominent saturation effect also suggest a modification to the polariton-polariton interaction constant g. The revised g with additional saturation term showed an excellent agreement with what we obtained in experiment. Our work demonstrated the non-negligible contribution of excitonic saturation to both polariton renormalization and interaction. The renormalized polariton dispersion affect the effective mass and interaction constant, which is crucial in the studies of polariton superfluid and polaritonic devices. In addition, the reflection measurement reveals the puzzling coexisting polaritons and Mott-transitioned excitons. The results will motivate and provide supports to the development of new theories, especially the full Fermion theory with BCS wavefunction ansatz for the electron and holes.

CHAPTER VI

Mode Engineering: Large Rabi-Splitting Cavity Using SWG

Starting from this chapter, I will present the engineering efforts toward a better SWG cavity. In this chapter, I will first introduce the vertical cavity mode engineering by using the very thin SWG. The content of this chapter has been submitted to Applied Physics Letters for publication.

6.1 Introduction

Strong coupling between semiconductor quantum well (QW) excitons and cavity photons leads to new quasi-particles – microcavity polaritons. Since their discovery [12], planar microcavity polaritons have become a fruitful ground for research on fundamental cavity quantum electrodynamics, macroscopic quantum coherence, and novel device applications [134, 135, 136]. Crucial for polariton research is a cavity with a strong vacuum field strength E at the QW plane and a high quality factor Q. A strong vacuum field leads to stronger exciton-photon coupling and thus a larger vacuum Rabi splitting between the polariton modes. A high quality factor leads to long lifetime and coherence time of the cavity photon and correspondingly the polariton. They together enable robust polariton modes, thermodynamic formation of

quantum phases, and polariton lasers with lower density threshold at higher operating temperatures [135].

Given the importance of a strong cavity field, there has been a few decades of effort to improve the cavity field strength. Most commonly used in polariton research are planar Fabry-Perot (FP) cavities formed by two distributed Bragg reflectors (DBRs), each DBR consisting of either epitaxially-grown, closely lattice-matched alloys or amorphous dielectric layers. This type of cavity can reach Q of tens of thousands in III-As based systems [137, 138], but only about a thousand for III-N [139, 140] and even lower for other material systems [141, 142]. The field penetrates many wavelengths into the DBR, hence the field strength is not optimal [143, 144]. To achieve a stronger field, different cavity structures have been developed with reduced effective cavity length, including using a metal mirror[145] and using Al-oxide [146, 147, 148] or air/GaAs DBRs [145, 149] with larger index contrast. These structures showed greater polariton splitting but unfortunately worse Q compared to AlGaAs-based DBRs; polariton lasing have not been possible in these structures. Recently, cavities using a high index-contrast sub-wavelength grating (SWG) [77] were demonstrated for polariton lasers [150]. Not only does SWG allow greater design flexibility [151, 152] and compatibility with unconventional materials, it is only a fraction in thickness compared to typical DBRs, making it promising for shorter effective cavity length. Yet the demonstrated SWG-based polariton cavity was not optimized for strong cavity field.

Here we demonstrate how to optimize these different types of cavity for the strongest field, and compare their polariton splitting, quality factors and practicality for fabrication. We show that SWG cavities may allow simultaneously stronger field and high Q.

6.2 The metrics and the system

The cavity field relevant to the exciton-photon coupling is the vacuum fluctuation field. Its strength E is normalized to the zero-point photon energy by

$$\int \epsilon(\boldsymbol{r})E(\boldsymbol{r})^2 dV = \frac{1}{2}\hbar\omega_c, \tag{6.1}$$

where ϵ is the permittivity, and $\hbar\omega_c$ is the cavity resonance energy. The integral is evaluated in the entire space with a spatial-dependent ϵ. For a planar cavity, we consider the field being confined in the z-direction but unbounded in the x and y directions. The integration is thus evaluated in a quantization volume (L_x, L_y, L_z), where L_x and L_y are set to be much larger than the wavelength, and L_z is set at some cutoff point where the field has decayed significantly ($\sim$1%).

The maximum field strength E_{max} serves as our main figure of merit for cavities designed for strong coupling. Specifically, for a QW placed at the field maximum, the vacuum Rabi splitting $\hbar\Omega$ is directly proportional to $\boldsymbol{d} \cdot \boldsymbol{E}_{max}$, for $\boldsymbol{d}$ the QW exciton dipole moment. We note that the E_{max} is closely related to the mode volume commonly used to characterize photonic crystals cavity[153, 154] as well as the effective cavity length L_c for planar cavities[143]. We choose E_{max} over L_c because the vacuum Rabi splitting is determined by not only L_c but also ϵ as $\hbar\Omega \propto (\epsilon L_c)^{-1/2}$,[144] while ϵ can vary by an order of magnitude in different cavities. Therefore the maximum vacuum field strength is the most unambiguous quantity to characterize the cavity for strong coupling. Also, we focus on high-Q cavities but do not optimize for Q. This is because for cavities designed to have sufficiently high Q, the experimentally achievable Q depends mainly on practical constrains such as chemical purity and structural integrity of the fabricated structure.

In the following, we optimize the maximum vacuum field strength E_{max} for different types of planar cavities. Based on Eq. 6.1, the E_{max} is enhanced in cavities with

(i) a tightly confined field profile $E(\boldsymbol{r})$ and (ii) materials of low refractive indices. A tightly confined field profile effectively reduces the range of integration, enhancing the field maximum. For a planar cavity, this means using the shortest possible cavity length (half wavelength) and using mirrors with shorter field penetration length. Equally important, lower refractive indices lead to higher $E(\boldsymbol{r})$, especially in the cavity layer where most of the field resides. Vacuum or air has the lowest refractive index. Although not applicable to crystalline QWs that needs mechanical support and surface protection, air-cavities can greatly enhance field strength for QWs formed by two-dimensional (2D) van der Waals materials.

We use transfer matrix method for calculations of DBR-based cavities, and rigorous coupled-wave analysis (RCWA) for SWG-based cavities. We obtain the cavity resonance from the reflection spectrum of the cavity, using the real-valued bulk permittivity ϵ_∞ for the QW layer. Then we compute complex field distribution at the resonance and normalize the field using Eq. 6.1. To include the exciton-photon coupling, we use a linear dispersion for the QW layer[68] modeled by a Lorentz oscillator[67]:

$$\epsilon(e) = n^2(e) = \epsilon_\infty + \frac{fq^2\hbar^2}{m\epsilon_0 L_z}\frac{1}{e_0^2 - e^2 - i\gamma e}, \tag{6.2}$$

where f is the oscillator strength per unit area, q and m are the charge and mass of the electron respectively, L_z is the QW thickness, e_0 is the exciton energy, and γ is the exciton linewidth. For a fair comparison of the different types of cavities, we focus on 2D half-wavelength cavities with a single QW placed at the field maximum.[1] We use III-As systems as an example, because polariton cavities of highest qualities are all based on III-As systems. The cavity is made of Al_xGaAs alloys where the different Al content gives different refraction index, with AlAs the lowest ($n = 3.02$), GaAs the highest ($n = 3.68$), and Al_xGaAs a linear interpolation ($n = 3.68 - 0.66x$). For the QW, we consider either a 12 nm GaAs/AlAs QW or a 7 nm InGaAs/GaAs

[1] In all cavities, multiple QWs can be used to enhance the polariton splitting.

QW. For simplicity and ease of comparison, we assume both to have the same exciton energy of 1.550 eV (800 nm)[150], oscillator strength of $f = 6 \times 10^{-4} \mathring{A}^{-2}$ [66] and $\gamma = 0.8$ meV.

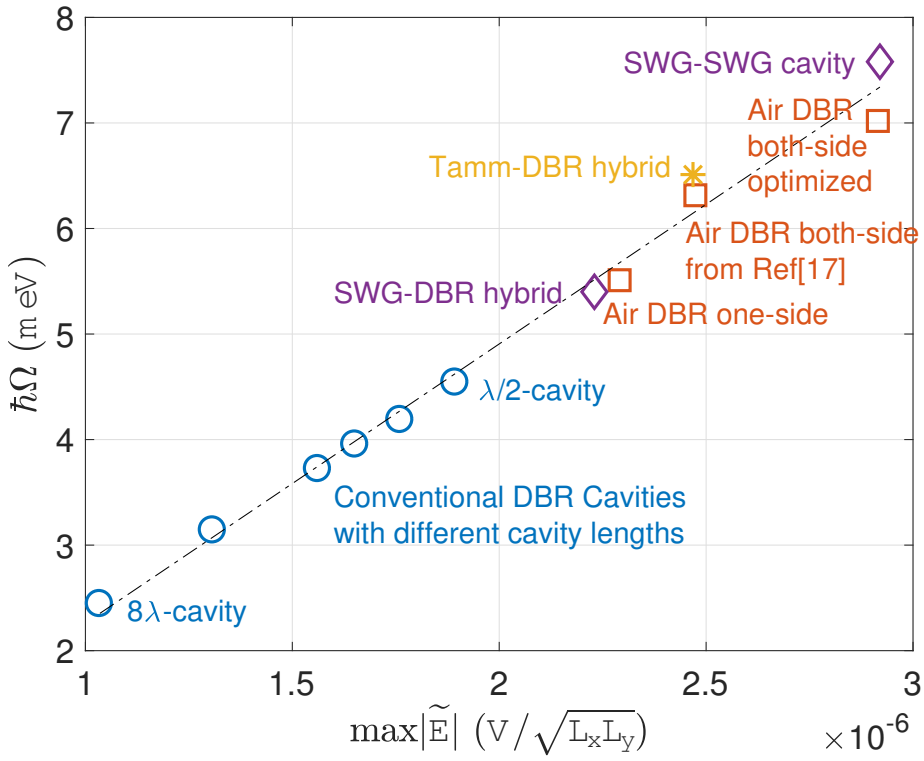

Figure 6.1: Calculated vacuum Rabi splitting $\hbar\Omega$ and maximum vacuum field strength $max|\widetilde{E}|$ for various optimized cavities. All cavities are based on III-As material system. Single QW is embedded at the field maximum. The vacuum field strength is calculated at the cavity resonance energy with QW dispersion turned off, while the Rabi splitting is measured from the two reflection dips when the QW dispersion is turned on. The dash-dotted line is a linear fit through all points.

6.3 DBR-DBR cavities

As a benchmark, we first describe the performance of the most widely used, monolithic DBR-DBR cavities. DBRs are typically made of multiple pairs of high- and low-index layers, all with an optical path length (OPL) of $\lambda/4$, for λ the cavity resonance wavelength. High reflectance is achieved by maximal constructive interference

among multi-reflections from the layer interfaces. Light decays in a distance inversely proportional to the refraction index contrast of the DBR pair. So a high index contrast is preferred for the DBR pair. For a monolithic III-As cavity with a GaAs QW, we use AlAs ($n = 3.02$) for the low-index layer and $Al_{0.15}Ga_{0.85}As$ ($n = 3.58$) for the high index layer, where 15% AlAs alloy is included instead of pure GaAs to avoid absorption at the QW exciton resonance. We consider a bottom DBR with 20 pairs on GaAs substrate, and a top DBR with 16.5 pairs, matching the reflectance of the bottom DBR. An experimental cavity Q of a few thousands can be readily achieved with this structure. More DBR pairs will lead to a higher Q, but will have negligible effect on the field confinement or the vacuum Rabi splitting.

To show the enhancement of the cavity vacuum field strength by reducing cavity length, we vary the cavity layer OPL from $\lambda/2$ to 8λ. As shown in Fig. 6.1, E_{max} increases with decreasing cavity length, and the polariton splitting scales linearly with E_{max}. This confirms the E_{max} as an appropriate figure of merit for optimizing exciton-photon coupling. The field distribution of the best-performing $\lambda/2$ cavity is shown in Fig. 6.2(a). The maximum field strength is $E_{max} = 1.89 \times 10^{-6} \mathrm{V}/\sqrt{\mathrm{L_x L_y}}$ at the QW, but the field extends many wavelengths into the DBRs due to the relatively small index contrast ($< 1.2 : 1$) of the DBR layers. The reflectance spectrum shows a polariton splitting of 4.54 meV (Fig. 6.2(b)). This conventional cavity can be fabricated by mature epitaxial growth technology as a monolithic crystalline structure with few impurities or defects. However, the requirement of lattice-matched materials, with resultantly small index contrast, leads to limited field confinement.

For the second type of cavity, we increase the index contrast of the DBR layer by replacing the AlAs layer by air or vacuum ($n = 1$), which we call an air-DBR. It can be created via selective wet etching [145, 149]. It represents the the highest possible refraction index contrast for a DBR. The GaAs QW still needs to be embedded inside an AlAs cavity (as opposed to an air cavity) to avoid detrimental surface

effects. Each material layer – both the cavity layer and the $Al_{0.15}GaAs$ layers in the DBRs, need to be sufficiently thick for mechanical stability. The experimentally realized structure used a minimum OPL of $3\lambda/4$ for each suspended layer [149], which we also adopt. Based on this, Fig. 6.2(c) shows the optimal structure we obtained. The top mirror consists of 3 pairs of $Al_{0.15}Ga_{0.85}As$/air layers. The air layer has $\lambda/4$ OPL, the $Al_{0.15}Ga_{0.85}As$ layer has $3\lambda/4$ OPL ($\sim$ 168 nm). The bottom DBR is the same as in the DBR-DBR cavity (Fig. 6.2(a)). The maximum field strength is increased to $E_{max} = 2.29 \times 10^{-6}\mathrm{V}/\sqrt{\mathrm{L_x L_y}}$. The corresponding vacuum Rabi splitting is $\hbar\Omega = 5.51$ meV, 21% larger than the conventional DBR cavity.

Further increase of the field confinement can be obtained by replacing the bottom DBR also by an air-DBR, as shown in Fig. 6.2(e). An experimentally fabricated air-DBR cavity [149] used a 7 nm $In_{0.13}GaAs$ QW embedded in a GaAs high-index λ-cavity. For this structure, we calculated $E_{max} = 2.47 \times 10^{-6}\mathrm{V}/\sqrt{\mathrm{L_x L_y}}$ and $\hbar\Omega =$ 6.32 meV (Fig. 6.1), which is 39% improvement over the conventional DBR cavity.

The structure can be further optimized by using a cavity layer of low refraction index. However, an AlAs-cavity is incompatible with the selective wet-etching required to create the bottom air-DBR; instead a Ga-rich layer is needed. Hence, for the cavity, we use a $Al_{0.4}Ga_{0.6}As$ ($n_r = 3.33$) layer of $\lambda/2$ OPL sandwiched between two $Al_{0.15}Ga_{0.85}As$ ($n_r = 3.58$) layers of $\lambda/4$ OPL, for a total OPL of λ. Similarly the $3/4\lambda$-OPL high-index DBR layer can also be replaced by such sandwich structure to improve the index contrast. The wet etching selectivity of AlAs over $Al_{0.4}Ga_{0.6}As$ has been shown to be 10^7.[155] A 12 nm GaAs QW is placed at the center of the cavity. We obtain $E_{max} = 2.91 \times 10^{-6}\mathrm{V}/\sqrt{\mathrm{L_x L_y}}$ and $\hbar\Omega = 7.02$ meV, 55% larger than conventional DBR cavity. This structure represents the best Rabi splitting in realistic DBR-based III-As cavities.

6.4 Tamm-Plasmon polariton cavities

To obtain even tighter field confinement, we consider another two types of cavities where the DBR is replaced by mirrors with shorter penetration depth – a metal mirror and a sub-wavelength grating mirror. Metal mirror, with a typical penetration depth of less than 100 nm, can be used to form Tamm-plasmon polaritons[156]. The optimal metal-DBR cavity we find consists of 45 nm thick gold layer as the top mirror (Fig. 6.3(a)), the same bottom DBR as in the conventional DBR-DBR cavity is used, and a $\lambda/2$ AlAs cavity layer slightly adjusted to compensate for the change of the reflection phase from π.

In this structure, the field decays rapidly in the gold layer, resulting in a much shorter effective cavity length (Fig. 6.3(a)), therefore a much higher vacuum field strength. We obtain $E_{max} = 2.47 \times 10^{-6}\mathrm{V}/\sqrt{\mathrm{L_x L_y}}$ [2] and $\hbar\Omega = 6.51$ meV, 43% larger than conventional DBR cavity. This is an impressive improvement considering only one side of the cavity is replaced by a metal mirror. Grossmann et al[145] additionally replaced the bottom DBR with an air DBR to further improve the vacuum Rabi splitting to about double that of the conventional DBR cavity.[3] However, the drawback of this structure is the very low cavity Q due to metal loss. The cavity linewidth is comparable to the Rabi splitting; the system remains in the intermediate coupling regime rather than the strong coupling regime (Fig. 6.3(b))[157, 145]. The large loss in metal also makes it difficult to achieve quantum degeneracy or low threshold laser.

To maintain both a high cavity Q and short cavity length, we use a III-As sub-wavelength grating (SWG) for the fourth type of cavity [77, 150]. The SWG is a thin layer of high-index dielectric grating suspended in air, acting as the high-reflective mirror (Fig. 6.4(a)).To avoid non-zero order evanescent diffraction waves entering the

[2]For strong dispersive media like metal, the energy density in field normalization equation 6.1 is modified by Eq.6.126 in Jackson, Classical Electrodynamics, 3rd edition, 2001

[3]We have not been able to reproduce the field profile or reflection spectrum shown in Ref. [145] in our simulation and instead found the 45 nm thick gold layer as the optimal for a Tamm-plasmon mirror.

cavity layer, we include a $3/4\lambda$ air-gap between the SWG and the bottom structure. The $\lambda/2$ cavity layer and bottom DBR are identical to the conventional DBR cavity as in Fig. 6.2(a). We obtain $E_{max} = 2.23 \times 10^{-6}\mathrm{V}/\sqrt{\mathrm{L_x L_y}}$ and $\hbar\Omega = 5.37$ meV, both 19% larger compared to the conventional DBR cavity and comparable to the single-sided air-DBR cavity. The advantage of the SWG-DBR cavity is its high cavity quality and simplicity in fabrication. The structure is first fabricated as a high-quality, monolithic crystal by epitaxial growth, as with the conventional DBR cavities. The SWG is then created by lithography and etching. Because the grating is the only air-suspended layer created, SWG-DBR hybrid cavity is easier to make and more robust mechanically than an air-DBR. Polariton lasing and excellent coherence properties have been demonstrated in SWG-DBR cavities [150, 158, 130], but not yet in cavities using air-DBR or metal mirrors.

6.5 SWG cavities

Tighter cavity field confinement can be achieved when replacing the bottom DBR also by an SWG. As shown in Fig. 6.4 (b), a $\lambda/2$ AlAs cavity layer sandwiched by two $Al_{0.15}Ga_{0.85}As$ $\lambda/4$ layers is air-suspended between two identical SWGs. Because of the evanescent diffraction waves from the SWGs, the field at the QW is not uniform. We record an average vacuum strength at the QW to be $2.92 \times 10^{-6}\mathrm{V}/\sqrt{\mathrm{L_x L_y}}$. The vacuum Rabi splitting is $\hbar\Omega = 7.58$ meV, 67% larger than that of the conventional DBR cavity.

The fabrication of such a double-SWG cavity is more challenging than the SWG-DBR hybrid cavity, but within reach of established fabrication techniques. The top-SWG and the rest of the structure can be fabricated separately at first, then they can be bonded together by cold welding [159] or stacked together using the micromanipulation technique successfully applied to making 3D photonic crystals[160]. Alternatively, one could make the SWGs from Si/SiO2 wafer, then do a wafer bonding

with the III-V active layer[161]. Finally we note that the SWG-based cavity may be particularly useful for coupling to 2D materials, where similar procedures of integration are already necessary. Additionally, it is possible to hold 2D material with lower index materials, further enhancing the vacuum field.

6.6 Summary

In summary, we have investigated the performance of strong coupling for several types of planar cavities. We use maximum vacuum field strength as the main figure of merit, in place of the effective cavity length or mode volume. The Tamm-Plasmon type cavity can provide $\sim$ 43% improvement with only one mirror replaced by a gold thin film. However, its very low quality factor due to metal loss limits its application. The air-DBR type cavities are shown to provide 21% (55%) improvement over conventional DBR cavities if one mirror (both mirror) is replaced with an air-DBR. SWG based cavities provide 19% (67%) improvement when one (two) SWG is used, comparable to (better than) that of air-DBR cavities. Both SWG and air-DBR cavities create diffraction-limited mode volumes and very large Rabi splittings. Among all alternative structures to conventional DBR-DBR cavities, SWG-based cavities are easier to fabricate and so far the only ones experimentally maintain high cavity quality factor and enable polariton lasing. Our findings here may guide the design of cavity systems for the research and applications of semiconductor exciton-polaritons, especially for increasing their operating temperature, lowering the density threshold for quantum phase transition and polariton lasing, and incorporating newer materials.

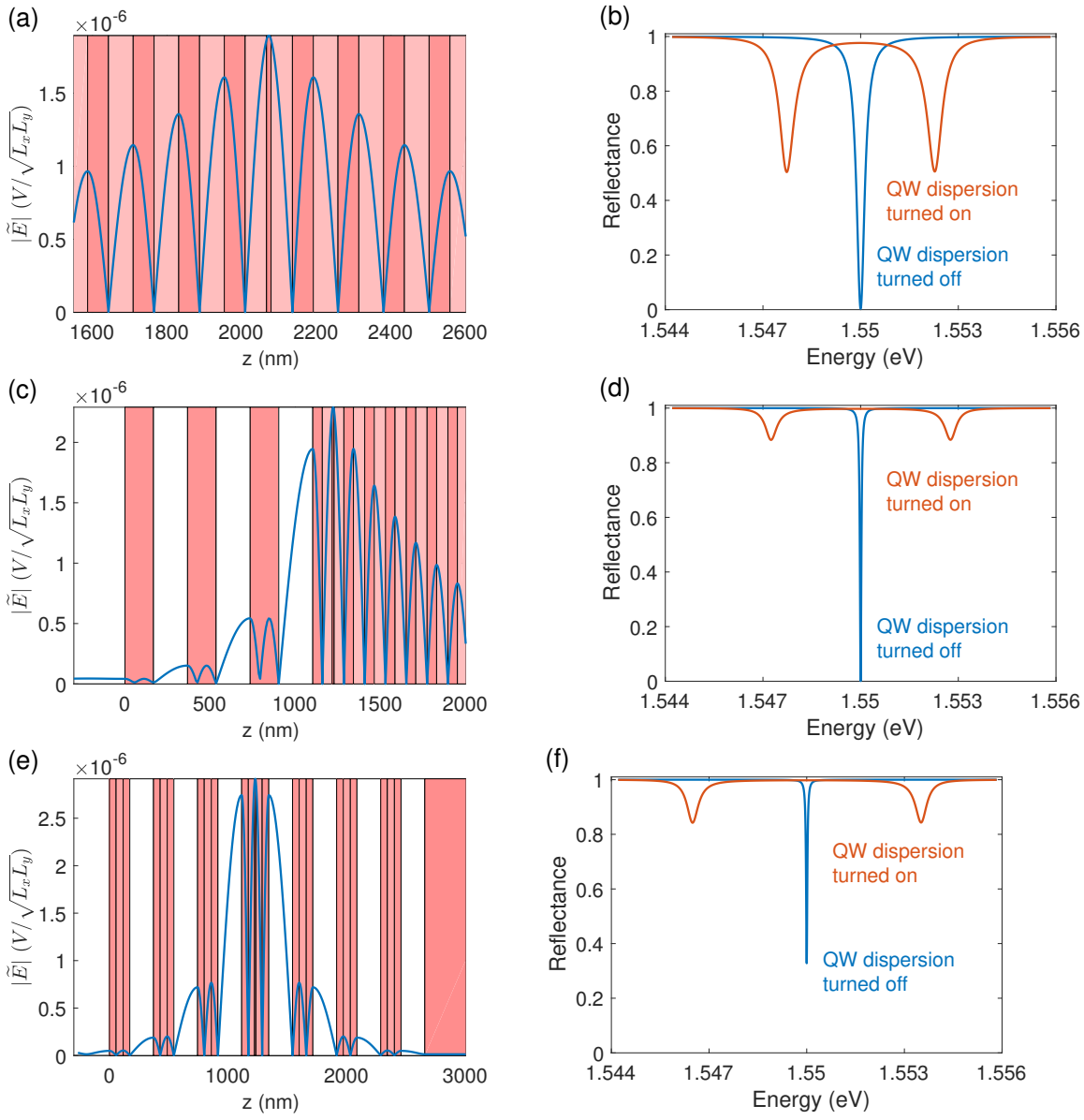

Figure 6.2: Vacuum field profile and Rabi splitting for conventional DBR cavity (a-b) and air DBR cavity (c-f). The color stripes represent different materials– red is $Al_{0.15}Ga_{0.85}As$, lighter red is the lower index AlAs, white region is air, and the thin stripe at the field maximum is a GaAs QW. All three structures sit on GaAs substrate, which is not shown in (a) and (c). The vacuum field strength has a unit of Volt/(normalization length in meters).

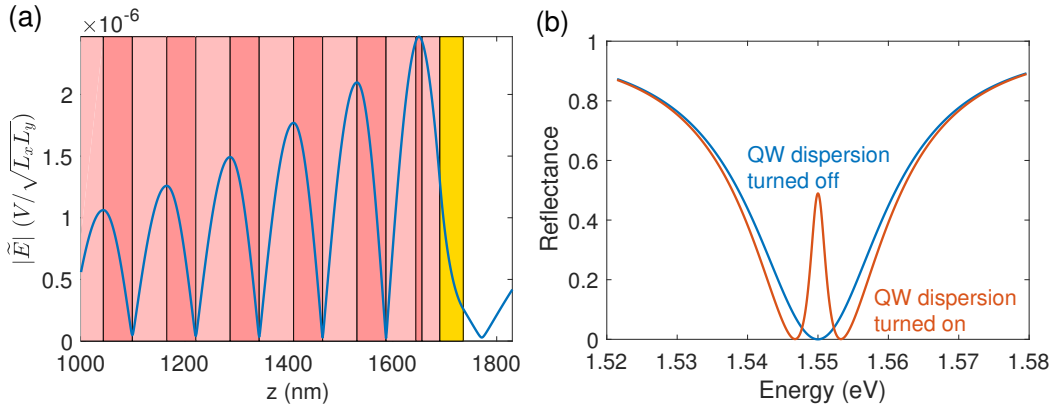

Figure 6.3: Vacuum field profile (a) and Rabi splitting (b) for Tamm-plasmon type cavity. The DBR structure is the same with previous DBR cavities. The excitation wave is launched from the substrate to top (left to right). The gold colored region represents a 45nm gold layer. Its refractive index is taken from Olmon, et al[11] for evaporated gold at 800nm. The cavity Q is around 60 inferred from the linewidth, mainly due to the loss in the metal. The polariton splitting is 6.51meV, 43% larger than conventional DBR cavity.

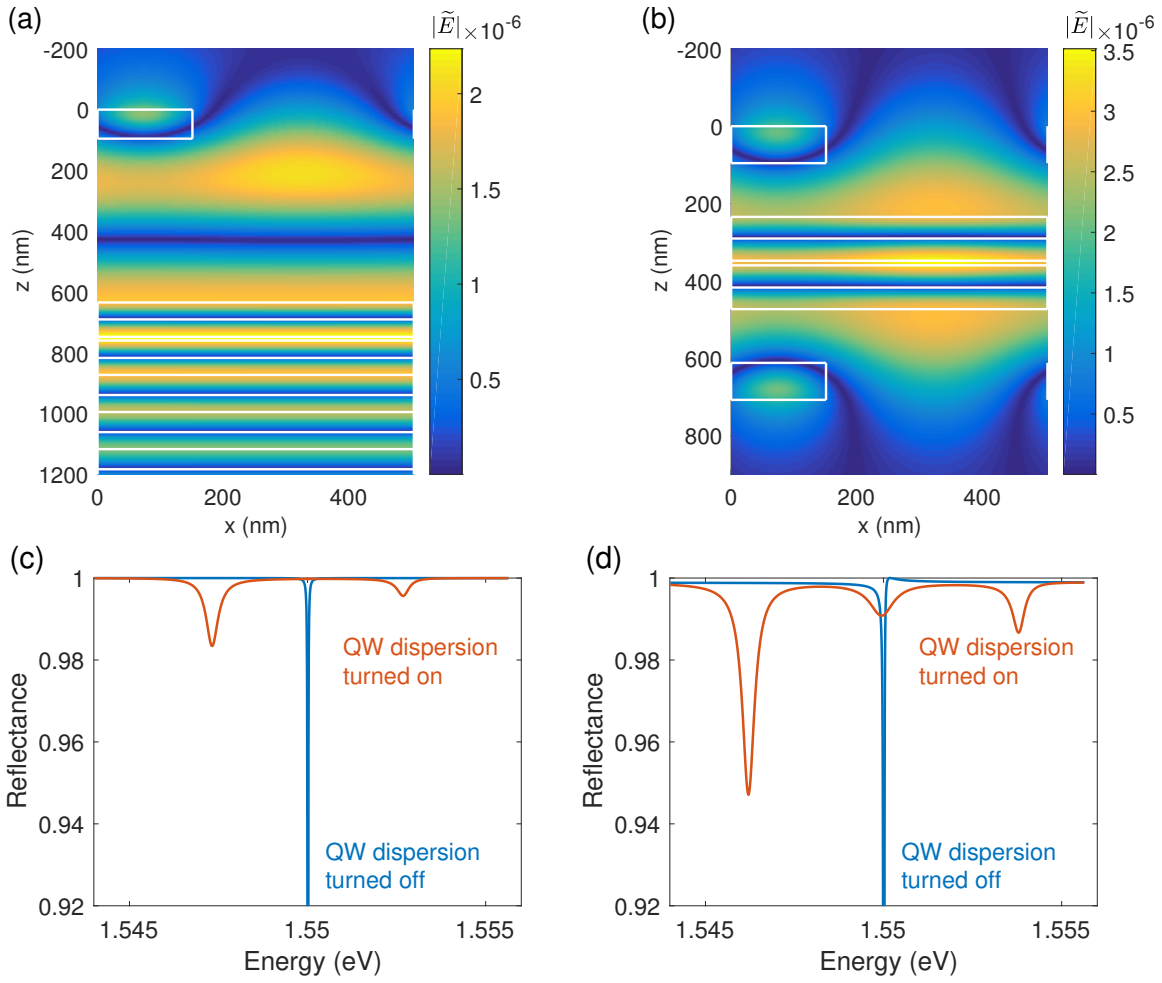

Figure 6.4: Vacuum field profile and Rabi splitting for SWG-DBR hybrid cavity (a-b) and double SWG cavity (c-d). The design parameters for the SWG are, thickness of grating 95.6nm, period 503nm, filling factor 0.3, using $Al_{0.15}GaAs$(n = 3.58), with air gap 511nm (left) and 144nm (right) between SWG and the cavity layer. Bottom DBR in the hybrid cavity is the same with conventional DBR cavity used above. The middle resonance in the reflection spectrum (d) is due to the exciton absorption of the first-order grating diffraction mode (evanescent in air but propagating in the cavity layer).

CHAPTER VII

Mode Engineering: Coupled and Quasi-1D Polariton Systems

In this chapter, I present the engineering efforts towards the lateral mode in our SWG cavity. The content of this chapter can be found in a published work[152].

7.1 Introduction: Surface Patterning Working Principle

The polariton system also provide an accessible venue for research on lattice physics [162] [39] and quantum optical circuits[23] [112] [40]. Along this line, we also construct de-coupled and couple polariton systems from the zero dimensional polariton quantum boxes.

The SWG-based polariton system not only can formulate the potential for the polariton systems, but also realize lower dimensional control. To realize the potential construction and probing an individual 0D system for a coupled-polariton system, here in this section, we introduce newly designed quasi-one dimensional SWG devices. These devices not only accomplish the effective potential control for the polariton system but also provide a 1D channel for polariton coupling.

To realize the coupling and dimensionality control for the confined polariton systems, we specifically designed surface patterns to surround the air-suspending gratings

in different devices. These patterns will create different potentials for the cavity photons, through which we achieve the control for the polariton systems. For a typical device surface pattern, it is composed of thorough-etched square holes and rectangular holes.

To create lower dimensional SWG-cavities, we first utilize the sudden change in the reflectance from the SWG region to the planar region surrounding it, which results in a large effective potential at the lateral boundaries of the SWG. To create additional potentials and to control the coupling among 0D SWG-cavities, we place through-etched long rectangular slots in the tether, which changes the boundary condition of the cavity and creates effectively potential barriers for the cavity modes. The potential is centered at the center of the slots, with its width and height controlled by the length of the slot. By arranging the positions and changing the lengths of the slots, we can create different effective potentials for the photon modes. In the strong-coupling regime, the photon potential is directly transcribed to the polaritons.

7.2 Uncoupled Polariton Systems

The first two devices have the same SWG of 7.5 μm in width and 30 μm in length, while different patterns in the tether create different potentials for the polaritons. In the first device, we create two separate 0D polariton quantum boxes by placing a pair of long slot of 8.5 μm in length, in the middle of both of the top and bottom tethers, as shown in the scanning electron microscopic (SEM) image in Fig 7.1(a). The resulting lower polariton (LP) modes were measured via spectrally resolved real space imaging, as shown in Fig 7.1(b). Two spatially separated groups LP modes were observed, with identical discrete energy levels. It suggests that the slots create a potential barrier, confining the LPs to two 0D quantum boxes on its two sides.

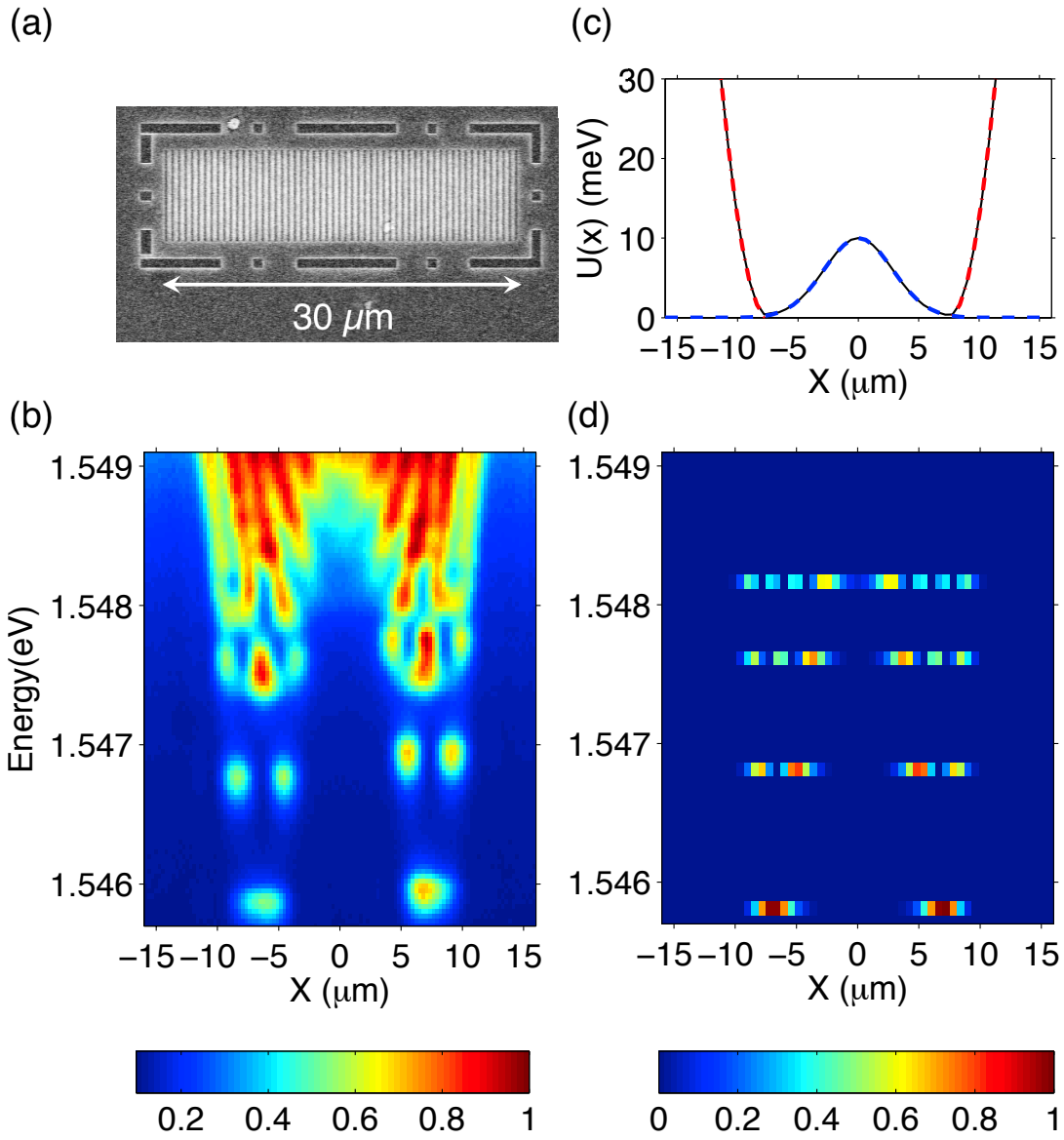

Figure 7.1: Two decoupled 0D polariton systems: (a) Device SEM image. (b) Real space spectroscopic characterization. (c) Effective photon potentials in the device. The black line − is the total potential. The blue dashed line indicates the Gaussian-shaped potential in the middle. The red dot-dashed line depicts the harmonic potential towards edges of the device. (d) Simulation results using the total photon potential.

We model the potential barriers created by the slots by Gaussian functions: $A * exp(\frac{x-x_0}{B})^2$. Here x is the position along the SWGs longer dimension measured from the center of the SWG. x_0 is given by the center of the slot. A and B correspond to height and width of the barrier, respectively, and are positively correlated with the width of the slot. For the long slot placed at the center of the wire, $x_0 = 0$, $A = 10$ meV and $B = 4$ μm. In addition, same as in Ref. [95], we model the effective harmonic potential at the two ends of the SWGs longer dimension as $U(x) = a(x-d)^2$. Here a=2meV, d=$\pm$7.2 μm, and. The total potential for the entire device is the sum of all the Gaussian barriers and edge harmonic potentials. The profile of each contributing potential and the total potential are plotted in Fig 7.1(c).

Using the total potential, we can first calculate the confined photon energy levels and the corresponding real space wave functions. Then the lower polariton energy levels can be calculated using Equation **??**. The resulting polariton energy levels and the corresponding spatial wave functions are shown in Fig 7.1(d), which match very well the experimental results in Fig 7.1(b).

7.3 Coupled Polariton Systmes

In the second SWG device, we demonstrate coupling among three 0D polariton quantum boxes, using two closely spaced, narrower and shallower potential barriers instead of a wide one at the center. We achieve this with two shorter slots, 7 μm apart, as shown in the SEM image in Fig 7.2(a).

The resulting LP modes were shown by the spectrally resolved real-space images of the PL in Fig 7.2(b). Similar to the first device, the energy levels are discrete, showing the zero-dimensionality of each constituent quantum boxes. At the same time, unlike having separate groups of LPs in the first device, LPs show renormalized energy

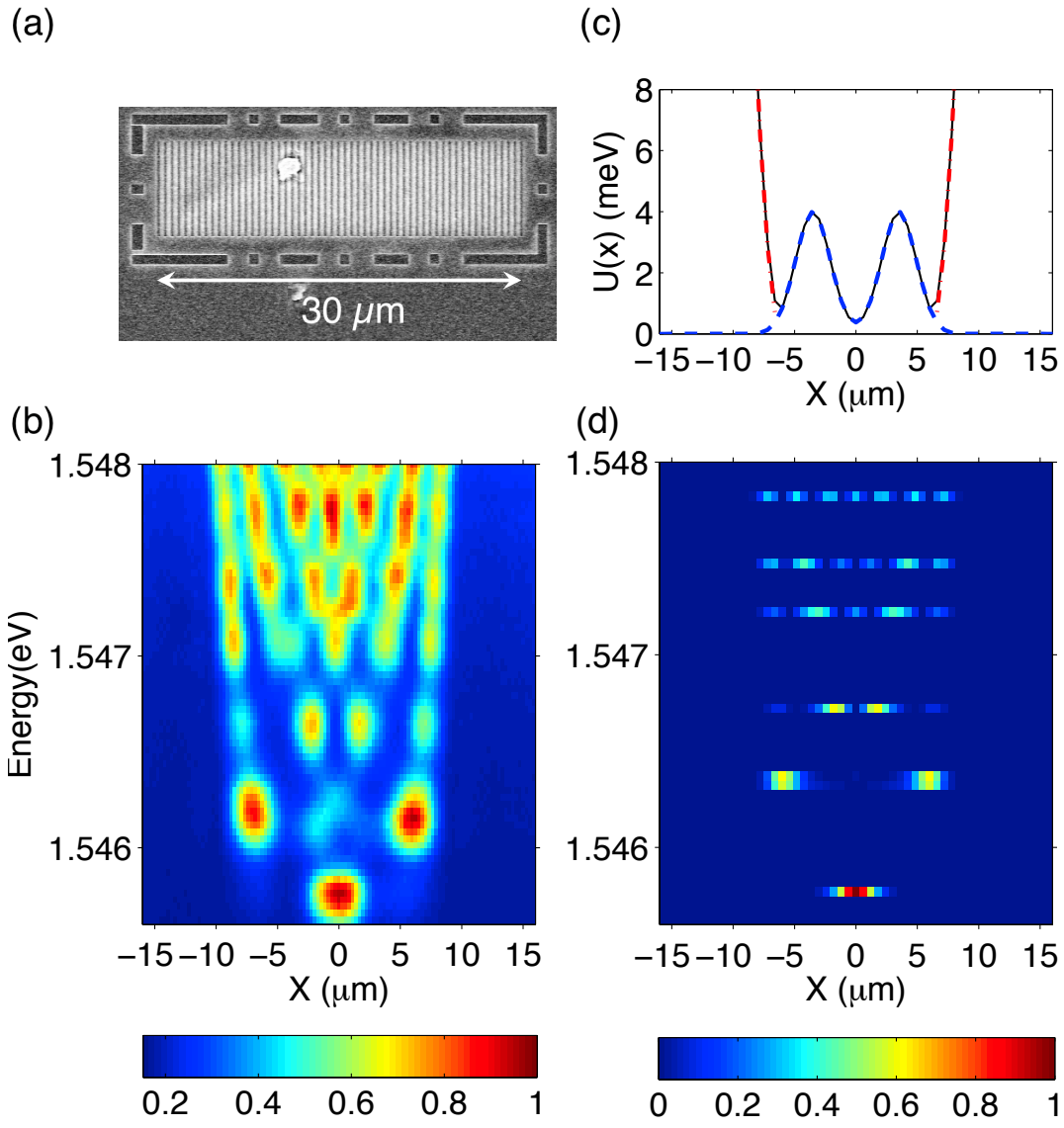

Figure 7.2: Coupled polariton systems from 0D polariton units: (a) Device SEM image. (b) Real space spectroscopic characterization. (c) Effective photon potentials: black line is the total potential; blue dashed line indicates the two shallow Gaussian barriers in the middle; The red dot-dashed line depicts the harmonic potential towards edges of the device. (d) Simulation results using the total photon potential.

levels and distinct features resulting from coupling among the three quantum boxes, or, tunneling through the barriers. For example, there exists a common ground state at a lower energy than the ground states in the first device. The spatial wavefunction of the ground state doesnt have a node and peaks at the center of the device. The first and second excited states are very closely spaced in energy, different from either three uncoupled quantum boxes or an unmodulated quantum wire.

To model the potentials, we use the same method as for the first device. The same harmonic potentials are used towards the two ends of the wire. The same Gaussian function is use for the barriers created by the slots. The two main barriers are centered at $x_0 = \pm 3.5$ μm and with a smaller height and width given by $A = 4$ meV and $B = 2$ μm. Similar to Device 1, harmonic potential at the two ends of the SWG's longer dimension is $U(x) = a(x - d)^2$, with a=2 meV, d=$\pm$6.6 μm. Each of these potentials and the total potential are plotted in Fig 7.2(c). The calculated energy levels and corresponding wavefunction distributions based on the total potential are shown in Fig 7.2(d). Due to the shallower barrier and closer spacing of the potential wells, quantum tunneling between the potential wells is prominent. The ground state and the first several excited states of the coupled system match very well with the measured results in Fig 7.2(b).

In the first two devices, the same tether pattern is used at both the top and bottom of the SWG, which create potentials symmetric around the center of the SWG along its width. A higher potential barrier would require a longer slot, limiting the number of the potential barriers or the height of them for given length of the SWG-wire. Moreover, the height and width of the barrier are both fixed with a given slot width.

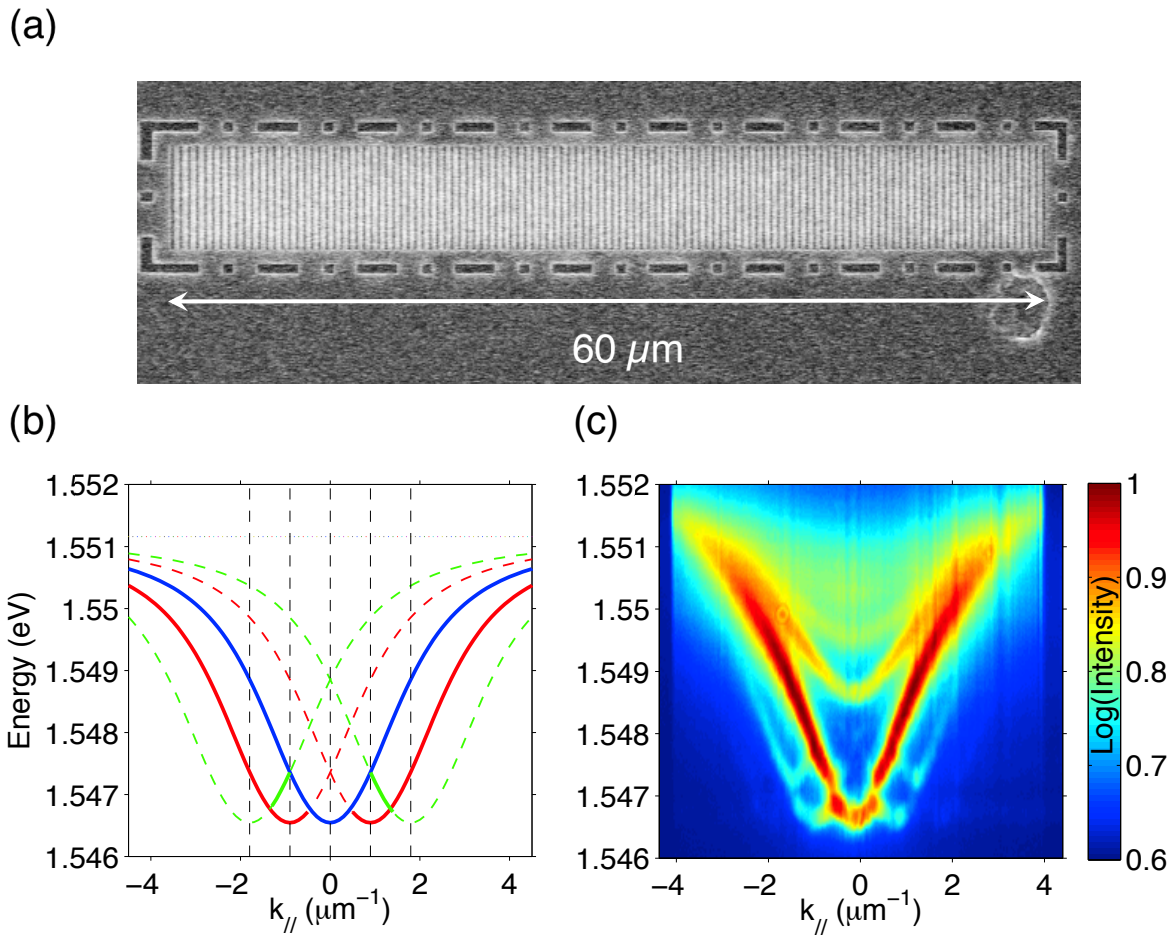

Figure 7.3: 1D polariton system: (a) Device SEM image. (b) Simulation results of dispersion relation in momentum space, based on device modulation periods of $\sim 7\mu$m. (c) Momentum space spectroscopic characterization.

7.4 1D Polariton Lattice

We also implement a quasi-1D polariton lattice by extending the two coupled 0D polariton quantum boxes in the second device to eight coupled ones. We use a long SWG wire of 60 μm in length and create the periodic potential with periodic slot-pattern in the tether. The slots have a width of 3 μm, same as in the second device, and they are placed ~ 7 μm apart. The SEM image of the device is shown in Fig 7.3(a). The energy-wavenumber dispersion of the LP modes is shown in Fig 7.3(c). Energy gaps can be identified at the edges of the 1st Brillouin zone at $\pm\pi/7\mu m^{-1}$ and $2\pi/7\mu m^{-1}$, corresponding to the lattice constant of 7μm.Up to three LP dispersion curves can be measured in the repeated-zone scheme. At higher energies, additional branches are also observed due the one-dimensional nature of the wire. In Fig 7.3(c), we calculated the LP dispersion on a lattice in the extended zone scheme. The five vertical black dashed lines indicate the minima of the dispersion branches, with a period of $\sim 2\pi/7\mu m^{-1}$. Each crossing point of the dispersion branches corresponds to the edge of the Brillouin zones and separates different energy bands. The calculated dispersions compare well with the measurement.

7.5 Polariton Device with Arbitrary Potential Shapes

In the first two devices, the same tether pattern is used at both the top and bottom of the SWG, which create potentials symmetric around the center of the SWG along its width. A higher potential barrier would require a longer slot, limiting the number of the potential barriers or the height of them for given length of the SWG-wire. Moreover, the height and width of the barrier are both fixed with a given slot width. In this asymmetric device, we show that by combining different tether patterns at the top and bottom of the SWG, additional potential barriers can be created. Moreover,

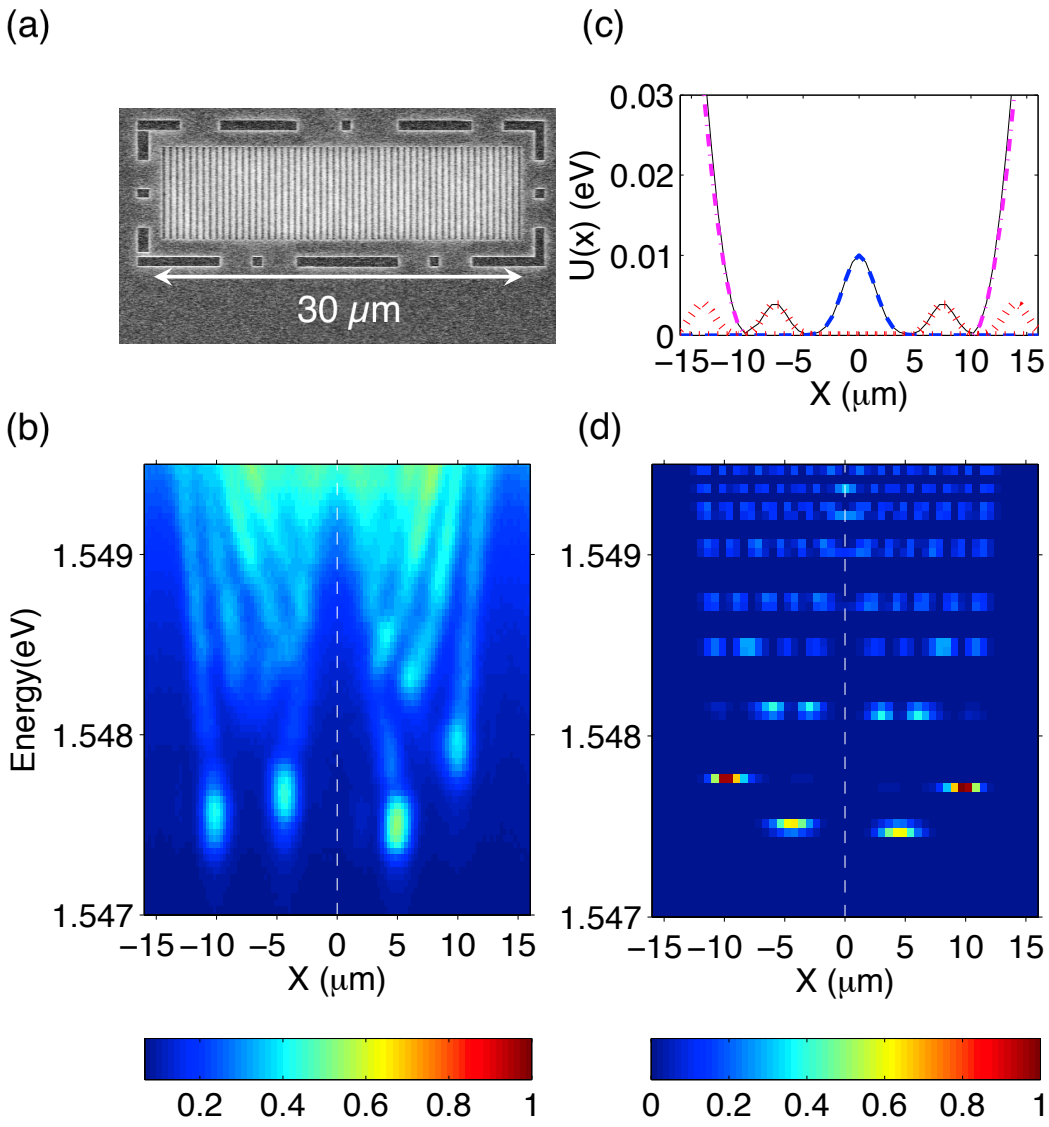

Figure 7.4: Coupling polariton system with designs of asymmetric surface patterns: (a) Device SEM image. (b) Real space spectroscopic characterization. (c) Effective photon potentials in the device. The black line − is the total potential. The blue dashed line indicates the Gaussian-shaped potential in the middle. The red dotted line is the Gaussian-shaped the potential with shorter bar-length. The magenta dash-dotted line depicts the harmonic potential towards edges of the device. (d) Simulation results using the total photon potential.

the barriers height can be adjusted independent from the width, enabling tall barriers with a narrow width. As shown in Fig 7.4(a), we place one long slot at the center of the top tether and two shorter slots at the bottom tether.

The resulting spectrally resolves spatial modes of the LPs are shown in Fig 7.4(b). The potentials are again modeled using the same method as before. Tentative potential modeling is demonstrated here. Since the bottom tether has the same pattern as in the first device, we use the same Gaussian potentials for the first device, but reducing the width B by half. Since the top two slots have the length between the longest slot in Device 1 and the shortest slot we see in Device 2, the A and B values chose to model these potentials will fall in between as well, A= 8meV and B= 3 μm. Compared to the symmetric devices 1 and 2, only one side was used, so these two values will also be reduced by half to A=4meV and B=1.5 μm. The total potential and constructing potentials are drawn in Fig 7.4(c) and simulation results are shown in Fig 7.4(d). The calculated results reproduce many of the major features of the measured results. In particular, the two spatially separated major branches on both sides of the device central axis are clearly seen. And the lowest energies match up as well.

To conclude, we have demonstrated the construction of confinement potentials for polaritons by design of the tether patterns in SWG-DBR cavities. De-coupled, coupled, and lattice polariton systems have been created. Together with the flexibility to design the SWGs themselves, such as polarization selectivity, resonance tuning, and dispersion engineering, the SWG-DBR cavities provide unique opportunities for matter-wave circuits and many body physics in open systems.

CHAPTER VIII

Mode Engineering: Dispersion Engineered Cavity Using SWG

In this chapter, I will introduce our engineering efforts towards the k-space modes of SWG cavity, or the fundamental energy dispersion. The content of this chapter can be found in a published work [151].

8.1 Introduction

The energy-momentum dispersion is a fundamental property of a photonic system. The capability to modify the dispersion using engineered photonic systems is at the heart of modern photonic technologies and the cavity quantum electro-dynamics (CQED) research. For example, dispersion determines the phase and group velocities, and, thus the propagation of the electromagnetic modes [163]. Dispersion also controls the density of states (DOS) of the photonic modes, and, thus the matter-light interactions in the system [164]. Recently, dispersion engineering has been used in manybody atomic systems to create synthetic magnetic fields [165], enabling the simulation of quantum orders in non-Abelian gauge fields. It was also proposed as a method to create exotic quantum orders in manybody photonic or matter systems [166].

Dispersion engineering has been realized using engineered photonic structures including metamaterials [167, 168, 169, 170] and photonic crystals (PhCs) [171, 172, 173]. However, metamaterials containing metal constituents suffer from intrinsic ohmic losses; 2D photonic crystals have large radiation losses for the modes in the light cone. In addition, due to the large surface-to-volume ratio of metamaterials and PhCs, active media embedded inside are prone to surface recombination. These effects limit their usage in applications requiring minimal loss or spatially extended matter-light coupling.

In this work, we demonstrate a new method to engineer the dispersions of all-dielectric 1D or 2D vertical microcavities, compatible with lossless embedment of active media. We revisit the century-old resonance condition of a Fabry-Perot cavity and demonstrate dispersion engineering by designing the angular dependence of the reflection phase of a non-conventional cavity mirror. We show that, strong angular dependence of a subwavelength grating(SWG)'s reflection phase can be achieved due to the unique symmetry properties of SWGs. As a result, photonic and polaritonic dispersions can be created with curvatures differing by many orders of magnitude. Flat or double-well shaped dispersions can also be created. Our method of dispersion engineering enables greater flexibility to control the photonic modes and matter-light interactions in widely used quantum-well and quantum-dot microcavities. It may allow, for example, change of the group velocity of the mode, enhanced Purcell effect without additional transverse confinement, and optimized carrier dynamics for polariton lasers with lower threshold. It may open a door to the creation of manybody polariton systems with unusual dispersions and quantum orders [174].

8.2 Principle of cavity dispersion engineering

The energy vs. in-plane momentum dispersion of a Fabry-Perot type cavity is governed by the angular dependence of the cavity mirrors's reflection phase. This is

shown by the round-trip phase condition for the cavity resonance:

$$\phi_1(\omega, k_\parallel) + \phi_2(\omega, k_\parallel) - 2k_{c\perp}d = 2m\pi. \tag{8.1}$$

Here ω is the angular frequency of the resonance, $k_\parallel$ and $k_{c\perp}$ are the in-plane and longitudinal wavenumbers in the cavity layer, respectively, d is the distance between the two cavity mirrors, and m is an integer. The first two terms ϕ_1 and ϕ_2 are the reflection phases of the two cavity mirrors. Eq. 8.1 uniquely determines the dispersion relation $\omega(k_\parallel)$.

Conventional microcavities use mirrors with a nearly constant phase over a wide range of angles, resulting in a rigid quadratic dispersion. Typical vertical microcavities are made of two distributed Bragg reflectors (DBRs), each consisting of multiple dielectric layers of alternating high and low refractive indices. Each layer in a DBR has an optical path length of $\lambda/4$, to maximize the reflectance at the design wavelength λ. As a result, the reflection phase of a DBR is integer times π at normal incidence and varies very slowly with increasing $k_\parallel$ [1]. For a $\lambda/2$ low-index cavity, $\phi_1(\omega, k_\parallel) \approx \phi_2(\omega, k_\parallel) \approx \pi$ and $m = 0$. Using $k_{c\perp} = \sqrt{(n_c\omega/c)^2 - k_\parallel^2}$, for small $k_\parallel$, we obtain a quadratic dispersion:

$$\omega(k_\parallel) \approx \omega_0[1 + \frac{k_\parallel^2}{2(n_c\omega_0/c)^2}]. \tag{8.2}$$

Here $\omega_0 = \omega(k_\parallel = 0)$ and n_c is the refraction index of the cavity. For an AlAs cavity, $k_\parallel^2/(n_c\omega_0/c)^2 < 0.1$ is satisfied for an incidence angle up to $\theta_0 = 44^\circ$ in vacuum. The curvature of the quadratic dispersion is determined by n_c and ω_0, with no additional tuning available.

8.3 The SWG-DBR cavity system

In contrast, we use an SWG as the cavity mirror[89, 74], which has many tunable parameters, enabling strong angular dependencies of the reflection phase and thus dispersion engineering. A schematic of a SWG-DBR cavity we propose for dispersion engineering is shown in Fig. 8.1(a). The top mirror consists of an SWG-suspended in air. The SWG has three grating parameters: its thickness (t_g), period (Λ) and duty cycle (η), as shown in Fig. 8.1(b). These parameters, together with the thickness of the air-gap beneath the SWG, can provide flexibilities in cavity design that are unavailable in DBR-DBR cavities. For example, polarization selectivity and resonance tuning have been demonstrated in vertical cavity surface-emitting lasers (VCSELs) using SWGs as top-mirrors [75, 77, 76, 175, 176]. Recently, strong-coupling and exciton-polariton lasing have been demonstrated in a zero-dimensional SWG-DBR cavity [150**?**]. These works on vertical SWG-cavities have mainly focused on modes with nearly zero in-plane momentum. Here we explore the angular dependence of the reflection phase of the SWG to demonstrate the unique capability of dispersion engineering in an SWG-based cavity.

Unlike from a DBR, reflection from the periodic SWG structure is produced by the scattering between the lateral modes inside the SWG and Floquet-form diffraction modes outside [9, 177, 10].

8.4 Physics Origin of Strong Angular Dependence of SWG's Reflection Phase

The lateral modes of an SWG is therefore the key to understand its reflection phase. We adopt the waveguide-array (WGA) modes formulation, which was introduced in [10] to explain intuitively the high reflectance of the SWG at normal

[1]See Supplementary Information I: Comparison of a DBR and an SWG's reflection phases at [url]

incidence. Below we generalize the work in [10] and derive the WGA modes in SWGs of arbitrary thickness in the general case of oblique incidence. We will show that, due to symmetry properties of the grating, the dispersion of the WGA-modes could shift considerably with the incidence angle, leading to large changes in the reflection phase.

8.4.1 WGA Modes

We treat the SWG as a waveguide array with the z-axis as the propagation direction, as shown in Fig. 8.1(b). It is periodic in the x-direction and translationally invariant in the y-direction. We focus the discussion on the case of an incident plane wave propagating in the x-z plane with an oblique angle θ_0 from z-direction. For a WGA mode with a transverse-magnetic (TM) polarization as labeled in Fig. 8.1(b), the lateral mode profile $H(x)$ and propagation constant β are determined by the eigenvalue equation,

$$(\frac{\partial^2}{\partial x^2} + n^2(x)\frac{\omega^2}{c^2})H(x) = \beta^2 H(x), \tag{8.3}$$

where $n(x)$ is the refractive index. Because of the periodicity of $n(x)$, the eigenmode can be expressed in the form of Bloch waves,

$$H(x) = e^{ik_x x}u_n(x),$$

where $e^{ik_x x}$ is the Bloch phase factor, k_x is the in-plane wavenumber of the incident wave: $k_x = \omega/c \sin\theta_0$, $u_n(x)$ is a periodic function, and the subscript n denotes the discrete mode number. Given ω and θ_0, we can solve for the eigenvalues β_n^2 and obtain

the $\omega - \beta$ dispersion of the WGA-modes through [2]:

$$\begin{aligned} 2n_b^2 k_a k_b(\cos k_a a \cos k_b b - \cos k_x \Lambda) \\ -(n_b^4 k_a^2 + k_b^2)\sin k_a a \sin k_b b = 0. \end{aligned} \tag{8.4}$$

Here n_b is the refractive index of the grating bar, a and b are the widths of the air and bar regions, and $k_{a,b}$ is the transverse wavenumber in the air or bar region, determined by $k_{a,b} = \sqrt{(n_{a,b}\omega/c)^2 - \beta^2}$. An example of a WGA mode dispersion is shown in Fig. 8.1(c).

In the case of normal incidence (blue lines), the incident wave matches the reflection symmetry of the grating about the center of the grating bars. Correspondingly, $TM_{0,2,4,...}$ modes have the same symmetry and thus can be excited, while the $TM_{1,3,5,...}$ modes have the odd symmetry and thus cannot be excited.

In the case of oblique-angle incidence, the incident plane waves no longer has the reflection symmetry, and thus the odd-order modes can also be excited. Avoided crossings between the odd-order and even-order modes lead to significant shift of the mode dispersions, as illustrated in Fig. 8.1(c).

8.4.2 The Connection between WGA Modes and SWG Reflection

Reflection from an SWG with a finite thickness t_g can be understood as resulting from the interference of WGA modes reflected from both the top and bottom SWG-air interfaces. For a given WGA, for example the WGA used in Fig. 8.1(c), we can visualize the dependence of the reflection on t_g using t_g-ω maps of the reflectance and reflection phase, as shown in Fig. 8.2.

At normal incidence, for each of the WGA mode in Fig. 8.1(c), the SWG forms a Fabry-Perot resonator when the approximated round-trip phase condition $\beta t_g = m\pi$ is satisfied, where m is an integer [178]. We mark the corresponding $t_g - \omega$ values in

[2] See Supplementary Information II: Derivation of the dispersion of WGA modes at [url]

Fig. 8.2(a)-(b) with white dashed and dash-dotted lines for the TM_0 and TM_2 modes, respectively. The reflectance is nearly zero around these lines and the reflection phase changes by π across the lines, which are signatures of Fabry-Perot resonances. Naturally, high reflectance region exist only between these lines, when two WGA modes co-exist and produce nearly perfect destructive-interference at the output plane of SWG [10, 179].

8.5 Examples of Dispersion Engineering

At oblique angles, the appearance of the odd-order WGA modes leads to large shifts of the WGA modes, which manifests as large shifts of the reflectance and phase patterns on the $t_g - \omega$ maps. An example is shown in Fig. 8.2(c)-(d) for $\theta_0 = 30°$. Consistent with the $\beta - \omega$ diagram (Fig. 8.1(c)), the Fabry-Perot resonance lines originated from the TM_0 mode barely move, while those from the TM_2 mode move toward lower frequencies. The high reflectance regions, as well as the phase in these regions, move with those "grid lines". For a certain SWG in the high-reflectance region, for example the point marked by a white star in Fig. 8.2, the reflection phase could become very different at oblique incidence angles.

Now we show a few examples of dispersion engineering using SWGs. Two examples of SWGs are shown in Fig. 8.3(a), whose reflection phases change significantly with the incidence angle but in opposite ways. SWG1's reflection phase increases by 0.35π from $\theta_0 = 0°$ to 22°, while SWG2's decreases by 0.25π. In comparison, the reflectance phase of the DBR mirror changes by 0.03π.

When using SWG1 and SWG2 as the top mirrors of SWG-DBR cavities, the cavity dispersion also changes drastically from that of the DBR-DBR cavity. As shown in Fig. 8.3(b), the SWG1-DBR cavity has a much steeper dispersion. Its resonance energy increases to 20 meV above the DBR-DBR cavity's resonance at $\theta_0 = 20°$. The SWG2-DBR cavity, on the other hand, features a nearly flat dispersion up to

$k_{\|} \sim 2\ \mu\text{m}^{-1}$, or $\theta_0 \sim 15°$.

If the bottom DBR is also replaced by an SWG [3], the round-trip phase change is doubled, giving more tuning of the cavity dispersion. Fig. 8.3(c) shows that the dispersions of the SWG1-SWG1 cavity becomes even steeper, while the dispersion of SWG2-SWG2 cavity reverses the sign and becomes negative. Moreover, dispersions of exotic shapes can also be created, such as the one shown in Fig. 8.3(d), which features a double-well shape.

These special dispersions are also robust against small variations in the grating parameters and thus are achievable with present fabrication technologies [4]. We consider variations in the thickness t_g by ± 5 nm due to errors in the epitaxial growth, and in the period Λ and bar width $\eta\Lambda$ by ± 2 nm due to the resolution of electron-beam lithography. For the SWG1-DBR cavity, its effective mass m^* changes by less than 13%; hence the steep dispersion is well maintained. For the SWG2-DBR cavity, designed to have a flat dispersion, the effective mass is reduced by 4-folds with 2 nm increase in $\eta\Lambda$, but remains heavier than that of the DBR-DBR cavity. The variations due to the e-beam resolution can be further reduced by using e-beam dose matrix to create SWGs with slightly varying Λ and η. For the SWG3-SWG3 cavity, its resonance changes by less than 0.3 meV, much less than the well-depth of ~ 4 meV; hence the double-well shape is robust against the fabrication errors.

Since dispersion is a fundamental property of a photonic system, such tunability of the dispersion may enable many novel applications. For example, it may be used to control the propagation of light, since the group velocity of the photon is proportional to $d\omega/dk$. A steeper or shallower dispersion leads to faster or slower propagation of light. A nearly flat dispersion may enable slow light and storage of light in the cavity. Changing the dispersion also changes the spontaneous decay rate of excitations

[3] For possible ways of fabricating SWG-SWG cavity, refer to [77, 161, 160]

[4] See Supplementary information III: Fabrication Error Tolerance Analysis at [url], which includes Refs.[180, 181, 182]

enclosed inside the cavity via Purcell enhancement or suppression [183]. The Purcell factor is proportional to the energy density of state (DOS) of photons, which in turn depends on the the effective mass $m^* \equiv \hbar^2(d^2E/dk^2)^{-1}$ of the cavity modes, or, the curvature of the dispersion curve. A steep dispersion will suppress spontaneous emission, while a flat dispersion would lead to divergent DOS and a very high Purcell enhancement. The SWG2-DBR cavity, for example, has an effective mass $m^* \approx -20 \times 10^{-5} m_e$, more than 6 times heavier than the DBR-DBR cavity's effective mass of $m^* \approx 3 \times 10^{-5} m_e$. It thus may allow a Purcell enhancement of 6-fold compared to a planar DBR-DBR cavity.

The proposed cavity structure can also be used in polariton systems to control the properties of polariton condensates and lasers [135, 184], and to create novel manybody systems. Unique to the proposed cavity, it simultaneous allows lossless integration of active media in the cavity layer and a high cavity quality factor due to the high reflectance of the SWG. A zero-dimensional polariton laser was recently demonstrated in a SWG-DBR cavity [150] with a cavity quality factor of a few thousands. All the SWGs shown in Fig. 8.3 are optimized for high reflectance at normal incidence, giving cavity $Q > 10^4$. At oblique angles, their reflectance vary, but the cavity Q remains above 10^3 up to $\theta = \pm 20^\circ$ [5]. Hence the strong-coupling regime should be readily reached when multiple QWs are placed at the anti-nodes of these high-Q cavities [12].

In the strong-coupling regime, the cavity dispersion is directly transcribed to the polariton's [6]. Changing the effective mass of the polariton, independent from changing the exciton fraction in the polariton mode, would allow one to control the dynamics

[5] See Supplementary Information IV: Angular dependence of the SWG-cavities' quality factors at [url]

[6] The effective mass of the lower polaritons (LPs) is given by $m_{LP}^{-1} = |X|^2/m_{exc} + |C|^2/m_{cav}$, where the X and C are Hopfield coefficients representing the exciton and cavity photon fractions in a LP [185], and m_{exc} and m_{cav} are the effective masses of the exciton and cavity, respectively. Since $m_{exc} \sim 10^4 m_{cav}$, $m_{LP} \approx m_{cav}/|C|^2$. Tuning of the photon dispersion thus directly tunes the polariton dispersion.

and condensate formation. Polaritons systems with a lighter effective mass without reduced exciton fraction, such as in the SWG1-DBR cavity, may achieve a higher phase space density at lower excitation densities. They may enable polariton lasers at an even lower threshold than demonstrated in DBR-DBR cavities [186, 139, 141, 187], and may facilitate the BEC-BCS crossover transition [188, 189, 190]. On the other hand, polaritons with a heavy effective mass without reduced photon fraction, such as in the SWG2-DBR cavity, may allow rapid thermalization of polaritons while maintaining robust coherence. That may facilitate the formation of equilibrium quantum phases in polaritons. Tuning the polariton dispersion also tunes its group velocity, enabling, for example, faster polariton transport within its short lifetime, or slow light and slow polariton delay lines in optical and polaritonic circuits [191]. Finally, the flexibility to create dispersion of unusual symmetries may open a door to novel physics. The double-well dispersion in the SWG3-SWG3 cavity may show spontaneous symmetry breaking when particles relaxes from the meta-stable zero-k state to the two degenerated ground states. It may also allow the observation of Josephson effect in momentum-space [192] and may be extended to create system with artificial magnetic fields and topological states [174, 166].

8.6 Conclusion

In short, we showed how to utilize the large angular dependence of reflection phase of SWGs to engineer the dispersion of a vertical cavity. The cavity can retain a high quality factor and is compatible with lossless integration of active media. The curvature of the dispersion of SWG based cavities can be tuned by several orders of magnitude. Even flat, inversed, or double-well shaped dispersions can be created. Such flexibility in dispersion engineering may benefit many research areas such as Purcell enhancement in 2D structures, polariton-based lasers and quantum circuits, and exotic quantum phases in polaritons.

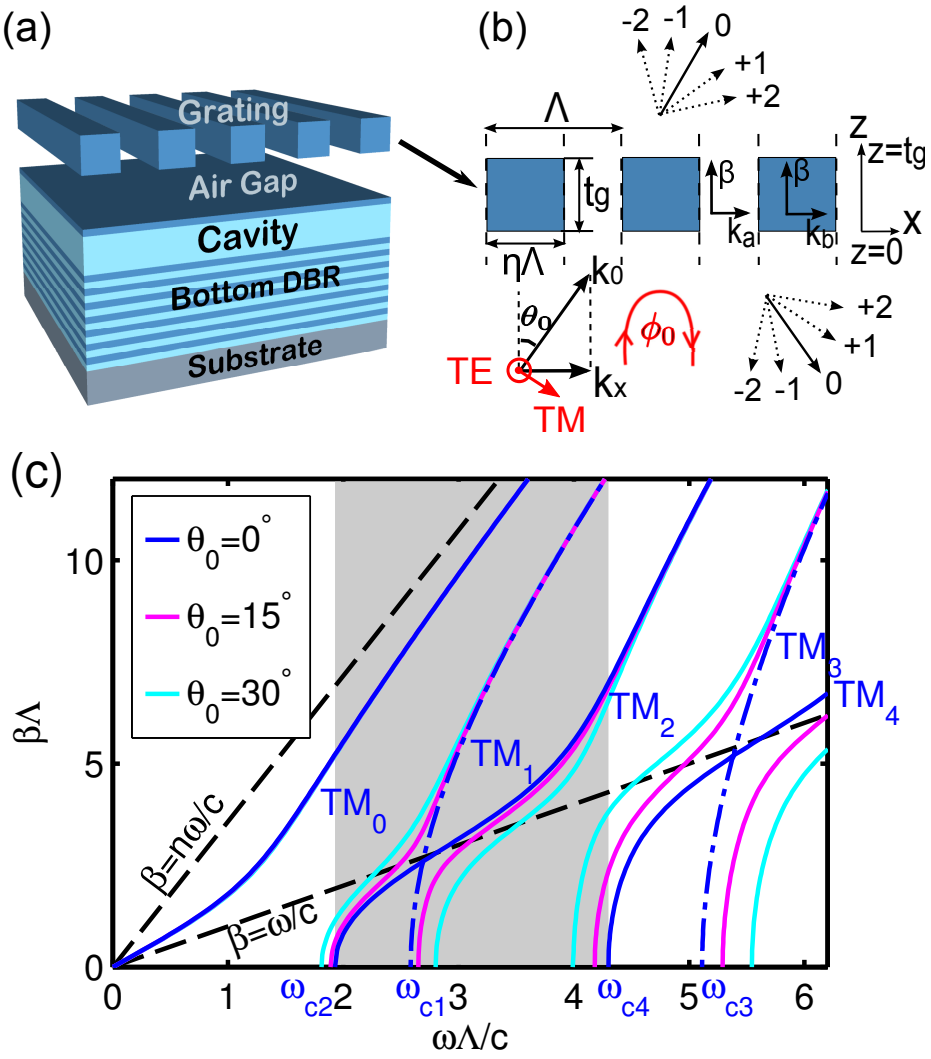

Figure 8.1: (a)Schematic of an SWG-DBR hybrid vertical cavity. The SWG followed by an air-gap and one high-index DBR layer comprise the top mirror. We use $Al_{0.15}Ga_{0.85}As$ (refractive index n_r=3.58) for the grating bars and high-index DBR layers, and AlAs (n_r=3.02) for the low-index DBR and cavity layers. (b) Cross section of an SWG and the wavevectors inside and outside the SWG. The SWG is treated as a WGA between input plane $z = 0$ and output plane $z = t_g$. The light outside the WGA is the superposition of diffraction modes, with only the zero-order mode propagating for an SWG and the higher-order ones evanescent. ϕ_0 is the reflection phase of the zero-order wave. (c) The $\beta - \omega$ dispersions of the TM WGA-modes in an SWG with a duty cycle $\eta = 65\%$, for incidence angles of 0° (blue line), 15° (pink) and 30° (cyan). Dash-dotted lines mark modes that cannot be excited. The zeroth WGA-modes at different angles almost overlap with the TM_0 mode. The higher modes shift with the incidence angle, leading to large changes in the reflection phase. The gray shade marks the dual-mode regime at normal incidence. The black dashed lines are the dispersions of light in homogeneous air and grating-bar dielectric medium.

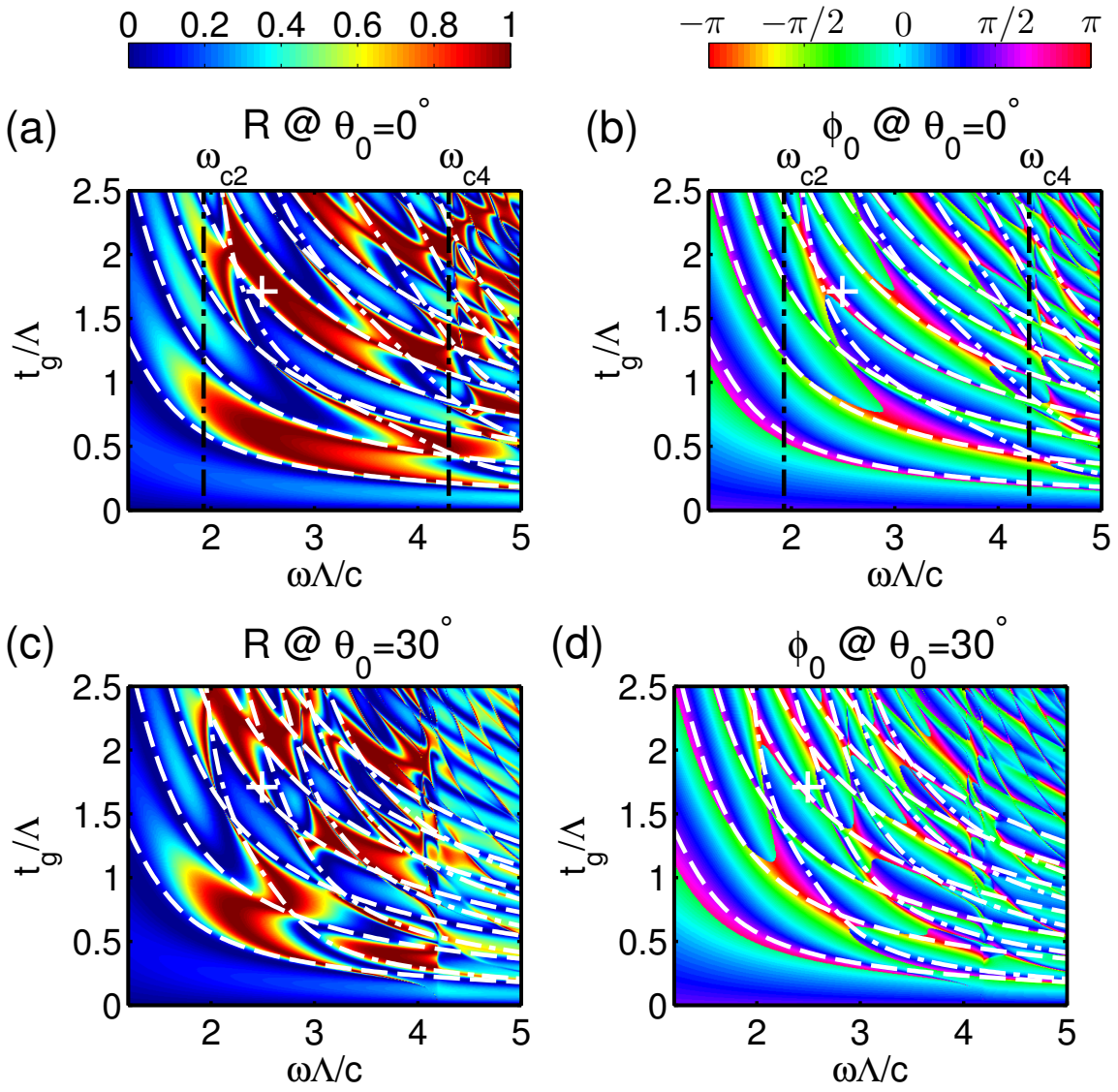

Figure 8.2: $t_g - \omega$ maps of the reflectance ((a) and (c)) and reflection phase((b) and (d)) of a SWG with $\eta = 65\%$ for the TM polarization, under normal incidence ((a) and (b)) and $\theta_0 = 30°$ oblique incidence ((b) and (d)). The black dash-dotted lines in (a) and (b) show the dual-mode regime defined by ω_{c2} and ω_{c4} obtained in Fig. 8.1(c). The dispersions of the dual WGA modes are plotted as the two sets of white dashed and dash-dotted lines in all four figures, using the approximated Fabry-Perot resonance condition of $\beta t_g = \pi$. These lines overlap well with the zero-reflectance (blue) stripes in (a) and (c). Broadband high-reflectance regions (red) can be found between those lines. Each point on the figure corresponds to one SWG design. An example is marked by the white '+' symbol, which has a phase shift of $\sim 0.4\pi$ over 30° while maintaining high-reflectance (> 0.995). The large phase shift is caused by the large WGA-mode shift, as seen by comparing the dash-dotted white lines in (b) and (d).

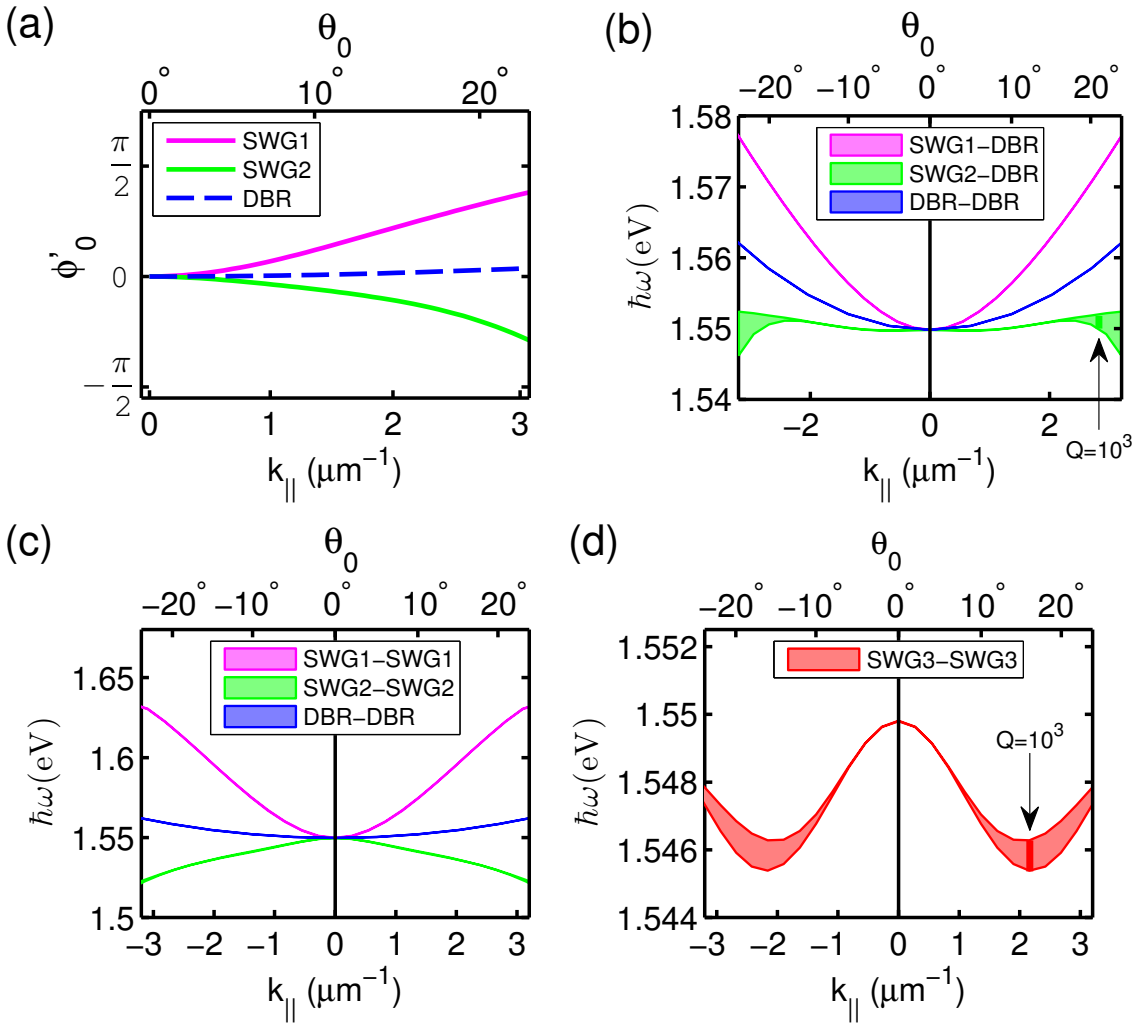

Figure 8.3: (a) Comparison of the angular dependence of the reflection phase of two SWGs with a DBR. ϕ_0' is the shifted reflection phase that starts with zero at normal incidence. (b) Energy dispersions of cavities with the SWGs and DBR as in (a) as the top mirror and a bottom DBR with 30 $\lambda/2$ pairs. The linewidths of the cavity resonances $\delta(\hbar\omega)$ are shown as the shades, to indicate the quality factors of the cavities $Q = \omega/\delta\omega$. The linewidth corresponding to $Q = 10^3$ is marked. The curvature of dispersion is proportional to the effective mass defined as $m^* \equiv \hbar(d^2\omega/dk^2)^{-1}$. We obtain at $k_{\|} \sim 0$ an effective mass $m^* \approx 3 \times 10^{-5} m_e$ for the DBR-DBR cavity, where m_e is the mass of an electron. In comparison, $m^* \approx 1 \times 10^{-5} m_e$ for SWG1-DBR, $m^* \approx -20 \times 10^{-5} m_e$ for SWG2-DBR. (c) Energy dispersions of SWG1-SWG1 and SWG2-SWG2 cavities compared to the DBR-DBR cavity, showing more substantial tuning of the dispersion than SWG-DBR cavities. At $k_{\|} \sim 0$, we obtain $m^* \approx 0.3 \times 10^{-5} m_e$ for SWG1-SWG1, and $m^* \approx -0.6 \times 10^{-5} m_e$ for the SWG2-SWG2 cavity. (d) A double-well shaped dispersion for TM-polarized light in the SWG3-SWG3 cavity. The materials used in the cavities are given in Section 2. All dimensions are scaled to give a resonance of 1.55 eV at normal incidence. The structural parameters are as follows: SWG1: Λ=539 nm, t_g=350 nm, η=0.31, TE polarization. SWG2: Λ=328 nm, t_g=557 nm, η=0.65, TM polarization. SWG3: Λ=300 nm, t_g=584 nm, η=0.62, TM polarization.

CHAPTER IX

Conclusion and Future Work

9.1 Conclusions

This thesis is motivated by the exciting new physics in the field of exciton-polaritons and the need of a practical microcavity system to confine and manipulate polaritons. Along this line,

I have demonstrated a promising microcavity platform that can be engineered for exciton-polaritons research. A single layer sub-wavelength gratings (SWG) has been used to replace the bulky and rigid DBR to be the top cavity mirror. The SWG was shown to be as good as the DBR in terms of reflectance and stop-band-width. Compared to major competitor cavity systems based solely on DBR, our cavity has its advantages such as fully protected QWs compared to the deep-etched micro-pillars, fast iteration speed and electro-mechanical tuning capability compared to the mesa-embedding during the sample growth. Our system was also demonstrated with other unique benefits such as pre-defined linear polarization and photon dispersion tuning.

Lateral confinement of polaritons was demonstrated through SWG size control and patterning. The zero-dimensional (0D) device was demonstrated in Chapter IV in which full three-dimensional confinement was achieved. Coupled polariton 0D boxes and quasi-1D polariton lattice were also demonstrated (Chapter VII, through device surface patterning. These confined low-dimensional systems are proof-of-concept of

the fully controlled, single-cell accessible polariton circuits, which is crucial for realizing quantum simulators and high-speed photonic circuits.

To study new many-body physics, quantum coherence needs to be established first. Therefore, polariton condensation (or lasing) was demonstrated through the zero dimensional system (Chapter IV). The signature nonlinear increase of the emission intensity, continuous energy blue shifting, and the decrease in linewidth at lasing were all clearly observed from the device.

New physics in the high density nonlinear regime of our SWG polariton system was discovered. By utilizing the polarization anisotropy of the SWG, we were able to directly monitor the exciton reservoir together with the polariton condensate, which is not possible in conventional DBR systems. Contrary to the common belief that polariton blueshifts is primarily due to the excitonic Coulomb interaction, the excitons in our system do not exhibit the same blueshift. The saturation of exciton oscillator strength has to be considered to explain the energy shifts from both excitons and polaritons. The saturation pair density, as carefully calibrated through the exciton emission, agrees well with theory. Further, the discrepancy between the saturation model and the polariton blueshift after lasing threshold (near Mott-density) is found to be highly non-trivial. It suggests polaritons may not be well described by the normal Bosonic theory with phenomenological interaction constant. A first-principle Fermionic theory is in development to explain our data. This ongoing work points to the actively researched polariton BCS state and the photon mediated binding between electrons and holes. Our unambiguous high-density experiments can provide valuable evidences toward clarifying the controversies in the BEC to BCS crossover for not only polariton systems, but any composite boson systems.

To make our system more robust and suitable for more new physics, we performed mode engineering for our SWG devices. In Chapter VI, specially designed SWG-DBR and SWG-SWG cavities were shown to significantly reduce the effective cavity

length (mode volume) of the system, therefore improve the Rabi splitting when it is coupled to QW exciton. It helps maintain a robust strong coupling even at room-temperature with GaAs QWs. The design principles can be well extended to the heated research area of 2D material based polaritons. In Chapter VIII, we also showed how to engineer the photon dispersion using the large angular dependence of reflection phase of SWGs. The curvature of the energy dispersion can be tuned by several orders of magnitude. Even flat, inversed, or double-well shaped dispersions can be created. Such flexibility in dispersion engineering may benefit many research areas such as Purcell enhancement in 2D structures, polariton-based lasers and quantum circuits, and exotic quantum phases in polaritons.

In one sentence, we have created a new system, SWG cavity, and studied some new physics in a many-body polariton system. SWG cavity 2.0 is on its way.

9.2 Future Work

This thesis only shows the tip-of-iceberg of what the SWG cavity system can achieve. Here I list a few directions that I hope new students in the group or other groups to carry on.

For the cavity design side, one promising structure is to use a recently emerged zero-contrast grating. It requires no air gap between the cavity and the grating. The grating is sitting on the cavity layer, removing the possibility of grating bending and collapsing. This will help to make truly 2D polariton systems, arbitrary-long 1D systems and more effectively coupled systems. It will make quantum simulator and polariton circuits easier to achieve. Gratings with 2D periodic symmetry and chiral symmetry may also worth looking into. They may create more exotic quantum phases of polaritons.

For the experiment side, the nonlinear regime of SWG polariton system is worth more thorough studies. The sample is currently easy to be damaged by high pumping power, probably due to the heat deposited in the air-suspended grating. If applying the right chopping (pulsed experiment) or making airgapless version of the SWG cavity as mentioned before, the chances are we can push into the very high density region, where optical gain can be observed. Actually, I already observed the gain in several experiments, although at the price of destroying some of the best devices. This could help test the polariton BCS theory at the whole density regime, which is an active area for polariton research.

APPENDICES

APPENDIX A

Rate Equation Modeling

A.1 Determine Average Exciton Lifetime via Simple Rate Equation

From Chap. 5, the average reservoir exciton lifetime τ_X should in principle be different from the radiative lifetime τ_X^r of the TM excitons we measured. Since the excitons with in-plane momentum exceeding the light momentum actually don't decay, their lifetimes should be the relaxation time into the lower energy states. To model this process, we roughly consider three groups of particles– e-h plasmas created by the pump, large-k exciton states outside the light cone and the small-k states inside the light cone. The population of the three states is expressed as N_{plasma}, $N_{large-k}$ and $N_{small-k}$ respectively. The relaxation process can be described by the

following rate equations,

$$\frac{dN_{plasma}}{dt} = P - \frac{1}{\tau_{plasma}}N_{plasma} - \frac{1}{\tau_{LO}}N_{plasma},$$
$$\frac{dN_{large-k}}{dt} = \frac{1}{\tau_{plasma}}N_{plasma} - (\frac{1}{\tau_{LA,X-X}} + \frac{1}{\tau_{NR}})N_{large-k},$$
$$\frac{dN_{small-k}}{dt} = \frac{1}{\tau_{LA,X-X}}N_{large-k} - \frac{1}{\tau^{back}_{LA,X-X}}N_{small-k} - \frac{1}{\tau^{r}_{X}}\alpha_{bright}N_{small-k},$$

where τ_{plasma} is the radiative recombination time of the e-h plasma, which is usually on the order of $\sim 1\,\mathrm{ns}$. τ_{LO} is the longitudinal optical phonon emission time, on the order of 1ps. $\tau_{LA,X-X}$ is the process of longitudinal acoustic phonon emission and exciton-exciton scattering time from the large-k excitons to the small-k excitons, on the order of 100 ps as indicated from the rising time (Fig. 3). τ_{NR} is the exciton non-radiative recombination time, on the order of 1 ns. $\tau^{back}_{LA,X-X}$ is the backward scattering time from the small-k state to the large-k state, which is much longer than the $\tau_{LA,X-X}$. τ^{r}_{X} is the radiative lifetime of the small-k bright exciton. α_{bright} is the fraction of the bright (spin ± 1) exciton states. Considering the fast spin relaxation time $\sim 1\,\mathrm{ps}$, the dark states and bright states are assumed to keep equal with each other [Amand 1997, Tassone 1999], which gives $\alpha_{bright} = 0.5$. Neglecting the much smaller contributions from the τ_{plasma} term and τ_{NR} term, we obtain the exciton population in steady state as,

$$N_{large-k} + N_{small-k} = P\tau_{LA,X-X} + P\tau^{r}_{X}/\alpha \approx P\tau^{r}_{X}/\alpha \tag{A.1}$$

Therefore the averaged lifetime $\tau_X = 2\tau^{r}_{X}$.

A.2 Lumped Rate Equations for SWG-Cavity Polariton System

A.2.1 Semiclassical Boltzmann Rate Equation

Consider an exciton state with in-plane momentum k, the population change rate can be modeled by

$$\begin{aligned} dN_k/dt =& P_k - N_k/\tau_k - \sum_{k'} W_{kk'} N_k (N_{k'}+1) + \sum_{k'} W_{k'k} N_{k'} (N_k+1) \\ & - \sum_{k_1 k' k_1'} Y_{k k_1 k' k_1'} N_k N_{k_1} (N_{k'}+1)(N_{k_1'}+1) + \sum_{k_1 k' k_1'} Y_{k' k_1' k k_1} N_{k'} N_{k_1'} (N_k+1)(N_{k_1}+1). \end{aligned} \tag{A.2}$$

N_k is the population of exciton at state k. P_k is the pump rate into state k. τ_k is the lifetime of state k. $W_{kk'}$ is the phonon scattering rate for the process of exciton being scattered from state k to state k'. $Y_{kk_1k'k_1'}$ is the exciton-exciton (X-X) scattering rate, where k and k_1 are the two initial states, k' and k_1' are the two final states. The $(N+1)$ terms reflect the bosonic stimulation.

In small-k region, there are more complicated scatterings involved with the polariton branches. Because the same processes (phonon scattering and X-X scattering) happen for polaritons, the above rate equation will still hold, but one need to think the k as the state index including the branch index instead of just momentum.

In the following, I attempt to divide the exciton states into a few groups, thus consider 'lumped' rate equations for those super-states. The division is the following:

1. Hot Plasma: Directly created by high-energy pump and fast thermalized ($< 100fs$).

2. Large-k Exciton: Fall on the heavy-hole exciton band, but out of light cone, thus cannot radiatively recombine.

3. Small-k Exciton: Exciton states within the light cone, including both bright (decay can be measured) and dark states. It also includes the TE polariton states near the exciton energy (due to the decreasing density of state, only the exciton-like states have considerable occupation)

4. Polariton Condensate: We refer the polariton ground state as the condensate state, even before condensation. It has negligible population at low power, but could become significant after condensation threshold.

As discussed before, plasma state is very easy to model

$$dN_{pl}/dt = P - N_{pl}/\tau_{pl} - N_{pl}/\tau_{pl-exc} \tag{A.3}$$

where τ_{pl} is very long $> 1ns$, while the exciton formation time τ_{pl-exc} is $\sim 20\,\mathrm{ps}$ [Damen 1990]. The steady state plasma population $N_{pl} = P\tau_{pl-exc}$.

So in the following I will focus on deriving rate equations for excitons and condensate states.

A.2.2 Derivation of Large-k Exciton Rate Equation

Let's consider the large-k exciton state using Eq. A.2. To obtain a lumped rate equation, we sum over all state indices of large-k exciton.

$$\begin{aligned} d\sum_{k\in large-k} N_k/dt = &\sum_{k\in large-k} P_k - \sum_{k\in large-k} N_k/\tau_k - \sum_{k\in large-k}\sum_{k'} W_{kk'}N_k(N_{k'}+1) \\ &+ \sum_{k\in large-k}\sum_{k'} W_{k'k}N_{k'}(N_k+1) \\ &- \sum_{k\in large-k}\sum_{k_1k'k'_1} Y_{kk_1k'k'_1}N_kN_{k_1}(N_{k'}+1)(N_{k'_1}+1) \\ &+ \sum_{k\in large-k}\sum_{k_1k'k'_1} Y_{k'k'_1kk_1}N_{k'}N_{k'_1}(N_k+1)(N_{k_1}+1). \end{aligned} \tag{A.4}$$

Because the pump is from plasma, $\sum_{k\in large-k} P_k = N_{pl}/\tau_{pl-exc} = P$, the total pump of the whole system. The lifetime of large-k exciton is very large (through non-radiative recombination), $\tau_{exc,large-k} > 1\,\text{ns}$. The second term can be safely neglected from the equation.

Let's now look at the phonon scattering term. Because the energy of LA phonon is small, the condensate state is irrelevant here. So let's decompose the sum $\sum_{k'} = \sum_{k'\in large-k} + \sum_{k'\in small-k}$. The phonon scattering terms become

$$\begin{aligned} &- \sum_{k\in large-k} (\sum_{k'\in large-k} + \sum_{k'\in small-k}) W_{kk'} N_k (N_{k'} + 1) \\ &+ \sum_{k\in large-k} (\sum_{k'\in large-k} + \sum_{k'\in small-k}) W_{k'k} N_{k'} (N_k + 1) \end{aligned} \tag{A.5}$$

The large-large terms are canceled. For the cross terms, assuming the back scattering rate $W_{k'k}$ is much smaller compared to $W_{kk'}$, only one term remains

$$- \sum_{k\in large-k} \sum_{k'\in small-k} W_{kk'} N_k (N_{k'} + 1). \tag{A.6}$$

The scattering rate from large-k to small-k depends on the actual energy difference $E_{k'} - E_k$ of the two states, but in order to simplify the equation, let's use a constant averaged scattering rate $W_{kk'} \equiv W_{LA}$.

$$-W_{LA} \sum_{k\in large-k} N_k \sum_{k'\in small-k} (N_{k'} + 1) = -W_{LA} N_{large-k} (N_{small-k} + M_{small-k}), \tag{A.7}$$

where $N_{large-k}$ and $N_{small-k}$ are the large-k and small-k populations. $M_{small-k}$ is the number of exciton states in the small-k state. Usually $N_{small-k} << M_{small-k}$. To see this is true, we can actually estimate the number for $M_{small-k}$. We know one state take up $(\pi/L)^2$ of the 2D k-space, where L is the system size $\sim 5\mu m$. The k-space volume for the small-k state in our system is $\sim 200\,\mu\text{m}^{-2}$(Light cone radius

$8\mu m^{-1}$), which contains 2000 states considering the 4-folder spin degeneracy. The 2000 states, if all filled, will contribute $1.0 \times 10^{12}\,\mathrm{cm}^2$ to the exciton density, which we never reached in our experiment.

In the following, we always assume $N_{exc} << M_{exc}$ for excitons, only the condensate population can get above 1.

So the phonon scattering term reduces to

$$-W_{LA} M_{small-k} N_{large-k}, \tag{A.8}$$

The averaged LA phonon scattering rate W_{LA} may be estimated phenomenologically through the rise time of the small exciton emission under pulsed excitation.

Now let's consider the X-X scattering terms. Fix the k index within the large-k exciton, the k_1, k', k_1' can choose from one of the three super-states, large-k (denoted as $'l'$), small-k (denoted as $'s'$), condensate (denoted as $'c'$). That's 3x3x3=27 possible processes. Because of energy conservation, some of the processes will be considered as 'impossible'. For example, $l + l \rightarrow s + s$. They will be excluded. Some processes seems impossible, but because of the large energy range of both large-k (15meV) and small-k excitons(3meV) are actually possible, for example, $l + s \rightarrow s + s$. In the end, the following processes survived:

1. $X_{large-k} + X_{large-k} \rightarrow X_{large-k} + X_{large-k}$
2. $X_{large-k} + X_{large-k} \rightarrow X_{large-k} + X_{small-k}$ or $X_{small-k} + X_{large-k}$
3. $X_{large-k} + X_{large-k} \rightarrow X_{large-k} + X_{cond}$ or $X_{cond} + X_{large-k}$
4. $X_{large-k} + X_{small-k} \rightarrow X_{large-k} + X_{large-k}$
5. $X_{large-k} + X_{small-k} \rightarrow X_{large-k} + X_{small-k}$ or $X_{small-k} + X_{large-k}$
6. $X_{large-k} + X_{small-k} \rightarrow X_{large-k} + X_{cond}$ or $X_{cond} + X_{large-k}$

7. $X_{large-k} + X_{small-k} \to X_{small-k} + X_{small-k}$

8. $X_{large-k} + X_{cond} \to X_{large-k} + X_{large-k}$

9. $X_{large-k} + X_{cond} \to X_{large-k} + X_{small-k}$ or $X_{small-k} + X_{large-k}$

10. $X_{large-k} + X_{cond} \to X_{large-k} + X_{cond}$ or $X_{cond} + X_{large-k}$

11. $X_{large-k} + X_{cond} \to X_{small-k} + X_{small-k}$

Change a bit the notation of the indices of the second sum for the X-X scattering term, we obtain

$$\begin{aligned}
&- \sum_{k\in large-k} \sum_{k_1k'k'_1} Y_{kk_1k'k'_1} N_k N_{k_1} (N_{k'}+1)(N_{k'_1}+1) \\
&+ \sum_{k\in large-k} \sum_{k_1k'k'_1} Y_{k'k'_1kk_1} N_{k'} N_{k'_1} (N_k+1)(N_{k_1}+1) \\
=& - \sum_{(k\in large-k)\, k_1k'k'_1} Y_{kk_1k'k'_1} N_k N_{k_1} (N_{k'}+1)(N_{k'_1}+1) \\
&+ \sum_{kk_1(k'\in large-k)\, k'_1} Y_{kk_1k'k'_1} N_k N_{k_1} (N_{k'}+1)(N_{k'_1}+1)
\end{aligned} \tag{A.9}$$

Using the above energy allowable processes, we can decompose the sum $\sum_{(k\in large-k)\, k_1k'k'_1}$ into 11 sums

$$\sum_{kk_1k'k'_1\in llll} +2\sum_{\in llls} +2\sum_{\in lllc} +\sum_{\in lsll} +2\sum_{\in lsls} +2\sum_{\in lslc} +\sum_{\in lsss} +\sum_{\in lcll} +2\sum_{\in lcls} +2\sum_{\in lclc} +\sum_{\in lcss} \tag{A.10}$$

Flipping the initial states and final states, we decompose the sum $\sum_{kk_1(k'\in large-k)\, k'_1}$ into 11 sums

$$\sum_{kk_1k'k'_1\in llll} +2\sum_{\in lsll} +2\sum_{\in lcll} +\sum_{\in llls} +2\sum_{\in lsls} +2\sum_{\in lcls} +\sum_{\in ssls} +\sum_{\in lllc} +2\sum_{\in lslc} +2\sum_{\in lclc} +\sum_{\in sslc} \tag{A.11}$$

Because the '+' and '-' sign in front of the two big sums in eqn Eq. A.10 and Eq. A.11, the 1st, 5th, (6th $\leftrightarrow$ 9th), 10th terms cancel. Totally, the X-X scattering terms become

$$(-\sum_{\in llls}-\sum_{\in lllc}-\sum_{\in lsss}-\sum_{\in lcss}+\sum_{\in lsll}+\sum_{\in lcll}+\sum_{\in ssls}+\sum_{\in sslc})Y_{kk_1k'k'_1}N_kN_{k_1}(N_{k'}+1)(N_{k'_1}+1) \tag{A.12}$$

Then assuming a constant X-X scattering rate $Y_{kk_1k'k'_1} \equiv Y_{X-X}$ and using the facts $N_{exc} << M_{exc}$ and $M_c = 1$, we obtain

$$\begin{aligned} &- Y_{X-X}N_l^2(M_{ll\to ls}+(N_c+1)) + Y_{X-X}N_lN_s(M_{ls\to ll}-M_{ls\to ss}) \\ &+ Y_{X-X}N_lN_c(M_{lc\to ll}-M_{lc\to ss}) + Y_{X-X}N_s^2(M_{ss\to ls}+(N_c+1)) \end{aligned} \tag{A.13}$$

where $M_{ll\to ls}$ are the number of possible energy configurations of the two final states $\in l$ and s super-state given the two initial states. Other M_{xxxx} have the same meaning. Of course, one has to be wary that given two initial states, there may be zero energy configurations of the final states that satisfy energy conservation. In this case, we have to treat M_{xxxx} in the averaged sense. Apparently, M_{xxxx} are related to the density of state of the final states, but they have to be treated as tuning parameter for the present.

The meaning of Eq. A.13 is obvious: 1) two large-k excitons can scatters into one large-k and one small-k excitons or condensate, thus lose some population. 2) one large-k scatters with one small-k can replenish the large-k population ($ls \to ll$) or all go to the small-k ($ls \to ll$). 3) Same thing happens for large-k and condensate. 4) Two small-k can replenish the large-k population.

A.2.3 Derivation of Small-k Exciton Rate Equation

Similar to large-k exciton, we derive the rate equation for small-k exciton. Summing over small-k on Eq. A.2

$$\begin{aligned} d\sum_{k\in small-k} N_k/dt = &\sum_{k\in small-k} P_k - \sum_{k\in small-k} N_k/\tau_k - \sum_{k\in small-k}\sum_{k'} W_{kk'}N_k(N_{k'}+1) \\ &+ \sum_{k\in small-k}\sum_{k'} W_{k'k}N_{k'}(N_k+1) \\ &- \sum_{k\in small-k}\sum_{k_1k'k'_1} Y_{kk_1k'k'_1}N_kN_{k_1}(N_{k'}+1)(N_{k'_1}+1) \\ &+ \sum_{k\in small-k}\sum_{k_1k'k'_1} Y_{k'k'_1kk_1}N_{k'}N_{k'_1}(N_k+1)(N_{k_1}+1). \end{aligned} \tag{A.14}$$

First, there's no direct pump. The pump term is zero. Assuming a uniform radiative lifetime τ_{exc}, the second term becomes $N_{small-k}/\tau_{exc}$. Decompose the sum $\sum_{k'} = \sum_{k'\in large-k} + \sum_{k'\in small-k} + \sum_{k'\in cond}$. The phonon scattering terms become

$$\begin{aligned} &- \sum_{k\in small-k}\Big(\sum_{k'\in large-k} + \sum_{k'\in small-k} + \sum_{k'\in cond}\Big)W_{kk'}N_k(N_{k'}+1) \\ &+ \sum_{k\in small-k}\Big(\sum_{k'\in large-k} + \sum_{k'\in small-k} + \sum_{k'\in cond}\Big)W_{k'k}N_{k'}(N_k+1) \end{aligned} \tag{A.15}$$

The small-small terms are canceled. For the cross terms, assuming the back scattering rate is small, the terms reduce to

$$-\sum_{k\in small-k}\sum_{k'\in cond} W_{kk'}N_k(N_{k'}+1) + \sum_{k\in small-k}\sum_{k'\in large-k} W_{k'k}N_{k'}(N_k+1). \tag{A.16}$$

Using state-averaged scattering rates,

$$-W_{LA,cond}N_{small-k}(N_{cond}+1) + W_{LA}M_{small-k}N_{large-k}. \tag{A.17}$$

The first term is the relaxation term from small-k exciton to condensate. The second term represents the injection coming from the large-k exciton.

Similarly we consider the X-X scattering terms. Fixing the k index within the small-k exciton, the k_1, k', k_1' can be chosen from one of the three super-states, large-k (denoted as $'l'$), small-k (denoted as $'s'$), condensate (denoted as $'c'$). That's 3x3x3=27 possible processes. Because of energy conservation, some of the processes will be excluded. In the end, the following processes survived:

1. $X_{small-k} + X_{large-k} \rightarrow X_{large-k} + X_{large-k}$
2. $X_{small-k} + X_{large-k} \rightarrow X_{large-k} + X_{small-k}$ or $X_{small-k} + X_{large-k}$
3. $X_{small-k} + X_{large-k} \rightarrow X_{large-k} + X_{cond}$ or $X_{cond} + X_{large-k}$
4. $X_{small-k} + X_{large-k} \rightarrow X_{small-k} + X_{small-k}$
5. $X_{small-k} + X_{small-k} \rightarrow X_{large-k} + X_{small-k}$ or $X_{small-k} + X_{large-k}$
6. $X_{small-k} + X_{small-k} \rightarrow X_{large-k} + X_{cond}$ or $X_{cond} + X_{large-k}$
7. $X_{small-k} + X_{small-k} \rightarrow X_{small-k} + X_{small-k}$
8. $X_{small-k} + X_{small-k} \rightarrow X_{small-k} + X_{cond}$ or $X_{cond} + X_{small-k}$
9. $X_{small-k} + X_{cond} \rightarrow X_{small-k} + X_{small-k}$
10. $X_{small-k} + X_{cond} \rightarrow X_{small-k} + X_{cond}$ or $X_{cond} + X_{small-k}$

Change a bit the notation of the indices of the second sum for the X-X scattering

term, we obtain

$$\begin{aligned}
&- \sum_{k\in small-k} \sum_{k_1k'k'_1} Y_{kk_1k'k'_1} N_k N_{k_1} (N_{k'}+1)(N_{k'_1}+1) \\
&+ \sum_{k\in small-k} \sum_{k_1k'k'_1} Y_{k'k'_1kk_1} N_{k'} N_{k'_1} (N_k+1)(N_{k_1}+1) \\
=& - \sum_{(k\in small-k)\, k_1k'k'_1} Y_{kk_1k'k'_1} N_k N_{k_1} (N_{k'}+1)(N_{k'_1}+1) \\
&+ \sum_{kk_1(k'\in small-k)\, k'_1} Y_{kk_1k'k'_1} N_k N_{k_1} (N_{k'}+1)(N_{k'_1}+1)
\end{aligned} \tag{A.18}$$

Using the above energy allowable processes, we can decompose the sum $\sum_{(k\in small-k)\, k_1k'k'_1}$ into 10 sums

$$\sum_{kk_1k'k'_1\in slll} +2\sum_{\in slls} +2\sum_{\in sllc} +\sum_{\in slss} +2\sum_{\in ssls} +2\sum_{\in sslc} +\sum_{\in ssss} +2\sum_{\in sssc} +\sum_{\in scss} +2\sum_{\in scsc} \tag{A.19}$$

Flipping the initial states and final states, we decompose the sum $\sum_{kk_1(k'\in small-k)\, k'_1}$ into 10 sums

$$\sum_{kk_1k'k'_1\in llsl} +2\sum_{\in lssl} +2\sum_{\in lcsl} +\sum_{\in sssl} +2\sum_{\in lsss} +2\sum_{\in lcss} +\sum_{\in ssss} +2\sum_{\in scss} +\sum_{\in sssc} +2\sum_{\in scsc} \tag{A.20}$$

After some algebra, the X-X scattering terms become

$$\begin{aligned}
&-(\sum_{\in slll} +2\sum_{\in sllc} +\sum_{\in ssls} +2\sum_{\in sslc} +\sum_{\in sssc}) + (\sum_{\in llsl} +2\sum_{\in lcsl} +\sum_{\in lsss} +2\sum_{\in lcss} +\sum_{\in scss}) \\
&\qquad\qquad Y_{kk_1k'k'_1} N_k N_{k_1} (N_{k'}+1)(N_{k'_1}+1)
\end{aligned} \tag{A.21}$$

Then assuming a constant X-X scattering rate $Y_{kk_1k'k'_1} \equiv Y_{X-X}$ and using the

facts $N_{exc} << M_{exc}$ and $M_c = 1$, we obtain

$$\begin{aligned}
&- Y_{X-X} N_s N_l (M_{sl\to ll} + 2(N_c+1) - M_{ls\to ss}) - Y_{X-X} N_s^2 (M_{ss\to ls} + 3(N_c+1)) \\
&+ Y_{X-X} N_l^2 M_{ll\to sl} + Y_{X-X} N_l N_c (2M_{lc\to sl} + 2M_{lc\to ss}) + Y_{X-X} N_s N_c M_{sc\to ss}
\end{aligned} \tag{A.22}$$

where M_{xxxx} have the same meaning as before.

A.2.4 Derivation of Condensate Rate Equation

Because condensate has only one state, we don't need to sum over the condensate. Apply Eq. A.2 directly,

$$\begin{aligned}
dN_c/dt =& P_c - N_c/\tau_p ol - \sum_{k'} W_{ck'} N_c (N_{k'}+1) \\
&+ \sum_{k'} W_{k'c} N_{k'} (N_c+1) \\
&- \sum_{k_1 k' k_1'} Y_{ck_1 k' k_1'} N_c N_{k_1} (N_{k'}+1)(N_{k_1'}+1) \\
&+ \sum_{k_1 k' k_1'} Y_{k' k_1' c k_1} N_{k'} N_{k_1'} (N_c+1)(N_{k_1}+1).
\end{aligned} \tag{A.23}$$

First, there's no direct pump. The pump term is zero. Second, assuming back phonon scattering is small. The phonon scattering terms reduce to

$$+W_{LA,cond} N_s (N_c+1). \tag{A.24}$$

Similarly we consider the X-X scattering terms. Fixing the k index to be the condensate, the k_1, k', k_1' can be chosen from one of the three super-states, large-k (denoted as $'l'$), small-k (denoted as $'s'$), condensate (denoted as $'c'$). That's 3x3x3=27 possible processes. Because of energy conservation, some of the processes will be excluded. In the end, the following processes survived:

1. $X_{cond} + X_{large-k} \to X_{large-k} + X_{large-k}$

2. $X_{cond} + X_{large-k} \to X_{large-k} + X_{small-k}$ or $X_{small-k} + X_{large-k}$

3. $X_{cond} + X_{large-k} \to X_{large-k} + X_{cond}$ or $X_{cond} + X_{large-k}$

4. $X_{cond} + X_{large-k} \to X_{small-k} + X_{small-k}$

5. $X_{cond} + X_{small-k} \to X_{small-k} + X_{small-k}$

6. $X_{cond} + X_{small-k} \to X_{small-k} + X_{cond}$ or $X_{cond} + X_{small-k}$

7. $X_{cond} + X_{cond} \to X_{cond} + X_{cond}$

Change a bit the notation of the indices of the second sum for the X-X scattering term, we obtain

$$
\begin{aligned}
&-\sum_{k=c}\sum_{k_1k'k'_1} Y_{kk_1k'k'_1} N_k N_{k_1}(N_{k'}+1)(N_{k'_1}+1) + \sum_{k=c}\sum_{k_1k'k'_1} Y_{k'k'_1kk_1} N_{k'} N_{k'_1}(N_k+1)(N_{k_1}+1) \\
&= -\sum_{(k=c)\,k_1k'k'_1} Y_{kk_1k'k'_1} N_k N_{k_1}(N_{k'}+1)(N_{k'_1}+1) + \sum_{kk_1(k'=c)\,k'_1} Y_{kk_1k'k'_1} N_k N_{k_1}(N_{k'}+1)(N_{k'_1}+1)
\end{aligned}
\tag{A.25}
$$

Using the above energy allowable processes, we can decompose the sum $\sum_{(k\in small-k)\,k_1k'k'_1}$ into 7 sums

$$
\sum_{kk_1k'k'_1\in clll} + 2\sum_{\in clls} + 2\sum_{\in cllc} + \sum_{\in clss} + \sum_{\in csss} + 2\sum_{\in cssc} + \sum_{\in cccc} \tag{A.26}
$$

Flipping the initial states and final states, we decompose the sum $\sum_{kk_1(k'\in small-k)\,k'_1}$ into 10 sums

$$
\sum_{kk_1k'k'_1\in llcl} + 2\sum_{\in lscl} + 2\sum_{\in lccl} + \sum_{\in sscl} + \sum_{\in sscs} + 2\sum_{\in sccs} + \sum_{\in cccc} \tag{A.27}
$$

After some algebra, the X-X scattering terms become

$$-(\sum_{\in clll}+2\sum_{\in clls}+\sum_{\in clss}+\sum_{\in csss})+(\sum_{\in llcl}+2\sum_{\in lscl}+\sum_{\in sscl}+\sum_{\in sscs})Y_{kk_1k'k'_1}N_kN_{k_1}(N_{k'}+1)(N_{k'_1}+1) \tag{A.28}$$

Then assuming a constant X-X scattering rate $Y_{kk_1k'k'_1} \equiv Y_{X-X}$ and using the facts $N_{exc} << M_{exc}$ and $M_c = 1$, we obtain

$$\begin{aligned} &- Y_{X-X}N_cN_l(M_{cl\to ll}+2M_{clls}+M_{cl\to ss}) - Y_{X-X}N_cN_sM_{cs\to ss} \\ &+ Y_{X-X}N_l^2(N_c+1) + 2Y_{X-X}N_lN_s(N_c+1) + Y_{X-X}N_s^2(N_c+1) \end{aligned} \tag{A.29}$$

where M_{xxxx} have the same meaning as before.

A.2.5 Final Result

$$\begin{aligned} dN_{pl}/dt &= P - N_{pl}/\tau_{pl} - N_{pl}/\tau_{pl-exc} \\ dN_l/dt &= P - W_{LA}M_sN_l - Y_{X-X}N_l^2(M_{ll\to ls}+(N_c+1)) + Y_{X-X}N_lN_s(M_{ls\to ll}-M_{ls\to ss}) \\ &\quad + Y_{X-X}N_lN_c(M_{lc\to ll}-M_{lc\to ss}) + Y_{X-X}N_s^2(M_{ss\to ls}+(N_c+1)) \\ dN_s/dt &= -N_s/\tau_{exc} - W_{LA,cond}N_s(N_c+1) + W_{LA}M_sN_l \\ &\quad - Y_{X-X}N_sN_l(M_{sl\to ll}+2(N_c+1)-M_{ls\to ss}) - Y_{X-X}N_s^2(M_{ss\to ls}+3(N_c+1)) \\ &\quad + Y_{X-X}N_l^2M_{ll\to sl} + Y_{X-X}N_lN_c(2M_{lc\to sl}+2M_{lc\to ss}) + Y_{X-X}N_sN_cM_{sc\to ss} \\ dN_c/dt &= -N_c/\tau_{pol} + W_{LA,cond}N_s(N_c+1) \\ &\quad - Y_{X-X}N_cN_l(M_{cl\to ll}+2M_{clls}+M_{cl\to ss}) - Y_{X-X}N_cN_sM_{cs\to ss} \\ &\quad + Y_{X-X}N_l^2(N_c+1) + 2Y_{X-X}N_lN_s(N_c+1) + Y_{X-X}N_s^2(M_{ss\to cl}+M_{ss\to cs})(N_c+1) \end{aligned} \tag{A.30}$$

The short notations

pl: plasma |l: large-k exciton |s: small-k exciton |c: condensate

Till now, we haven't considered momentum conservation. One reason is, the finite size of the SWG breaks the translational symmetry. The polariton modes are discrete instead of following the continuous dispersion. Another reason is, the exciton dispersion is also affected by the disorders in the quantum wells. According to my simulation, although the large-k exciton follows the continuous dispersion closely (has some spread because the scattering of the disorder potential), the small-k excitons range from localized states to extended state. Therefore, the momentum conservation is 'soft' in our system.

Nevertheless, we can still use momentum conservation to prune those least possible X-X scattering terms. Let's look at the X-X scattering terms for large-k, small-k and condensate below

$$
\begin{aligned}
&large-k \\
&(-\sum_{\in llls}-\sum_{\in lllc}-\sum_{\in lsss}-\sum_{\in lcss}+\sum_{\in lsll}+\sum_{\in lcll}+\sum_{\in ssls}+\sum_{\in sslc})Y_{kk_1k'k'_1}N_kN_{k_1}(N_{k'}+1)(N_{k'_1}+1) \\
&small-k \\
&-(\sum_{\in slll}+2\sum_{\in sllc}+\sum_{\in ssls}+2\sum_{\in sslc}+\sum_{\in sssc})+(\sum_{\in llsl}+2\sum_{\in lcsl}+\sum_{\in lsss}+2\sum_{\in lcss}+\sum_{\in scss}) \\
&Y_{kk_1k'k'_1}N_kN_{k_1}(N_{k'}+1)(N_{k'_1}+1) \\
&condensate \\
&-(\sum_{\in clll}+2\sum_{\in clls}+\sum_{\in clss}+\sum_{\in csss})+(\sum_{\in llcl}+2\sum_{\in lscl}+\sum_{\in sscl}+\sum_{\in sscs})Y_{kk_1k'k'_1}N_kN_{k_1}(N_{k'}+1)(N_{k'_1}+1)
\end{aligned}
\tag{A.31}
$$

Processes $lc \to ss$, $sl \to lc$ and their reverse processes will be pruned, which left us

only the following

$$
\begin{aligned}
&large-k \\
&(-\sum_{\in llls}-\sum_{\in lllc}-\sum_{\in lsss}+\sum_{\in lsll}+\sum_{\in lcll}+\sum_{\in ssls})Y_{kk_1k'k'_1}N_kN_{k_1}(N_{k'}+1)(N_{k'_1}+1) \\
&small-k \\
&-(\sum_{\in slll}+\sum_{\in ssls}+\sum_{\in sssc})+(\sum_{\in llsl}+\sum_{\in lsss}+\sum_{\in scss})Y_{kk_1k'k'_1}N_kN_{k_1}(N_{k'}+1)(N_{k'_1}+1) \\
&condensate \\
&-(\sum_{\in clll}+\sum_{\in csss})+(\sum_{\in llcl}+\sum_{\in sscs})Y_{kk_1k'k'_1}N_kN_{k_1}(N_{k'}+1)(N_{k'_1}+1)
\end{aligned}
\tag{A.32}
$$

Therefore, the final result Eq. A.30 will be simplified to

$$
\begin{aligned}
dN_{pl}/dt &= P - N_{pl}/\tau_{pl} - N_{pl}/\tau_{pl-exc} \\
dN_l/dt &= P - W_{LA}M_sN_l - Y_{X-X}N_l^2(M_{ll\to ls}+(N_c+1)) + Y_{X-X}N_lN_s(M_{ls\to ll}-M_{ls\to ss}) \\
&\quad + Y_{X-X}N_lN_cM_{lc\to ll} + Y_{X-X}N_s^2M_{ss\to ls} \\
dN_s/dt &= -N_s/\tau_{exc} - W_{LA,cond}N_s(N_c+1) + W_{LA}M_sN_l \\
&\quad - Y_{X-X}N_sN_l(M_{sl\to ll}-M_{ls\to ss}) - Y_{X-X}N_s^2(M_{ss\to ls}+(N_c+1)) \\
&\quad + Y_{X-X}N_l^2M_{ll\to sl} + Y_{X-X}N_sN_cM_{sc\to ss} \\
dN_c/dt &= -N_c/\tau_{pol} + W_{LA,cond}N_s(N_c+1) \\
&\quad - Y_{X-X}N_cN_lM_{cl\to ll} - Y_{X-X}N_cN_sM_{cs\to ss} \\
&\quad + Y_{X-X}N_l^2(N_c+1) + Y_{X-X}N_s^2(N_c+1)
\end{aligned}
\tag{A.33}
$$

APPENDIX B

Supplementary Material for "Dispersion Engineering with SWG"

B.1 Comparison of DBR and SWG's Reflection Phases

DBRs are constructed by many $\lambda/4$ layers with alternating high and low refractive indices. The reflection phase at the interface of low-index cavity and adjacent high-index DBR is exactly π at normal incidence at the cavity resonance, and it changes only slightly at oblique incidence. We use $\phi'(\omega, \theta_c) = \phi(\omega, \theta_c) - \pi$ to denote the deviation of the reflection phase from π. As an example, we show in Fig. B.1(a) the angular and wavelength dependence of ϕ' for a typical DBR, calculated by the Transfer Matrix method. At the design wavelength 800 nm, the deviation is less than 0.04π up to an incidence angle of 25°.

In contrast, an SWG's reflection phase can have a stronger and more complicated wavelength and angular dependence. To compare with DBRs, we define a π-reference plane as the effective boundary of an SWG-mirror, corresponding to $\phi = \pi$ at normal incidence at the cavity resonance. As an example, Fig. B.1(b) shows $\phi'(\omega, \theta_c) = \phi - \pi$ for the SWG1 used in the main text, calculated by RCWA. The phase at 800 nm can

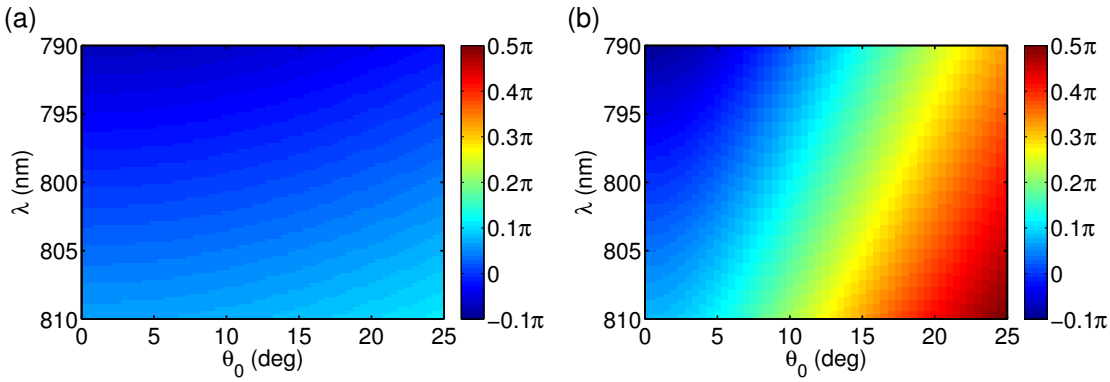

Figure B.1: Comparison of the angular and wavelength dependence of typical DBR and SWG's reflection phases. (a) Reflection phase of a DBR consisting of 30 pairs of $Al_{0.15}Ga_{0.85}As$ and AlAs layers on a GaAs substrate. Light is incident from an AlAs cavity medium. (b) Reflection phase of an air-surrounded SWG with $\Lambda = 539$nm and $\eta = 0.31$, $t_g = 350$nm for incident light of TM polarization. The SWG displays a much larger phase variation over incident angles compared to the DBR.

change up to 0.4π over $25°$, one order of magnitude larger than the DBR does. Larger or a different angular dependence of ϕ' can be obtained by different SWG designs.

B.2 Derivation of the dispersion of WGA modes

In this section, we solve for the dispersions of WGA modes. We start with the general form of the magnetic field of TM polarized light in a WGA:

$$H_y(x,z) = H(x)[a^+ exp(+i\beta z) + a^- exp(-i\beta z)],$$

where $H_y(x,z)$ is the y-component of the magnetic field, $H(x)$ is the lateral field profile in x-direction, β is the propagation constant, a^+ and a^- are the coefficients for the waves propagating in the $+z$ and $-z$ directions, respectively.

The lateral field $H(x)$ is determined by the following eigenvalue equation:

$$(\frac{\partial^2}{\partial x^2} + n^2(x)k_0^2)H(x) = \beta^2 H(x), \tag{B.1}$$

where $n(x)$ is the profile of refractive index in the SWG region as shown in Fig. B.2 and $k_0 = \omega/c$ is the wavenumber in vacuum. Because of the binary grating profile, the

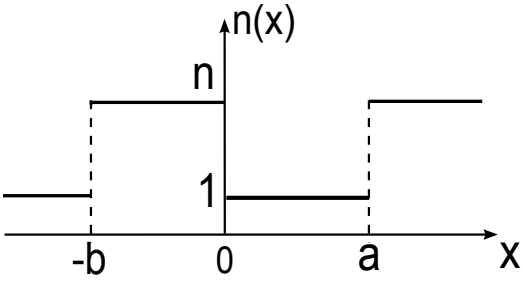

Figure B.2: Refractive index profile of an SWG with dielectric bar width b and air width a.

solution of Eq. B.1 can be obtained by connecting its homogeneous-medium solutions in the air and bar regions piecewise by boundary conditions. For a grating with a and b as the widths of the air and bar regions, in the air region $0 < x < a$,

$$H_a(x) = c_a^+ exp(+ik_a x) + c_a^- exp(-ik_a x)$$

where

$$k_a = (k_0^2 - \beta^2)^{1/2} \tag{B.2}$$

is the transverse wavenumber in the air region. In the bar region $-b < x < 0$,

$$H_b(x) = c_b^+ exp(+ik_b x) + c_b^- exp(-ik_b x)$$

where

$$k_b = (n^2 k_0^2 - \beta^2)^{1/2} \tag{B.3}$$

is the transverse wavenumber in the bar region, $c_{a,b}^{+,-}$ are amplitude coefficients. In other periods $-b < x < a$, the Bloch-Floquet theorem requires:

$$H(x + \Lambda) = e^{ik_x \Lambda} H(x),$$

where k_x is the transverse wavenumber:

$$k_x = \omega/c \sin\theta_0. \tag{B.4}$$

Imposing the boundary conditions of the tangential field components at boundary $x = 0$ and $x = a$,

$$H_y(0^-) = H_y(0^+), E_x(0^-) = E_y(0^+)$$

$$H_y(a^-) = H_y(a^+), E_y(a^-) = E_y(a^+),$$

where the electric field

$$E_x(x) = \frac{i\mu_0 c}{n^2(x)k_0}\frac{\partial H_y(x)}{\partial x},$$

we obtain the mode dispersion relation

$$2n^2 k_a k_b(\cos k_a a \cos k_b b - \cos k_x \Lambda) = (n^4 k_a^2 + k_b^2)\sin k_a a \sin k_b b. \tag{B.5}$$

Substituting equation Eq. B.2 and Eq. B.3 for $k_{a,b}$ and equation Eq. B.4 for k_x into equation Eq. B.5, we obtain the $\omega - \beta$ dispersion of WGA-modes at an incident angle θ_0. Equation Eq. B.5 defines a complete set of WGA-modes. In the special case of normal incidence ($k_x = 0$), the dispersion has even and odd branches as shown in Fig.1(c) of the main text.

B.3 Fabrication error tolerance Analysis

In experimental implementation of the proposed structures, fabrication errors are inevitable. Here we will discuss the error tolerance of the SWGs with special dispersions. We show that those designs should be within reach of current nano-fabrication technologies.

Changes in the grating parameters (Λ, t_g and η) will lead to changes in the reflec-

tion phase and in turn changes in the SWG-cavity dispersion. This can be quantified using the Fabry-Perot resonance condition (Eq.(1) in main text):

$$\phi_1(\omega, k_\parallel, \alpha) + \phi_2(\omega, k_\parallel) - 2k_{\perp c}d = 2m\pi \tag{B.6}$$

Here α represents one of the grating parameters. A change in α by $\delta\alpha$ will lead to perturbation to the SWG-mirror's reflection phase ϕ_1, which will cause a shift of resonance frequency ω by $\delta\omega$. They satisfy the following total differential equation for small $\delta\alpha$:

$$\delta\phi_{1,\alpha} \equiv \frac{\partial\phi_1}{\partial\alpha}\delta\alpha = -\frac{\partial\phi_1}{\partial\omega}\delta\omega - \frac{\partial\phi_2}{\partial\omega}\delta\omega + 2\frac{\partial(k_{\perp c}d)}{\partial\omega}\delta\omega. \tag{B.7}$$

Here use $\delta\phi_{1,\alpha}$ to denote the $\delta\alpha$-induced change of the SWG-mirror's reflection phase ϕ_1. The three terms on the righthand side of the equation are the $\delta\omega$-induced changes to the reflection phases of the top mirror, the reflection phase of the bottom mirror, and the round-trip traveling phase. The derivatives in these terms can be approximated as constants as they change by less than 1% for $|k_\parallel| < 3\mu\text{m}^{-1}$ for the three example SWGs discussed in the main text. We list their values in Table B.1. The values in the last column give the $\delta\phi_{1,\alpha}$ corresponding to 1 meV shift in the cavity resonance. Using these values, we can evaluate $\delta\omega$ for given $\delta\phi_{1,\alpha}$.

Table B.1: Derivatives in Eq. B.7 for SWG1-3

	$\partial\phi_1/\partial\omega$ [meV^{-1}]	$\partial\phi_2/\partial\omega$ [meV^{-1}]	$\partial(k_{\perp c}d)/\partial\omega$ [meV^{-1}]	$\delta\phi_{1,\alpha}$
SWG1	-0.0052	-0.011 (DBR)	-0.0020	$\sim 0.012\delta\omega$
SWG2	-0.0049			
SWG3	-0.015	-0.015 (SWG3)		$\sim 0.026\delta\omega$

In Fig. B.3-Fig. B.5, we show how $\delta\phi_{1,\alpha}$ and the resulting $\delta\omega$ vary with $k_\parallel$ at the presence of fabrication errors in the grating parameters: t_g, Λ, and η. The values are off-set by $\delta\phi_{1,\alpha}(k_\parallel = 0)$ and $\delta\omega(k_\parallel = 0)$ for easy comparison. The grating thickness t_g is determined by the epitaxial growth. By careful calibration of the growth condition,

the layer thickness can be well controlled within a few atomic layers ($\sim$ 1 nm). Because of the common difficulty in the calibration of multilayer structures, we relax the accuracy to 10 nm (Fig. B.3). The period Λ and bar-width $\eta\Lambda$ of the grating are determined by the e-beam lithography. Typical resolutions of current e-beam systems are less than 5 nm [180, 181, 182], hence we consider ± 2 nm variation in Λ and $\eta\Lambda$ in Fig. B.4 and Fig. B.5.

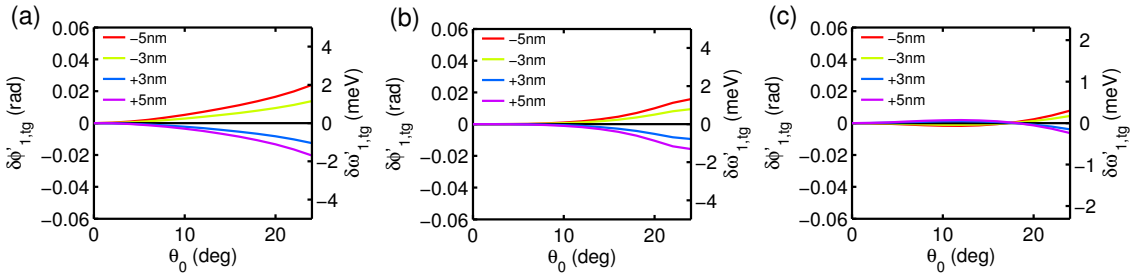

Figure B.3: The changes in the SWG-mirror's reflection phase (left axis) and the cavity dispersion (right axis) of SWG1-DBR (a), SWG2-DBR (b) and SWG3-SWG3 (c) cavities when the SWG-mirrors are subject to fabrication errors of $\delta t_g = \pm 3$ nm and ± 5 nm, where $\delta\phi'_{1,tg} \equiv \delta\phi_{1,tg} - \delta\phi_{1,tg}(\theta_0 = 0)$ and $\delta\omega'_{1,tg} \equiv \delta\omega_{1,tg} - \delta\omega_{1,tg}(\theta_0 = 0)$

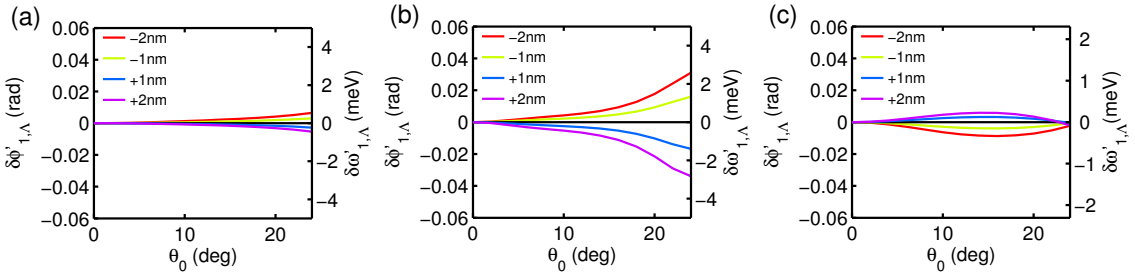

Figure B.4: The changes in the SWG-mirror's reflection phase (left axis) and the cavity dispersion (right axis) of SWG1-DBR (a), SWG2-DBR (b) and SWG3-SWG3 (c) cavities when the SWG-mirrors are subject to fabrication errors of $\delta\Lambda = \pm 1$ nm and ± 2 nm, where $\delta\phi'_{1,\Lambda} \equiv \delta\phi_{1,\Lambda} - \delta\phi_{1,\Lambda}(\theta_0 = 0)$ and $\delta\omega'_{1,\Lambda} \equiv \delta\omega_{1,\Lambda} - \delta\omega_{1,\Lambda}(\theta_0 = 0)$

Comparing $\delta\omega(k_\parallel)$ shown in Fig. B.3-Fig. B.5 with the originally designed dispersion $\omega(k_\parallel)$, we can evaluate the impact of the fabrication errors. For SWG1-DBR and SWG2-DBR cavities, designed to tune the effective mass m^* of the cavity mode,

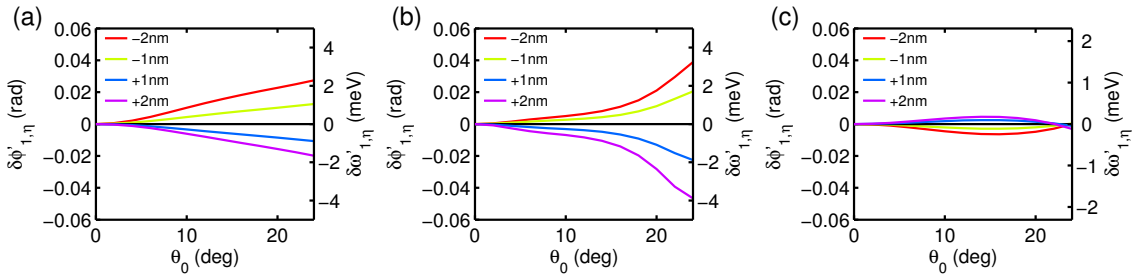

Figure B.5: The changes in the SWG-mirror's reflection phase (left axis) and the cavity dispersion (right axis) of SWG1-DBR (a), SWG2-DBR (b) and SWG3-SWG3 (c) cavities when the SWG-mirrors are subject to fabrication errors of $\delta\eta\Lambda = \pm 1$ nm and ± 2 nm, where $\delta\phi'_{1,\eta} \equiv \delta\phi_{1,\eta} - \delta\phi_{1,\eta}(\theta_0 = 0)$ and $\delta\omega'_{1,\eta} \equiv \delta\omega_{1,\eta} - \delta\omega_{1,\eta}(\theta_0 = 0)$

we calculated δm^* due to the fabrication errors evaluated above. The results are summarized in Table B.2. For the SWG1-DBR cavity, m^* changes less than $\pm 13\%$ from the original design. Therefore the much steeper dispersion of SWG1-DBR is well maintained. For the SWG2-DBR cavity, designed to have a very flat dispersion, the effective mass becomes more sensitive to Λ and $\eta\Lambda$ errors. A small change in the cavity resonance can easily change m^* by an order of magnitude and even change the sign. Nevertheless, m^* remains larger than the $3 \times 10^{-5} m_e$ of the DBR-DBR cavity. For the double-well shaped dispersion of the SWG3-SWG3 cavity, the most important feature is the well-depth. Fig. B.3-Fig. B.5 show its cavity resonance varies by less than 0.3 meV, much less than the 4 meV well-depth of the original dispersion. Therefore the double-well dispersion is also robust against the fabrication errors.

Table B.2: Effective mass of the cavity mode considering fabrication errors.)

(Unit:m_e)	Designed Value	± 5 nm error in t_g	± 2 nm error in Λ	± 2 nm error in $\eta\Lambda$
SWG1	1.0×10^{-5}	$0.9 \sim 1.05 \times 10^{-5}$	$0.98 \sim 1.01 \times 10^{-5}$	$0.87 \sim 1.09 \times 10^{-5}$
SWG2	-20×10^{-5}	$-21 \sim -18 \times 10^{-5}$	$49 \sim -6.4 \times 10^{-5}$	$21 \sim -5 \times 10^{-5}$

B.4 Quality Factor of the SWG based Cavities

In the main text, we use the linewidth of the cavity resonance to indicate the cavity's quality factor Q when it is less than $\sim 10^4$. Here, we show how the quality factors change over the incidence angles or $k_{\|}$ for all the example cavities discussed in the main text. As shown in Fig. B.6, the quality factor of the SWG-based cavities does not have a simple relation with the angle. Different SWGs feature very different angular dependencies. For all the cavities, Q vary between 10^3 (thick black line) and 2×10^6 within $\pm 20°$. For the SWG2-DBR cavity only, Q drops below 10^3 at $|\theta| > 20°$ (or $k_{\|} > 2.8 \mu m^{-1}$).

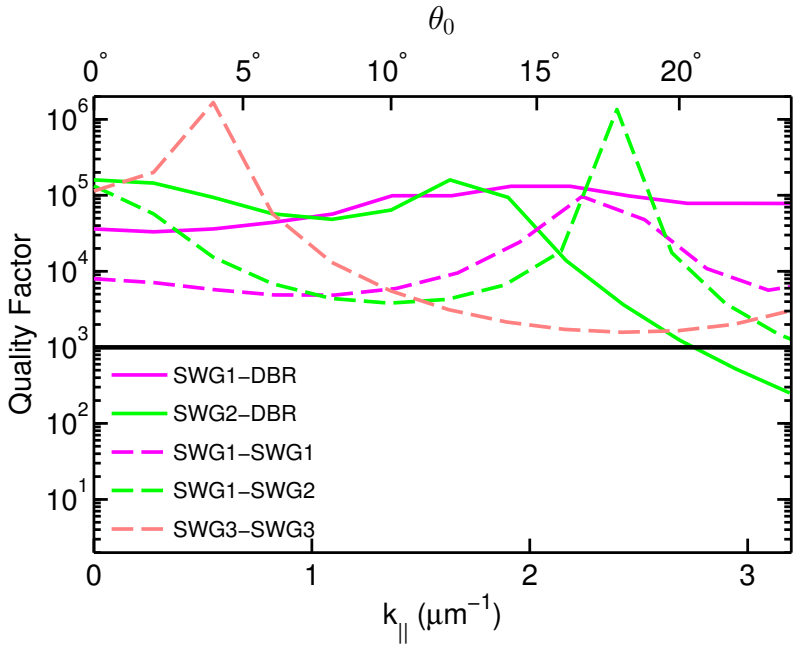

Figure B.6: The quality factor Q of SWG-based cavities presented in Fig. 3 of the main text.

BIBLIOGRAPHY

BIBLIOGRAPHY

[1] Charles Kittel. *Introduction to solid state physics*. 2005.

[2] John D. Joannopoulos, Steven G. Johnson, Joshua N. Winn, and Robert D. Meade. *Photonic Crystals: Molding the Flow of Light*. Princeton University Press, 2nd edition, 2008.

[3] Hui Deng, Hartmut Haug, and Yoshihisa Yamamoto. Exciton-polariton bose-einstein condensation. *Rev. Mod. Phys.*, 82:1489–1537, May 2010.

[4] Tim Byrnes, Na Young Kim, and Yoshihisa Yamamoto. Excitonpolariton condensates. *Nature Physics*, 10(11):803–813, 2014.

[5] Feng-Kuo Hsu. *CONTROL OF LASING FROM A HIGHLY PHOTOEXCITED SEMICONDUCTOR*. PhD thesis, Michigan State University, 2016.

[6] Kenji Kamide and Tetsuo Ogawa. What determines the wave function of electron-hole Pairs in polariton condensates? *Physical Review Letters*, 105(5):1–4, 2010.

[7] Hartmut Haug and Stephan Koch. *Quantum Theory of the Optical and Electronic Properties of Semiconductors, 4th ed*. World Scientific, 2004.

[8] T. B. Norris. Excitons in strongly coupled semiconductor microcavities. In *Semiconductor Quantum Optoelectronics: From Quantum Physics to Smart Devices*, page 121. 1999.

[9] M. G. Moharam, Eric B. Grann, Drew A. Pommet, and T. K. Gaylord. Formulation for stable and efficient implementation of the rigorous coupled-wave analysis of binary gratings. *Journal of the Optical Society of America A*, 12(5):1068, May 1995.

[10] Vadim Karagodsky, Forrest G Sedgwick, and Connie J Chang-Hasnain. Theoretical analysis of subwavelength high contrast grating reflectors. *Optics express*, 18(16):16973–88, August 2010.

[11] Robert L Olmon, Brian Slovick, Timothy W Johnson, David Shelton, Sanghyun Oh, Glenn D Boreman, and Markus B Raschke. Optical dielectric function of gold. *Phys. Rev. B*, 86(235147):1–9, 2012.

[12] C. Weisbuch, M. Nishioka, a. Ishikawa, and Y. Arakawa. Observation of the coupled exciton-photon mode splitting in a semiconductor quantum microcavity. *Physical Review Letters*, 69(23):3314–3317, 1992.

[13] Hui Deng, Gregor Weihs, Charles Santori, Jacqueline Bloch, and Yoshihisa Yamamoto. Condensation of semiconductor microcavity exciton polaritons. *Science*, 298(5591):199–202, October 2002.

[14] J Kasprzak, M Richard, S Kundermann, a Baas, P Jeambrun, J M J Keeling, F M Marchetti, M H Szymaska, R André, J L Staehli, V Savona, P B Littlewood, B Deveaud, and Le Si Dang. Bose-Einstein condensation of exciton polaritons. *Nature*, 443(7110):409–14, September 2006.

[15] R Balili, V Hartwell, D Snoke, L Pfeiffer, and K West. Bose-Einstein condensation of microcavity polaritons in a trap. *Science*, 316(5827):1007–10, May 2007.

[16] Alberto Amo, Jérôme Lefrère, Simon Pigeon, Claire Adrados, Cristiano Ciuti, Iacopo Carusotto, Romuald Houdré, Elisabeth Giacobino, and Alberto Bramati. Superfluidity of polaritons in semiconductor microcavities. *Nature Physics*, 5(11):805–810, September 2009.

[17] K. G. Lagoudakis, M. Wouters, M. Richard, A. Baas, I. Carusotto, R. Andre, Le Si Dang, and B. Deveaud-Pledran. Quantized vortices in an exciton-polariton condensate. *Nat Phys*, 4(9):706–710, 09 2008.

[18] M. H. Anderson, J. R. Ensher, M. R. Matthews, C. E. Wieman, and E. A. Cornell. Observation of BoseEinstein condensation in a dilute atomic vapor. *Science*, (269):198–201, 1995.

[19] K. Davis and et al. BoseEinstein condensation in a gas of sodium atoms. *Physics Review Letters*, (75):3969–3973, 1995.

[20] Michael J. Hartmann, Fernando G. S. L. Brandão, and Martin B. Plenio. Strongly interacting polaritons in coupled arrays of cavities. *Nature Physics*, 2(12):849–855, nov 2006.

[21] Iulia Buluta and Franco Nori. Quantum simulators. *Science (New York, N.Y.)*, 326(5949):108–11, October 2009.

[22] Martin Leib and Michael J Hartmann. BoseHubbard dynamics of polaritons in a chain of circuit quantum electrodynamics cavities. *New Journal of Physics*, 12(9):093031, September 2010.

[23] T. Liew, a. Kavokin, and I. Shelykh. Optical Circuits Based on Polariton Neurons in Semiconductor Microcavities. *Physical Review Letters*, 101(1):016402, jul 2008.

[24] Alberto Amo, T. C. H. Liew, Claire Adrados, Romuald Houdré, Elisabeth Giacobino, a. V. Kavokin, and Alberto Bramati. Excitonpolariton spin switches. *Nature Photonics*, 4(June 2016):361–366, 2010.

[25] H. S. Nguyen, D. Vishnevsky, C. Sturm, D. Tanese, D. Solnyshkov, E. Galopin, A. Lemaître, I. Sagnes, A. Amo, G. Malpuech, and J. Bloch. Realization of a double-barrier resonant tunneling diode for cavity polaritons. *Phys. Rev. Lett.*, 110:236601, Jun 2013.

[26] D Ballarini, M De Giorgi, E Cancellieri, R Houdré, E Giacobino, R Cingolani, a Bramati, G Gigli, and D Sanvitto. All-optical polariton transistor. *Nature communications*, 4:1778, jan 2013.

[27] a. Imamoglu, R. Ram, S. Pau, and Y. Yamamoto. Nonequilibrium condensates and lasers without inversion: Exciton-polariton lasers. *Physical Review A*, 53(6):4250–4253, 1996.

[28] Michiel Wouters and Vincenzo Savona. Superfluidity of a nonequilibrium Bose-Einstein condensate of polaritons. *Physical Review B - Condensed Matter and Materials Physics*, 81(5):1–6, 2010.

[29] David A B Miller. Optical Physics of Quantum Wells. In *Quantum Dynamics of Simple Systems*, number September, pages 239–266. 1996.

[30] G. Christmann and J. J. Baumberg. The Future Prospects of Room-Temperature Polariton Lasers. In *Exciton Polaritons in Microcavities: New Frontiers*, chapter 13, page 332. Springer, 2012.

[31] Paul R. Berman and Vladimir S. Malinovsky. The Quantized, Free Radiation Field. In *Principles of Laser Spectroscopy and Quantum Optics*, chapter 12, pages 280–281. Princeton University Press, 2011.

[32] J. J. Hopfield. *Physics Review*, (112):1555, 1958.

[33] Jonathan Keeling, P. Eastham, M. Szymanska, and P. Littlewood. BCS-BEC crossover in a system of microcavity polaritons. *Physical Review B*, 72(11):115320, September 2005.

[34] Tim Byrnes, Tomoyuki Horikiri, Natsuko Ishida, and Yoshihisa Yamamoto. BCS wave-function approach to the BEC-BCS crossover of exciton-polariton condensates. *Physical Review Letters*, 105(18):2–5, 2010.

[35] Jan Klaers, Julian Schmitt, Frank Vewinger, and Martin Weitz. Bose-einstein condensation of photons in an optical microcavity. *Nature*, 468(7323):545–548, 11 2010.

[36] Natsuko Ishida, Tim Byrnes, Tomoyuki Horikiri, Franco Nori, and Yoshihisa Yamamoto. Photoluminescence of high-density exciton-polariton condensates. *Physical Review B - Condensed Matter and Materials Physics*, 90(24):1–5, 2014.

[37] T. Horikiri. *J. Phys. Soc. Jpn*, (82):084709, 2013.

[38] Tomoyuki Horikiri, Makoto Yamaguchi, Kenji Kamide, and Yasuhiro Matsuo. High-energy side-peak emission of exciton-polariton condensates in high density regime. *Nature Publishing Group*, pages 1–11, 2016.

[39] Andrew a. Houck, Hakan E. Türeci, and Jens Koch. On-chip quantum simulation with superconducting circuits. *Nature Physics*, 8(4):292–299, April 2012.

[40] Iacopo Carusotto and Cristiano Ciuti. Quantum fluids of light. *Reviews of Modern Physics*, 85(1):299–366, February 2013.

[41] Davide Rossini and Rosario Fazio. Mott-Insulating and Glassy Phases of Polaritons in 1D Arrays of Coupled Cavities. *Physical Review Letters*, 99(18):186401, October 2007.

[42] R. B. Balili, D. W. Snoke, L. Pfeiffer, and K. West. Actively tuned and spatially trapped polaritons. *Applied Physics Letters*, 88(3):031110, 2006.

[43] a. Rahimi-Iman, C. Schneider, J. Fischer, S. Holzinger, M. Amthor, S. Höfling, S. Reitzenstein, L. Worschech, M. Kamp, and a. Forchel. Zeeman splitting and diamagnetic shift of spatially confined quantum-well exciton polaritons in an external magnetic field. *Physical Review B*, 84(16):165325, October 2011.

[44] a. V. Larionov, V. D. Kulakovskii, S. Höfling, C. Schneider, L. Worschech, and a. Forchel. Polarized Nonequilibrium Bose-Einstein Condensates of Spinor Exciton Polaritons in a Magnetic Field. *Physical Review Letters*, 105(25):256401, December 2010.

[45] V. D. Kulakovskii, a. S. Brichkin, S. V. Novikov, C. Schneider, S. Höfling, M. Kamp, a. Forchel, and N. a. Gippius. Magnetic field control of polarized polariton condensates in rectangular microcavity pillars. *Physical Review B*, 85(15):155322, April 2012.

[46] Alex Hayat, Christoph Lange, Lee Rozema, Ardavan Darabi, Henry van Driel, Aephraim Steinberg, Bryan Nelsen, David Snoke, Loren Pfeiffer, and Kenneth West. Dynamic Stark Effect in Strongly Coupled Microcavity Exciton Polaritons. *Physical Review Letters*, 109(3):1–5, July 2012.

[47] Georgios Roumpos, Wolfgang H. Nitsche, Sven Höfling, Alfred Forchel, and Yoshihisa Yamamoto. Gain-Induced Trapping of Microcavity Exciton Polariton Condensates. *Physical Review Letters*, 104(12):126403, March 2010.

[48] G. Tosi, G. Christmann, N. G. Berloff, P. Tsotsis, T. Gao, Z. Hatzopoulos, P. G. Savvidis, and J. J. Baumberg. Sculpting oscillators with light within a nonlinear quantum fluid. *Nature Physics*, 8(2):1–5, January 2012.

[49] P. Cristofolini, a. Dreismann, G. Christmann, G. Franchetti, N. G. Berloff, P. Tsotsis, Z. Hatzopoulos, P. G. Savvidis, and J. J. Baumberg. Optical Superfluid Phase Transitions and Trapping of Polariton Condensates. *Physical Review Letters*, 110(18):186403, May 2013.

[50] C W Lai, N Y Kim, S Utsunomiya, G Roumpos, H Deng, M D Fraser, T Byrnes, P Recher, N Kumada, T Fujisawa, and Y Yamamoto. Coherent zero-state and pi-state in an exciton-polariton condensate array. *Nature*, 450(7169):529–32, November 2007.

[51] Na Young Kim, Kenichiro Kusudo, Congjun Wu, Naoyuki Masumoto, Andreas Löffler, Sven Höfling, Norio Kumada, Lukas Worschech, Alfred Forchel, and Yoshihisa Yamamoto. Dynamical d-wave condensation of excitonpolaritons in a two-dimensional square-lattice potential. *Nature Physics*, 7(9):681–686, June 2011.

[52] N Y Kim, K Kusudo, a Löffler, S Höfling, a Forchel, and Y Yamamoto. Excitonpolariton condensates near the Dirac point in a triangular lattice. *New Journal of Physics*, 15(3):035032, March 2013.

[53] Na Young Kim, Kenichiro Kusudo, Andreas Löffler, Sven Höfling, Alfred Forchel, and Yoshihisa Yamamoto. ¡Span Class="Aps-Inline-Formula"¿¡Math¿¡Mi¿F¡/Mi¿¡/Math¿¡/Span¿-Band Condensates in Exciton-Polariton Lattice Systems. *Physical Review B*, 89(8):085306, February 2014.

[54] a. Baas, O. El Daïf, M. Richard, J.-P. Brantut, G. Nardin, R. Idrissi Kaitouni, T. Guillet, V. Savona, J. L. Staehli, F. Morier-Genoud, and B. Deveaud. Zero dimensional exciton-polaritons. *Physica Status Solidi (B)*, 243(10):2311–2316, August 2006.

[55] O. El Daif, a. Baas, T. Guillet, J.-P. Brantut, R. Idrissi Kaitouni, J. L. Staehli, F. Morier-Genoud, and B. Deveaud. Polariton quantum boxes in semiconductor microcavities. *Applied Physics Letters*, 88(6):061105, 2006.

[56] Karol Winkler, Julian Fischer, Anne Schade, Matthias Amthor, Robert Dall, Jonas Geler, Monika Emmerling, Elena A Ostrovskaya, Martin Kamp, Christian Schneider, and Sven Hfling. A polariton condensate in a photonic crystal potential landscape. *New Journal of Physics*, 17(2):023001, 2015.

[57] Daniele Bajoni, Pascale Senellart, Esther Wertz, Isabelle Sagnes, Audrey Miard, Aristide Lemaître, and Jacqueline Bloch. Polariton Laser Using Single Micropillar GaAs-GaAlAs Semiconductor Cavities. *Physical Review Letters*, 100(4):1–4, January 2008.

[58] Lydie Ferrier, Esther Wertz, Robert Johne, Dmitry Solnyshkov, Pascale Senellart, Isabelle Sagnes, Aristide Lemaître, Guillaume Malpuech, and Jacqueline Bloch. Interactions in Confined Polariton Condensates. *Physical Review Letters*, 106(12):1–4, March 2011.

[59] Marta Galbiati, Lydie Ferrier, Dmitry Solnyshkov, Dimitrii Tanese, Esther Wertz, Alberto Amo, Marco Abbarchi, Pascale Senellart, Isabelle Sagnes, Aristide Lemaître, Elisabeth Galopin, Guillaume Malpuech, and Jacqueline Bloch. Polariton Condensation in Photonic Molecules. *Physical Review Letters*, 108(12):1–5, March 2012.

[60] E. Wertz, L. Ferrier, D. D. Solnyshkov, R. Johne, D. Sanvitto, A. Lemaître, I. Sagnes, R. Grousson, A. V. Kavokin, P. Senellart, G. Malpuech, and J. Bloch. Spontaneous formation and optical manipulation of extended polariton condensates. *Nature Physics*, 6(11):860–864, August 2010.

[61] T. Jacqmin, I. Carusotto, I. Sagnes, M. Abbarchi, D.D. Solnyshkov, G. Malpuech, E. Galopin, a. Lemaître, J. Bloch, and a. Amo. Direct Observation of Dirac Cones and a Flatband in a Honeycomb Lattice for Polaritons. *Physical Review Letters*, 112(11):116402, March 2014.

[62] Michael Chung-yi Huang. Nano-Electromechanical Optoelectronic Tunable Lasers. 2008.

[63] Eugen Merzbacher. *Quantum Mechanics*. Wiley, 1998.

[64] Y. Yamamoto, T. Tassone, and Hui Cao. *Semiconductor Cavity Quantum Electrodynamics*. Springer, 2000.

[65] L. C. Andreani, E. Burstein, and C. Weisbuch. Plenum, New York, 1995.

[66] Lucio Claudio Andreani and Alfredo Pasquarello. Accurate theory of excitons in GaAs- Ga 1 x Al x As quantum wells. *Physical Review B*, 42(14):8928–8938, 1990.

[67] R. Houdré, R. P. Stanley, U. Oesterle, M. Ilegems, and C. Weisbuch. Room-temperature cavity polaritons in a semiconductor microcavity. *Physical Review B*, 49(23):16761–16764, 1994.

[68] Yifu Zhu, Daniel J. Gauthier, S. E. Morin, Qilin Wu, H. J. Carmichael, and T. W. Mossberg. Vacuum Rabi splitting as a feature of linear-dispersion theory: Analysis and experimental observations. *Physical Review Letters*, 64(21):2499–2502, 1990.

[69] B. I. Green, J. Orenstein, and S. Schmitt-Rink. *Science*, (247):679, 1989.

[70] V. S. Williams, S. Mazumdar, N. R. Armstrong, Z. Z. Ho, and N. Peyghambarian. *J. Phys. Chem.*, (96):4500, 1992.

[71] M. de Lima, M. van der Poel, P. Santos, and J. Hvam. Phonon-Induced Polariton Superlattices. *Physical Review Letters*, 97(4):045501, July 2006.

[72] K. Winkler, C. Schneider, J. Fischer, A. Rahimi-Iman, M. Amthor, A. Forchel, S. Reitzenstein, S. Hofling, and M. Kamp. Electroluminescence from spatially confined exciton polaritons in a textured microcavity. *Applied Physics Letters*, 102(4):041101, 2013.

[73] a. S. Brichkin, S. I. Novikov, a. V. Larionov, V. D. Kulakovskii, M. M. Glazov, C. Schneider, S. Höfling, M. Kamp, and a. Forchel. Effect of Coulomb interaction on exciton-polariton condensates in GaAs pillar microcavities. *Physical Review B*, 84(19):195301, November 2011.

[74] Carlos F R Mateus, Student Member, Michael C Y Huang, Lu Chen, Connie J Chang-hasnain, and Yuri Suzuki. Broad-Band Mirror (1.12-1.62 um) Using a Subwavelength Grating. *IEEE Photonics Technology Letters*, 16(7):1676–1678, 2004.

[75] Steven J Schablitsky, Lei Zhuang, Rick C Shi, and Stephen Y Chou. Controlling polarization of vertical-cavity surface-emitting lasers using amorphous silicon subwavelength transmission gratings. *Applied Physics Letters*, 69(July):7–9, 1996.

[76] Michael C. Y. Huang, Ye Zhou, and Connie J. Chang-Hasnain. A nanoelectromechanical tunable laser. *Nature Photonics*, 2(3):180–184, February 2008.

[77] Michael C.Y. Huang, Y. Zhou, and Connie J. Chang-Hasnain. A surface-emitting laser incorporating a high-index-contrast subwavelength grating. *Nature Photonics*, 1(2):119122, February 2007.

[78] Lord Rayleigh. On the dynamical theory of gratings. *Proceedings of the Royal Society of London A: Mathematical, Physical and Engineering Sciences*, 79(532):399–416, 1907.

[79] D. Maystre. A new general integral theory for dielectric coated gratings. *J. Opt. Soc. Am.*, 68(4):490–495, Apr 1978.

[80] E. Popov and M. Nevière. Differential theory for diffraction gratings:a new formulation for tm polarization with rapid convergence. *Opt. Lett.*, 25(9):598–600, May 2000.

[81] M. G. Moharam and T. K. Gaylord. Rigorous coupled-wave analysis of planar-grating diffraction. *J. Opt. Soc. Am.*, 71:811–818, 1981.

[82] M. G. Moharam and T. K. Gaylord. Rigorous coupled-wave analysis of dielectric surface-relief gratings. *J. Opt. Soc. Am.*, 72:1385–1392, 1982.

[83] G. Raoult J. Chandezon, D. Maystre. A new theoretical method for diffraction gratings and its numerical application. *J. Optics (Paris)*, 11:235–241, 1980.

[84] G. Raoult J. Chandezon, D. Maystre. Multicoated gratings: A differential formalism applicable in the entire optical region. *J. Opt. Soc. Am.*, 72:839–846, 1982.

[85] M. G. Moharam, Drew a. Pommet, Eric B. Grann, and T. K. Gaylord. Stable implementation of the rigorous coupled-wave analysis for surface-relief gratings: enhanced transmittance matrix approach. *Journal of the Optical Society of America A*, 12(5):1077, may 1995.

[86] Philippe Lalanne and G Michael Morris. Highly improved convergence of the coupled-wave method for TM polarization. *Journal of the Optical Society of America A*, 13(4):779–784, 1996.

[87] Lifeng Li. Use of Fourier series in the analysis of discontinuous periodic structures. *Journal of the Optical Society of America A*, 13(9):1870–1876, 1996.

[88] Lifeng Li. New formulation of the Fourier modal method for crossed surface-relief gratings. *Journal of the Optical Society of America A*, 14(10):2758, oct 1997.

[89] Carlos F R Mateus, Student Member, Michael C Y Huang, Yunfei Deng, Andrew R Neureuther, and Connie J Chang-hasnain. Ultrabroadband mirror using low-index cladded subwavelength grating. *IEEE Photonics Technology Letters*, 16(2):518520, 2004.

[90] Virginie Lousse, Wonjoo Suh, Onur Kilic, Sora Kim, Olav Solgaard, and Shanhui Fan. Angular and polarization properties of a photonic crystal slab mirror. *Optics express*, 12(8):1575–82, apr 2004.

[91] G. A. Samara. Temperature and pressure dependences of the dielectric constants of semiconductors. *Physical Review B*, 27:3494–3505, 1983.

[92] Robert Magnusson. Wideband reflectors with zero-contrast gratings. *Opt. Lett.*, 39(15):4337–4340, Aug 2014.

[93] Mehrdad Shokooh-Saremi and Robert Magnusson. Properties of two-dimensional resonant reflectors with zero-contrast gratings. *Optics Letters*, 39(24):6958, 2014.

[94] M. Gebski, M. Dems, A. Szerling, M. Motyka, L. Marona, R. Kruszka, D. Urbanczyk, M. Walczakowski, N. Palka, A. Wojcik-Jedlinska, Q. J. Wang, D. H. Zhang, M. Bugajski, M. Wasiak, and T. Czyszanowski. Monolithic high-index contrast grating: a material independent high-reflectance {VCSEL} mirror. *Optics Express*, 23(9):11674–11686, 2015.

[95] Bo Zhang, Zhaorong Wang, Sebastian Brodbeck, Christian Schneider, Martin Kamp, Sven Höfling, and Hui Deng. Zero-dimensional polariton laser in a subwavelength grating-based vertical microcavity. *Light: Science & Applications*, 3(1):e135, January 2014.

[96] a. P. D. Love, D. N. Krizhanovskii, D. M. Whittaker, R. Bouchekioua, D. Sanvitto, S. Al Rizeiqi, R. Bradley, M. S. Skolnick, P. R. Eastham, R. André, and Le Si Dang. Intrinsic Decoherence Mechanisms in the Microcavity Polariton Condensate. *Physical Review Letters*, 101(6):067404, August 2008.

[97] C Weisbuch, M Nishioka, a Ishikawa, and Y Arakawa. Observation of the coupled exciton-photon mode splitting in a semiconductor quantum microcavity., December 1992.

[98] Le Dang, D. Heger, R. André, F. Bœuf, and R. Romestain. Stimulation of Polariton Photoluminescence in Semiconductor Microcavity. *Physical Review Letters*, 81(18):3920–3923, 1998.

[99] F. Tassone. Exciton-exciton scattering dynamics in a semiconductor microcavity and stimulated scattering into polaritons. *Physical Review B*, 22(16):389–10842, April 1999.

[100] Pg Savvidis, Jj Baumberg, Rm Stevenson, Ms Skolnick, Dm Whittaker, and Js Roberts. Angle-resonant stimulated polariton amplifier. *Physical review letters*, 84(7):1547–50, February 2000.

[101] P. Senellart, J. Bloch, B. Sermage, and J. Y. Marzin. Microcavity polariton depopulation as evidence for stimulated scattering. *Physical Review B - Condensed Matter and Materials Physics*, 62(24):263–266, 2000.

[102] et al T. Horikiri. Higher order coherence of excitonpolariton condensates. *Phys. Rev. B*, 81:033307, 2010.

[103] Marc Assmann, Jean-Sebastian Tempel, Franziska Veit, Manfred Bayer, Arash Rahimi-Iman, Andreas Löffler, Sven Höfling, Stephan Reitzenstein, Lukas Worschech, and Alfred Forchel. From polariton condensates to highly photonic quantum degenerate states of bosonic matter. *Proceedings of the National Academy of Sciences of the United States of America*, 108(5):1804–9, feb 2011.

[104] Matthias Amthor, Sebastian Weißenseel, Julian Fischer, Martin Kamp, Christian Schneider, and Sven Höfling. Electro-optical switching between polariton and cavity lasing in an ingaas quantum well microcavity. *Opt. Express*, 22(25):31146–31153, Dec 2014.

[105] J. Kasprzak, M. Richard, a. Baas, B. Deveaud, R. André, J.-Ph. Poizat, and Le Dang. Second-Order Time Correlations within a Polariton Bose-Einstein Condensate in a CdTe Microcavity. *Physical Review Letters*, 100(6):067402, February 2008.

[106] Hui Deng, G.S. Solomon, Rudolf Hey, K.H. Ploog, and Yoshihisa Yamamoto. Spatial coherence of a polariton condensate. *Physical review letters*, 99(12):126403, 2007.

[107] Neil Na and Yoshihisa Yamamoto. Massive parallel generation of indistinguishable single photons via the polaritonic superfluid to Mott-insulator quantum phase transition. *New Journal of Physics*, 12(12):123001, dec 2010.

[108] M. Vladimirova, S. Cronenberger, D. Scalbert, K. V. Kavokin, A. Miard, A. Lemaître, J. Bloch, D. Solnyshkov, G. Malpuech, and a. V. Kavokin. Polariton-polariton interaction constants in microcavities. *Physical Review B*, 82(7):075301, aug 2010.

[109] D. N. Krizhanovskii, D. Sanvitto, a. P D Love, M. S. Skolnick, D. M. Whittaker, and J. S. Roberts. Dominant effect of polariton-polariton interactions on the coherence of the microcavity optical parametric oscillator. *Physical Review Letters*, 97(9):1–4, 2006.

[110] Wei Xie, Hongxing Dong, Saifeng Zhang, Liaoxin Sun, Weihang Zhou, Yanjing Ling, Jian Lu, Xuechu Shen, and Zhanghai Chen. Room-temperature polariton parametric scattering driven by a one-dimensional polariton condensate. *Physical Review Letters*, 108(16):1–5, 2012.

[111] a. Verger, C. Ciuti, and I. Carusotto. Polariton quantum blockade in a photonic dot. *Physical Review B*, 73(19):193306, May 2006.

[112] T. C. H. Liew, A. V. Kavokin, T. Ostatnický, M. Kaliteevski, I. A. Shelykh, and R. A. Abram. Exciton-polariton integrated circuits. *Physical Review B*, 82(3):033302, July 2010.

[113] S Schmitt-Rink, D S Chemla, and D A B Miller. Theory of transient excitonic optical nonlinearities in semiconductor quantum-well structures. *Phys. Rev. B*, 32(10):6601–6609, 1985.

[114] C. Ciuti, V. Savona, C. Piermarocchi, a. Quattropani, and P. Schwendimann. Role of the exchange of carriers in elastic exciton-exciton scattering in quantum wells. *Physical Review B*, 58(12):7926–7933, sep 1998.

[115] M Richard, J Kasprzak, R André, R Romestain, and Le Si Dang. Experimental evidence for nonequilibrium Bose condensation of exciton polaritons. *Phys. Rev. B*, pages 1–4, 2005.

[116] D. Sanvitto, a. Amo, L. Viña, R. André, D. Solnyshkov, and G. Malpuech. Exciton-polariton condensation in a natural two-dimensional trap. *Physical Review B - Condensed Matter and Materials Physics*, 80(4):1–6, 2009.

[117] C. Ciuti, P. Schwendimann, B. Deveaud, and a. Quattropani. Theory of the angle-resonant polariton amplifier. *Physical Review B*, 62(8):R4825–R4828, aug 2000.

[118] G. Rochat, C. Ciuti, V. Savona, C. Piermarocchi, a. Quattropani, and P. Schwendimann. Excitonic Bloch equations for a two-dimensional system of interacting excitons. *Physical Review B*, 61(20):13856–13862, 2000.

[119] R Houdre. Saturation of the strong-coupling regime in a semiconductor microcavity: Free-carrier bleaching of cavity polaritons. *Phys. Rev. B*, 52(11):7810–7813, 1995.

[120] J. K. Rhee, D. S. Citrin, T. B. Norris, Y. Arakawa, and M. Nishioka. Femtosecond dynamics of semiconductor-microcavity polaritons in the nonlinear regime. *Solid State Communications*, 97(11):941–946, 1996.

[121] Raphaël Butté, Jacques Levrat, Gabriel Christmann, Eric Feltin, Jean-François Carlin, and Nicolas Grandjean. Phase diagram of a polariton laser from cryogenic to room temperature. *Physical Review B*, 80(23):233301, dec 2009.

[122] Georg Rossbach, Jacques Levrat, Eric Feltin, Jean-François Carlin, Raphaël Butté, and Nicolas Grandjean. Impact of saturation on the polariton renormalization in III-nitride based planar microcavities. *Physical Review B*, 88(16):165312, oct 2013.

[123] K S Daskalakis, S a Maier, R Murray, and S Kéna-Cohen. Nonlinear interactions in an organic polariton condensate. *Nature materials*, 13(3):271–8, March 2014.

[124] Michael C.Y. Huang, Y. Zhou, and Connie J. Chang-Hasnain. A surface-emitting laser incorporating a high-index-contrast subwavelength grating. *Nature Photonics*, 1(2):119–122, February 2007.

[125] K. G. Lagoudakis, F. Manni, B. Pietka, M. Wouters, T. C H Liew, V. Savona, a. V. Kavokin, R. André, and B. Deveaud-Plédran. Probing the dynamics of spontaneous quantum vortices in polariton superfluids. *Physical Review Letters*, 106(11):1–4, 2011.

[126] Milena De Giorgi, Dario Ballarini, Paolo Cazzato, George Deligeorgis, Simos I. Tsintzos, Zacharias Hatzopoulos, Pavlos G. Savvidis, Giuseppe Gigli, Fabrice P. Laussy, and Daniele Sanvitto. Relaxation oscillations in the formation of a polariton condensate. *Physical Review Letters*, 112(11):1–5, 2014.

[127] T Amand, D Robart, X Marie, M Brousseau, P Le Jeune, and J Barrau. Spin relaxation in polarized interacting exciton gas in quantum wells. *Physical Review B*, 55(15):9880, 1997.

[128] J Keeling, F M Marchetti, M H Szymaska, and P B Littlewood. Collective coherence in planar semiconductor microcavities. *Semiconductor Science and Technology*, 22(5):R1–R26, May 2007.

[129] Erich Runge. Excitons in semiconductor nanostructures. *Solid State Physics*, 57:149 – 305, 2003.

[130] Seonghoon Kim, Bo Zhang, Zhaorong Wang, Julian Fischer, Sebastian Brodbeck, Martin Kamp, Christian Schneider, Sven H??fling, and Hui Deng. Coherent polariton laser. *Physical Review X*, 6(1):1–9, 2016.

[131] S. Utsunomiya, L. Tian, G. Roumpos, C. W. Lai, N. Kumada, T. Fujisawa, M. Kuwata-Gonokami, a. Löffler, S. Höfling, a. Forchel, and Y. Yamamoto. Observation of Bogoliubov excitations in exciton-polariton condensates. *Nature Physics*, 4(9):700–705, aug 2008.

[132] Tomoyuki Horikiri, Yasuhiro Matsuo, Yutaka Shikano, Andreas Loeffler, Sven Hoefling, Alfred Forchel, and Yoshihisa Yamamoto. Temperature Dependence of Highly Excited Exciton Polaritons in Semiconductor Microcavities. 2012.

[133] P B Littlewood, P R Eastham, J M J Keeling, F M Marchetti, B D Simons, and M H Szymanska. Models of coherent exciton condensation. *Journal of Physics: Condensed Matter*, 16(35):S3597–S3620, September 2004.

[134] G Khitrova and H M Gibbs. Nonlinear optics of normal-mode-coupling semiconductor microcavities. *Reviews of Modern Physics*, 71(5), 1999.

[135] Hui Deng and Yoshihisa Yamamoto. Exciton-polariton bose-einstein condensation. *Reviews of Modern Physics*, 82(2):14891537, May 2010.

[136] Daniele Sanvitto and Stéphane Kéna-Cohen. The road towards polaritonic devices. *Nature Materials*, 15(July):doi:10.1038/nmat4668, 2016.

[137] S. Reitzenstein, C. Hofmann, A. Gorbunov, M. Strau, S. H. Kwon, C. Schneider, A. Lffler, S. Hfling, M. Kamp, and A. Forchel. Alasgaas micropillar cavities with quality factors exceeding 150.000. *Applied Physics Letters*, 90(25):251109, 2007.

[138] Bryan Nelsen, Gangqiang Liu, Mark Steger, David W. Snoke, Ryan Balili, Ken West, and Loren Pfeiffer. Dissipationless flow and sharp threshold of a polariton condensate with long lifetime. *Phys. Rev. X*, 3:041015, Nov 2013.

[139] Gabriel Christmann, Raphael Butte, Eric Feltin, Jean-Francois Carlin, and Nicolas Grandjean. Room temperature polariton lasing in a GaN/AlGaN multiple quantum well microcavity. *Applied Physics Letters*, 93:051102–3, 2008. 5.

[140] Ayan Das, Junseok Heo, Marc Jankowski, Wei Guo, Lei Zhang, Hui Deng, and Pallab Bhattacharya. Room temperature ultralow threshold GaN nanowire polariton laser. *Phys. Rev. Lett.*, 107:066405, 2011.

[141] S Kena-Cohen and S. R. Forrest. Room-temperature polariton lasing in an organic single-crystal microcavity. *Nat Photon*, 4(6):371–375, June 2010.

[142] Xiaoze Liu, Tal Galfsky, Zheng Sun, Fengnian Xia, and Erh-chen Lin. Strong light-matter coupling in two-dimensional atomic crystals. *Nature Photonics*, 9(1):30–34, 2015.

[143] Y. Yamamoto, S. MacHida, and G. Björk. Microcavity semiconductor laser with enhanced spontaneous emission. *Physical Review A*, 44(1):657–668, 1991.

[144] Tb Norris, J Rhee, C Sung, Y Arakawa, M Nishioka, and C Weisbuch. Time-resolved vacuum Rabi oscillations in a semiconductor quantum microcavity. *Physical review. B, Condensed matter*, 50(19):14663–14666, nov 1994.

[145] C. Grossmann, C. Coulson, G. Christmann, I. Farrer, H. E. Beere, D. a. Ritchie, and J. J. Baumberg. Tuneable polaritonics at room temperature with strongly coupled Tamm plasmon polaritons in metal/air-gap microcavities. *Applied Physics Letters*, 98(23):231105, 2011.

[146] T. R. Nelson, J. P. Prineas, G. Khitrova, H. M. Gibbs, J. D. Berger, E. K. Lindmark, J.-H. Shin, H.-E. Shin, Y.-H. Lee, P. Tayebati, and L. Javniskis. Room-temperature normal-mode coupling in a semiconductor microcavity utilizing native-oxide AlAl/GaAs mirrors. *Applied Physics Letters*, 69(20):3031, 1996.

[147] L A Graham, Q Deng, D G Deppe, and D L Huffaker. Exciton spectral splitting near room temperature from high contrast semiconductor microcavities. *Applied Physics Letters*, 70(Feburary):814–816, 1997.

[148] a. R. Pratt, T. Takamori, and T. Kamijoh. Photoluminescence study of cavity-polariton-mode splitting using high-contrast selectively oxidized AlAs/GaAs mirrors. *Applied Physics Letters*, 74(13):1869, 1999.

[149] J. Gessler, T. Steinl, A. Mika, J. Fischer, G. Sęk, J. Misiewicz, S. Höfling, C. Schneider, and M. Kamp. Low dimensional GaAs/air vertical microcavity lasers. *Applied Physics Letters*, 104(8):081113, 2014.

[150] Bo Zhang, Zhaorong Wang, Sebastian Brodbeck, Christian Schneider, Martin Kamp, Sven Höfling, and Hui Deng. Zero-dimensional polariton laser in a subwavelength grating-based vertical microcavity. *Light: Science & Applications*, 3(1):e135, January 2014.

[151] Zhaorong Wang, Bo Zhang, and Hui Deng. Dispersion Engineering for Vertical Microcavities Using Subwavelength Gratings. *Physical Review Letters*, 114(7):1–6, 2015.

[152] Bo Zhang, Sebastian Brodbeck, Zhaorong Wang, Martin Kamp, Christian Schneider, Sven Höfling, and Hui Deng. Coupling polariton quantum boxes in sub-wavelength grating microcavities. *Applied Physics Letters*, 106(5), 2015.

[153] J. S. Foresi, P. R. Villeneuve, J. Ferrera, E. R. Thoen, G. Steinmeyer, S. Fan, J. D. Joannopoulos, L. C. Kimerling, Henry I. Smith, and E. P. Ippen. Photonic-bandgap microcavities in optical waveguides. *Nature*, 390(6656):143–145, 1997.

[154] P. T. Kristensen, C. Van Vlack, and S. Hughes. Generalized effective mode volume for leaky optical cavities. *Optics Letters*, 37(10):1649, 2012.

[155] Eli Yablonovitch, T. Gmitter, J. P. Harbison, and R. Bhat. Extreme selectivity in the lift-off of epitaxial GaAs films. *Applied Physics Letters*, 51(26):2222–2224, 1987.

[156] M. Kaliteevski, I. Iorsh, S. Brand, R. A. Abram, J. M. Chamberlain, A. V. Kavokin, and I. A. Shelykh. Tamm plasmon-polaritons: Possible electromagnetic states at the interface of a metal and a dielectric Bragg mirror. *Physical Review B - Condensed Matter and Materials Physics*, 76(16):1–5, 2007.

[157] V. Savona, L. C. Andreani, P. Schwendimann, and A. Quattropani. Quantum well excitons in semiconductor microcavities: Unified treatment of weak and strong coupling regimes. *Solid State Communications*, 93(9):733–739, 1995.

[158] J. Fischer, S. Brodbeck, B. Zhang, Z. Wang, L. Worschech, H. Deng, M. Kamp, C. Schneider, and S. Hfling. Magneto-exciton-polariton condensation in a subwavelength high contrast grating based vertical microcavity. *Applied Physics Letters*, 104(9):–, 2014.

[159] S Kéna-Cohen, M. Davanço, and S. Forrest. Strong Exciton-Photon Coupling in an Organic Single Crystal Microcavity. *Physical Review Letters*, 101(11):1–4, 2008.

[160] Kanna Aoki, Denis Guimard, Masao Nishioka, Masahiro Nomura, Satoshi Iwamoto, and Yasuhiko Arakawa. Coupling of quantum-dot light emission with a three-dimensional photonic-crystal nanocavity. *Nature Photonics*, 2(11):688–692, October 2008.

[161] C. Sciancalepore, B. Ben Bakir, C. Seassal, X. Letartre, J. Harduin, N. Olivier, J. Fedeli, and P. Viktorovitch. Thermal, Modal, and Polarization Features of Double Photonic Crystal Vertical-Cavity Surface-Emitting Lasers. *IEEE Photonics Journal*, 4(2):399–410, April 2012.

[162] Michael J. Hartmann, Fernando G. S. L. Brandão, and Martin B. Plenio. Strongly interacting polaritons in coupled arrays of cavities. *Nature Physics*, 2(12):849–855, November 2006.

[163] Robert W Boyd and Daniel J Gauthier. Controlling the velocity of light pulses. *Science (New York, N.Y.)*, 326(5956):10747, November 2009.

[164] Serge Haroche and Daniel Kleppner. Cavity quantum electrodynamics. *Physics Today*, 42(1):24–30, 1989.

[165] Y.-J. Lin, K. Jimnez-Garca, and I. B. Spielman. Spin-orbit-coupled bose-einstein condensates. *Nature*, 471(7336):83–86, March 2011.

[166] Hannah M. Price, Tomoki Ozawa, and Iacopo Carusotto. Quantum mechanics under a momentum space artificial magnetic field. *arXiv:1403.6041 [cond-mat, physics:quant-ph]*, March 2014. arXiv: 1403.6041.

[167] Vladimir M. Shalaev. Optical negative-index metamaterials. *Nature Photonics*, 1(1):4148, January 2007.

[168] Z. Jacob, J.-Y. Kim, G. V. Naik, A. Boltasseva, E. E. Narimanov, and V. M. Shalaev. Engineering photonic density of states using metamaterials. *Applied Physics B*, 100(1):215–218, June 2010.

[169] M A Noginov, H Li, Yu A Barnakov, D Dryden, G Nataraj, G Zhu, C E Bonner, M Mayy, Z Jacob, and E E Narimanov. Controlling spontaneous emission with metamaterials. *Optics letters*, 35(11):1863–5, June 2010.

[170] Harish N. S. Krishnamoorthy, Zubin Jacob, Evgenii Narimanov, Ilona Kretzschmar, and Vinod M. Menon. Topological transitions in metamaterials. *Science*, 336(6078):205–209, April 2012. PMID: 22499943.

[171] T F Krauss. Slow light in photonic crystal waveguides. *Journal of Physics D: Applied Physics*, 40(9):26662670, May 2007.

[172] Toshihiko Baba. Slow light in photonic crystals. *Nature Photonics*, 2(8):465473, August 2008.

[173] Susumu Noda, Masayuki Fujita, and Takashi Asano. Spontaneous-emission control by photonic crystals and nanocavities. *Nature Photonics*, 1:449–458, 2007.

[174] Jean Dalibard, Fabrice Gerbier, Gediminas Juzeliūnas, and Patrik Öhberg. *Colloquium* : Artificial gauge potentials for neutral atoms. *Rev. Mod. Phys.*, 83:1523–1543, Nov 2011.

[175] Vadim Karagodsky, Bala Pesala, Christopher Chase, Werner Hofmann, Fumio Koyama, and Connie J. Chang-Hasnain. Monolithically integrated multiwavelength VCSEL arrays using high-contrast gratings. *Optics Express*, 18(2):694–699, January 2010.

[176] Yi Rao, Christopher Chase, and Connie J. Chang-Hasnain. Multiwavelength HCG-VCSEL array. *22nd IEEE International Semiconductor Laser Conference*, pages 11–12, September 2010.

[177] Robert Magnusson and Mehrdad Shokooh-Saremi. Physical basis for wideband resonant reflectors. *Optics express*, 16(5):3456–62, March 2008.

[178] Vadim Karagodsky, Christopher Chase, and Connie J Chang-Hasnain. Matrix Fabry-Perot resonance mechanism in high-contrast gratings. *Optics letters*, 36(9):1704–6, May 2011.

[179] Vadim Karagodsky and Connie J Chang-hasnain. Physics of near-wavelength high contrast gratings. *Optics Express*, 20(10):1088810895, 2012.

[180] Nima Arjmandi, Liesbet Lagae, and Gustaaf Borghs. Enhanced resolution of poly(methyl methacrylate) electron resist by thermal processing. *Journal of Vacuum Science & Technology B*, 27(4):1915–1918, 2009.

[181] Huigao Duan, Vitor R. Manfrinato, Joel K. W. Yang, Donald Winston, Bryan M. Cord, and Karl K. Berggren. Metrology for electron-beam lithography and resist contrast at the sub-10 nm scale. *Journal of Vacuum Science & Technology B*, 28(6):C6H11–C6H17, 2010.

[182] Vitor R. Manfrinato, Lihua Zhang, Dong Su, Huigao Duan, Richard G. Hobbs, Eric A. Stach, and Karl K. Berggren. Resolution limits of electron-beam lithography toward the atomic scale. *Nano Letters*, 13(4):1555–1558, 2013. PMID: 23488936.

[183] E. M. Purcell, H. C. Torrey, and R. V. Pound. Resonance absorption by nuclear magnetic moments in a solid. *Physical Review*, 69(1-2):37–38, January 1946.

[184] Iacopo Carusotto and Cristiano Ciuti. Quantum fluids of light. *Reviews of Modern Physics*, 85(1):299–366, 2013.

[185] J. J. Hopfield and D. G. Thomas. Theoretical and experimental effects of spatial dispersion on the optical properties of crystals. *Physical Review*, 132:563, 1963. 2.

[186] H. Deng, G. Weihs, D. Snoke, J. Bloch, and Y. Yamamoto. Polariton lasing vs. photon lasing in a semiconductor microcavity. *Proceedings of the National Academy of Sciences of the United States of America*, 100(26):15318, 2003.

[187] Tien-Chang Lu, Ying-Yu Lai, Yu-Pin Lan, Si-Wei Huang, Jun-Rong Chen, Yung-Chi Wu, Wen-Feng Hsieh, and Hui Deng. Room temperature polariton lasing vs. photon lasing in a ZnO-based hybrid microcavity. *Opt. Express*, 20(5):5530–5537, February 2012.

[188] C. Comte and P. Nozières. Exciton bose condensation: the ground state of an electrion-hole gas i. mean field description of a simplified model. *J. Phys.*, 43:1069—1081, 1982.

[189] P. B. Littlewood, P. R. Eastham, J. M. J. Keeling, F. M. Marchetti, B. D. Simon, and M. H. Szymanska. Models of coherent exciton condensation. *J. Phys.: Cond. Matt.*, 16:S3597—S3620, 2004. 35.

[190] Tim Byrnes, Tomoyuki Horikiri, Natsuko Ishida, and Yoshihisa Yamamoto. BCS wave-function approach to the BEC-BCS crossover of exciton-polariton condensates. *Physical Review Letters*, 105(18):186402, October 2010.

[191] T.C.H. Liew, I.a. Shelykh, and G. Malpuech. Polaritonic devices. *Physica E: Low-dimensional Systems and Nanostructures*, 43(9):15431568, July 2011.

[192] Roberto E. Troncoso and lvaro S. Nez. Josephson effects in a boseeinstein condensate of magnons. *Annals of Physics*, 346(0):182 – 194, 2014.